Bioinspired Control of Rudderless Morphing UAVs

by

Lawren L. Gamble

A dissertation submitted in partial fulfillment
of the requirements for the degree of
Doctor of Philosophy
(Aerospace Engineering)
in the University of Michigan
2018

Doctoral Committee:

Professor Daniel J. Inman, Chair
Professor Douglas L. Altshuler, University of British Columbia
Professor Carlos E. Cesnik
Professor Henry A. Sodano

Lawren L. Gamble
llgamble@umich.edu
ORCID iD: 0000-0002-9568-9562

2018

This work in its entirety is dedicated to my mother without whom this academic journey would not have been possible.

ACKNOWLEDGEMENTS

I'd like to give my deepest appreciation to all those who have helped me throughout this grand undertaking. I feel incredibly lucky to have had such a wonderful support system.

First and foremost, I'd like to thank my advisor Dr. Daniel J. Inman. He took a chance on me when no one else would. Over the years his support, mentorship, and friendship is what allowed me to thrive through academic perseverance and self-discovery. He's allowed me to forge my own path in research and has listened to (and encouraged!) each of my crazy ideas. But more importantly he's made research fun. Most would say he's a kid at heart, with a can-do attitude and a genuine curiosity for the unknown, excited to discover the undiscovered. This mentality at times seems to have been forgotten throughout the sciences, but that I attribute to my overall success. I am so grateful for the environment of openness, trust and mutual respect which he strives to achieve.

I also owe a big thank you to my entire committee for providing their expert insight and opinion. This endeavor proved to be fully multidisciplinary, covering aerodynamics, composite materials, and biology simultaneously. Dr. Carlos Cesnik's expertise on aerodynamics and aeroelasticity as both my teacher and committee member was invaluable to the fluid modeling and experiments. Dr. Henry Sodano's expertise on composite and multifunctional materials was instrumental to the development and analysis of the custom Macro Fiber Composite (MFC)s. Doug Altshuler's expertise on avian flight mechanics was extremely influential in the design and development of the bioinspired actuator. Furthermore, I have appreciated both Henry Sodano and Doug Altshuler's input throughout this dissertation as joint members of our grant.

Additional thanks go out to my lab mates Jared Hobeck, Alex Pankonien, Katie Reichl,

Brittany Essink, Andrew Lee, Krystal Acosta, and Lori Groo who have been nothing but supportive. I can't imagine a better group of peers and colleagues to have worked alongside throughout this process. A special thanks is also owed to Alex Pankonien, who I feel very lucky to have worked with. His expertise and mentorship shaped the foundation of my path forward for the better. Without him, my experiments would not nearly have gone as seamlessly as they did.

I am deeply thankful for the assistance of the technical staff within the department as well. The wind tunnel assistance provided by Chris Chartier, precision manufacturing of Terry Larrow, and overall technical support provided by Tom Griffin were all key to my success. The department would be nothing without them.

I'd also like to thank the faculty and staff at the Smith College Picker Engineering Program. The support and education that I received was unparalleled and no doubt instrumental in my pursuit of a doctoral degree. They gave me the tools, confidence and fearlessness to find solutions to problems which I did not know the answer. I learned to not be afraid of the unknown, and to tackle it headfirst.

Lastly, I'd like to thank the University of Michigan and the US Air Force Office of Scientific Research for providing the funding which supported this research. This work is supported in part by the US Air Force Office of Scientific Research under a grant number FA9550-16-1-0087, titled "Avian-Inspired Multifunctional Morphing Vehicles" monitored by Dr. BL Lee.

TABLE OF CONTENTS

LIST OF FIGURES

LIST OF TABLES

LIST OF ABBREVIATIONS

ABL Atmospheric Boundary Layer

CFD Computational Fluid Dynamics

FEM Finite Element Method

PZT Lead Zirconate Titanate

LLT Lifting Line Theory

MFC Macro Fiber Composite

MACW Mission Adaptive Compliant Wing

MLT MultiStripe Laser Triangulation

RANS Reynolds Averaged Navier Stokes

RMSE Root Mean Squared Error

SMA Shape Memory Alloy

SNR Signal to Noise Ratio

SMTE Spanwise Morphing Trailing Edge

UAV Unmanned Aerial Vehicle

VCCTEF Variable Camber Continuous Trailing Edge Flap

LIST OF SYMBOLS

Geometric Parameters

AR	Aspect ratio
b	Wing span
c	Airfoil chord
g	Gravity
l	Length
m	Mass
S	Reference area
t	Thickness
W	Weight
w	Width
δ	Tip deflection
η	Effective flap angle

Piezoelectric Material Parameters

D	Electric displacement
d_{31}	Piezoelectric coefficient, electrode direction
d_{33}	Piezoelectric coefficient, rod direction
E	Electric field
E_1	Modulus of elasticity, electrode direction
E_3	Modulus of elasticity, rod direction
F_{block}	Blocking force
G_{12}	Shear modulus

s Electrode spacing

S^E Compliance

α_{31} Thermal expansion coefficient, electrode direction

α_{33} Thermal expansion coefficient, rod direction

ΔT Thermal loading

ϵ Strain

ϵ_{free} Free srain

ζ Permittivity coefficient

θ Fiber angle

ν_{12} Poisson ratio

σ Stress

Ψ_3 Potential voltage, rod direction

Motion Parameters

a Acceleration

$\overline{U}$ Nondimensional velocity

U_R Resultant flight velocity

$\overline{U_R}$ Nondimensional resultant flight velocity

$\vec{U}_R$ Resultant flight velocity vector

$\overline{U_v}$ Nondimensional translational velocity

$\dot{\overline{U}}_v$ Nondimensional translational acceleration

U_∞ Glide velocity

$\vec{U}_\infty$ Glide velocity vector

U_0 Wind velocity

$\vec{U}_0$ Wind velocity vector

Δv Translational velocity

λ Time constant

Aerodynamic Parameters

C_D	Wing drag coefficient
$C_{D,i}$	Induced wing drag coefficient
C_{D_β}	Drag-sideslip stability derivative
C_L	Wing lift coefficient
C_l	Section lift coefficient
C_m	Pitch moment coefficient
$C_{m\delta}$	Pitch control derivative
C_η	Yaw moment coefficient
$C_{\eta\beta}$	Yaw stability derivative
D	Drag force
dC_l	Change in section lift coefficient
$d\alpha_{eff}$	Change in effective angle of attack
j	Spanwise section number
L	Lift force
MAC	Mean aerodynamic chord
N	Yaw moment
n	Iteration number
T	Thrust
V	Flow velocity
w_{ind}	Induced downwash
y_j	Spanwise section location
α	Angle of attack
α_{eff}	Effective angle of attack
α_{geo}	Geometric angle of attack
α_0	Zero lift angle of attack
β	Sideslip angle

β_0 Wind angle

Γ Circulation

η_k Spanwise integration points

μ Artificial viscosity

ρ Fluid density

ω Relaxation factor

ABSTRACT

Morphing to seamlessly alter aircraft geometry for either multi-mission or adaptive fly-by-feel flight has recently become an emerging field of research. With the added benefits of tailored aerodynamics, an aircraft no longer needs to be designed to suit a single cruise flight condition. This is particularly useful for small Unmanned Aerial Vehicle (UAV)s which, like birds and insects, tend to operate at lower altitudes and even in urban environments where the flow can frequently change drastically.

The primary objective of this research is to investigate morphing applications for rudderless UAVs, which have seldom been studied prior to this point, through bioinspiration. As natural fliers undergo multi-scale low-altitude morphing to adapt to changes in either flight objective or aerodynamic conditions, they are prime subjects for investigation. This is accomplished through both analytical aerodynamic modeling, and experimental design and investigation of novel morphing actuators using MFCs. Using these smart material actuators, complex shape change such as spanwise camber morphing and three-dimensional bending-twisting coupling is achieved.

This dissertation presents three main contributions to the field of morphing aircraft. The first contribution is an analytical derivation that assesses the impact of scale and altitude on flight. This is aimed at justifying the need for morphing technologies particularly at the UAV scale by assessing the impact of winds on flight velocity and direction. More specifically, both a steady wind and a quasi-steady sharp-edge cross wind were assessed to characterize the response, and showed that low-altitude fliers are prone to drastic changes in flight path, acceleration, and sensitivity with respect to winds.

A nonlinear Lifting Line Theory (LLT) model was also developed specifically for spanwise

morphing aircraft. With this model, the spanwise geometry of a morphing wing can be tailored and optimized to achieve a desired aerodynamic outcome. As this model is capable of characterizing nonlinear aerodynamics, the spanwise wing geometry is tailored to recover from stall. A comprehensive analysis of possible adaptation scenarios is also conducted to characterize the limitations of the system and demonstrated excellent recovery capabilities of the spanwise morphing wing.

Lastly, a novel bioinspired tail actuator is developed for multifunctional pitch and yaw control using MFCs. Two Finite Element Method (FEM) models are compared to determine both an appropriate method of modeling MFC actuators with custom non-rectangular geometries and fiber orientations, and the optimal fiber orientation to obtain adequate transverse and out-of-plane displacements. The optimized actuator was integrated into a bioinspired aircraft for wind tunnel testing. Experimental investigation was geared towards quantifying both pitch and yaw response of the actuator with respect to both changes in angle of attack and sideslip.

CHAPTER 1

Introduction and Literature Review

Aircraft design has remained relatively unchanged in the past century; however, morphing aircraft offer a new opportunity to advance aircraft technology. They are distinguished from traditional aircraft in that they exhibit smooth shape change from one configuration to another, maintaining a continuous surface even in actuated states. Frequently composed of smart material actuators which can be lighter, faster, and experience complex and/or continuous deformations, the advantages of morphing are plentiful. In fact, the pursuit of morphing aircraft follows two main catalysts- performance and cost. At some level, these catalysts are interrelated. Increased performance with respect to drag reduction or flight efficiency results in reduced fuel consumption and hence reduced fuel costs. But the advantages offered by smart materials allow for improvements in performance maneuverability and aerodynamic adaptability as well, particularly on the UAV scale where aircraft are prone to more severe aerodynamics and may require more drastic adaptive maneuvers [1].

1.1 Motivation and Scope

Birds, bats, and insects fly within the lower portion of the Atmospheric Boundary Layer (ABL) at low speeds and are capable of extreme maneuverability through morphing wing camber, sweep, dihedral, etc. coupled with intricate tail movements [2–8]. Yet while the first entrepreneurs of aviation like Otto Lilienthal, John Montgomery and the Wright Brothers aspired to achieve bird-like flight stability and control through camber and wing warping [9–12], the quest for larger and faster air transportation produced heavy rigid aircraft with discrete control surfaces [13, 14]. This allowed planes to carry heavier loads and fly at high speeds in the upper troposphere where the air is smooth. Figure 1.1 depicts the relationship between typical flight velocity and weight.

In particular, the troposphere exhibits semi-unidirectional currents due to the formation of Hadley cells, with most wind currents within 22° of the prevailing wind direction [15]. In contrast, low-altitude environments, where natural fliers and small UAVs tend to operate, are prone to unbiased winds due to local weather interactions and urban flow patterns [16], and are characterized by high turbulence levels approaching 50% in cities or urban environments with a wide range of turbulence length scales [17–19]. This can make controlled flight quite challenging and motivates the pursuit of more adaptive flight technologies at this scale.

Recent interests within UAVs have focused on these challenges, namely developing drones for flying in complex urban environments. One such project is the DARPA Fast Lightweight Autonomy (FLA) project which hopes to develop technologies for flying drones in urban or cluttered environments for use in disaster relief, terrain assessment, and surveillance [20, 21]. This in part requires superior maneuverability for collision avoidance, perching and landing maneuvers, and pursuit scenarios. In many instances, the requirements extend to biological camouflage as well.

However the FLA project focuses on vision technologies for collision avoidance of multicopters, omitting further research into urban UAV flight efficiency and performance.

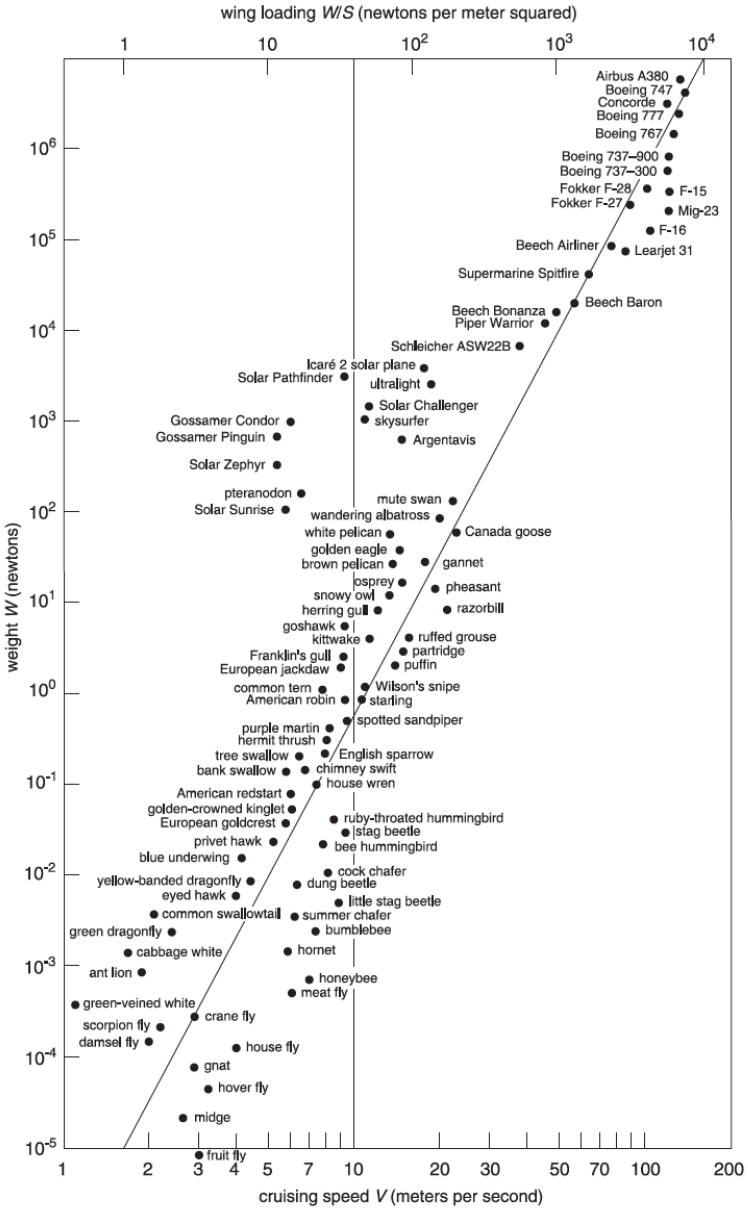

Figure 1.1: Observed relationship between flight speed and flier size [22]

The scope of the current work aims to develop a new method of control for morphing rudderless UAVs which enhances current maneuverability and performance, addresses some of the pitfalls of current rudderless designs, and informs current biological studies by providing insight

into the force and moment response of the active horizontal tail of birds. Adaptability to more extreme aerodynamics than have been previously considered should be ensured. Furthermore controllability should be on par if not exceed traditional standards.

1.2 Biological Inspiration

Nature can provide tremendous inspiration for engineers. Birds in particular provide a unique opportunity for the aerospace community to draw inspiration from when designing small UAVs as they operate in similar aerodynamic conditions. Birds exhibit tremendous maneuverability and stability, and have a unique ability to drastically morph their geometry with both large scale and fine-tuned maneuvers [3, 4, 23–25] in order to respond to a change in aerodynamic conditions. This capability provides a highly effective method of adapting to adverse aerodynamic conditions due to wind gusts, prey payload, etc. [3]. Interestingly, it has also been shown that wing shape dictates not only maneuverability with respect to rapid rotations and sharp turns [26], but also wing performance at various Reynolds numbers [27], indicating that natural fliers may attempt to optimize their wing, tail, and body geometry in-flight.

For example wing sweep in swifts, a high speed flyer, was shown to effectively broaden the aerodynamic performance over a large range allowing the swift to fine-tune its aerodynamic profile to achieve a specific flight condition. Most notably, their glide performance at high speeds is maximized at large sweep angles by reducing drag and maintaining adequate lift [3]. This, in part, is due to the reduction in planform area that is coupled with biological sweep. The wings alone have also been shown to provide static directional stability [28–31] due to either inherent sweep in the slotted primary feathers and the hand-wing. Alternately, the steppe eagle, a passive soaring

flyer, has been observed to deliberately stall a section of the inside wing during banked turns to increase the rate of maneuvering in roll and yaw [4], motivating research into spanwise morphing wing studies (see Figure 1.2). And falcons have been observed during wind tunnel testing to actively adjust their wing span to maximize their lift-to-drag across multiple glide speeds [32].

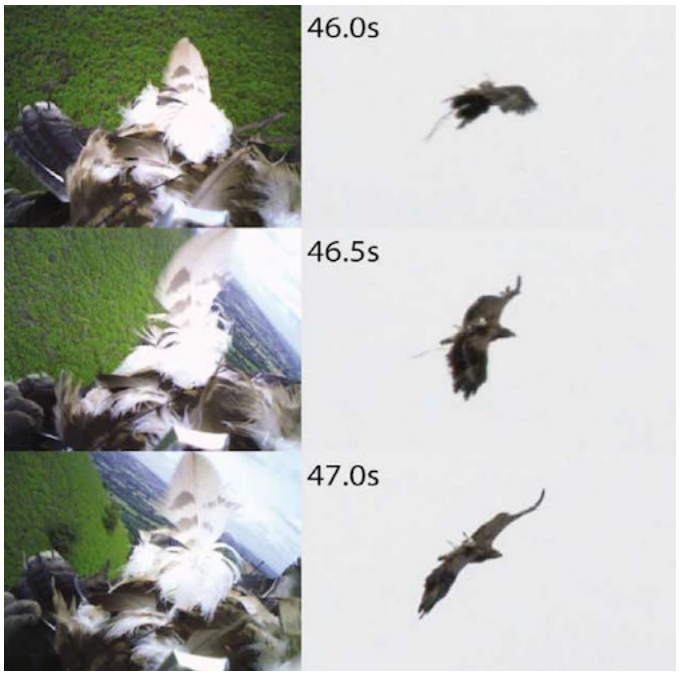

Figure 1.2: In flight images depicting tail depression and some spanwise wing variability going into a banked turn from [4]

Like aircraft, the cambered wings generate the majority of the total lift during soaring maneuvers, but their tail are unique in that it performs rapid fine-tuned movements including pitch, twist and spread to stabilize the body in gusty conditions [4, 33]. While current state-of-the art research into rudderless aircraft may still struggle with stability and control, birds are unfazed by such challenges, even in chaotic aerodynamic conditions. This is exceptionally impressive given the large magnitude of wind gusts relative to a bird's flight speed which can lead to major destabilization [1]. In fact, a bird's tail plays a key role in maintaining stability and control, both actively

and passively [4, 33–35].

The geometry of the tail itself provides static stability due to its asymmetric drag contribution aft of the center of gravity during sideslip which provides a restoring moment, as demonstrated in Figure 1.3a. The magnitude of stability in particular is dependent upon tail aspect ratio. This allows birds to have relatively unswept wings in gliding flight without sacrificing yaw stability, a configuration which rudderless aircraft cannot afford. Large scale deformations are used as methods of flight and attitude control, while small scale corrective movements are used to stabilize the body like those shown in Figure 1.3b. These tail movements in particular play a large role in pitching maneuvers. Actively, the tail has been observed to depress to generate a nose down pitching motion, and elevate to generate a nose up pitching motion [4, 23]. Hence the pitching motion of the tail acts almost identically to the elevator mechanism in aircraft. Further studies have also shown that the tail plays a major contribution in increasing off-peak flight performance [36].

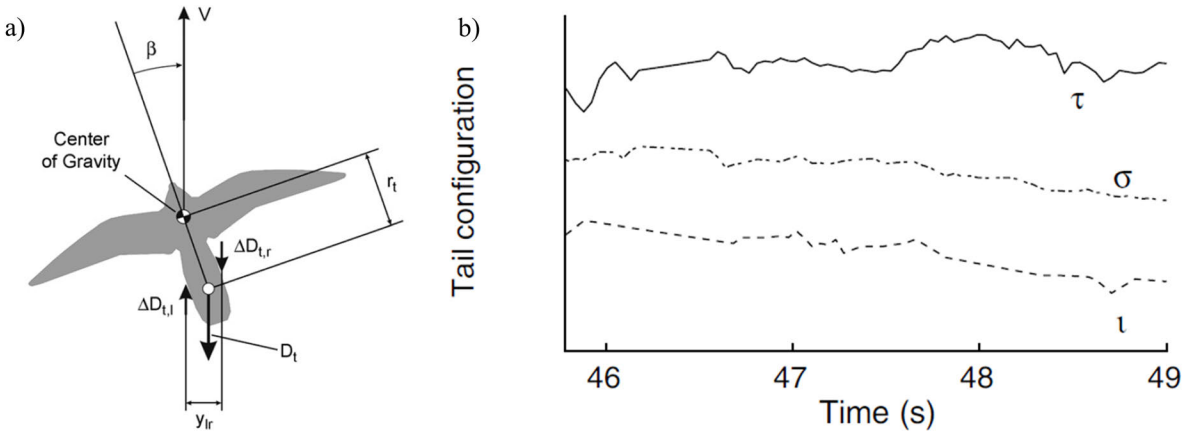

Figure 1.3: a) Depiction of tail effects on drag in sideslip from [33] b) in flight measurements of tail pitch l, twist τ, and spread θ going into a banked turn from [4]

Overall, this ability to morph geometry allows birds to operate effectively over a range of flight conditions. Thus, a hypothesized key advantage of morphing UAVs over their rigid and discrete

counterparts is their ability to adapt to multiple flight conditions via geometric tailoring as birds do in nature.

1.3 History of Morphing Aircraft

One of the first instances of morphing aircraft was the Wright Brothers Flyer that was developed in 1903 and utilized twisting wings to employ flight control. But at the onset of World War 1, rigid aircraft quickly dominated the field due to their robust design. Large-scale adaptive aircraft technologies were forsaken at the price of heavy, multifaceted, and expensive designs [37]. The few concepts which eclipsed these pitfalls, like the F-111 [38] and B-1 Lancer, are distinguish by their necessity to undergo large changes in wing loading [13] such as transitioning between loitering and high speed flight like birds of prey [4]. This focus on commanded changes in mission requirements overlooks the potential need to adapt to environmental disturbances in real time. However one notable exception to this trend is the development of NASA's Morphing Project which began in the 1990's and aimed to develop an array of bioinspired and adaptive technologies for active flow control of modern transonic aircraft [39–41].

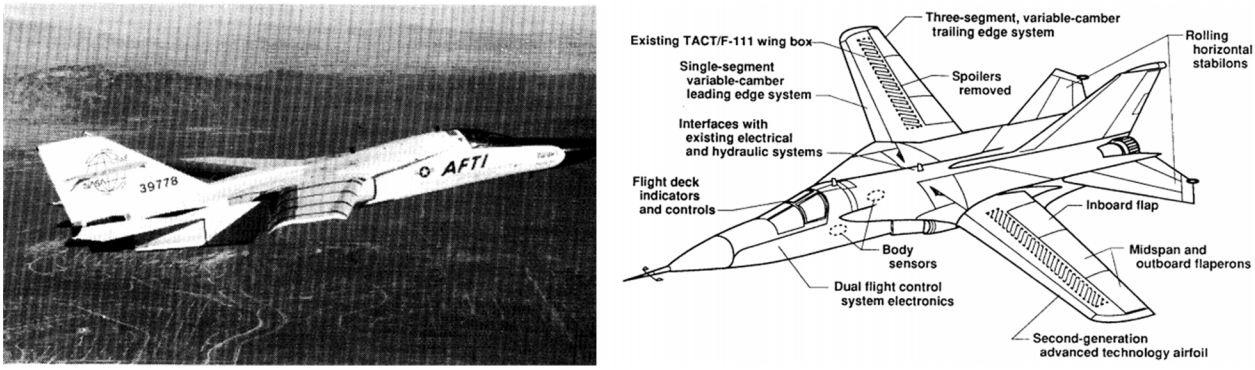

Figure 1.4: Depiction of the F-111 test article and detailed concept drawing from [38]

In contrast, recent advances in morphing UAVs [42–44] have targeted local shape change using smart materials like Shape Memory Alloy (SMA)s [45] and piezoelectrics, and have been motivated by sense-and-adapt (i.e. fly-by-feel) control methods [46, 47]. The goal of these modern morphing aircraft studies is to achieve efficient flight outside of the principal design by altering parameters such as camber, sweep, twist, or planform area [37]. In small UAVs which operate at low Reynolds numbers, this can be advantageous since unfavorable aerodynamic phenomenon such as wind gusts, and static imbalance due to payload shift and delivery can heavily impact gliding flight.

1.3.1 Wing Morphing Mechanisms

The majority of recent morphing aircraft studies have focused almost entirely on the wings of the aircraft, as they are the main lifting surface and contain the majority of the control surfaces. At the transonic scale, recent research within morphing wings has focused on cruise performance, notably the VCCTEF by NASA and Boeing [48–50], and the FlexSys Mission Adaptive Compliant Wing (MACW) [51, 52], although some effort has been dedicated to assessing adaptive morphing outlets for larger air vehicles [53, 54]. The VCCTEF, shown in Figure 1.5 harnessed the rapid timescale benefits of conventional electromechanical motors in addition to the weight-to-power benefits of shape memory alloy torque tubes. Alternately, the MACW utilized conventional actuators for adequate power consumption, bandwidth, and range of displacement in order to tailor the airfoil camber of an optimized internal compliant structure which maintained reasonable stresses, stability and dynamic behavior.

These advances highlight the importance of developing integrated morphing technologies for

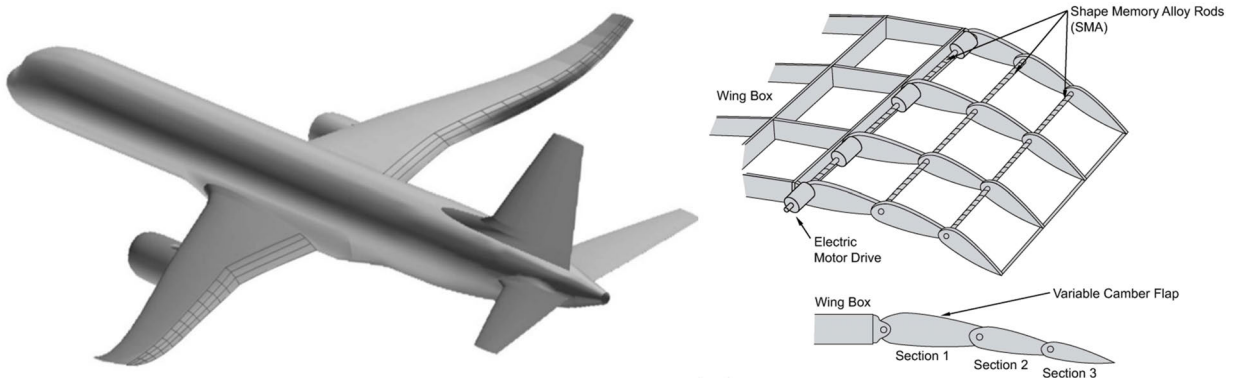

Figure 1.5: Depiction of the VCCTEF test article and detailed concept drawing from [48]

commercial and military aircraft operating at cruising speeds, as even slight decreases in drag can amount to tremendous savings in fuel consumption. But while a slight reduction in drag can contribute to significant savings in fuel consumption at transonic cruising speeds, these aircraft remain designed for a specific cruise condition meaning that any deviation from this optimized case incurs additional aerodynamic and financial costs.

An alternative approach to morphing is to design the wing with the intention of adaption in order to accommodate for changes in flight conditions or mission requirements. With the simultaneous advancement of smart materials, 3D printed compliant skins, and sensor networks, new morphing concepts on the UAV scale have been enabled. By introducing one or more of these advancements into a single design, morphing UAVs are capable of outperforming their traditional counterparts. Such advances include integrating SMA wires into additive manufactured airfoils to achieve high work density hinge mechanisms [55, 56], combining spiral spooling pulleys with tailored fishbone airfoils to achieve smooth camber morphing [57, 58], and optimization of compliant spars for span morphing [59]. However, one obstacle when implementing morphing structures is satisfying the concurrent needs of both structural compliance and load resistance. Accounting for both is of utmost importance, preferably through design optimization [60].

Such adaptive morphing concepts include the cascading bimorph concept developed by Bilgen *et al.* [61,62] shown in Figure 1.6 which achieved a camber morphing airfoil using MFC actuators, and the SMTE concept developed by Pankonien *et al.* [63–65] which was designed to achieve continuous shape change across 6 spanwise piezoelectric actuators. Pankonien's work, directly relevant to the current study, optimized the spanwise deflections of a morphing finite wing using Prandtl's LLT to recover from an off-design flight condition at small angles of attack and showed that the SMTE, which exhibits smooth spanwise changes in trailing edge deflection, provided substantial drag reduction due to the elimination of vortex formations at surface discontinuities when compared to a wing with rigid discrete control surfaces of equivalent spanwise geometry. However, the assessment of aerodynamic performance of morphing aircraft at large angles and near stall has been limited in part by difficulties in modeling the post-stall aerodynamic behavior of a finite wing.

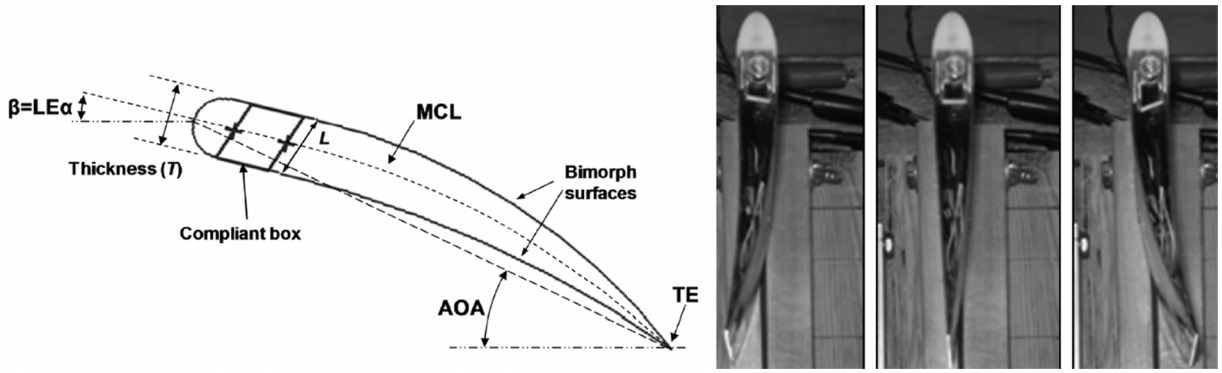

Figure 1.6: Depiction of the cascading bimorph test article and detailed concept drawing from [61]

Additionally, since small UAVs are capable of exotic flight maneuvers [66], adaptation to recover from the post-stall regime is highly significant. Yet, while the capabilities of a smooth morphing MALE/LALE wing have been proven to favorably adapt to off-design flight conditions in the linear regime [63–65], it has yet to be proven effective at large angles of attack past stall.

This is one area where camber and spanwise morphing wings have lacked detailed investigations. However, a secondary gap in morphing aircraft research exists with respect to rudderless aircraft.

1.3.2 Rudderless Morphing

Rudderless or tailless aircraft, desirable for their low radar signature and highly efficient aerodynamics, are a challenging engineering design. Not only are all of their control surfaces located on the wings which are the main lifting surface, but they also lack a vertical rudder which provides yaw stability and control. Current non-morphing designs such as the B-2 and more recently the X-48B [67] employ methods of control via elevens, split flaps, etc. within the wings of the aircraft. However, while research into rudderless designs have shown benefits namely drag reduction [68], performance flaws have also been discovered including limited directional control, reduced lift with multiple deflected elevons [69], and limited pitch authority at large angles of attack [70]. Improving pitch authority in rudderless aircraft has frequently been achieved by further sweeping the wings backwards which increases the elevon moment arm; however, this can introduce some unwanted vortex effects at high angles of attack [70].

Large-scale forms of morphing rudderless aircraft include the Lockheed-Martin Agile Hunter, shown in Figure 1.7, which achieves changes in span via large scale folding mechanisms to tailor the geometry for loitering and dash maneuvers [71, 72]. But these designs do not address the lack of directional instability in rudderless or flying wing aircraft, the inherent coupled effects of having all control surfaces on the lifting surface, and the frequently slow actuation response of large-scale morphing mechanisms. These designs are more practical for transitioning between two flight regimes as opposed to adapting to adverse aerodynamic conditions.

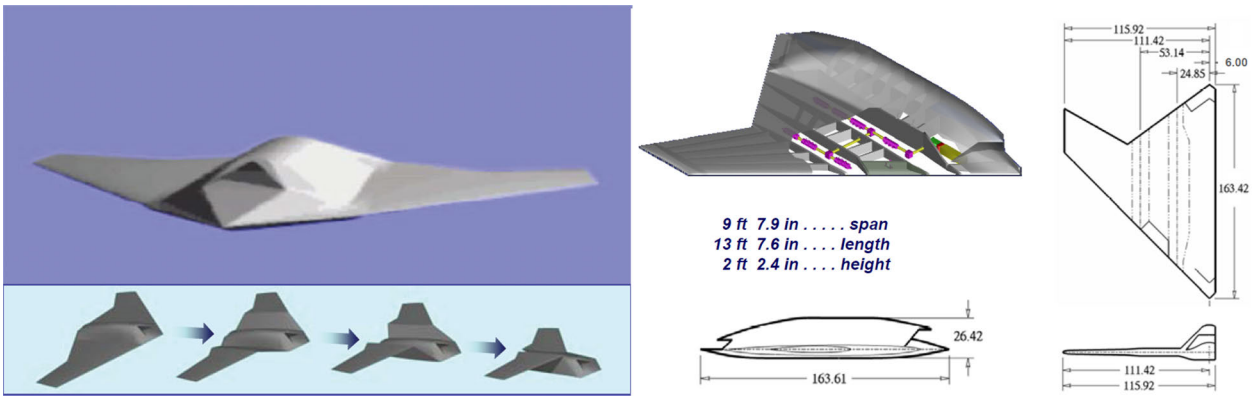

Figure 1.7: Depiction of the Lockheed-Martin Agile Hunter concept and detailed detailed drawing from [72]

Furthermore, there has been little research conducted towards developing morphing rudderless UAVs to date. Past research has focused on either developing new morphing mechanisms for flying wings but failed to do further aerodynamic testing [73, 74], or applying traditional wing morphing concepts to flying wing configurations such as camber morphing or wing twisting with the aim of improving efficiency and controllability through cambered actuation and/or eliminating gaps at the elevons [68, 75–77]. One such example is shown in Figure 1.8.

The performance of morphing wings is variable depending on the mechanism. Cambered actuators, generally speaking, are more effective at aerodynamic control of rudderless aircraft, demonstrating larger lift and pitching moment coefficients and some increase in roll performance [43]. Spanwise distributed camber morphing actuators provide some drag reduction benefits due to their ability to tailor the lift distribution along the wing; however, due to strict pitching moment constraints associated with rudderless aircraft a local minimum is not always possible [68,75]. Though in summary these designs can reduce drag, they often experience less control authority [75] which is already problematic in rudderless aircraft.

Although small rudderless UAVs encounter similar aerodynamic challenges as natural fliers

due to their comparable geometry, size and weight; they rarely incorporate bioinspired designs. Many small-scale UAVs use traditional yaw control methods such as vertical stabilizers and rudders like the Elbit Skylark, RQ-11 Raven, and Desert Hawk [78], which add drag and increase the aircraft's radar signature. This is drastically different from previous efforts in rudderless or flying wing designs in transonic aircraft, such as the X-45C and the B-2. Without a vertical stabilizer, these aircraft actively control yaw using split ailerons or spoilers [79, 80] and rely on a swept wing configuration to provide static yaw stability.

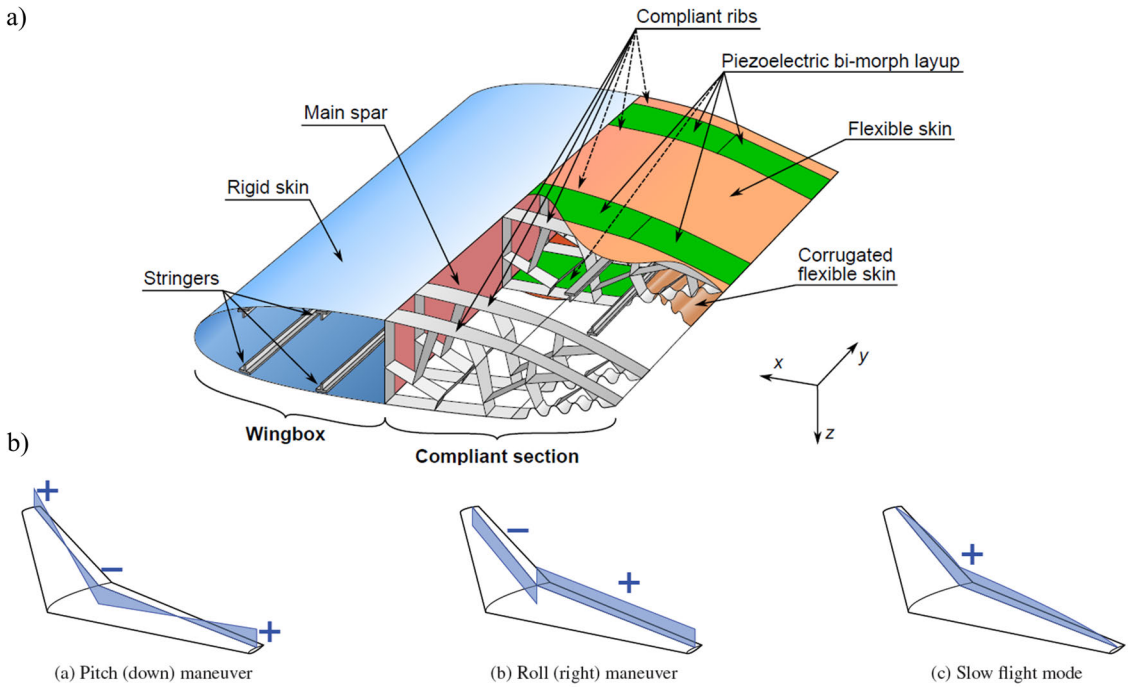

Figure 1.8: Wing morphing concept and proposed configurations for a rudderless aircraft from [75]

Scaling down these designs to the size of a small UAV or bird introduces additional complexities regarding stability and control, as these aircraft are designed specifically for efficient high altitude and high speed flight. At low altitudes where low-speed fliers typically operate, wind gusts are non-biased in direction and can exceed the magnitude of the flight velocity which can cause the

bird or UAV to experience substantial sideslip. In current rudderless or flying wing designs, this could be devastating and cause loss of aileron authority [81].

1.4 Outline of Dissertation

The contents of this dissertation are divided into seven chapters. Chapter 1 delves into the biological background that motivates the pursuit of rudderless low-altitude UAVs. Further context is provided detailing the historical perspective and current state-of-the-art in morphing and rudderless aircraft designs. Lastly, focus is drawn to the existing pitfalls and design challenges with respect to rudderless aircraft and spanwise morphing adaptation.

Chapter 2 further motivates the pursuit of morphing UAVs by deriving an analytical model to correlate flier scale and resulting wind disturbance. A broad literature review was conducted to obtain reported experimental data of flight speed and corresponding wind speed for a variety of fliers ranging from small insects to transonic aircraft. This information was used to quantify an easily determinable parameter which could be used to assess the static and dynamic response based on flier scale. This assessment focused on both static wind disturbances and time-dependent sharp-edged crosswinds. The analysis highlights the impact of scale (and inherently altitude) and winds on flight speed, direction, and stability.

Chapter 3 introduces the rudderless aircraft concept. The development of the aircraft concept is described, detailing both the spanwise morphing wing and 3D morphing tail actuator, as care was taken to be consistent with current bioinspired studies. In particular, the tail actuator was designed with custom MFCs in order to achieve bending twisting coupling. This resembled the pitching and twisting mechanics of a bird's tail for pitch and yaw control. Further improvements on the existing

SMTE sensing capabilities were also investigated.

Chapter 4 details the aerodynamic model and subsequent experiments which investigate the impact of spanwise morphing on nonlinear high angle of attack adaptation, including stall recovery. An extended nonlinear LLT model was adapted specifically for spanwise morphing wings. This was used to optimize the spanwise geometry of the SMTE for stall recovery. Wind tunnel tests were used to validate the model and compare the results between a morphing and non-morphing wing of equivalent geometry. Lastly a comprehensive analysis was performed to quantify the extent of aerodynamic scenarios of which the SMTE was capable of adapting to.

Chapter 5 presents the development of the customized MFC actuator for coupled pitch and yaw control. Two FEM models were compared for accuracy and robustness, specifically a Lead Zirconate Titanate (PZT) model and a thermal analogy. The thermal analogy was implemented with the customized geometry detailed in Chapter 4. A parameter study was conducted to determine the PZT fiber direction which would maximize out-of-plane and transverse deflections. The final custom MFC's actuated profile was compared to the model's predicted profile using 3D scanning technology.

Chapter 6 describes the test methods used to analyze and quantify the performance capabilities of the custom MFC actuator. Preliminary validation of the actuated geometry was conducted using Computational Fluid Dynamics (CFD) simulations to verify the extent of aerodynamic control. Further characterization of the MFC actuator was performed upon full integration into the aircraft model. Lastly, the nondimensional aerodynamic coefficients and control effectiveness were determined experimentally with respect to both angle of attack and sideslip.

Finally, Chapter 7 summarizes the results of this dissertation, elaborates on their impact, fortifies their contributions to the field, and provides concluding remarks. A detailed list of the accom-

panying publications for this dissertation is also provided.

CHAPTER 2

Correlating Morphology and Scale

Though natural fliers have been shown to morph their geometry to adapt to unfavorable wind loadings, there exists heavy skepticism within the aviation community regarding the benefits and necessity of morphing aircraft technology. In fact, practically no research had been conducted on morphing aircraft between the development of the Wright Flyer, a keystone design within the history of morphing aircraft, and the end of the 20^{th} century. This is starkly evident upon assessing the rate of publications within morphing aircraft over time as shown in Figure 2.1. This shows a clear initiation of interest at the start of the 21^{st} century which increases exponentially over the next decade. As such, progress has been left to the occasional experimental aircraft with the vast majority of research occurring on the academic scale.

As mentioned in the Introduction, the epicenter of these works has revolved around small-to-mid sized UAVs. This scale of aircraft more readily resembles the scale of biological morphing flyers and is easy to test both experimentally and with simulations. Additionally, as lower aerodynamic loads are expected with smaller aircraft, it allows for the use of more novel materials like MFCs, elastomeric skins and 3D printed polymers, which may not be as rigid as traditional metals and composites. For large-scale aircraft, the decision to implement morphing technologies is much more complex as major concerns must be weighed regarding development costs relative to the an-

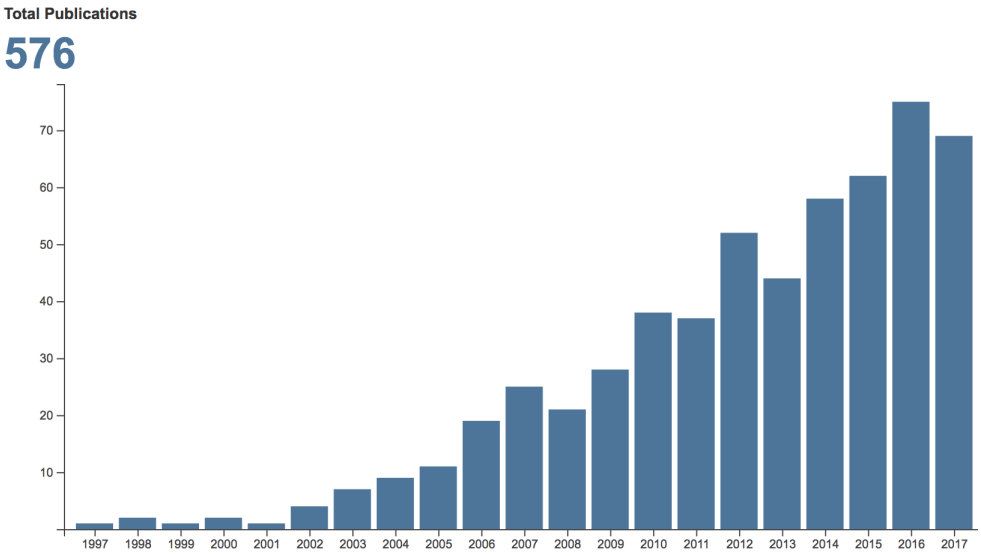

Figure 2.1: Search results of yearly publications containing both 'morphing' and 'aircraft', generated with Google Scholar

ticipated performance or financial gains. In fact, there is little incentive to explore new high-risk methodologies like morphing without comprehending how aircraft of various scales benefit from it. Accordingly, this work aims to analytically assess the aerodynamic challenges that fliers face at different scales and thus determine the need for morphing mechanisms in aircraft design.

In this chapter, a straightforward vector derivation and sensitivity calculations were developed to demonstrate the effects of an in-plane wind on flyer attitude relative to the global coordinate system, aiming to both inform current research demonstrating the aerodynamic benefits of morphing geometry in birds, and justify the inclusion of morphing technology in small-scale low-altitude UAVs. In particular, this analysis describes the deviation of sideslip in gliding flight in the absence of corrective measures such as wing morphing or actuator response. Gliding flight in particular represents a scenario in which a bird's wing geometry is not impacted by wing beat, providing a comparable scenario between aircraft and birds. This derivation is formulated in such a way that

only a single non-dimensional velocity parameter is needed to quantify the response.

We show mathematically that in high winds, low-altitude fliers are more prone to substantial changes in sideslip angle, struggle to maintain gliding velocity, and experience five times the peak sideslip sensitivity when compared to high-altitude fliers. In order to counteract these adverse changes, low-altitude fliers would require a high degree of controllability which can be achieved through extreme morphological changes. The results presented here highlight the importance of integrating morphing concepts into future low-altitude aircraft designs and provide a formulation to help designers decide whether or not to pursue adaptive morphing technology based on a single readily determinable parameter. Lastly, a brief dynamic analysis was conducted which considers how the aerodynamic force due to a sharp-edged crosswind affects the flier acceleration

2.1 Data Acquisition

Anticipating that the sideslip response will differ based on the ratio of the wind speed to the flight speed, characterizing these quantities across a spectrum of fliers is crucial. A comprehensive literature review was performed to assess both the flight speed of a variety of natural and man-made fliers, in addition to the atmospheric wind conditions experienced by each flier. This was conducted by manually sifting through journal articles using Google Scholar and it's capabilities of incorporating Boolean operators such as **AND**, **OR**, and **NOT** into the search terms to narrow the scope of the request.

This was essential, as the scope of this data acquisition was geared towards finding articles which reported both the flier's flight speed in addition to the wind speed during testing. With this information, the following analysis represents a typical flight experience that characterizes

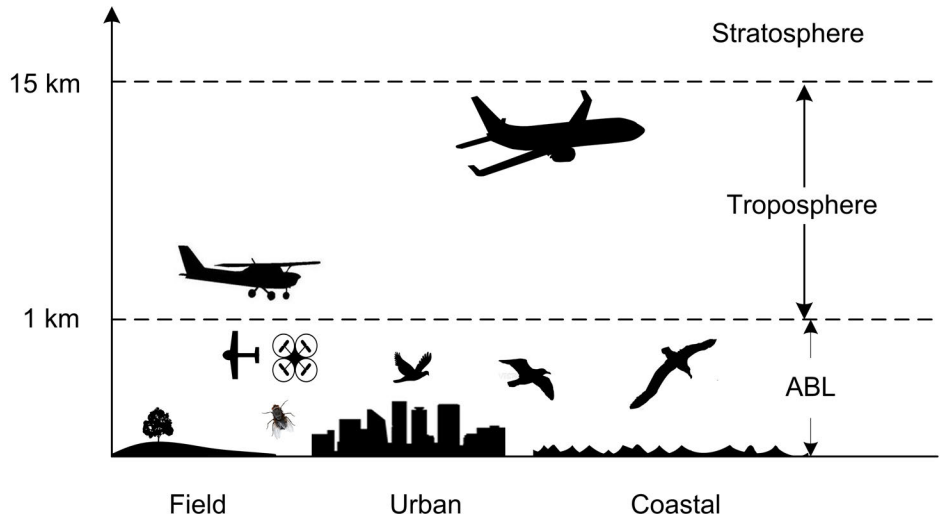

Figure 2.2: Visual representation of natural and engineered flier operational region and altitude

normal day-to-day flow. This removes any influence of extreme atmospheric conditions either due to global weather patterns or urban flow interactions. In essence, this analysis represents a best case scenario, particularly for low-altitude fliers. Though plenty of peer-reviewed journal articles exist which report either atmospheric weather conditions and flyer flight speeds, few exist which report them simultaneously. Even given these challenges, a conscious effort was made to acquire data which represents a full spectrum of fliers from insects to transonic aircraft.

Figure 2.2 provides a visual comparison between a variety of fliers and their altitudes and turbulence environments. Intuitively, flier scale directly correlates to the flight altitude. This has been observed to vary linearly on a log scale [22]. Smaller fliers tend to operate in the ABL in challenging flow environments ranging from fields to coasts to urban environments. Conversely, large aircraft operate at much higher altitudes.

Table 2.1 compiles the mined data in an organized fashion. Experimental data of the flight and corresponding wind speeds are reported where available. If no wind speed is available, the non-dimensional velocity is calculated using the appropriate atmospheric data provided. When

available, the measurement environment is also reported which can provide some additional insight into turbulent environments. Aircraft data shown here on flight speed and altitude is publicly available. Lastly, a parameter is introduced called the maximum non-dimensional wind speed $\overline{U}_{max}$ which is calculated as the ratio of the maximum wind speed to the minimum glide speed.

Table 2.1: Comparison of non-dimensional wind speeds across a spectrum of fliers

	Flight Speed (m/s)		Wind Speed (m/s)			
Flyer	Min	Max	Min	Max	Measurement Environment	$\overline{U}_{max}$
Fly [22]	2	5	-	-	Field-Urban	4
Swallow [82]	3.7	19.4	1	6	Field-Urban	1.62
Gulls [16]	8.1	19.9	1.9	12.4	Urban-Costal	1.53
Albatros [83]	9.1	17.9	5.6	12.5	Coastal	1.37
Fixed Wing UAV [84]	5.5	13.8	1.5	9.5	Field	1.73
		Cruise Speed (m/s)			Operating Altitude (km)	
Predator		60			6.1	0.67
Cesna Caravan		100			7.6	0.40
Pilatus PC-12NG		144			9	0.28
Boeing 777		288			12	0.14
		Wind Speed (m/s)				
Atmosphere		Min		Max	Measurement Altitude (km)	
Lower Troposphere [84]		2.5		8	0.5	
Upper Troposphere [85]		13		40	12	

The data show that unlike aircraft, many natural fliers experience wind speeds equal to or greater than their range of flight velocities. The maximum non-dimensional wind speed $\overline{U}_{max}$ decreases for high-altitude fliers due to the large cruise speeds and relative lack of substantial winds in the upper troposphere. Low-altitude fliers such as natural fliers and UAVs experience a smaller maximum wind speed, but the corresponding wind magnitude is frequently larger than the flight speed. Though experimental data with both glide speed and corresponding wind speed is not widely available, the cruise speeds for a wide array of natural fliers has been well studied, showing glide speeds topping off at approximately 20 m/s for heavier birds [22] [86]. Thus the data presented in Table 2.1 roughly captures the full spectrum of natural fliers.

2.2 Wind Effects on the Resultant Velocity Vector

Using the correlation between nondimensional velocity and scale which was presented in the prior section, the effects of a static wind gust on the flier's resultant flight path and speed will be assessed.

2.2.1 Problem Statement

In gliding flight, the aircraft or bird experiences a forward velocity due to the thrust of the engine or intermittent wing flapping. This velocity can be represented as a vector $\vec{U}_\infty$, describing both the magnitude and direction of flight, shown in Figure 2.3. However, in the event of wind incoming at an arbitrary angle β_0, a second vector $\vec{U}_0$ is introduced which will impact the resultant magnitude and direction of the flow that is observed by the body. Adding these separate velocity vectors forms a resultant vector $\vec{U}_R$ which is dependent upon the relative magnitude and direction between the gliding velocity and wind velocity vectors. The angle β represents the sideslip angle or the angle of the resultant velocity vector relative to the local body axis. This implies substantially different responses between birds and aircraft which fly in very different flight conditions due to gliding velocity, altitude, and wind magnitude.

In response to wind, the bird or pilot has two potential response actions. The first response is to not correct for the disturbance and thus the flier's geometry would remain constant. The aerodynamic force due to wind acting on the flier would ultimately cause the aircraft to change its acceleration and thus its flight path relative to the ground as a result of Newton's 2^{nd} law. The second response is to adapt the control surfaces to generate restoring forces such that the desired flight path is maintained. Though the core of this work is static in nature, some analysis is geared

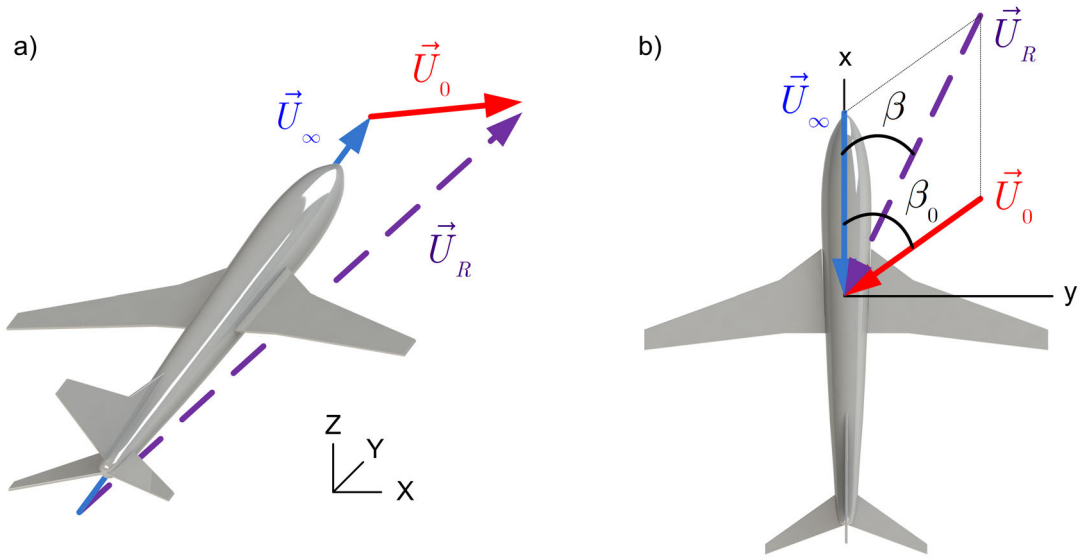

Figure 2.3: Velocity vectors relative to a stationary body a) vector diagram in 3D relative to the global axis (X,Y,Z). b) vector diagram in 2D relative to the local body axis (x,y,z) considering only in-plane velocities

towards understanding how the resultant velocity is affected by changes in wind speed, and if or how the velocity and acceleration responses may vary between high and low-altitude fliers in the absence of corrective maneuvers.

2.2.2 Vector Derivation

Upon establishing the difference in $\overline{U}_{max}$ between low and high-altitude fliers, the vector equations that govern the flight response as graphically described by Figure 2.3b can be derived. Due to the definition of the problem statement, the gliding velocity vector consists of a single component in the negative x direction. The wind velocity vector may impact the body at an angle β_0, thus it contains components in both the x and y directions. Written in indicial notation, the x and y components (i and j respectively) are expressed separately. The expressions for the glide and wind

velocity vectors are written as

$$\vec{U}_\infty = -U_\infty i + 0j \tag{2.1}$$

and

$$\vec{U}_0 = -U_0 cos(\beta_0) i - U_0 sin(\beta_0) j \tag{2.2}$$

where U_0 represents the magnitude of the wind vector, and U_∞ represents the magnitude of the glide vector. The resultant velocity vector is composed of both the wind velocity vector and the gliding velocity vector. Accordingly, using the principle of superposition, the two vectors can be added to obtain the resultant velocity vector by summing the respective *i* and *j* components as shown below

$$\vec{U}_R = \big(U_{\infty_i} + U_{0_i}\big) + \big(U_{\infty_j} + U_{0_j}\big) \tag{2.3}$$

The velocity components from the free stream and wind vector can be substituted into Equation 2.3 to obtain the following expression

$$\vec{U}_R = \big(- U_\infty - U_0 cos(\beta_0)\big) i + \big(0 - U_0 sin(\beta_0)\big) j \tag{2.4}$$

For ease of analysis, the non-dimensional wind speed representing the ratio of wind disturbance to free stream magnitude is defined as $\overline{U} = \frac{U_0}{U_\infty}$ and the resultant velocity vector can be rewritten accordingly

$$\vec{U}_R = \big(-U_\infty - \overline{U}U_\infty cos(\beta_0)\big)i + \big(0 - \overline{U}U_\infty sin(\beta_0)\big)j \tag{2.5}$$

The vector $\vec{U}_R$ has both magnitude and direction. The magnitude of the non-dimensional resultant velocity vector can be calculated by taking the Euclidean Norm $\sqrt{\vec{U}_{R_i}^2 + \vec{U}_{R_j}^2}$, thus the resultant speed is described as

$$\overline{U}_R = \sqrt{\big(1 + \overline{U}cos(\beta_0)\big)^2 + \big(\overline{U}sin(\beta_0)\big)^2} \tag{2.6}$$

As was done previously, this quantity has been non-dimensionalized such that $\overline{U}_R = \frac{U_R}{U_\infty}$. Lastly, the direction of the vector, i.e. the equation for the resultant sideslip angle β, is then calculated using Pythagorean theorem: $tan^{-1}\big(\frac{U_{R_j}}{U_{R_i}}\big)$, accordingly the sideslip angle is described by

$$\beta = tan^{-1}\big(\frac{\overline{U}sin(\beta_0)}{1 + \overline{U}cos(\beta_0)}\big) \tag{2.7}$$

The system has overall been simplified from 3 unknowns (U_0, U_∞, and β_0), to 2 unknowns ($\overline{U}$ and β_0) and allows the equations to be easily plotted and subsequently analyzed. Note that as per the definition of the problem statement in Figure 2.3, $\mid \beta_0 \mid < 90^\circ$ represents a tailwind (i.e. the *y*-components of the flight velocity and wind velocity are in the same direction) and $\mid \beta_0 \mid > 90^\circ$ represents a headwind, as this analysis has been performed relative to the local body axis. From this expression, we see mathematically how the sideslip angle and resultant speed are dependent upon the direction of the wind angle (β_0) and non-dimensional wind speed ($\overline{U}$). By definition, $\overline{U}$ must always be positive indicating that any changes in sign are the result of the β_0 contribution. This motivates segmenting the analysis into increments of 90° for which the sign of the sine and

cosine terms alternate.

2.2.3 Results

The results of the preceding analysis will be presented here. The results are broken down into the static wind's effect on sideslip, sideslip sensitivity, and the resultant speed.

2.2.3.1 Sideslip Response

Figure 2.4 shown below represents the resultant sideslip angle in response to wind. Recall that the sideslip angle represents the angle between the resultant flow direction and the flyer's body axis. The data is grouped by quadrants and should be read counterclockwise starting from quadrant a in the upper right corner. Each quadrant depicts the resultant sideslip angle with respect to the non-dimensional velocity for wind angles encompassing the full 360° spectrum. For conciseness, the legend is written in indicial notation of the form $\beta_{0,i} \rightarrow \beta_{0,j}$. For example in quadrant a, $\beta_{0,i}$ and $\beta_{0,j}$ correspond to $\beta_{0,0}$ and $\beta_{0,90}$ respectively. Lastly, the dashed line marks the divide between low and high-altitude flyer values for $\overline{U}_{max}$ as was assessed in Section 2.1.

Our analysis shows that in tailwinds (Figure 2.4a, d), the magnitude of the resultant sideslip angle increases with both $\overline{U}$ and β_0. For a given $\overline{U}$, increasing β_0 increases sideslip due to the addition of a velocity component perpendicular to the flight direction. Alternately, at a given β_0 the resultant sideslip is characterized by a rapid increase before plateauing and reaching steady-state. This steady-state was observed to equal the initial wind angle. These results imply that the sideslip of low-altitude fliers is more heavily impacted than high-altitude fliers since they operate at greater $\overline{U}$ values and are more prone to experience larger incoming wind angles. In fact, the sideslip experienced by low-altitude fliers in tailwinds is up to 3 times larger than that of high-

altitude fliers.

In response to these changes in sideslip the flier may either recover such that the flier experiences no sideslip, or restore the initial heading or flight course. With a high susceptibility to very large incoming gust angles, low-altitude flyers require more drastic changes in control surface geometry, including greater rudder actuation or more efficient cambered actuation, to achieve either of these responses. An example of such a camber morphing mechanism is the cascading bimorph concept [61] which has been further integrated into camber morphing trailing edges [63]. This has been shown to exhibit larger control derivatives for a given tip deflection, in addition to improved lift to drag performance.

For headwinds (Figure 2.4b, c), the response is much more complex and depends upon whether or not the wind speed is greater or less than the gliding speed. When $\overline{U}$ is greater than 1, the sideslip exhibits a similar response to tailwinds, though the sideslip angle is almost twice as large. Furthermore, low-altitude fliers may experience a resultant sideslip greater than 90°, representing a scenario where the resultant velocity vector no longer has a forward component. This phenomenon only occurs in the region of low-altitude fliers and is most severe in direct headwinds, where the sideslip angle may reverse entirely from 0° to 180°. The flier would require greater propulsion (thus decreasing $\overline{U}$) to return to forward flight. When $\overline{U}$ is less than 1, the sideslip angle of high-altitude fliers does not always increase with β_0 and is most succinctly described by the rightward shifting point of inflection with increasing wind angle. The sideslip is hardly affected as the wind approaches a direct headwind and the overall sideslip angle is up to an order of magnitude smaller than that of low-altitude fliers.

Though not evident from Figure 2.4, another detriment of headwinds is their tendency to asymmetrically affect the wing loadings in swept wing configurations. An angled headwind will impact

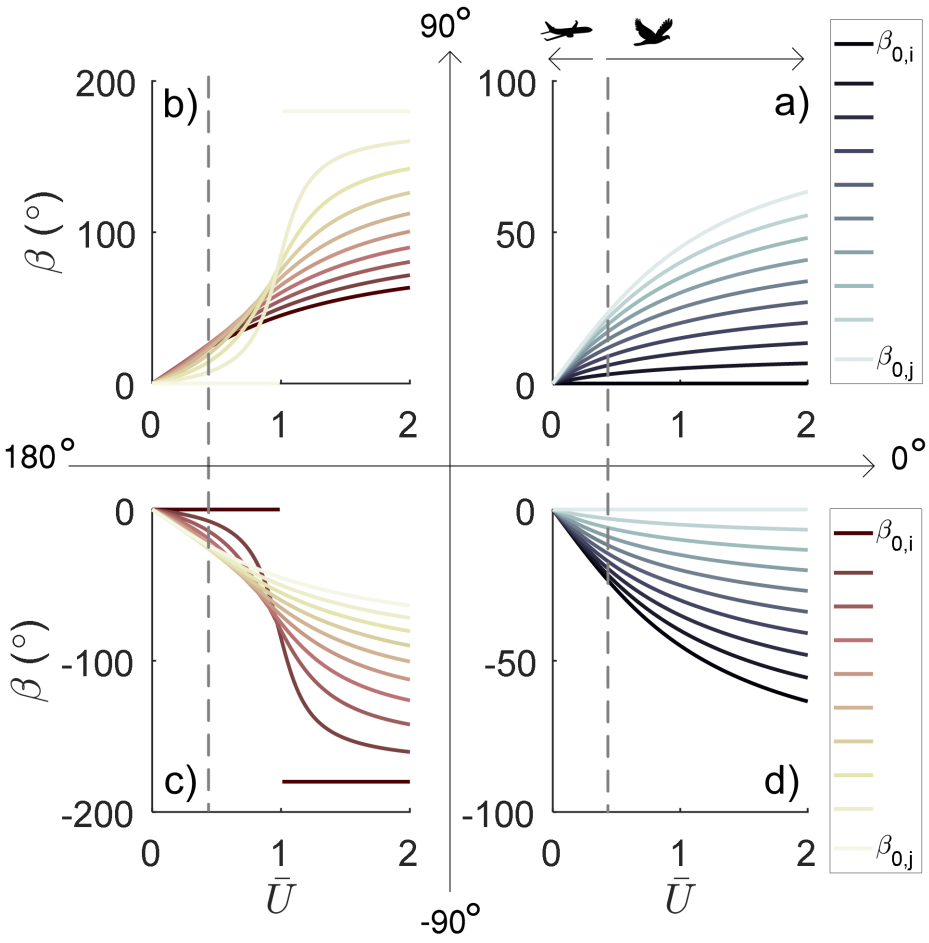

Figure 2.4: Sideslip response with respect to incoming wind magnitude and direction

the forward wing's leading edge, increasing its lift. This asymmetric lift induces roll which can lead to instabilities, tip stall and loss of actuator authority. One method of preventing this would be to decamber the wing to decrease lift and locally adjust the twist to decrease the angle of attack at the tips and prevent stall. Since the sideslip response is symmetric about the gliding direction (Figure 2.4 c, d), further analysis will focus solely on sideslip angles between $0°$ and $180°$.

2.2.3.2 Sensitivity Analysis

Given the drastically different sideslip curves discussed prior, it is clear that sideslip may be more susceptible to changes in wind speed and angle under certain conditions. A sensitivity parameter is introduced, represented as $\frac{\partial \beta}{\partial \overline{U}}$, which describes the degree to which changes in $\overline{U}$ affect sideslip angle. It is important to note that here $\overline{U}$ is being used to infer the dynamic effect of wind turbulence on sideslip angle by assuming a constant glide speed, and thus variations in $\overline{U}$ are the result of changes in wind speed with time.

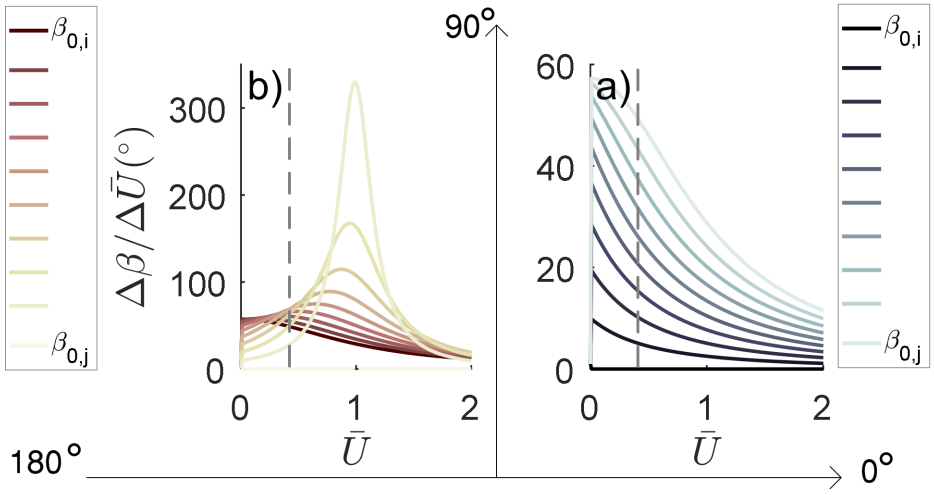

Figure 2.5: Effects of wind on sideslip sensitivity for a) Tailwinds and b) Headwinds

The data presented in Figure 2.5a shows that high-altitude fliers are most sensitive in tailwinds, and the sensitivity intensifies with increasing wind angle. However, even though variations in wind speed caused by turbulent environments are prone to causing variations in sideslip for high altitude fliers, the resultant sideslip is quite small as seen in Figure 2.4, therefore; any resulting oscillations would be small amplitude. As the sideslip plateaus, the sensitivity decreases substantially. This trend is partly extended for winds above 90° (Figure 2.5b); however, the trend shows a strong peak in sensitivity as $\overline{U}$approaches 1. Physically, these peaks are the result of the headwind

magnitude and direction being so large that the resultant velocity vector reverses in direction in a snap-through-like phenomenon. Low-altitude fliers in particular are extremely sensitive as winds approach direct headwinds ($\beta_0 = 180°$) with over 5 times the maximum sensitivity for tailwinds.

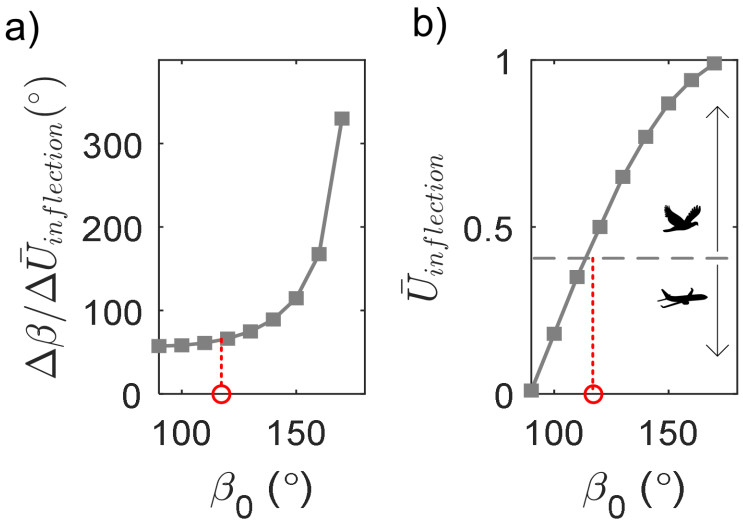

Figure 2.6: Characterization of sideslip inflections for a) peak sensitivity and b) non-dimensional speed

These peaks in sensitivity correspond to the points of inflection in the sideslip curves shown in Figure 2.4. Figure 2.6 characterizes the points of inflection relative to the incoming gust angle. Here, the sideslip sensitivity in addition to the non-dimensional wind speed at the point of inflection is shown. The point of distinction between high and low altitude fliers is marked in red and is distinguished first by non-dimensional wind speed. This is then associated with the wind angle at which inflection is experienced and can be translated to the sideslip sensitivity to comprehend the difference between high and low altitude fliers sensitivity.

This data further indicates that low-altitude fliers are subject to these large increases in sensitivity for a broader range of wind angles, as high altitude fliers do not typically experience adequate wind magnitudes to substantially induce this phenomenon. This represents a dangerous scenario

for low-altitude fliers where the magnitude of the sideslip angle and the sensitivity are both very large and is of particular concern in low-altitude highly turbulent environments where the wind velocity may fluctuate rapidly with time resulting in high amplitude oscillations if left uncorrected. High frequency actuator mechanisms which are capable of undergoing large scale deformation would be needed to negate these effects.

2.2.3.3 Resultant Speed

While winds can potentially influence the direction of flight by altering the sideslip angle, they also affect the resultant wind speed by effectively altering the flight speed relative to the ground. In tailwinds (Figure 2.7a), $\overline{U}_R$ is always greater than 1, signifying that the resultant speed is greater than the original glide speed for both low and high-altitude fliers, since the wind vector and gliding vector both have negative j components. However, low-altitude fliers exhibit much larger $\overline{U}_R$ values particularly in direct tailwinds. For headwinds (Figure 2.7b), the response decreases due to the addition of a j component in the opposite direction. As is indicated by values of $\overline{U}_R$ less than 1, both low and high-altitude fliers can experience a decrease in resultant speed from the gliding speed. However for large values of $\overline{U}_R$, the sideslip angle may also exceed 90° (shaded in gray), meaning that the flier would no longer have a forward velocity. This phenomenon only occurs in low-altitude fliers. Overall, low-altitude fliers experience a much larger range in $\overline{U}_R$, and thus are not able to maintain their initial ground speed as effectively as high-altitude fliers.

Though seemingly harmless, the consequences that arise due to the inability to properly regulate flight speed are further exacerbated by the fact that the flier's lift force is proportional to the squared speed

$$L = \frac{1}{2}\rho S C_l V^2 \tag{2.8}$$

where L is the force of lift, ρ is the air density, S is the lifting surface area, C_l is the lift coefficient, and V is the velocity between the flier and the air. In steady level flight, the force of lift equals the weight of the flier and thus the flier is neither loosing or gaining altitude [84]. But if for example a low-altitude flier's speed was halved as the result of heavy headwinds ($\overline{U}_R = 0.5$), then the difference between the flier and air velocity would actually be 50% larger and the flier would experience a significant upwards acceleration due to an increase in lift. The flier would need to adapt its geometry to return to its original lift state. This is most effectively achieved by either changing the wing span by extending or folding the wings, or changing the total wing camber.

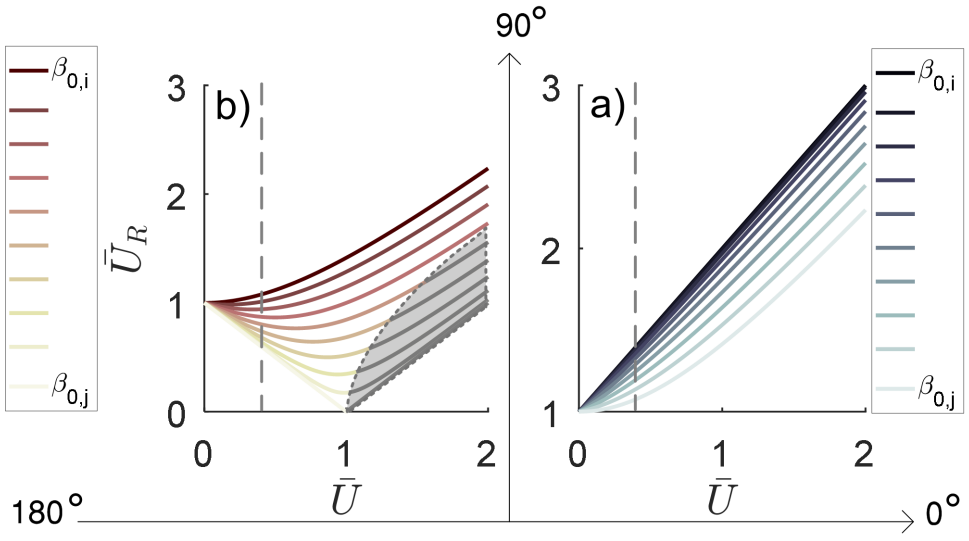

Figure 2.7: Non-dimensional glide magnitude for a) tailwinds and b) headwinds

2.3 Quasi-Steady Sharp-Edged Crosswind Response

Thus far, the preceding analysis has focused on how wind effects the resultant velocity vector and ignores aerodynamic forces. In the following section, a brief analysis will be conducted which assesses how the force due to an idealized sharp-edge crosswind affects the velocity and acceleration of the flier [87]. The aim is to determine how the response differs for high and low altitude fliers.

2.3.1 Aerodynamic Force Components

For this analysis, three basic assumptions are made. First, the crosswind is spatially constant. Second, the dynamic response only considers the translational degree of freedom. While the analysis is independent of sideslip, knowledge about how the aerodynamic forces change in sideslip is required as will be seen shortly. Lastly, the unsteady aerodynamic effects are neglected. A force diagram demonstrating the problem is shown in Figure 2.8.

In steady forward flight, the flier is neither accelerating nor decelerating. Thus, the in-plane forces must be equal and opposite according to Newton's 2^{nd} law, indicating that the force of thrust T equals the initial force of drag D_0

$$T - D_0 = ma = 0 \tag{2.9}$$

where m is the flier mass and a is the flier acceleration. However, in the event of a sharp-edged crosswind, an additional force is introduced causing a change in in-plane drag $\Delta D(t)$. This wind ultimately causes the flier to accelerate. Performing another force balance, the unsteady equation is determined to be

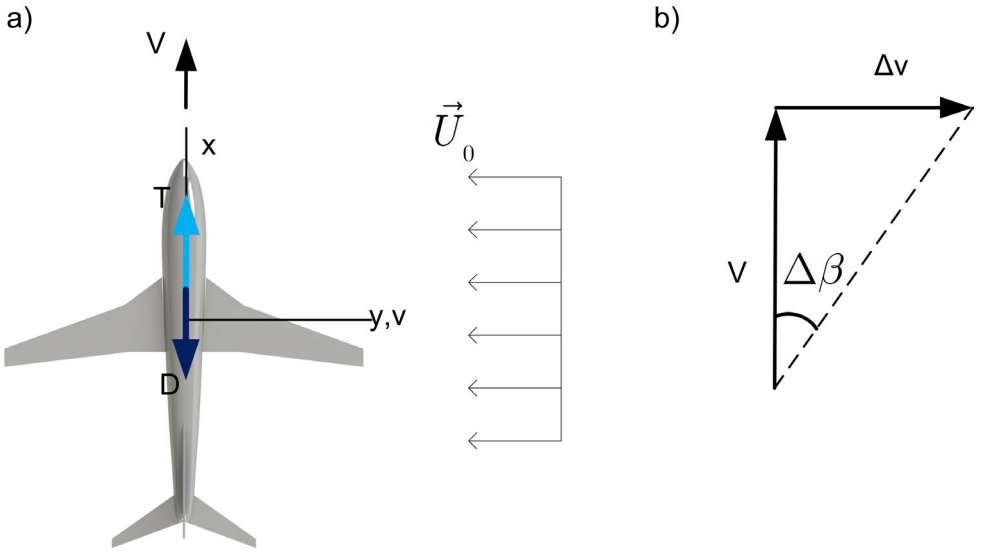

Figure 2.8: Depiction of a) aerodynamic forces in a sharp-edge crosswind and b) sideslip perturbation from gliding flight

$$T - D_0 - \Delta D(t) = ma = \frac{W}{g}\frac{d\Delta v}{dt} \tag{2.10}$$

where W represents the flier weight, g represents the acceleration due to gravity, t represents the time, and Δv represents the translational velocity. Note that the term $\frac{d\Delta v}{dt}$ can also be interpreted as the translational acceleration and will be written as $\Delta\dot{v}$ from here on.

Combining the steady and unsteady equations 2.9 and 2.10 respectively, the change in drag force is shown to be given by the following equation.

$$\Delta D(t) = -\frac{W}{g}\Delta\dot{v} \tag{2.11}$$

Recall that the drag force can also be written with respect to the aerodynamic flow

$$D = \frac{1}{2}\rho V^2 S C_D \tag{2.12}$$

where C_D represents the drag coefficient.

Upon observing the equation above it is clear that, given the assumptions made in this analysis, any changes in the drag force would be due to a change in the drag coefficient. An expression for the change in drag coefficient can be determined by recalling the definition of the dimensionless derivatives

$$C_{D_\beta} = \frac{\Delta C_D}{\Delta \beta} = \frac{C_D - C_{D_0}}{\beta - \beta_0} \tag{2.13}$$

which describes how the nondimensional coefficient changes with a rotational degree of freedom. Here, the derivative in question describes how drag changes as the result of changes in sideslip. Though cruise sideslip angle is typically zero, the total sideslip perturbation is written as the difference between the cruise sideslip and the sideslip due to the crosswind.

$$\Delta \beta = \frac{\Delta v}{V} - \frac{\Delta U_0}{V} \tag{2.14}$$

Equations 2.14 and 2.13 can then be substituted into Equation 2.12 to obtain the following equation for the change in drag

$$\Delta D = \frac{1}{2}\rho V^2 S C_{D_\beta} \left(\frac{\Delta v}{V} - \frac{\Delta U_0}{V}\right) \tag{2.15}$$

Setting Equations 2.15 and 2.11 equal to each other and simplifying the resulting expression, the governing linear 1^{st} order differential equation is derived as

$$\frac{2W}{g\rho V S C_{D_\beta}}\Delta\dot{v} + \Delta v = \Delta U_0 \tag{2.16}$$

which can be simplified as

$$\lambda\Delta\dot{v} + \Delta v = \Delta U_0 \tag{2.17}$$

where λ represents the time constant. Lastly, the sharp-edged crosswind can be incorporated. Assuming the flier encounters the crosswind at $t = 0$, the velocity in time is characterized as

$$\Delta U_0(t) = -U_0 1(t) \tag{2.18}$$

where $1(t)$ represents a step function.

2.3.2 Non-dimensional Solution

At this time, the differential equation will be non-dimensionalized for continuity with the preceding analysis. Recall that the non-dimensional velocity has been previously defined as $U_0 = \overline{U}U_\infty$. But note that for crosswinds, $U_\infty = V$. The translational velocity must also be non-dimensionalized

$$\Delta v = \overline{U}_v V \tag{2.19}$$

where $\overline{U}_v$ represents the non-dimensional translational velocity. However, the translational acceleration is also dependent upon this parameter and must be non-dimensionalized as well using Equation 2.19 and the chain rule as shown below.

$$\frac{d\Delta v}{dt} = \frac{d(\overline{U}_v V)}{dt} = V\dot{\overline{U}}_v \tag{2.20}$$

Equation 2.17 can now be re-written in terms of the non-dimensional parameters

$$\frac{2W}{g\rho V S C_{D_\beta}} V\dot{\overline{U}}_v + \overline{U}_v V = -\overline{U} V 1(t) \tag{2.21}$$

where equation 2.21 can then be simplified by factoring out V. Interestingly, upon simplification the form of the nondimensional differential equation is equivalent to the form of the equation prior to nondimensionalization. In fact, the time constant is identical to that derived in Equation 2.17.

The form of the solution to the non-dimensionalized differential equation is

$$\overline{U}_v(t) = -\overline{U}\left(1 - e^{-t/\lambda}\right)1(t) \tag{2.22}$$

which describes how the non-dimensional velocity changes with time. Upon differentiation, the non-dimensional acceleration is calculated

$$\dot{\overline{U}}_v(t) = -\frac{\overline{U}}{\lambda}\left(e^{-t/\lambda}\right) \tag{2.23}$$

The maximum acceleration experienced occurs at $t = 0$ and is equal to the non-dimensional velocity divided by the time constant. As was determined in Section 2.1, the non-dimensional velocity is directly related to the flyer's altitude. While it is tempting to assess the implications of Equation 2.23 strictly on the properties of $\overline{U}$, it is not yet known whether or not the time constant λ is dependent on the altitude as well. For ease of analysis, the leading term of the exponential equation is written out below in full

$$\frac{\overline{U}}{\lambda} = \frac{\overline{U} g \rho V S C_{D_\beta}}{2W} \tag{2.24}$$

The gravitational constant g remains relatively constant with altitude and the non-dimensional derivative C_{D_β} is also not anticipated to undergo much change with operating Reynolds number (and thus altitude). However, the density ρ is inversely related to altitude, thus low-altitude fliers would experience higher accelerations as seen from Equation 2.23. The influence of weight W, area S, and velocity V are slightly more complicated, particularly as all 3 parameters are interconnected. However, it has been proven by Tennekes [22] that W/S substantially increases with cruise velocity and thus altitude, and that W/V also increases with respect to velocity. Accordingly, the inverse product of these terms $\frac{VS}{W}$, would increase acceleration for low-altitude fliers. As both ρ and $\frac{VS}{W}$ reduce with altitude, it is beyond reasonable to conclude that the time constant λ of low-altitude fliers is much smaller than that of high-altitude fliers. Accordingly, acceleration due to crosswinds is much larger for low-altitude fliers.

These results can be seen in detail in Figure 2.9. Both the acceleration with respect to time, and the maximum acceleration with respect to non-dimensional velocity are depicted. As was shown in the prior analysis, the acceleration varies based on the time constant. The data in Figure 2.9a shows that the maximum acceleration begins at $t = 0$ and decays in time. The magnitude of the time constant effectively influences both the maximum experienced acceleration as well as the rate of decay. This demonstrates that low-altitude fliers, who's flight is characterized by much smaller time constants as justified prior, experience drastically larger changes in acceleration with time and approach an unaccelerated state rapidly. This is effectively characterizing how quickly the flier reaches the steady-state velocity as a result of the crosswind.

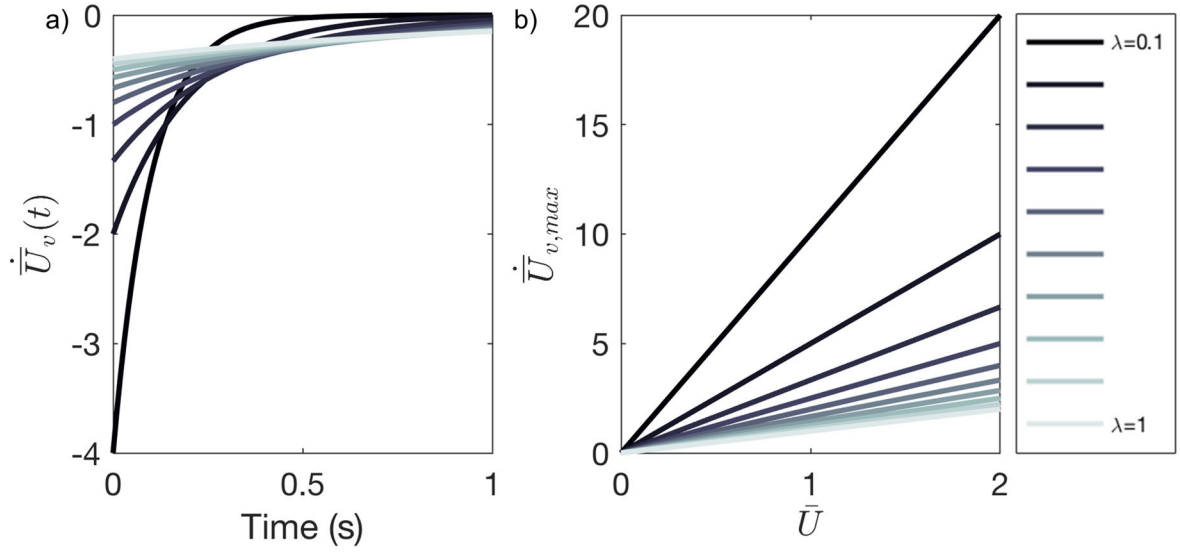

Figure 2.9: Acceleration response for various time constants a) with respect to time for a constant $\overline{U} = 0.4$ and b) for the maximum acceleration with respect to non-dimensional velocity

Furthermore, Figure 2.9b plots the maximum acceleration versus non-dimensional velocity. While the response for multiple values of λ are shown, note that both the time constant and non-dimensional constant are dependent upon altitude. The data show that low-altitude fliers, which experience small time constants and large non-dimensional velocities, can experience very large maximum accelerations making flight control quite challenging. Conversely, the combination of low non-dimensional velocities and large time constants for high-altitude fliers result in much smaller accelerations, potentially up to an order of magnitude smaller.

2.4 Chapter Summary

In this chapter, the effects of scale on flight response were assessed for a variety of parameters via analytical derivation. The purpose of this derivation was to simultaneously provide an understanding of the adverse aerodynamic conditions which natural fliers experience, and to further

motivate pursuing adaptive morphing technologies particularly at the UAV scale. In demonstrating the extreme aerodynamic conditions that low-altitude fliers are subject to, this work fortifies the justification of implementing morphing technology.

This derivation assessed how the addition of a wind vector affected both the magnitude and the direction of the resultant flight velocity vector. This was formulated in terms of a non-dimensional velocity parameter which was shown to be dependent on the cruise altitude of the flier with a cutoff occurring at approximately $\overline{U} = 0.4$. The results showed that low-altitude fliers like insects, birds and small UAVs are exposed to higher sideslip angles, peak sideslip sensitivities, and resultant speeds. Furthermore, the dynamic effects of the aerodynamic loading were considered by conducting a force-based derivation. The results showed that low-altitude fliers are very prone to large changes in acceleration. Not only is the maximum acceleration much larger than high-altitude fliers, but the rate at which the acceleration approaches steady state is much more rapid due to the impact of the solution time constant λ. This indicates that the velocity of low-altitude fliers will approach steady state velocity very rapidly compared to high-altitude fliers. To counteract these disturbances, the low-altitude flyer must be able to rapidly respond with large changes in geometry in order to maintain their initial heading and proper control of attitude and glide speed as is seen in nature [4], [6].

The demand for both high speed and large scale deformations begs for the implementation of morphing actuators and mechanisms. For small UAVs, actuators like soft actuators, microrobotics and smart materials provide a unique solution that can accommodate large strains, rapid actuation and low profiles for small-scale integration [43], [44]. While mid to high-altitude aircraft can still benefit from modern morphing technologies from an efficiency and mission-adaptive standpoint [13], this work reinforces the need to incorporate morphing technologies in future designs of low-

altitude aircraft and UAVs to properly maintain control authority and effectiveness in unpredictable aerodynamics.

CHAPTER 3

Bioinspired Rudderless Morphing Aircraft Concept

This work in its entirety focuses on the design, development and analysis of a bioinspired rudderless morphing aircraft concept. While this concept harnesses three separate research specialties (bioinspired aircraft, rudderless aircraft, and morphing aircraft), each was implemented with a specific intention in mind and is important in the culmination of this design.

As was mentioned in the Introduction, bioinspiration plays a key roll in design as it can help engineers brainstorm ways to improve functionality and efficiency. One of the prime reasons why birds are excellent sources of design inspiration is due to their extreme geometric adaptability and their smooth aerodynamic profile even upon adaptation. Though very complex in nature, this is frequently accomplished in a much simpler manner than what can be achieved with modern mechanics. Conversely, the discrete nature of traditional aircraft control mechanisms are severely limited in comparison and also exhibit drag-inducing vortices upon actuation [52].

The justification for studying a rudderless aircraft concept is twofold. Intertwined with the previous discussion, birds have evolved without the presence of vertical stabilizers though their tails have been shown to have similar function [33]. In aircraft, rudderless designs are also desirable due to their increased efficiency and low radar signature. Pursuing a rudderless design at the UAV scale is aimed at attaining both benefits in addition to potentially masking the aircraft within an urban

environment. Though bioreplication is not the aim in the current study, a bird-like aircraft is more likely to go unnoticed than one which resembles a standard aircraft. Ultimately, the rudderless aspect of the current design comes down to stealth and efficiency.

Finally, implementing morphing mechanisms into the aircraft design to achieve adaptive control is the crux of the matter. Morphing technology can provide a solution to both the discontinuous nature of traditional control surfaces in addition to improving actuation times for rapid adaptive maneuvers that parallel those of birds. Furthermore, little to no research has been conducted specifically on rudderless morphing aircraft outside of wing studies. Thus assessing yaw control and stability, a major concern in rudderless aircraft, from a novel morphing actuator standpoint will prove first of its kind. Combined, these attributes of the proposed aircraft concept allow for high-level basic research initiatives into new actuation mechanisms, furthering the field of morphing rudderless aircraft.

Accordingly, this chapter details the motivation, mechanisms, development and design inspiration that encompass this bioinspired rudderless aircraft concept. As this work represents one of the first efforts to develop novel rudderless actuators, the focus is on the development and assessment of the following morphing mechanisms, leaving out further multidisciplinary design optimization. Lastly an analysis of internal sensors within the morphing wing concept will be conducted, and sensor monitoring within the tail will be briefly discussed.

3.1 Motivating Bioinspired Design

Unlike aerospace engineers, biologists have much less control authority over their test subjects. The types of research which can be conducted with living specimens is limited in comparison and

typically requires extensive training within the cognitive abilities of the specimen, or manipulation through internal/external stimulation. Even with trained live specimens, there are very few methods of collecting the types of aerodynamic data that is commonly used to assess flight performance from an engineering perspective like aerodynamic forces and moments. Those methods which can measure forces measure total in-flight forces largely generated by flapping maneuvers [88] and thus cannot isolate the effects of specific in-flight wing or tail maneuvers.

Alternately, conducting experiments with nonliving specimens can be a heated topic of debate as the structural properties of frozen, dried and fresh specimens are not equivalent. While these specimens can be mounted to a load cell within a wind tunnel to collect in-depth aerodynamic data like lift, drag, pitching moment etc., they are not active structures. Any changes in shape are prescribed manually and thus a) might not capture the actual geometries and b) potentially reduces repeatability between configurations due to changes in mounting alignment, external factors like atmospheric pressure, etc. Ultimately, these experiments are limited to investigating solely the effects of geometry on the aerodynamic performance as opposed to actuation and control.

These challenges inherently limit the types of information that can be inferred about the function and performance of biological flight and control mechanisms. Thus this work aims to advance biological knowledge by recreating similar morphing mechanisms in engineered systems and assessing their performance and function quantitatively through comprehensive experiments. In designing and developing an active morphing mechanism which is inspired by that of birds, some knowledge can be gained regarding function and effectiveness as well.

3.2 Bioinspired Rudderless Morphing Aircraft Concept

This work develops morphing mechanisms for a bioinspired rudderless morphing aircraft, building upon both the SMTE concept [89] in addition to prior studies into the tail effect in birds [33] [34]. Combined, these mechanisms represent a complete morphing aircraft. This design in its completeness, shown in Figure 3.1, implements the SMTE concept to achieve smooth spanwise variations in wing camber. This mechanism is capable of reproducing the smooth cambered airfoil shape of birds while also maintaining the ability to tailor the camber along the span. Though a serpentine trailing edge is portrayed, any shape within the constraints of the SMTE can be achieved. Furthermore, with the rapid response time of the morphing actuators, the rate of control mirrors that of biological muscle. This makes the SMTE an excellent candidate for adaptive maneuvers.

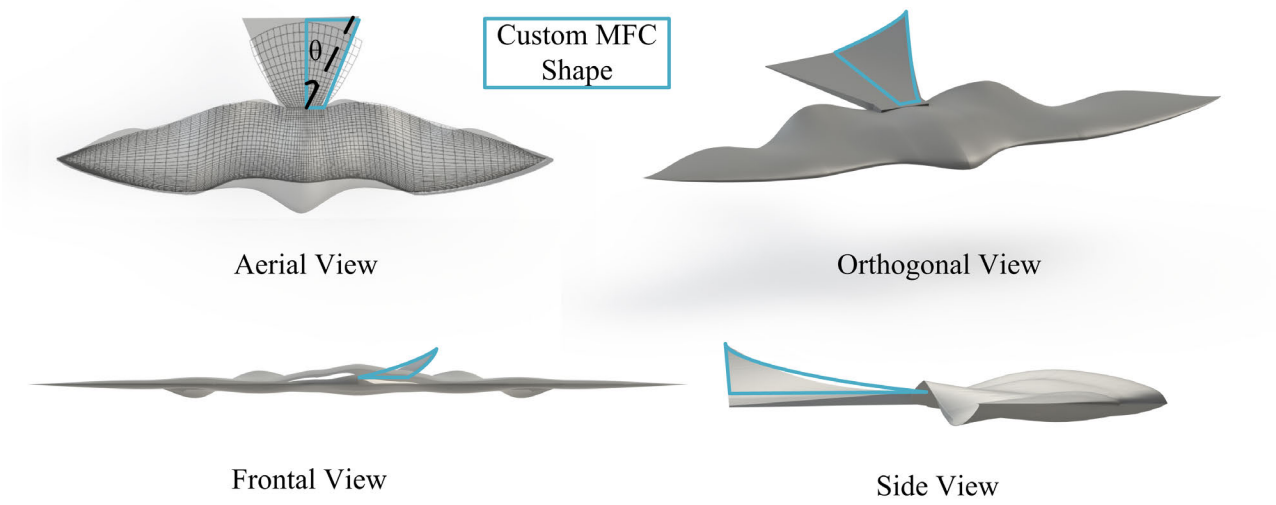

Figure 3.1: Demonstration of the bioinspired aircraft with left actuator deflected where θ represents the fiber angle

Secondly, the proposed design utilizes a bioinspired horizontal control surface or ”tail” for

small UAVs which is designed with two custom MFCs, one on each half of the tail. While this design is still considered rudderless since it lacks a vertical stabilizer, the term tail in the current work is used as a comparison to bird anatomy. This tail-like actuator aims to address the reduced directional stability of flying wings by capitalizing on the stability characteristics of the tail of birds. The tail acts as a high aspect ratio control surface aft of the center of gravity which provides a restoring moment in sideslip [33]. As in traditional aircraft, this control surface decouples control from the wings, the main lifting surface. In the current design, the wings maintain lift during gliding flight while the piezoelectric tail actuator undergoes large scale deformations to control pitch and yaw, or it can utilize continuous corrective input to dynamically stabilize the body due to the rapid actuation time of the MFCs. Lastly, by implementing MFCs with a custom geometry and fiber orientation, this design proves to be multifunctional and effective over a range of sideslip angles.

3.2.1 Aircraft Body

While typical morphing airfoil studies are frequently conducted on 2D infinite sections, the tail-like control surface proposed here cannot be approximated as two-dimensional and requires integration into a full aircraft body to study the full 3D effects due to the asymmetric nature of actuation. This could be accomplished using one of three designs: a straight rectangular wing, a classic flying wing body, or a biological body. A straight rectangular wing would be the simplest solution; however, this would be a stark departure from traditional rudderless aircraft bodies. A classic flying wing body would provide a more realistic comparison for rudderless aircraft. Many of these designs have been well studied and thus could be used comparatively with this work. But

these designs exhibit a swept wing configuration which inherently affects the yaw stability and would make isolating the effects due to the proposed control mechanisms more challenging. The final and best solution is to use a bioinspired body shape with non-swept wings which has been previously studied.

Accordingly, the aircraft body was designed using the same planform shape as the studies conducted by Hummel [34] and Sachs, *et al.* [33] as shown in Figure 3.2. However unlike those studies, the wing geometry was designed with a symmetric NACA0012 airfoil to eliminate the camber effects on lift, drag and pitching moment. The aircraft was designed to be a half scale model with approximately a 0.3 m wingspan so that it was properly sized to test in the 0.6 m x 0.6 m wind tunnel at the University of Michigan.

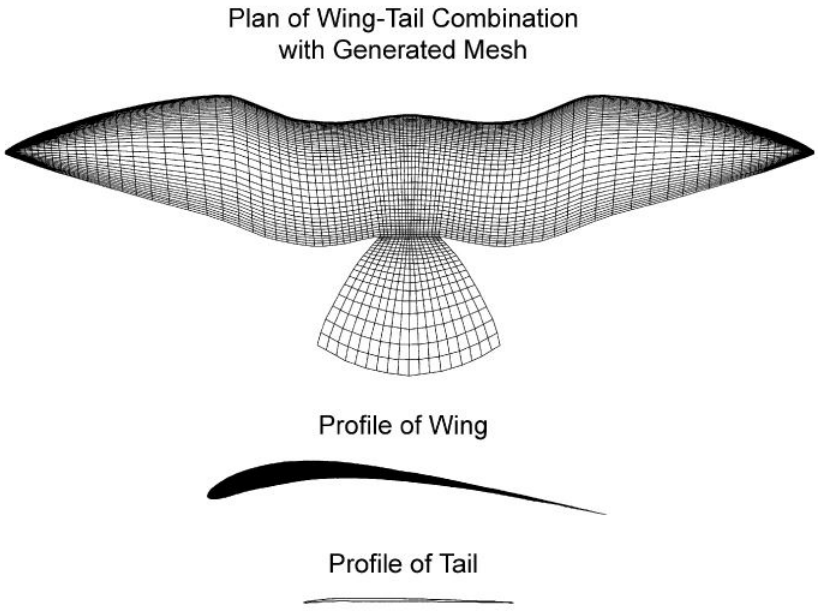

Figure 3.2: Planform wing geometry of the rudderless aircraft consistent with prior studies on tail effects [33]

3.2.2 Wing Morphing Mechanism

While the ultimate design of the bioinspired aircraft in question takes on the wing profile detailed in Section 3.2.1, assessing the fundamentals of spanwise morphing wings on such a geometry would be challenging. This would be a particularly troublesome issue upon attempting to isolate the effects of spanwise morphing from the unique shape of the bioinspired wing. For this matter, the proceeding analysis will focus on a standard symmetric rectangular wing, keeping in mind that this technology can be applied to other geometries after comprehensive analysis.

In this section, the mechanics behind the MFC actuators in the SMTE wing will be discussed in addition to methods of improving sensor integration for measuring the morphed tip deflection.

3.2.2.1 Conformal Morphing

One key distinction between the morphing airfoil studied here and traditional actuators is the ability to produce a smooth camber with a flexible piezoelectric composite. On the 2D scale, this is primarily achieved through the use of MFCs. As shown in Figure 3.3, the MFC is a composite actuator that is comprised of layers of adhesive, polymer, electrodes, and PZT which has been processed into thin fibers. Although bulk ceramics like PZT are typically very brittle, the reduced 2^{nd} moment of area makes the fibers much more flexible and capable of withstanding large out-of-plane strains.

The inherent piezoelectricity of the Navy Type II PZT used here induces strain and elongates longitudinally about the neutral axis. This occurs upon applying an electric field to the MFC in the form of a voltage between -500 V and 1500 V. Although the actuator only experiences very small strains, fairly large deformations can be achieved upon bonding the MFC to a thin rigid substrate.

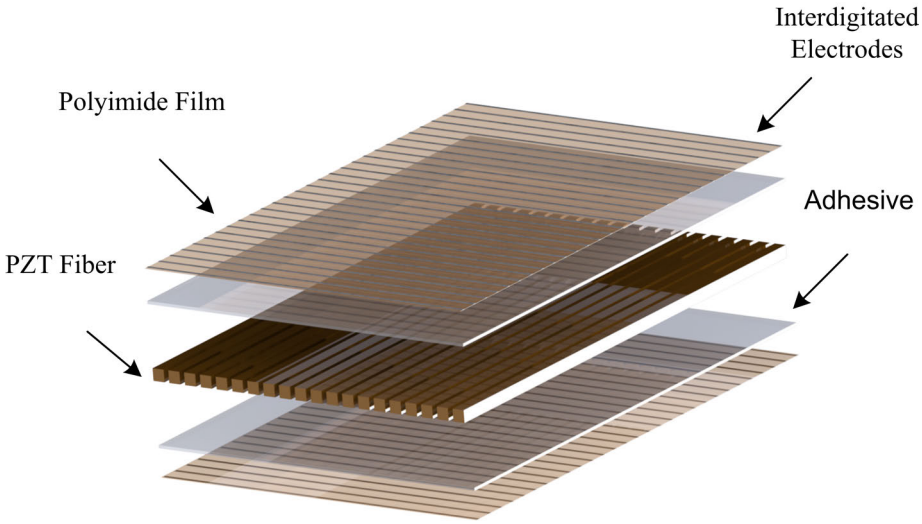

Figure 3.3: Exploded simplified graphic representation of the MFC lamina

With this addition, the neutral axis of the assembly has been shifted such that the applied strain from the MFC occurs at some height above or below the neutral axis and thus induces bending. This allows for the MFCs to be used as flexible camber morphing actuators.

With this knowledge, it's easy to see how this smart material actuator can be integrated into an airfoil section in order to achieve camber morphing. However, for completeness, the design originally developed by Bilgen *et al.* [61] [44] and later adapted by Pankonien *et al.* [90] will be briefly discussed. The latter design employs two MFC actuators in a cooperative fashion as shown in Figure 3.4 such that the bi-directional actuation capabilities of the actuator are utilized. More specifically, for upwards deflection, the bottom MFC is actuated at maximum positive voltage while the top MFC is actuated at maximum negative voltage. The camber morphing section is integrated into the leading edge of an airfoil using a compliant 3D printed flexure box. This box enables some degree of rotation at the root of the MFCs allowing for maximized, unconstrained actuation. Lastly, Spectra Symbol's Flex sensors, a type of variable resistor, were integrated into

the trailing edge in order to monitor deflection.

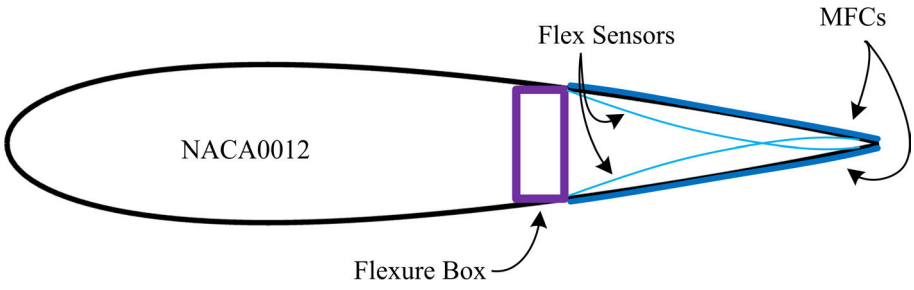

Figure 3.4: Depiction of the 2D MFC trailing edge section

3.2.2.2 Spanwise Morphing Trailing Edge Concept

The foundation for this section relies not only on the camber morphing capabilities of the MFC actuator, but also the ability to tailor the geometry along the span of a wing. One of the major hinderances of developing morphing mechanisms is the essential compliance of the underlying structure. There is an inherent tradeoff between inducing large scale shape change and maintaining distributed loadings. Typically, in order to undergo large scale deformations a structure must be compliant enough to be deformed. One method of accommodating this is to discretize the system such that compliance is only mandatory between the active morphing sections. The SMTE mechanism harnesses this concept.

The SMTE, shown in Figure 3.5, is composed of repeating active and inactive sections. The rigid active sections produce the conformal bending discussed in Section 3.2.2.1. Their trilateral structure allows them to withstand larger out-of-plane loadings than a single MFC would be capable of. Each active section can be controlled independently of the others allowing for a tailored spanwise geometry within the limits of the actuators. The continuity between the actuators is maintained by using an elastomeric inactive section. The inactive sections are composed of a 3D printed

honeycomb which has been bonded to a silicone skin and wrapped around the entire trailing edge of the wing. While the elastomeric skin alone would effectively maintain a continuous surface, the 3D printed honeycomb serves greater function. In addition to allowing for in-plane strains upon actuation of the adjacent active sections, the structure of the honeycomb also withstands some out of plane loadings, reducing unwanted aeroelastic deformation between actuators. In its absence, the skin would flutter and balloon under loading. Additionally, with this modular assembly it is clear to imagine how a) single off-the-shelf components could be manufactured for easy assembly and b) the structure could be further discretized in order to obtain smoother spanwise geometries if needed.

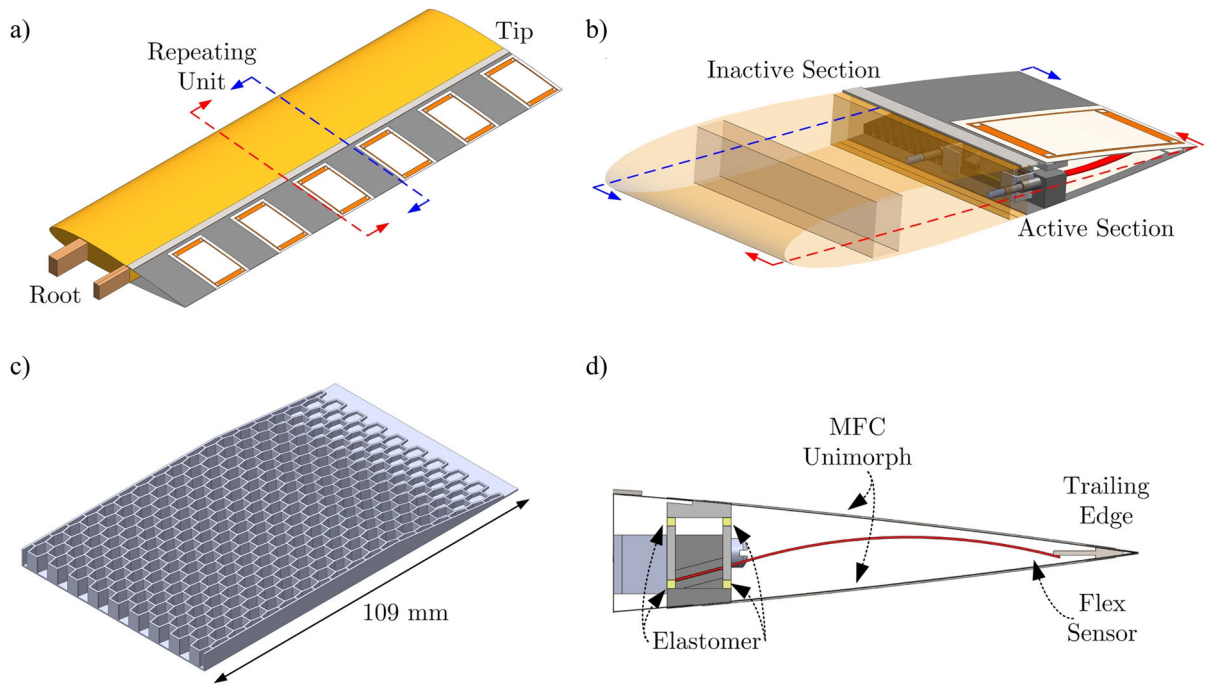

Figure 3.5: Diagram of a) SMTE full isometric view b) repeated section isometric view c) inactive honeycomb d) cross-sectional view of the active trailing edge components

3.2.3 Tail Morphing Mechanism

As with the morphing wing detailed prior, the tail actuator proposed here is also composed of MFCs. In developing this control surface, the goal was to simplify the complex mechanism of a bird's tail into a single actuator. A bird can pitch, spread and twist its tail to act as both a rudder, an elevator, and an airbrake to control yaw, pitch, and drag or speed respectively.

The tail was was developed using two customized MFC actuators. These actuators were manufactured with the custom geometry shown in Figure 3.1 such that the tail aspect ratio and geometry would resemble the planform shape of prior studies such as that shown in Figure 3.2. Implementing MFCs with a custom tail geometry in a 2D camber morphing fashion but would effectively act solely as an elevator in traditional aircraft by influencing the pitching moment. However, the MFCs can be manufactured with customized PZT fiber orientation as well. The customized fiber orientation is key to the multifunctionality and control robustness of this design.

As mentioned prior, the MFCs are composed of thin PZT fibers which elongate in the fiber direction in the presence of an electric field. Harnessing fundamental fiber composite theory, the MFCs will experience bending-twisting coupling if the fiber direction is rotated in-plane. This mechanism, which effectively generates displacements in 3D as opposed to 2D in the case of camber morphing MFC actuators, is meant to resemble the actuation authority of bird tails in a more simplified albeit coupled manner which can pitch and rotate. This design provides an advantage over traditional yaw steering control surfaces due to the nature of its complex curvature. Unlike traditional flat control surfaces, whose area perpendicular to the wind vector will decrease with sideslip, the 3D deformation of this actuator retains surface area perpendicular to the flow even at large angles of sideslip as can be seen in Figure 3.1. The 3D deformation also allows

for the control surfaces to remain entirely continuous. This continuity eliminates the formation of vortices which develop at geometric discontinuities and increase drag in traditional discrete control surface designs [91] [92] [64].

Furthermore, MFCs have a rapid actuation frequency of up to 10 kHz. Though the maximum achievable deflection has been shown to decline with frequency of cyclical actuation, it is still estimated to perform optimally within a fraction of a second in the current configuration [93]. Lastly, given the modular nature of the tail, a variety of actuation configurations are possible. Deploying only one side of the control surface will allow for yaw control, deploying both sides symmetrically will allow for pitch control, and deploying both sides asymmetrically could potentially be used as an airbrake. These configurations are demonstrated in Figure 3.6. Ultimately, this actuation mechanism would be incorporated in an aircraft along with the spanwise morphing capabilities of the SMTE in the wings to provide complete aircraft control coupled with a sensor network to monitor the mechanical and aerodynamic status of the aircraft and inform the response of the actuators.

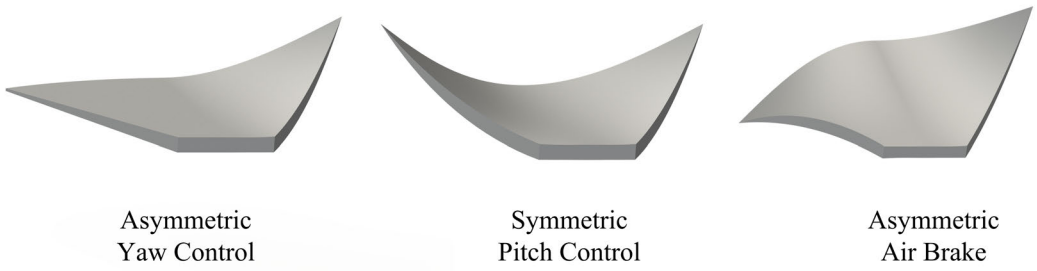

Figure 3.6: Morphing tail configurations and their control response

3.3 Sensor Improvement

Unlike traditional servo-based ailerons which include embedded sensors and integrated encoders for precise positional feedback, the MFCs alone don't completely have the ability to do so. Not only do they experience hysteresis, but their flexibility makes them prone to further deformation under external loadings. This makes direct control of high aspect ratio MFCs by voltage alone very unfeasible. Instead, the deformation of the MFC trailing edge must be monitored with internal sensors to inform a positional controller. While the original morphing trailing edge design incorporated Flex Sensors shown in Figure 3.4, their performance is not ideal particularly as they also experience some hysteresis in this configuration.

3.3.1 Sensor Summary

In an attempt to improve the sensing capabilities of the SMTE, a brief cost-benefit analysis was conducted to potentially identify better strain or displacement sensors. A summary of these sensors can be found in Table 3.1. One of the most popular methods of sensing uses linear or rosette strain gauges. Given their relatively low cost, low profile, and good precision they are an excellent choice in many applications. However there are two major reason why they are not ideal for the current configuration. Primarily, they measure single point strain. In the present trailing edge mechanism, uniform strain is not guaranteed due to the compliance of the assembly. For example, if the gauge is located near the root of the MFC but the aerodynamic loading causes the tip to deform, then the sensor's reading can't accurately be correlated to the tip deflection.

Contrarily, some fiberoptic strain sensors are capable of providing continuous sensing along the fiber length. While continuous strain measurements sound ideal, post-processing the tip deflection

from this data would be quite challenging and perhaps computationally expensive. This would prove problematic for use in real-time control. Another option would be to use MFCs. Though MFCs have been discussed as an actuator up to this point, they also have sensitive strain sensing capabilities when unpowered. Using high-aspect ratio MFCs could potentially provide a viable solution by measuring the strain along the entirety of the cambered actuator, but some drawbacks include their high price tag and lengthy installation process.

The final sensor to discuss is the Flex sensor. Detailed in Figure 3.4, the Flex sensors are mounted with one end fixed to the root of the flexure box while the other is constrained to the tip of the trailing edge. With this configuration, the sensor curvature (and thus voltage output) can be directly related to the tip deflection. While Flex sensors are low profile, cheap and easy to install, they experience some thermal dependency (which is not a high priority in the current work) and experience lower precision than many of the other sensors. Given their clear advantages, methods of improving their performance were investigated.

Table 3.1: Cost-benefit comparison between various strain sensors

Sensor	Precision	Profile	Thermal Dependency	Installation	Cost
Strain Gauge	Medium	Low	High	Hard	Low
Piezoelectric	High	High	Low	Simple	High
Fiberoptic	High	Low	Low	Hard	Medium
MFC	High	Low	Low	Hard	High
Flex Sensor	Low	Low	High	Simple	Low

3.3.2 Flex Sensor Characterization

To begin, the sensor's current capabilities of measuring the tip displacement were assessed. This provides a starting point for further analysis. In this configuration, the Flex sensors are em-

bedded as-is into the trailing edge of the SMTE. The sensor's performance was tested by manually cycling the tip displacement of the morphing SMTE section like that shown in Figure 3.4. The trailing edge displacement was measured using a high-precision Keyence LK-G402 laser displacement sensor. The internal Flex sensors, which have a nominal resistance of approximately 10 kΩ, were wired in a voltage divider configuration shown in Figure 3.7a. As the Flex sensors are unidirectional, incorporating two Flex sensors into the circuit ensures that displacement readings can be obtained regardless of the direction of actuation. Lastly, the output signal was read from between the Flex sensors.

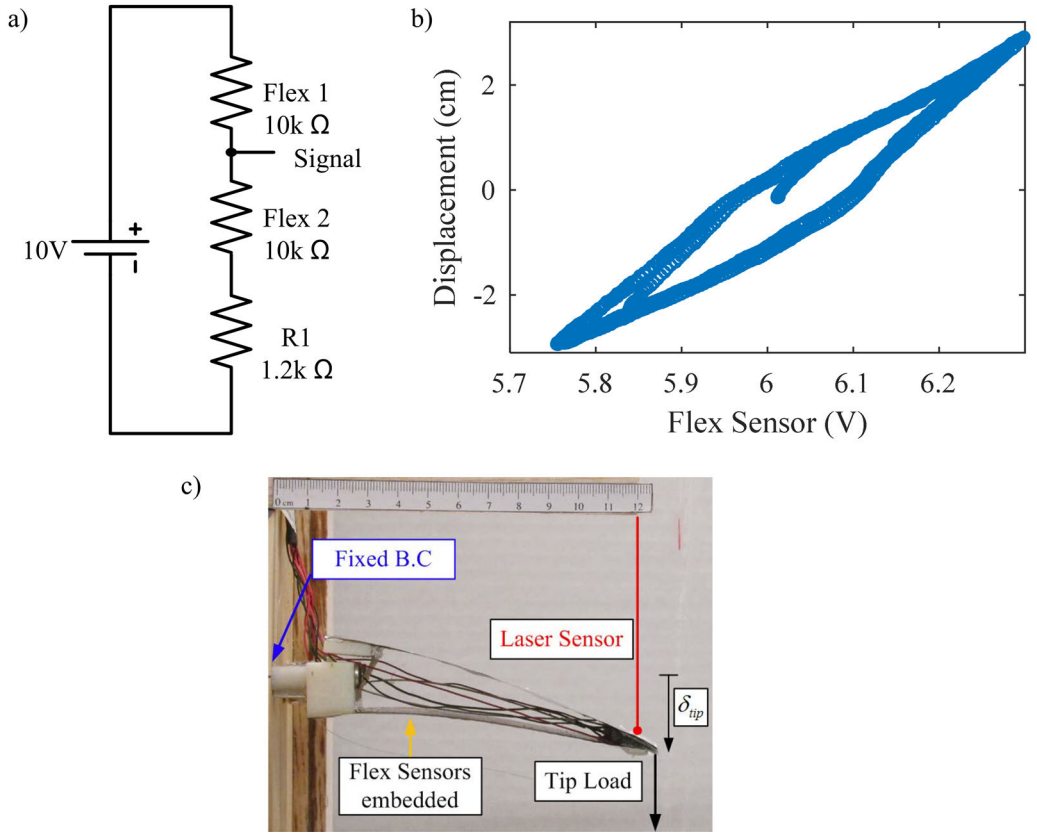

Figure 3.7: Characterization of the initial Flex sensor configuration given a) a voltage dividing circuit, and resulting in b) a hysteresis plot of the output signal versus actuator dip displacement for the c) experimental setup used by Pankonien [89]

The initial results, shown in Figure 3.7b, demonstrate that the Flex sensors experience what can be approximated as a linear relationship between tip deflection and output signal. However, it is clear that this configuration experiences substantial hysteresis. This is evident in that the data follows a looped path where two output signals can represent a single displacement. When the curve is at its widest, near approximately an output sensor voltage of 6 V, the range in displacements is between -1.2 cm and 0.2 cm. This is thought to be due to plastic deformations within the sensors due to the polymer packaging. Given this large range, it is clear that investigations into improving the sensor performance would be valuable.

3.3.3 Substrate Testing

As the initial issues with the preliminary configuration were hypothesized to be the result of the Flex sensor's inherent material properties, the first attempt to improve the performance was geared towards increasing the rigidity of the sensor itself while still allowing for adequate tip displacements. This was achieved by bonding a $1/100^{th}$ in. thick steel substrate to the sensor. While the added rigidity was hypothesized to improve performance, the substrate also shifted the neutral axis about which the sensor bends. This effectively increases the strain experienced by the sensor and would also improve performance.

To test the performance of the new Flex sensor with bonded substrate alone, it was mounted at its root to a fixed support. Again, the tip was cyclically loaded and the displacement was measured using the laser displacement sensor. As this configuration only consists of a single Flex sensor, a voltage divider like that shown in Figure 3.7a was used without the 2^{nd} Flex Sensor. It is important to note that this results in a different output voltage range than previously seen.

Figure 3.8 shows a comparison between the cyclically loaded sensor with and without the substrate. The data provide substantial insight into how the substrate affects the sensor performance. First the sensitivity, defined as the ratio of the change in output voltage per unit measurement, can be assessed. From this it is evident that the sensitivity is increased dramatically upon adding the substrate. Using a linear fit, the sensitivity of the sensor without substrate is 0.019 V/cm while the sensitivity of the sensor with substrate is 0.1 V/cm. Furthermore, the range of the sensor improves dramatically with the addition of the substrate. This is evident in the increase in voltage that the sensor reads.

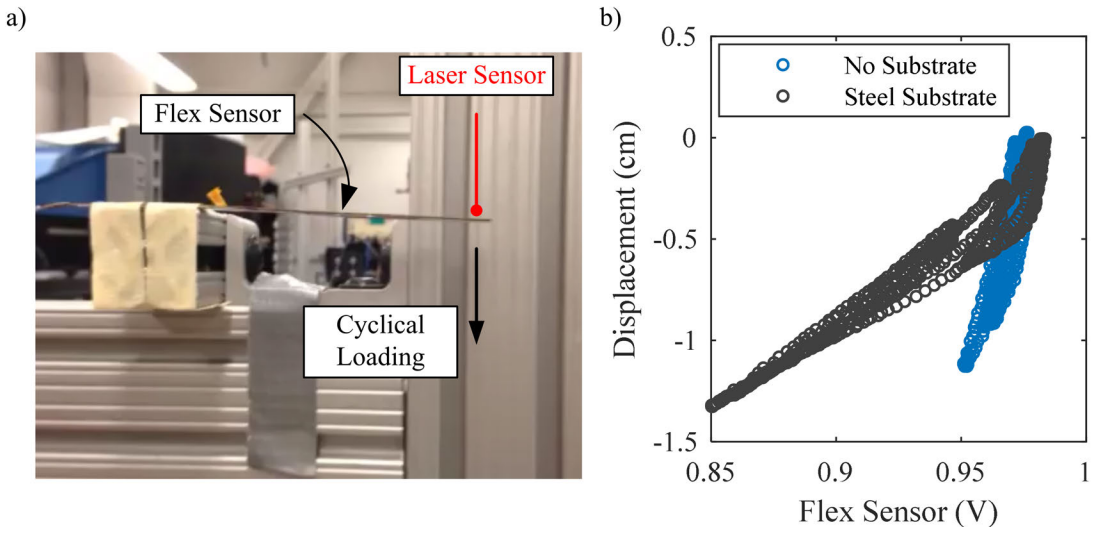

Figure 3.8: a) Experimental setup of Flex sensor characterization b) Flex sensor response results

3.3.4 Quantifying Error Improvements

To further improve error and check the performance of the sensors, they were re-incorporated back into the MFC trailing edge for testing. The dual sensor configuration described in Figure 3.7c was implemented in order to capture both positive and negative trailing edge deflections.

Additionally, as opposed to the sole voltage divider implemented prior, a bypass capacitor was also integrated into the sensor's circuitry in order to increase the SNR. While initial testing did not observe that the sensor was particularly noisy, adding a capacitor to filter out AC noise and eliminate crosstalk between devices on the same power supply would further improve the sensor's performance. The final circuit is shown in Figure 3.9.

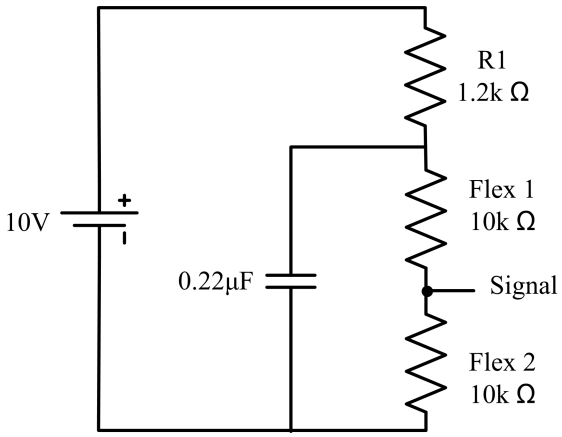

Figure 3.9: Bypass capacitor circuit for noise reduction and improved SNR

The trailing edge was actuated sinusoidally at 0.5 Hz and the tip displacement and sensor output was measured. For completeness, this experiment was conducted both with and without the steel substrate bonded to the sensors. Figure 3.10 shows that as determined prior, the addition of the substrate increases the range of output voltages as can be seen from the peak to peak range. Note that the shift in voltage output between the sensors with and without the substrate is due to differences in the internal resistance of each sensors. While the sensors are nominally 10 kΩ, they are subject to fairly large variations. While not ideal, this is easily accounted for through a calibration process which must be performed regardless. Though not clearly evident, the time response of the sensor without substrate is not completely sinusoidal and experiences some clipping at the lower peak. This indicates that the sensitivity at this deflection is much lower than experienced by

the sensor with substrate.

The sensor response relative to the displacement can also provide very useful insight. Primarily, this data confirms that the output voltage range of the sensor without substrate is substantially smaller. Furthermore, the response is expected to be linear which is seen in the sensor data with substrate, but not without substrate. This can be quantified by assessing the Root Mean Squared Error (RMSE) which measures how closely the data matches a linear fit. The Flex sensor data without the substrate has a RMSE of 11.5%, while the RMSE of the Flex sensor data with substrate is 3.3%. The error of the latter is quite good and thus these changes to the sensor and circuit design will be implemented through the proceeding analysis.

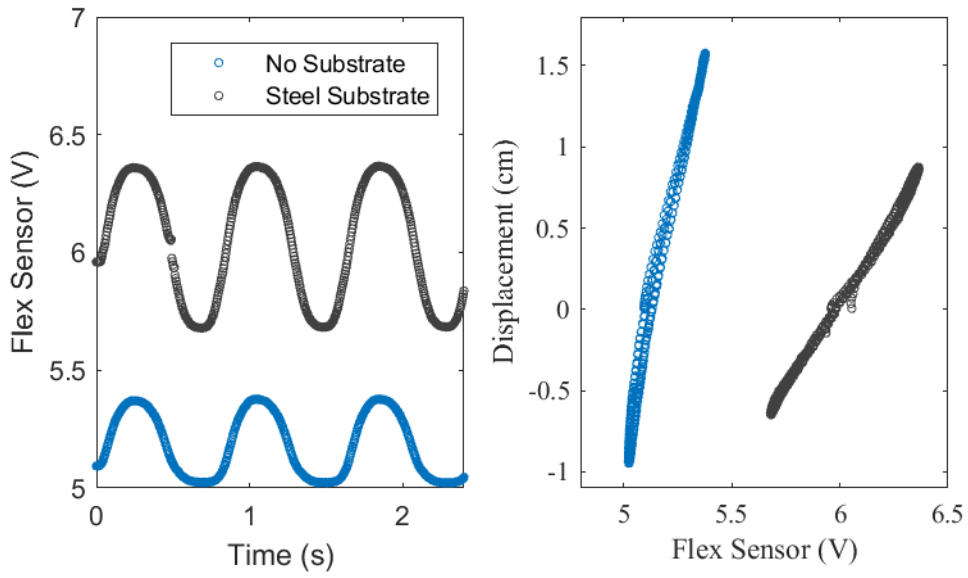

Figure 3.10: Sensor response to cyclical loading in time and with respect to displacement

3.3.5 Tail Sensor Considerations

While the morphing wing detailed above implements internal Flex sensors to monitor the true displacement of the actuator, this technology is not appropriate for the tail morphing mechanism.

This is due to the scale and 3D curvature of the actuator. That being said, the development of new distributed flexible sensing networks is rapidly progressing and may one day be ideal for this particular application. This would allow for continuous monitoring along the entirety of the deformed surface which would prove particularly useful given that this actuator deals with 3D shape change. But in addition to difficulties in sensor network manufacturing and testing, it is clear to imagine the difficulties of multi-input (and potentially multi-output) control.

For these reasons the control of the tail actuator in the proceeding analysis will rely solely upon direct voltage application. Given the relatively low aspect ratio of the tail geometry, the aeroelastic deformations are expected to be relatively small with respect to sideslip. However, this will ultimately be quantified upon aerodynamic testing.

3.4 Chapter Summary

In this chapter, the complete aircraft concept studied in this work was detailed in full. This provides a concrete foundation and overview for the design and analysis that will be discussed in the proceeding chapters. The concept was broken down into three sections, detailing the spanwise morphing wing, multifunctional morphing tail, and embedded sensor improvement. Inspired by nature, both morphing concepts produce organic deformations by utilizing the flexible nature of MFC smart material actuators to achieve continuous deformations.

In summary, the purpose of the spanwise morphing wing is to locally alter the lift along the wing, allowing for targeted aerodynamics. By adjusting the wing's aerodynamics along the span, this further allows for localized adaptation which, as an example, could be useful for recovering from tip or root stall. Furthermore, the continuous nature allows for more efficient standard 2D

actuation due to the elimination of vortices at geometric discontinuities. The internal sensors were also drastically improved allowing for more accurate control of the MFCs.

Finally, the purpose of the tail actuator is to aid in control and stability of rudderless UAVs. The novel design is intended to serve a multifunctional purpose by exhibiting yaw and pitch control, like the tail of birds, in a simplified package. This was accomplished through the development of customized MFCs, which will be discussed in full in the following chapters.

CHAPTER 4

Stall Recovery via Spanwise Morphing

Chapter 2 demonstrated how low-altitude fliers in particular may benefit from adaptive morphing mechanisms and set up the framework for the proceeding analysis. However, designing and implementing the appropriate morphing mechanisms in aircraft remains a challenge in its own. In contrast, birds readily morph their wings which provides a highly effective method of adapting to adverse aerodynamic conditions due to winds, prey payload, etc. [3]. As an example, the steppe eagle is capable of deliberately stalling sections of their wings [4], motivating research into spanwise morphing wing studies. This ability to morph geometry allows both birds and aircraft to operate effectively over a range of flight conditions. In aircraft, this allows for efficient flight outside of the principal design by altering parameters such as camber, sweep, twist, or planform area [37]. In small UAVs which operate at low Reynolds numbers, this can be advantageous since unfavorable aerodynamic phenomenon such as winds, and static imbalance due to payload shift and delivery can heavily impact gliding flight. Yet, while research within aircraft morphing has been rapidly growing in recent years, the focus has lingered on linear aerodynamic conditions.

Previous research by Pankonien *et al.* [63] on the SMTE concept has shown that smooth morphing wings have a distinct advantage over conventional discrete control surfaces, in part by reducing drag by eliminating vortex formations that occurs at the aileron's geometric discontinuities. Yet

the complex and multidisciplinary challenge associated with assessing these advantages near stall motivates this chapter. The SMTE employs MFCs, a piezoelectric smart material, as the active sections of the camber-morphing wing with alternating elastomeric honeycomb sections. The conformal bending and large bandwidth properties of the MFC allow for a quick and precise trailing edge camber response while the elastomeric honeycomb eliminates geometric discontinuities. By using MFCs, which act as both the aileron structure and actuator, the system's mechanical complexity can be reduced providing an advantage to other morphing concepts which rely on conventional actuators.

Inspired by the dynamic capability of birds which continuously change their wing shape to suit an arbitrary flight condition, the current work uses model-informed experiments to investigate the effects of smooth spanwise variations in camber of a morphing wing on aerodynamic stall via the SMTE concept. Using this morphing mechanism, the trailing edge deflection of the 6 actuators can be tailored along the span of the wing to target local aerodynamics. In order to predict the actuator configurations for stall recovery, a model which accurately captures the nonlinear behavior of finite wing aerodynamics must be utilized.

The most widely used nonlinear LLT models are frequently criticized for their inability to converge past stall where the lift-curve slope is negative [94], saw-tooth oscillations in their post-stall circulation distributions, and non-unique post-stall solutions [95] making them unsuitable for near-stall analysis and optimization. A more recent nonlinear method developed by Chattot resolved these issues by incorporating an artificial viscosity term into the governing equation and consequently showed excellent post-stall agreement with an analytical solution [96].

Upon development of an accurate model in this work, the wing performance during static stall was assessed for a 0.3 m chord, aspect ratio 6, finite wing of half span in a wind tunnel. Flow

visualization was implemented for verification. The resultant forces were compared to those of a conventional, articulated wing of equal dimensions with servo-driven ailerons. In this novel approach, it can be shown that adaptation, including stall recovery, can be achieved solely through geometric tailoring as opposed to attitude correction for a range of flight conditions while reducing the drag penalty associated with operating at the unadapted condition. The range of conditions for which the wing can recover are restricted by the limited trailing edge deflections and the inability of the actuators to drastically shift the stall angle of the 2D lift curve. These results provide insight into improving morphing wing designs, indicating that by adding another degree of freedom to the chord-wise deformation such as a morphing hinge capable of larger actuation and reflex camber, stall recovery via geometric tailoring may be feasible for an even larger range of conditions.

4.1 Problem Statement

Using the loosely-coupled viscous model mentioned prior, this work aims to quantify the capabilities of a morphing wing to adapt to nonlinear aerodynamics and recover from stall. The scenario under investigation assumes an aircraft adapts to unfavorable aerodynamic conditions which is detailed as follows [65]. The aircraft begins at its designed cruise conditions (on-design). Following a change in aerodynamic load such as a headwind or payload delivery which may change the location of the center of gravity, the aircraft now operates at an off-design condition defined by a change in angle of attack. This chapter will focus on the analysis of off-design conditions near stall where such changes could have disastrous consequences due to the severe decrease in lift and increase in drag. While remaining at the off-design state, the aircraft adapts to the unfavorable aerodynamics by morphing the spanwise trailing edge deflections to return to the initial on-design

lift condition. While this final flight condition will incur a drag penalty with respect to the on-design flight condition, this penalty will be substantially lower than it would be in the absence of adaptation as can be seen in Figure 4.1.

Overall, this proposed method of adaptation differs from the traditional reduced angle approach to stall recovery due to differences in the aerodynamic conditions between transonic aircraft and small UAVs. In particular, UAVs are prone to frequent changes in aerodynamics, especially in urban environments. It is clear to imagine how frequently changing the aircraft's angle of attack to induce recovery would be undesirable. It is important to note that, although the motivation for this work is partly attributed to unsteady conditions, the focus is on prolonged disturbances like steady winds and payload delivery. Transient loadings are not considered in this initial analysis, thus a steady aerodynamic model is used.

This adaptation scenario is specific to nontraditional aircraft including but not limited to low speed aircraft or small UAVs which operate in urban environments and gustier conditions, and variable-sweep wings which are prone to changes in stall location. This proposed spanwise variation in trailing edge camber allows the actuators to target specific stalled regions of the wing such as the root or tip, inspired by the adaptation of the steppe eagle. This ability would prove particularly useful for variable-sweep wings where the location of stall can vary between the inboard and outboard wing depending on the sweep configuration. While the model proposed here is not valid for largely swept wings, this does not detract from the SMTE's ability to tailor the spanwise geometry in the aforementioned scenario.

Furthermore, with the MFC's rapid actuation time, the spanwise shape of the wing can be quickly tailored to mitigate the effects of the nonlinear aerodynamics while in the disturbed state. Then when the disturbance has passed, the wing will return to its original on-designed geometry.

The alternative for traditional aircraft would be to either wait until the disturbance has passed, incurring an unadapted drag penalty shown in Figure 4.1 by the difference between points 2 and 1, or change the angle of attack via elevator control which would need to be restored after the disturbance had passed, resulting in a sinusoidal pitching motion and possible instabilities.

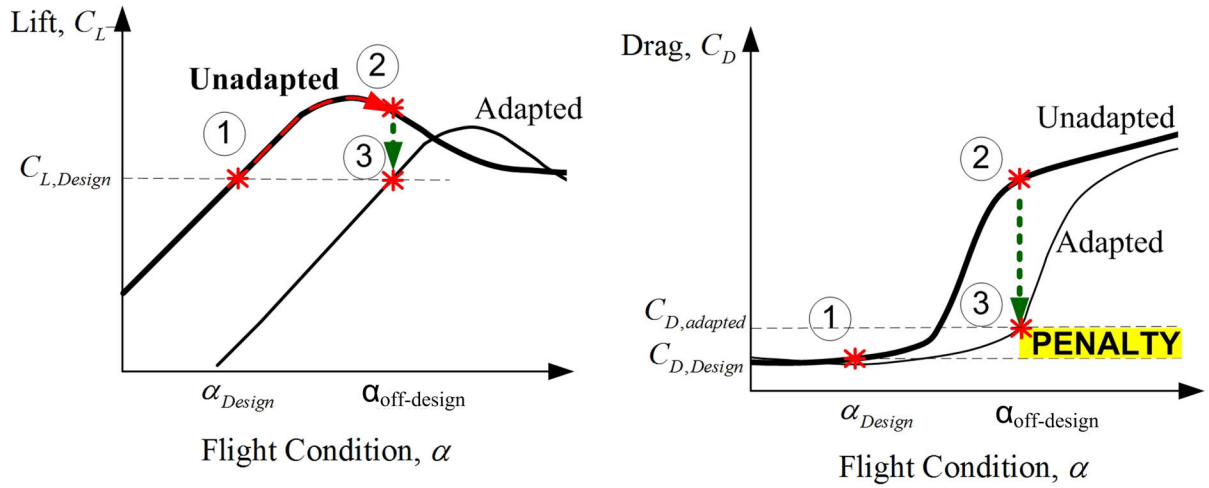

Figure 4.1: Graphic summary of the design scenario in terms of forces, depicting the adapted aerodynamic curves and associated drag penalty (between dashed lines)

Extended disturbances such as payload deliveries will also change the total lift and may alter the location of the center of gravity, resulting in long-term change in angle of attack. Like birds, which change their wing geometry while carrying prey, the wing design considered here is capable of morphing the spanwise shape to adapt to this change in payload. Finally, with the ongoing development of superior sensor networks and control laws which can respond semi-instantaneously, the change in angle between the initial and disturbed states would ultimately be small. Thus it is clear to imagine how this method of adaptation can be used to reject disturbances immediately allowing for more extreme maneuvers, near-stall flight and more stable longitudinal flight which, as an example, would be largely beneficial in flying wings with limited control surfaces or UAVs

carrying fixed cameras.

4.2 Nonlinear Model Development

4.2.1 Background

While linear aerodynamic models have been thoroughly investigated, nonlinear models have arguably been less successfully implemented and are more rarely used to analyze morphing aircraft. Those works which have focused on morphing aircraft have approached the problem by only assessing a small selection of potential morphed shapes [97, 98]. Perhaps the first nonlinear method was developed in 1934 by Tani [99] and relied on assuming an initial circulation distribution, calculating the induced followed by the effective angle of attack, and using this to lookup the section lift coefficient from nonlinear experimental data. With this, a new circulation distribution is calculated and the process is iterated until the solution converges. This method was popularized by Sievells and Neely in a NACA report [94] but criticized for its inability to handle instances where sections of the wing are stalled, implicitly having a negative lift-curve slope [100]. Further analysis by Piszkin and Levinsky [95] indicated that in fact, the post-stall solution is non-unique and frequently converges with saw-tooth oscillations that evidently aren't a true aerodynamic phenomenon.

More recently, a method developed by Chattot [96] resolves many of the issues discussed previously while maintaining a similar iterative format. Chattot's method employs the use of an artificial viscosity term that similar models fail to consider. This term helps to ensure a unique solution by maintaining diagonal dominance in the matrix equations. Not only does Chattot's

model show good agreement with experiments post-stall where the lift-curve slope is negative, but the circulation distribution also remains smooth and does not show saw-tooth oscillations.

This method has mainly been used to analyze wing/winglet combinations [101], turbine blades [102], and swept wings [103], yet it is modeled in such a way that analyzing a morphing wing is relatively straightforward since the section-based method allows for spanwise variation in the airfoil characteristics such as the section chord, section lift coefficient, and section lift-curve slope. However, a primary gap between the existing model and the morphing model developed in this work is the infinite domain of airfoil characteristics required to characterize an arbitrarily morphed wing.

4.2.2 Model Description

In order to identify and quantify nonlinear aerodynamic adaptation in a spanwise morphing aircraft, the analytical model discussed prior was used to predict the aerodynamic behavior of a finite wing in both the linear and nonlinear regions of the lift-curve. Upon validation of the model with experimental results, the model was used as the foundation for a constrained optimization which tailored the spanwise deflection of the wing to return to the on-design lift condition at the off-design angle of attack. The wing successfully recovered if it was capable of matching the on-design lift while at the off-design angle; however, this method can be extended to stall recovery as well. The morphing wing was said to have successfully recovered from stall if after adaptation, the off-design angle of the new wing configuration was less than or equal to the angle of maximum lift of the unadapted wing. This was computed at a variety of on and off-design conditions in order to quantify the limitations of nonlinear adaptation and stall recovery for a spanwise morphing aircraft.

4.2.2.1 Static 2D Simulations

Two-dimensional static simulations were generated using OVERTURNS [104] [105], a RANS solver for three airfoil shapes and angles of attack ranging from -25 ° to 25 ° in increments of 1°. A symmetric NACA0012 airfoil was chosen for the spanwise unactuated geometry. The symmetry of the airfoil allows for ease of analysis when comparing actuated an unactuated states, as the aerodynamic profiles should also be symmetric. The geometry for the actuated (i.e. morphed, adapted) airfoil was chosen to have the same geometry as the SMTE to include the conformal bending produced by the MFC actuators. This geometry can be seen in Figure 4.2. This was used to obtain the 2D section lift, profile drag, and pitching moment curves, which will be used as the sectional aerodynamic data in the nonlinear LLT model.

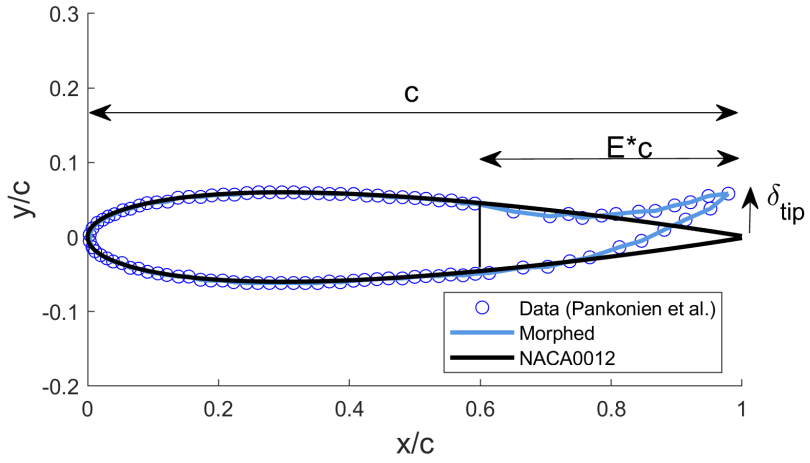

Figure 4.2: Morphed geometry of the airfoil profile compared to the unactuated geometry [89]

4.2.2.2 Nonlinear Lifting Line Model

The loosely-coupled circulation based method uses Prandtl's dimensionless integro-differential equation to model the 3D effects of a finite wing and is written as

$$\Gamma(y) = \frac{1}{2}c(y)C_l[\alpha_{geo} - \alpha_0(y) + arctan(w_{ind}(y))] \tag{4.1}$$

where the circulation has been normalized by the free-stream velocity. The wing is first discretized into spanwise stations with a cosine distribution generating a higher resolution at the tips to better capture the effects of the trailing vortices for $j = 1, 2, ...jx$ where

$$y_j = -cos\big(\frac{j-1}{jx-1}\pi\big) \tag{4.2}$$

and for this particular analysis *jx* was chosen to be equal to 49, comparable with previous studies. More sections can be implemented but increases the complexity and computational time. Integration points are defined between each of the stations to avoid singularities when calculating the induced downwash for $k = 1, 2, ...jx - 1$ where

$$\eta_k = -cos\big(\frac{k-\frac{1}{2}}{jx-1}\pi\big) \tag{4.3}$$

Then, an initial circulation distribution, often elliptical, is assumed in order to seed the model with a solution after which the induced downwash at each section can be calculated using a finite sum

$$w_{ind,j} = -\frac{1}{4\pi}\sum_{k=1}^{jx-1}\frac{\Gamma_{k+1}^n - \Gamma_k^n}{y_j - \eta_k} \tag{4.4}$$

Next, Prandtl's integro-differential governing equation is linearized using Newton's method given by

$$\Gamma_j + \Delta\Gamma_j = \frac{1}{2}c_j\big(C_{l,j} + \frac{dC_{l,j}}{d\alpha_{eff}}\Delta\alpha_{eff,j}\big) \tag{4.5}$$

where

$$\Delta\alpha_{eff,j} = \frac{\Delta w_{ind,j}}{1 + w_{ind,j}^2} \tag{4.6}$$

and

$$\Delta w_{ind,j} = -\frac{1}{4\pi}\big(\frac{1}{y_j - \eta_{j-1}} - \frac{1}{y_j - \eta_j}\big)\Delta\Gamma_j = a_j\Delta\Gamma_j \tag{4.7}$$

This can then be written in iterative form and the artificial viscosity term μ can be added to both the right and left hand sides of the governing equation so that the spanwise stations are now coupled, resulting in

$$\big(1 - \frac{1}{2}c_j\frac{dC_{l,j}}{d\alpha_{eff}}\frac{a_j}{1 + w_{ind,j}^2} + 2\mu\big)\frac{\Delta\Gamma_j}{\omega} = \frac{1}{2}c_jC_{l,j} - \Gamma_j^n + \mu\Gamma_{j+1}^n - 2\Gamma_j^n + \Gamma_{j-1}^{n+1} \tag{4.8}$$

$$where \begin{cases} \mu \geq max\big(\frac{1}{4}c_j\frac{dC_{l,j}}{d\alpha_{eff}}\frac{a_j}{1+w_{ind,j}^2}; 0\big) \\ \omega < 1(underrelaxed) \end{cases} \tag{4.9}$$

where a relaxation factor of 0.8 was used in this analysis. This value was chosen since iterative stability is guaranteed when $\omega < 1$, but the model further approximates the solution as the relaxation factor decreases. Note also that the artificial viscosity is defined as a lower bound of a maximum between two values, one of which is 0. Thus it is dependent upon the sign of the equation. Upon

further inspection, all but the terms a_j and $\frac{dC_{l,j}}{d\alpha_{eff}}$ are guaranteed to be positive. Furthermore, it is clear from Equation 4.7 that a_j is a negative quantity. With this in mind, the sign of the viscosity will be positive and thus greater than 0 when the lift-curve slope is negative. So, according to Equation 4.9, the viscosity term is 0 pre-stall and non-zero post-stall.

Looking at Equation 4.8 there are two unknowns, $\Delta\Gamma_j$ and Γ_{j-1}^{n+1}. The latter is dependent upon a future time step $n+1$, however, this iterative circulation distribution can be written with respect to the current time step as

$$\Gamma_{j-1}^{n+1} = \Gamma_{j-1}^{n} + \Delta\Gamma_{j-1} \tag{4.10}$$

This can then be substituted into Equation 4.8 and the linearized integro-differential equation is reduced to one unknown, $\Delta\Gamma_j$. Following this step, the next circulation distribution $n+1$ can then be calculated similarly

$$\Gamma_{j}^{n+1} = \Gamma_{j}^{n} + \Delta\Gamma_{j} \tag{4.11}$$

Equations 4.4 through 4.8 are then reiterated until the solution converges to the desired convergence criteria. For this analysis, a strict convergence criteria of 0.01% was chosen, where the circulation at every spanwise station must satisfy the criteria. Upon convergence, the lift and drag of the finite wing can be calculated using the converged circulation solution as

$$C_L = \frac{AR}{2}\int_{-1}^{1}\Gamma(y)dy \tag{4.12}$$

$$C_{D,total} = C_{D,profile} - \overbrace{\frac{AR}{2}\int_{-1}^{1}\Gamma(y)w(y)dy}^{C_{D,i}} \tag{4.13}$$

where the integrals have been written using substitution so that the bounds of integration are normalized and the wing profile drag is calculated through spanwise integration of the section drag coefficient. As is, this model works well for predicting the aerodynamic performance of static wing shapes such as wing/winglet combinations, turbine blades, and swept wings shown by Chattot [101] [102] and Gallay *et al.* [103]. However, the section-based approach is ideal for analyzing morphing wings which are not constrained to a given spanwise geometry.

4.2.3 Morphing Geometry Implementation

In spanwise morphing wings, the section lift and its respective derivative are no longer simply a function of the angle of attack; rather, the trailing edge deflection adds a second parameter which must also be considered. The deflection can be calculated based on the parameters depicted in Figure 4.2 as

$$\eta = tan^{-1}\left(\frac{\delta_{tip}}{E * c}\right) \tag{4.14}$$

where η represents the angular tip deflection, c represents the airfoil chord length, $E * c$ represents the length of the actuator, and δ_{tip} represents the vertical tip deflection.

Accordingly, both the trailing edge deflection and angle of attack are required in order to determine the lift coefficient at each section. Thus, the model requires a bounded domain of airfoil characteristics to interpolate from. This domain can be generated in the form of a surface, shown

in Figure 4.3, which correlates the lift coefficient to both the angle of attack and trailing edge deflection. From observations of the simulated data, the section lift-curves vary linearly with respect to the trailing edge deflection. Thus, linearly interpolating the curves from simulated airfoil data at the maximum, minimum, and neutral trailing edge deflections is appropriate. So by knowing the spanwise shape function of the morphing wing's trailing edge for arbitrary actuator displacements, the section lift characteristics at and between the actuators can be found.

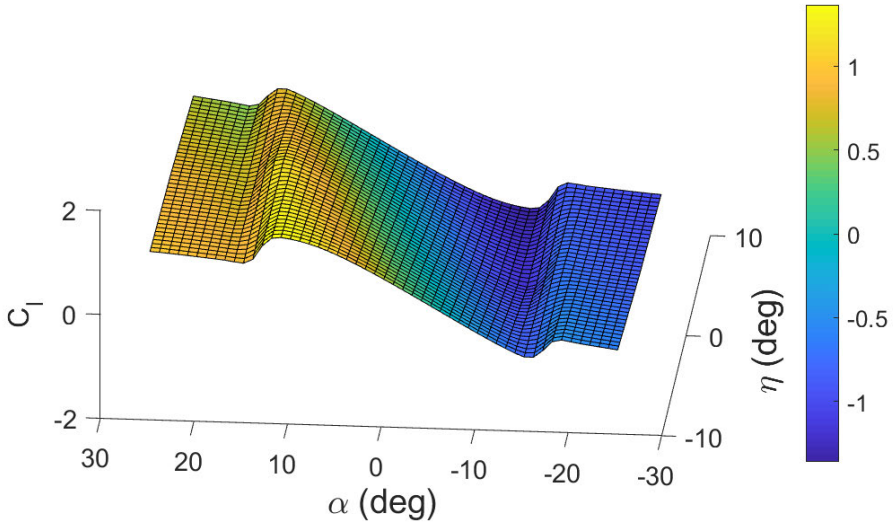

Figure 4.3: Three-dimensional surface of section lift data with respect to angle of attack and trailing edge deflection

This shape function, which describes the spanwise variation in trailing edge deflection, plays a key role in the outcome of the optimized nonlinear model due to the strong influence of the trailing edge deflection on the section lift coefficient. One of the main challenges of morphing aircraft is bridging the gap between two actuators without breaking the continuity of the surface while maintaining large strains. This model's section-based approach allows for easy incorporation of the SMTE's compliant sections in the trailing edge shape function. The SMTE's 6 actuators move independently from one another yet remain horizontal while the flexible honeycomb with elas-

tomeric skin linearly bridges the gap between the actuators. These transition sections are crucial to the continuous deformations of the SMTE; however, their inherent flexibility is unideal and future designs can improve upon this aspect.

A diagram of the modular structure of the SMTE can be seen in Figure 3.5. The representative shape function describes the spanwise distribution in trailing edge deflection for an arbitrary configuration and can be seen in Figure 4.4. Mathematically, this is achieved by prescribing 6 inputs corresponding to the tip deflections of the 6 actuators on one wing, and is represented as a constant value for the length of the actuator. Between actuators, the tip deflection is characterized as a linear function as mentioned previously. Lastly, the left and right wings are assumed to actuate symmetrically. It is worth noting that while the trilateral configuration of the active trailing edge is fairly resistant to torsion, some minor twisting may occur in instances where the deflection and thus elastomeric strain between actuators is large. Implementing a coupled FEM-CFD model within the optimization to account for this was outside the scope of this study given the agreement between modeled and experimental results which will be detailed shortly.

It is clear to imagine how more complex morphing shapes can be included in this model as morphing technologies progress. One such example would be a more discretized version of the SMTE which would allow for a smoother spanwise geometry, ultimately capable of approaching a sinusoidal trailing edge. This would be more representative of biological entities such as birds.

4.2.4 Assessment and Validation

As proof of concept, this model was validated against experimental data for a finite wing of NACA0012 profile and aspect ratio 6 at $Re = 2e^5$. The wing was constructed to scale for a small

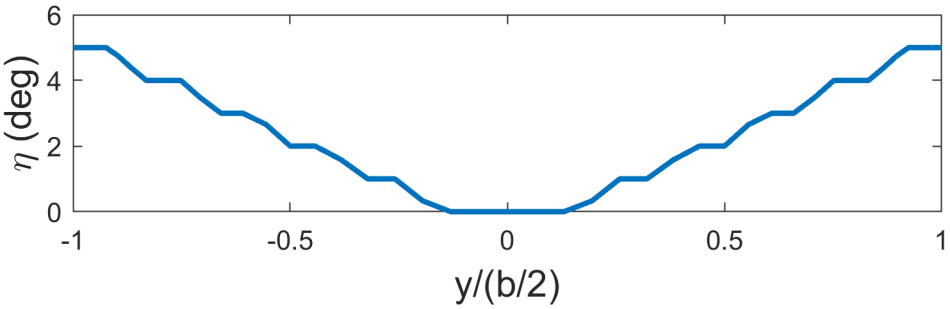

Figure 4.4: Sample user defined shape function representing the spanwise morphed deflection of the active and inactive sections where *b* represents the span

UAV with a chord of 0.305 m and was mounted vertically in the 1.5 m x 2.1 m closed loop wind tunnel at the University of Michigan. This wing has the same geometric properties as the SMTE but is more rigid by nature, providing a more realistic comparison to the model presented which does not include aeroelastic effects. Data was collected using a 6-axis force balance to obtain the $C_L - \alpha$ curves in addition to the drag and moment curves. Lastly, the system was automated using closed loop control to sweep through the angles of attack with accuracy up to $1/40^{th}$ of a degree. For further details of the experimental setup, see [92].

4.2.4.1 Effects of Viscosity

Shown in Figure 4.5 is a comparison between the experimental results and the modeled prediction for zero actuation across the span of the wing. It is important to note that the artificial viscosity term is defined as a lower bound, meaning that the value of the artificial viscosity can be tuned if necessary. This is of importance for the cases tested here as the aerodynamic conditions are near turbulent transition and thus discrepancies from the 2D simulated data could misinform the model. Note that increasing the artificial viscosity increases the severity of stall. At higher values of μ, the reduction in lift associated with stall increases.

Even post-stall, the model is able to predict the nonlinear aerodynamic behavior granted with less accuracy than the linear region. These preliminary results indicate that an addition between 0 and 0.5 to the artificial viscosity term defined in Equation 4.5 most accurately captures the experimental results shown here and thus will be carried throughout the rest of this analysis. This factor can be further optimized and may vary when applied to other scenarios since it is dependent upon the relative accuracy between the post-stall behavior of the 2D simulation and the experimental data.

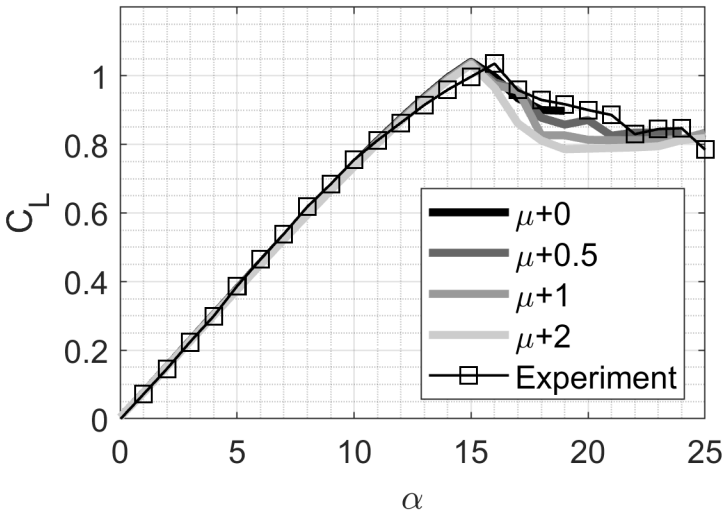

Figure 4.5: Comparison of NACA0012 experimental data to the nonlinear model with varying artificial viscosity

4.2.4.2 Effect of 2D Lift Curve

As mentioned previously, the simulated 2D curves play an important role in determining the results of the model and can thus provide insight into the limitations of the system even before optimization. This is evident when analyzing the effects of trailing edge displacement on the 2D lift curves as seen in Figure 4.6. In this figure, the section lift curves for a series of increasing

actuator deflections have been generated for comparison purposes. For proof of concept, markers for a sample on-design lift and off-design angle conditions have been labeled as well.

Not only does deflecting the trailing edge upwards, an expected response for most stall recovery, generate reduced lift shifting the lift curve down, but it also shifts the curve to the right thus delaying stall. However, the dominant response decreases the airfoil lift while the ability for the airfoil alone to delay stall is limited. This indicates that for a given off-design angle of attack, the airfoil may not physically be able to adapt to the on-design target lift condition. Therefore, the 2D lift curves show that the ability of a morphing wing to recover from stall is dependent upon the magnitude of both the on-design lift condition and the off-design angle of attack. It follows that the problem under consideration may be bounded by combinations of the on and off-design conditions.

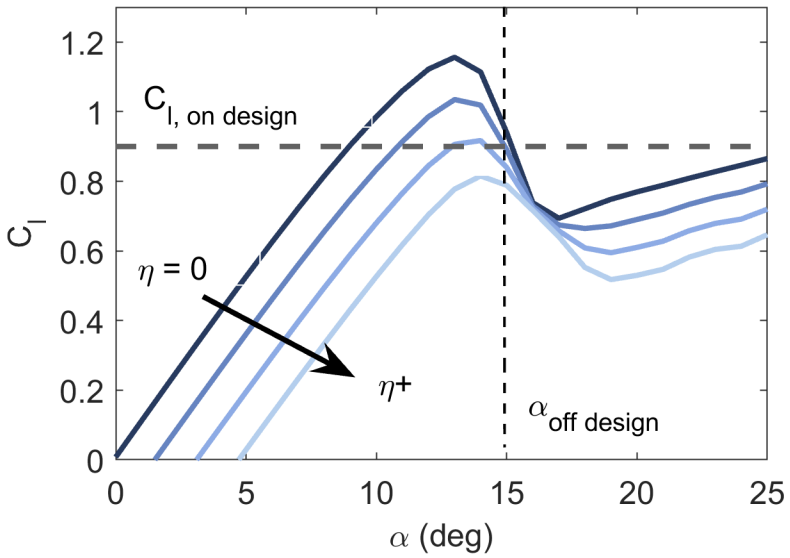

Figure 4.6: Effect of the 2D lift curve with respect to the SMTE's trailing edge deflection

4.2.5 Optimization

4.2.5.1 Constrained Minimization

Given that the wing under consideration presented in Figure 3.5 has a total of 6 actuators, testing all possible combinations would be cumbersome if not entirely useless. The most appropriate method of analyzing recovery via spanwise morphing is through optimization of the spanwise configuration using the nonlinear lifting line model. This was achieved using a constrained minimization algorithm which tailored the actuator deflections, where now η is a vector, to minimize the total drag. The model was constrained to reach the on-design lift while maintaining the off-design angle of attack. Each actuator deflection was bounded by a maximum tip deflection of 8.85° so as to not exceed the physical limitations of the wing, providing a realistic analysis for this particular morphing concept. The lower bound was chosen to be 0° to reduce the search space of the optimization. This is a reasonable simplification for on-design lift conditions that are lower than the stalled off-design lift state. Upon investigating the aerodynamic response shown in Figure 4.5 for this particular wing profile and aspect ratio, this is a reasonable assumption for on-design lift conditions at or below approximately 90% of $C_{L,max}$.

Lastly, due to the complex nature of optimizing the spanwise geometry of a morphing wing, assuming an elliptical circulation distribution for the initial iteration does not always result in successful optimization. Instead, the converged circulation distribution for this wing with no spanwise variation in trailing edge deflection was calculated at each angle of attack prior to optimization and was then used to seed the model. This helps the convergence of the solution. A final summary of the optimizer can be found in Table 4.1.

For this optimization, there exists significant trade-offs between the iterations to convergence

within the desired error and the tolerance of the optimization. A strict convergence criteria of 0.01% error from the previous iteration was chosen for this model defined by

$$\%error = \frac{\Gamma^{n-1} - \Gamma^{n}}{\Gamma^{n-1}} * 100 \tag{4.15}$$

Thus, circulations which did not meet this criterion for one or more spanwise sections were said to have not converged. Accordingly, by increasing the tolerance of the optimization function and lift constraint, the iterations required for the solution to converge increases. For practical purposes, the number of iterations was constrained to 2000 or less, limiting the tolerance to $1e^{-2}$ for the optimization function, output, and lift constraint. Given that for Prandtl's finite wing theory [91] the slope of the linear region of the lift curve for a finite wing of aspect ratio 6 is expected to be $(2\pi) * 0.75$, the error in angle of attack associated with a tolerance on C_L of $1e^{-2}$ is less than $0.1°$. This tolerance was deemed to be adequate for this analysis.

Table 4.1: Details of constrained optimization of nonlinear LLT model

Objective	Target
Minimize:	$C_{D,total}$
Given:	$\alpha_{OffDesign}$
Constrained by:	$C_{L,Design}$
Subject to:	$0 < \eta < 8.85°$

4.3 Modeled Stall Recovery

Using the methods described previously, the trailing edge deflections of a finite wing were optimized to adapt to nonlinear aerodynamic conditions and return to the initial lift. The results of a single optimized case will be discussed prior to investigating the limitations of a morphing

wing to adapt to stall conditions in order to demonstrate the effects of spanwise morphing on the aerodynamic behavior of the wing. The wing was optimized to return to an on-design lift of 80% of $C_{L,max}$ of the experimental data and an off-design angle of attack of 15° in order to investigate the capabilities of the optimized nonlinear lifting line model. This represents just one of multiple successful cases of adaptation as will be discussed in the latter section.

4.3.1 Optimized Geometric Adaptation

Shown in Figure 4.7 is the optimized spanwise deflection for the case mentioned prior. A few behaviors are evident. Primarily, the minimization algorithm overall predicts an upwards tip deflection for all 6 actuators, as noted by the positive angles. Recall that in the adaptation scenario in question here, the off-design angle is right at the stall angle where the lift is at a maximum. Thus, to achieve the on-design condition of 80% of $C_{L,max}$, this response alleviates the high-lift loading at the off-design condition. Note that this is not always the required response. If the off-design lift is much lower than the on-design lift condition, the actuators may be required to have a downward deflection in order to increase the lift. This scenario is not investigated in the current analysis, however it has been studied in prior works [65]. Secondly, the non-uniform distribution of deflections indicates some spanwise tailoring of the circulation distribution. These results show the input to the actuator's controller that would be prescribed to the physical model for testing.

The spanwise shape function that characterizes the SMTE with the prescribed actuator deflections can also be assessed. This is shown in Figure 4.8. Here, as opposed to plotting simply the desired tip deflection, the entire spanwise trailing edge shape is displayed which takes into consideration how the MFC actuators and the flexible elastomeric honeycomb sections are integrated.

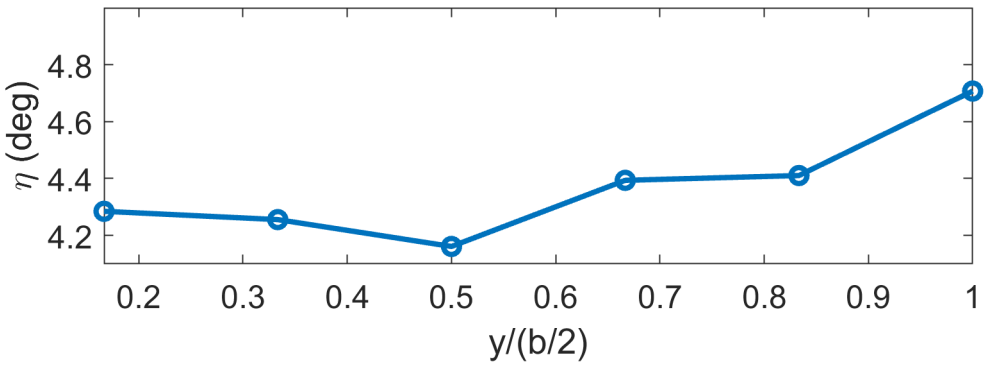

Figure 4.7: Optimized spanwise deflection for $0.8C_{L,max}$ at $15°$

This is the shape function which is used to determine the deflection and hence the lift-curve slope at each station *j* along the span as per Section 4.2.3

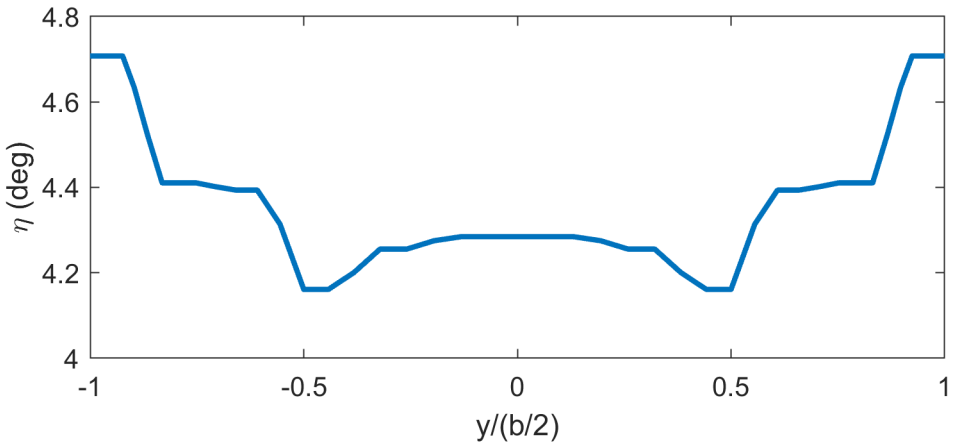

Figure 4.8: Spanwise trailing edge with optimized actuator inputs for $0.8C_{L,max}$ at $15°$

4.3.2 Target Lift Validation

The results of the optimization were compared to experimental results conducted with the SMTE for proof-of-concept. The optimized actuator deflections for the case detailed above were prescribed to the SMTE. The experimental setup and procedure used to collect the aerodynamic

data will be discussed in full detail in Section 4.4.2. As shown in Figure 4.9, the model matches fairly well with the experimental data particularly at pre-stall angles, but slightly underestimates the wing's lift overall. This can be attributed to differences between the underlying assumptions in the model and the physical attributes of the experimental wing. Specifically, this model does not include any effects of the compliance of the morphing wing trailing edge, particularly at the flexible transition areas, or aeroelastic effects of the wing in general which would affect the overall aerodynamic behavior especially post-stall due to passive deformations in the camber and twist of the wing. This could be improved upon with future iterations of the SMTE design in addition to incorporating aeroelastic effects into the model.

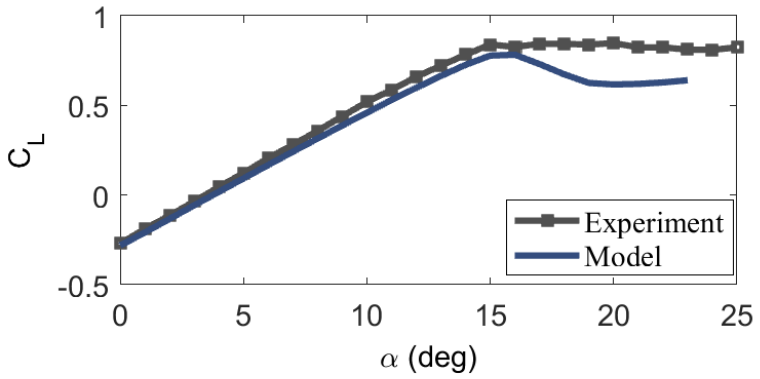

Figure 4.9: Comparison of modeled results and experimental results of optimized configuration for $0.8C_{L,max}$ at 15°

Furthermore, the model does not fully capture the post-stall behavior of the wing. This is due in-part to the fact that the artificial viscosity term was tuned to match experimental data for a non-flexible wing which closely resembles the assumptions of the model. However, it is important to note that the post-stall behavior observed in these experiments is quite uncommon as it does not experience a severe drop in lift. Recall from Figure 4.5 that even with the minimum artificial viscosity, the lift response sill experiences a substantial post-stall reduction in lift.

Even still, since this method of optimized recovery does not actually rely on the post-stall behavior of the experimental results it will not affect the model's ability to optimize the spanwise deflection to recover. Thus the only notable discrepancies between the model and the experimental results are due to the compliance of the wing and do not heavily affect the results of the model and the consequent analysis.

4.3.3 Circulation Response

The spanwise circulation distribution provides a simple method of assessing the successfulness of adaptation. Figure 4.10 depicts the circulation along the span of the wing for the initial on-design, unadapted off-design, and adapted off-design cases. The on-design case represents the initial or target circulation. This typically correlates to the designed cruise condition where the aerodynamic performance has been idealized. The unadapted off-design configuration represents the circulation upon encountering a disturbance. Lastly, the adapted off-design configuration represents the circulation after the geometry of the wing has been tailored. Since the core of this analysis focuses on stall recovery, the off-design angle will always be larger than the on-design angle. Given that most aircraft don't operate in the near-stall region of the lift curve, this typically implies that the off-design lift and thus circulation distribution will be larger.

The results shown in Figure 4.10 depict that for this specific scenario, the wing experiences an increase in circulation and thus lift in the unadapted off-design state. The spanwise geometry is tailored to reduce the circulation and recover to the designed state. For fully successful adaptation, the off-design adapted circulation will match the target on-design circulation. The adapted circulation distribution shown here almost completely replicates the on-design circulation, but there are

some discrepancies near the root of the wings. Overall, this clearly shows successful recovery.

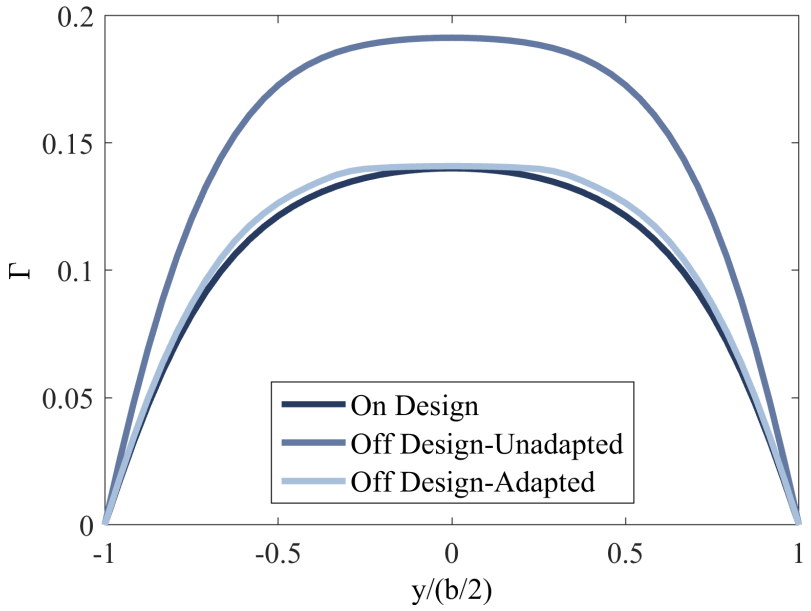

Figure 4.10: Modeled circulation distributions at target, off-design, and adapted configurations for $0.8C_{L,max}$ at $15°$

For completion, an additional handful of successful adaptation cases are also presented in Figure 4.11. These cases were specifically chosen to be post-stall. This is partly evident in the small dip in the lift curve at the root of the wing. Here, the data show that the adapted circulation distribution does not have to be identical to the target distribution in order for adaptation to be successful. Recall that the wing lift is found by integrating the circulation distribution, so in these cases the adapted circulation can locally over or undershoot the exact solution and still reach the target lift within the desired error. From the cases presented in Figure 4.11 the case 68% $C_{L,max}$ and $\alpha = 16°$ is the least successful of the set, as the entire spanwise distribution overshoots the target. However, this case also had to achieve the largest change in circulation distribution between the unadapted and adapted off-design states.

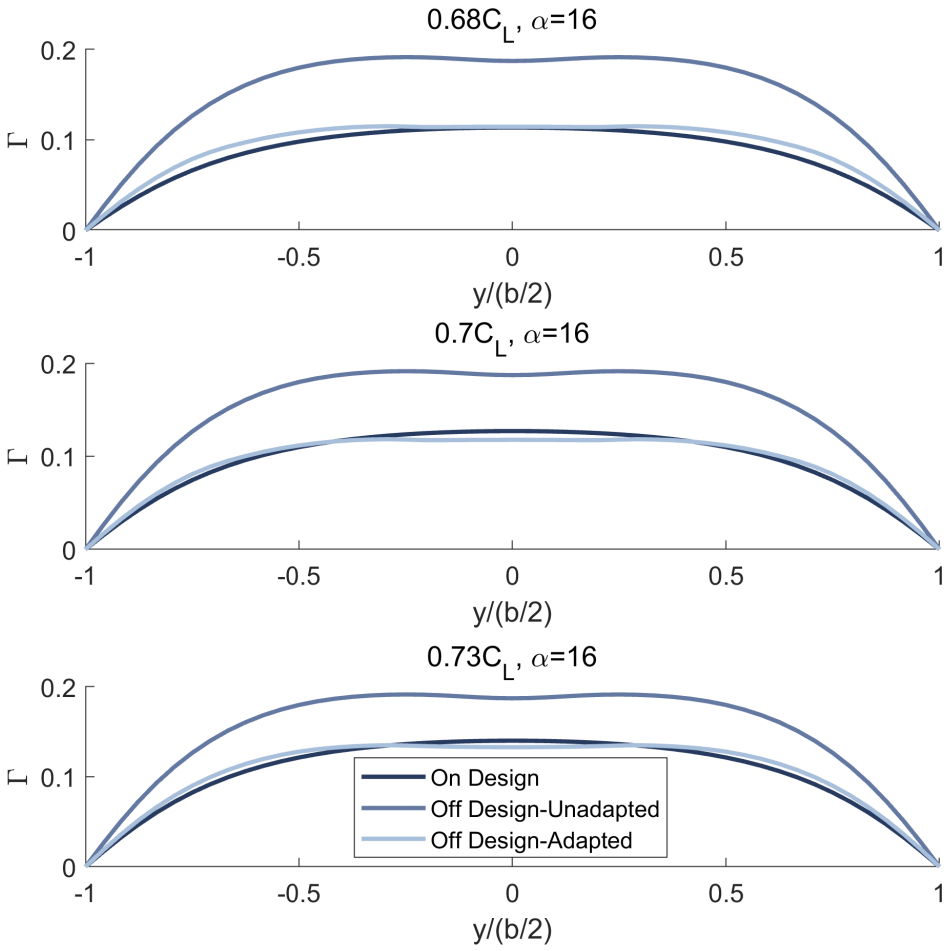

Figure 4.11: Comparison of circulation distributions for post-stall off-design conditions

4.3.4 Adapted Coefficient Response

First, by generating the lift curve for the adapted configuration at each stage during the scenario detailed in Figure 4.1, the success of the optimization was determined. The goal was to achieve the target (on-design) lift for the given off-design angle of attack; however, recovery was only deemed successful when this occurred at an angle less than or equal to that associated with $C_{L,max}$. As can be seen in Figure 4.12, the case under investigation successfully recovered from stall, as it matched the target lift for an angle of attack occurring prior for the adapted wing's stall angle.

This can be further validated with the circulation distributions depicted in the previous section in Figure 4.10 which demonstrated that the circulation and thus lift distribution is restored while in the off-design state. Recognizing that the on-design scenario represents the same flight condition as the reduced angle method, this demonstrates that tailoring the wing's geometry has the same effect as the traditional method of stall recovery.

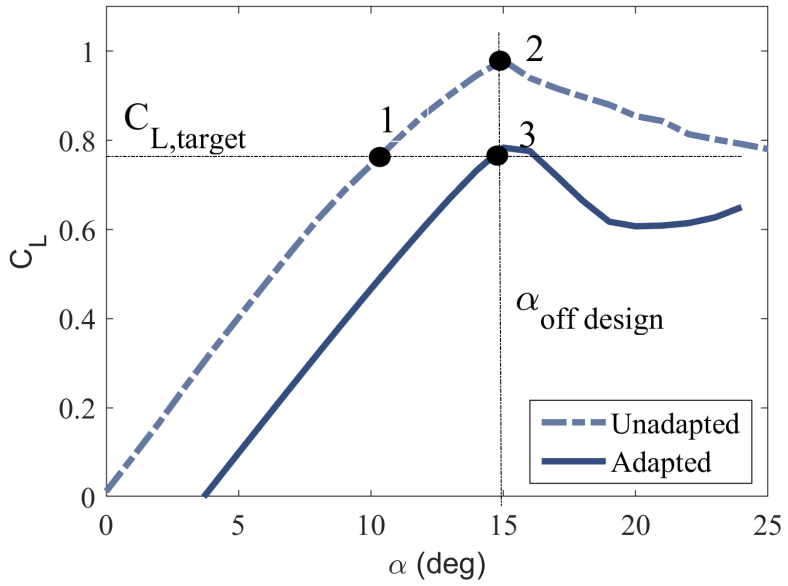

Figure 4.12: Effect of adaptation on the lift curves for a finite wing numbered in accordance with Figure 4.1

Furthermore, the drag can be analyzed to quantify the performance improvement due to adaptation. The output of the optimization relies on a constrained minimization of the total drag and should thus optimize away from stall where the drag increases dramatically. In the case presented here, the optimized configuration occurs just before the stall angle of the adapted lift curve, implying that the optimization may be near the limitations of the system. However, although the adapted configuration operates close to the stall angle, the drag penalties still indicated a significant improvement in the performance of the wing. The drag penalty for the unadapted configuration was

0.0545 while the adapted configuration experienced a penalty of 0.0338, resulting in a 38% reduction. This shows that by morphing the wing to adapt, the drag penalty was significantly reduced. It is also worth noting that the reduction in drag penalty for successfully optimized cases will increase with off-design angle of attack. Since this particular case was analyzed near stall, this metric is a lower bound and the performance benefits can potentially exceed this value substantially.

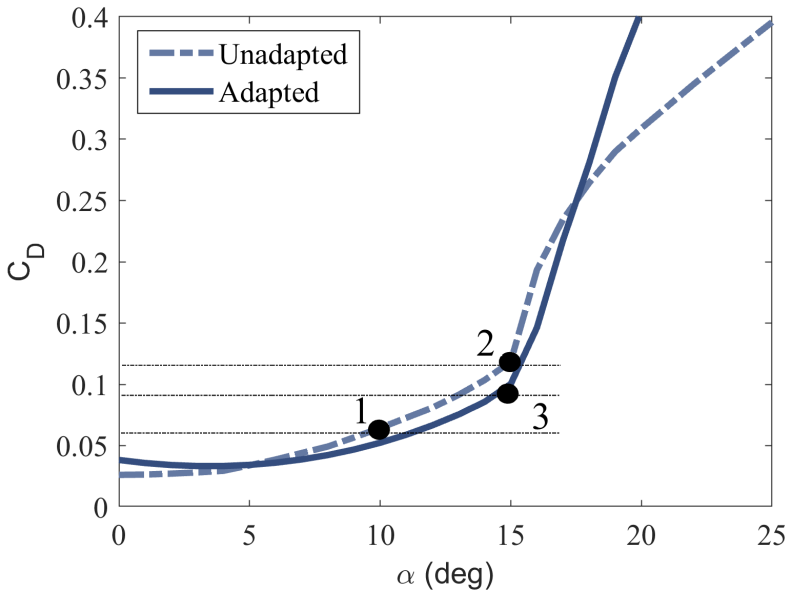

Figure 4.13: Effect of adaptation on the drag curves for a finite wing numbered in accordance with Figure 4.1

4.4 Comparing Morphing and Non-Morphing Adaptation

Upon development of the nonlinear model and verification of the optimization detailed in Section 4.2.5, a comparison between the morphing SMTE and a non-morphing articulated wing on the success of spanwise adaptation was conducted. It has previously been shown that two key parameters determine the results of the optimization. First the on-design lift, which constrains the

model, was defined as 86% of the maximum lift $C_{L,max}$. Secondly, the off-design case $\alpha_{off,design}$ was specified at 16° past stall.

4.4.1 Experimental Wing Comparison

Two half-span finite wings were used in the following experiments. The first wing was the SMTE which is known for improving control of aerodynamic forces and reducing the drag penalty associated with adaptation. This is due in part to the elimination of geometric discontinuities where chord-wise and spanwise losses occur due to vortex formation. The SMTE, shown in Figure 4.14, was manufactured with repeating MFC (active) and honeycomb (inactive) sections. Bridging the active sections with a flexible elastomeric section ensures a continuous surface particularly as the MFC produces smooth conformal actuation of the trailing edge. The second wing was a conventional articulated flap wing, driven by internalized mechanical servos. The construction of this wing can be seen in more detail in Figure 4.15. Both wings used closed loop control to regulate the actuator tip displacements. While the articulated flap wing relied on the internal controller of the servos, the SMTE utilized internalized Flex sensors shown in Figure 4.14 which translated the tip deflection to a change in resistance which can be read by the controller.

While the internal mechanisms of both wings were unique, they were constructed for comparison purposes and thus share the same undeformed geometry. The wings were built with a symmetric NACA0012 airfoil of aspect ratio 6 with a 0.305m chord and 6 active sections each. For each section, the width of the articulated flaps spans the same width as the repeating active-inactive section in the SMTE. Additional information on the construction of the models can be found in [64].

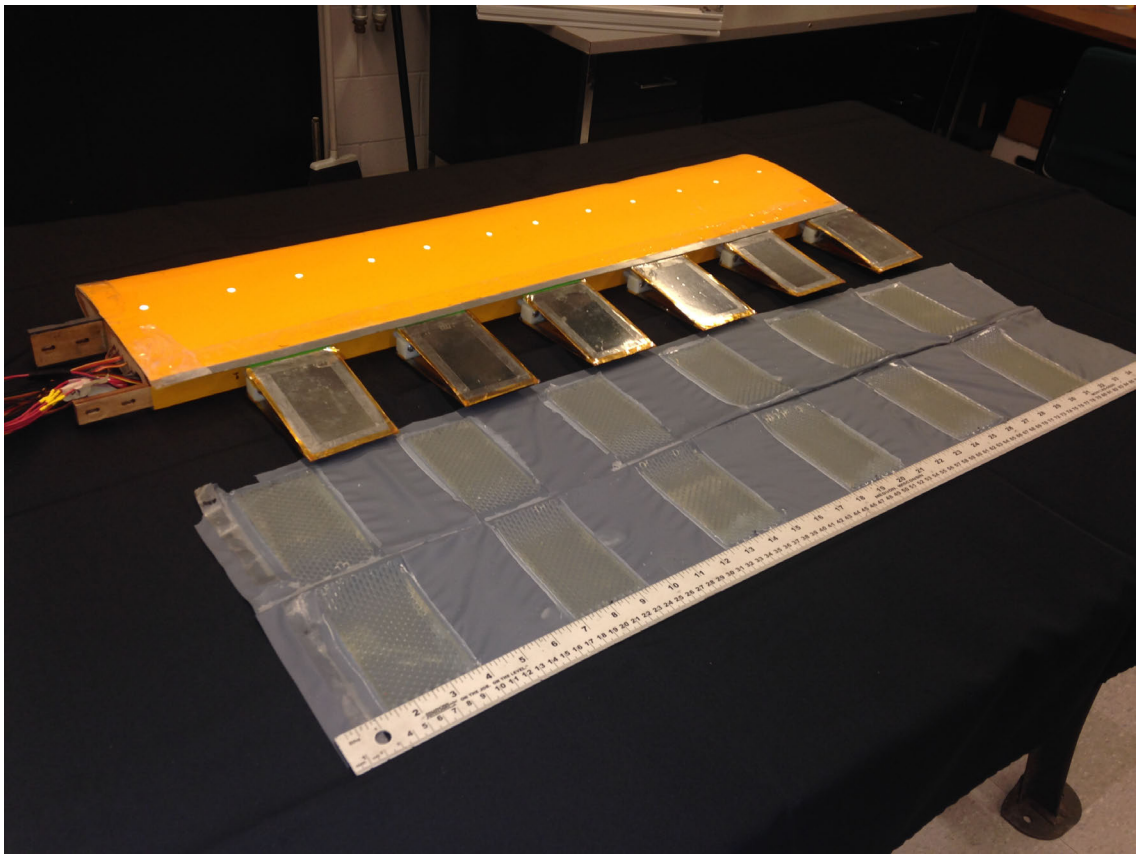

Figure 4.14: Internal construction of the SMTE wing with elastomeric skin and honeycomb removed for visibility

4.4.2 Wind Tunnel Testing

4.4.2.1 Optimized Adaptation

The optimized nonlinear LLT algorithm was implemented for both the morphing SMTE in addition to the articulated wing. It's important to note the two main difference between the two wings, as this is what distinguishes the results of the model. First, the MFC actuator produces cambered actuation unlike the straight and rigid actuation seen in the articulated wing. This translates to fairly large differences in the 2D aerodynamic characteristics such as the lift and drag profiles. Secondly, the spanwise trailing edge shape is different. The articulated wing's trailing edge can be

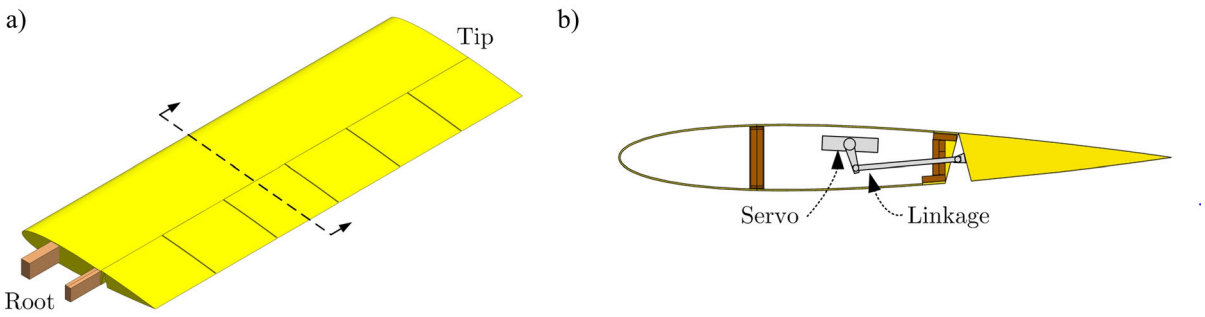

Figure 4.15: Diagram of a) Isometric view and b) cross-sectional view of the articulated flap wing

characterized as a step function, while the SMTEs trailing edge can be characterized as constant across the length of the MFCs and linear across the elastomeric sections. These shape functions are used to determine the 2D section aerodynamics mentioned prior. In reality, a third difference is thought to play a key roll. Namely, the articulated wing exhibits geometric discontinuities which will incur vortex formations at the gaps in the actuators as the flow tries to move from the high pressure lower surface to the low pressure upper surface. While this can't be modeled using the nonlinear LLT used here, its effects will still be present in the experimental aerodynamic data.

The data shown in Figure 4.16 represents the optimized actuator deflections for the articulated wing and the SMTE. Note that the optimizer predicts vey similar spanwise geometries for both wings even though their trailing edge shape functions are not identical due to the compliant elastomeric section. The optimized geometries generally exhibit an increase in deflection moving from the root to the tip. This is thought to be due to the inherently low circulation and thus section lift that is present at the tips of the wings. Upon further investigation, these results show that the optimizer predicts less actuation is required for the SMTE compared to the articulated wing. Recall that as per the requirements detailed in Table 4.1, the goal of the minimization algorithm is to match a constraint lift while minimizing the total drag. Thus, this data show that the SMTE

requires less actuation to achieve the same overall lift, indicating that the SMTE is more effective than the articulated flap wing at generating the required forces.

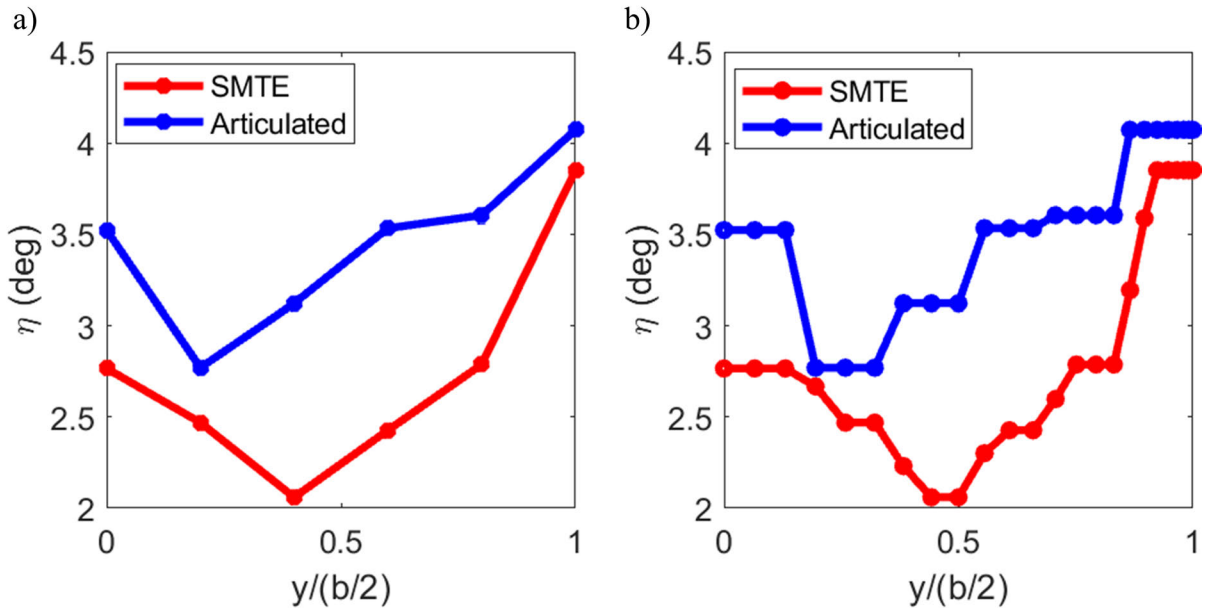

Figure 4.16: Optimized spanwise actuation for the articulated wing and SMTE at 0.86 $C_{L,max}$ and $\alpha = 16°$

The spanwise shape function for each of the wings is also shown. Here, the SMTE shows a smoother overall geometry along the wing's span due to the elastomeric sections which form a linear transition between actuators. The shape function has been implemented such that the model samples these linear transitions when determining the spanwise tip deflection at each station. Conversely, the articulated wing's spanwise geometry is constant along the length of each actuator. Note that the data points marked in the plots resemble each spanwise station. Although the articulated wing's spanwise shape function appears to also have linear transitions between actuators, this simply an artifact of plotting the data and does not resemble how the spanwise geometry is actually implemented in the model.

4.4.2.2 Wind Tunnel Setup

Wind tunnel tests were conducted in the 1.5 m x 2.1 m tunnel at the University of Michigan depicted in Figure 4.17. The wings were vertically mounted to the 6-axis ATI Delta force balance above a ground plate that raised the reflecting plane of the half-span wing by 30 cm, outside of the boundary layer of the wind tunnel. The mounting rig was shielded by attaching a fixed cowling in the shape of a NACA0012 airfoil that inherently extended the wing to the full aspect ratio and reduced the gap between the finite wing and the ground plate to 0.5 cm. Below the ground plate, a shroud shielded the force balance from the airflow.

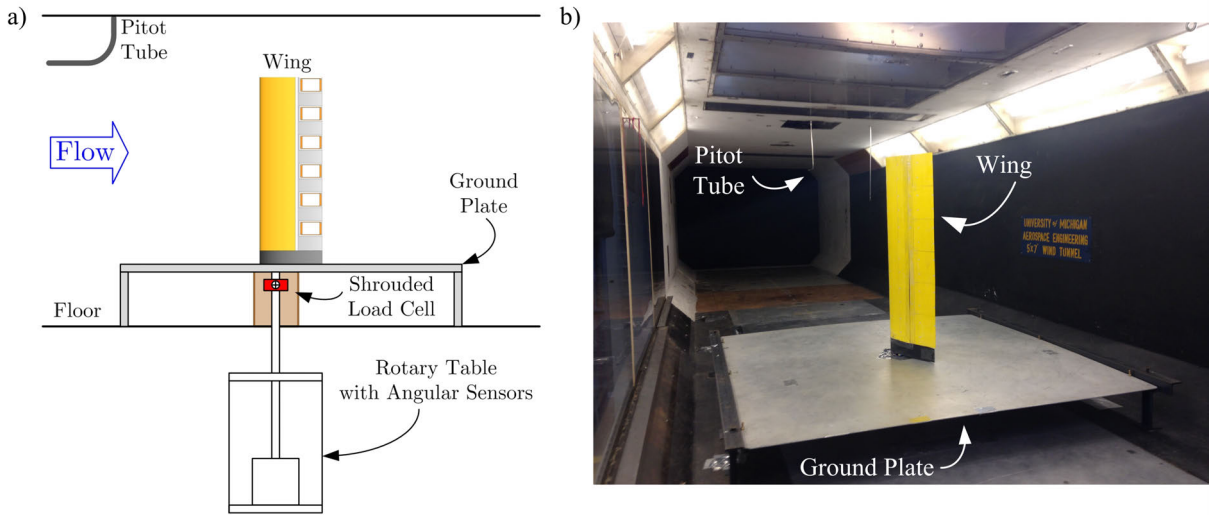

Figure 4.17: Experimental setup for the spanwise morphing wings depicting the a) detailed graphical setup and b) in-tunnel setup

Alpha sweeps were conducted in order to obtain the $C_L - \alpha$ curves for the on-design and off-design configurations by holding the aileron configurations constant and recording data from $0°$ to $25°$. The angle of attack was set using two high-precision Keyence LK-G402 laser displacement sensors configured to measure the rotation of the mount. This was achieved by directing the fixed lasers to a cross bar on either side of the mount, perpendicular to the wing's orientation. As the

mount rotated, the lasers effectively translated the change in out-of-plane displacement to a change in rotation via basic geometry. Lastly, the closed-loop control allowed for angular accuracy to up to $1/40^{th}$ of a degree.

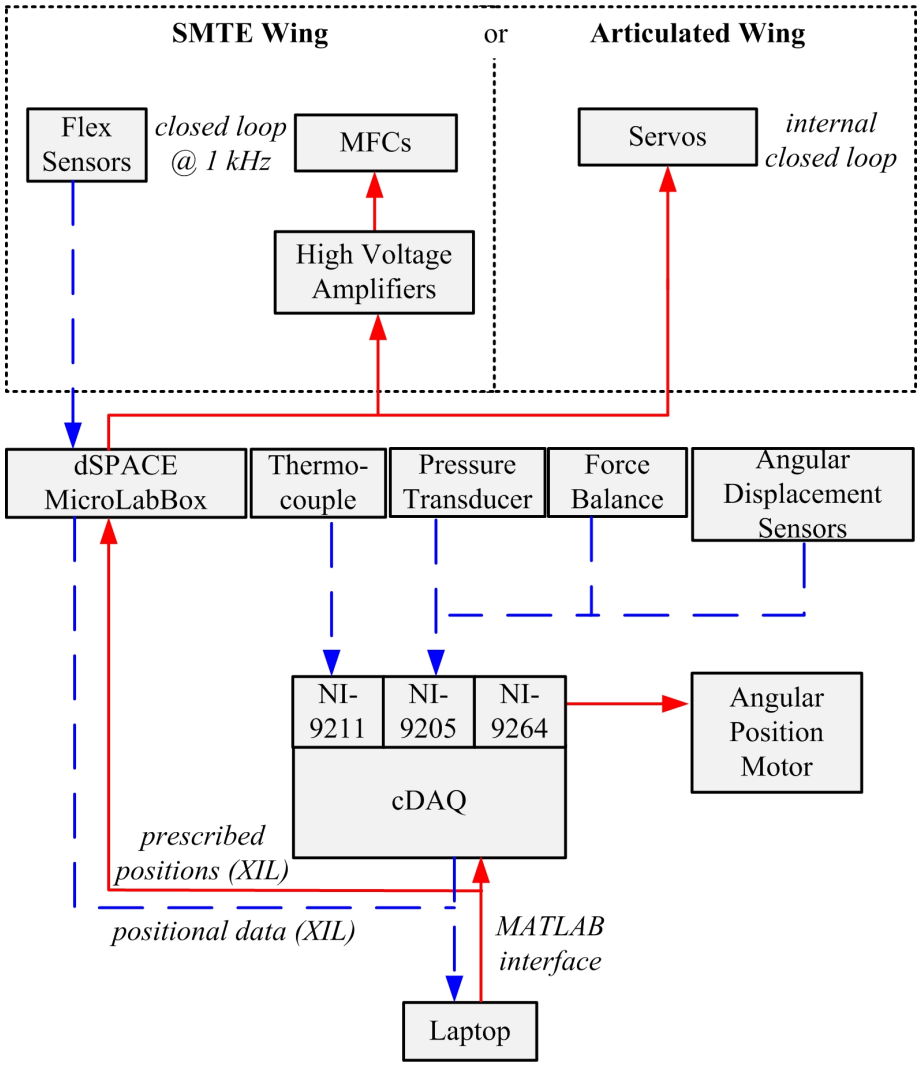

Figure 4.18: Experimental data flow for wind tunnel tests for the SMTE and articulated wings

Over the course of the test, the aerodynamic forces and moments, dynamic pressure, temperature, and MFC tip displacement readings were recorded. An ATI Delta 6-axis force balance with resolution capabilities of up to 1/32 N in force and 1/528 Nm in torque was used to collect all aerodynamic loadings, although only lift and drag are reported in the current analysis. The dynamic

pressure was recorded using an Omega PX2650 differential pressure transducer from a pitot tube 2 meters upstream of the wing. Finally, the tunnel temperature was recorded with a thermocouple mounted upstream at the base of the tunnel. The thermocouple and pressure transducer data was used to account for potential blockage at high angles of attack and ensure the flow speeds remained within 5% of the target velocity.

The experiment was orchestrated in MATLAB using both a dSPACE MicroLabBox and cDAQ system. This allowed for precise control of the ailerons at a much higher rate than the sampling rate of the sensors. The cDAQ collected all external sensor data and controlled the angular position of the wing while the dSPACE controlled the aileron deflections and collected the Flex sensor data from the SMTE. As mentioned in Section 4.4.1, the servos have their own internal controller; however, the dSPACE was used to execute a PI controller written in Simulink for the MFCs to prescribe the accurate tip displacements even if they experience aeroelastic deformations. This is summarized in a flow diagram of the experiment depicted in Figure 4.18.

4.4.2.3 Results

In this section, the aerodynamic forces of the SMTE and articulated wing are analyzed using the method described in Section 4.4.2.2. Preliminary analysis presented in Figure 4.5 indicated that the nonlinear model could accurately predict the aerodynamic behavior of a uniform finite wing to within 2.7% by tuning the artificial viscosity. Furthermore, it was proven in Section 4.3 that the optimized nonlinear model, when applied to spanwise variations in tip deflections, could accurately predict the aileron deflections required to recover from stall. Thus the goal of this section was to assess the recovery capabilities of the SMTE and the articulated wing and identify any advantages or disadvantages of the spanwise morphing wing.

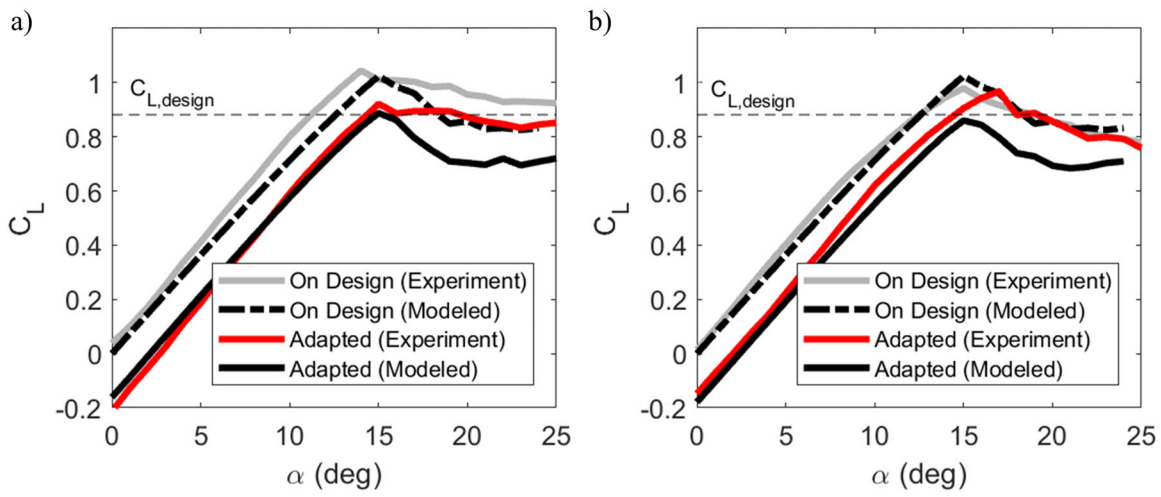

Figure 4.19: Experimental and modeled lift curves at the unadapted (on design) and adapted configurations for the a) SMTE wing and the b) articulated wing

The optimized model was set to reach a design lift condition of 0.8816 at an off-design angle of attack of $16°$. In both models, the tolerance of the lift constraint was relaxed to $1e^{-2}$ in order to meet the strict circulation convergence criteria of 0.01%. Figure 4.19 presents a comparison of the experimental and modeled results for both wings. The model captures the results of the articulated wing's on-design configuration quite well. However, as has been discussed previously the model underestimates the lift of the SMTE likely due to the compliance of the wing. That being said, the resulting error between the target lift and the optimized lift at the off-design condition for the articulated and SMTE wings was quite low at 4.2% and 7.1% respectively. Notice also how the modeled stall angle is lower than the off-design angle in both cases indicating that the wing has only partially recovered from stall. While the optimizer was designed to minimize the drag, ideally avoiding the post-stall regime where drag dramatically increases, this is not always feasible and is dependent upon the 2D lift and drag curves, and the design inputs $C_{L,target}$ and $\alpha_{current}$. The particular configuration analyzed in this study happened to correspond to a case where the closest

optimized solution occurs at one degree past stall.

Next, a brief comparison of the articulated and SMTE wings was conducted to determine if both wings were constructed identically. This is clearest to see in the measurements of drag. Due to the sensitivity in drag measurements, the data presented is the difference between the actual and minimum drag. While both wings are ideally symmetrical, there is some discrepancy between the articulated wing and the SMTE. In fact, Figure 4.20 indicates that the articulated wing stalls after the SMTE wing. This is important to note, as this trend will be carried through in the rest of the data. The lift-drag curve is also presented and shows that overall the SMTE exhibits greater lift-to-drag ratio and thus efficiency when compared to the articulated wing. The region in which the articulated wing outperforms the SMTE corresponds it's delayed stall angle.

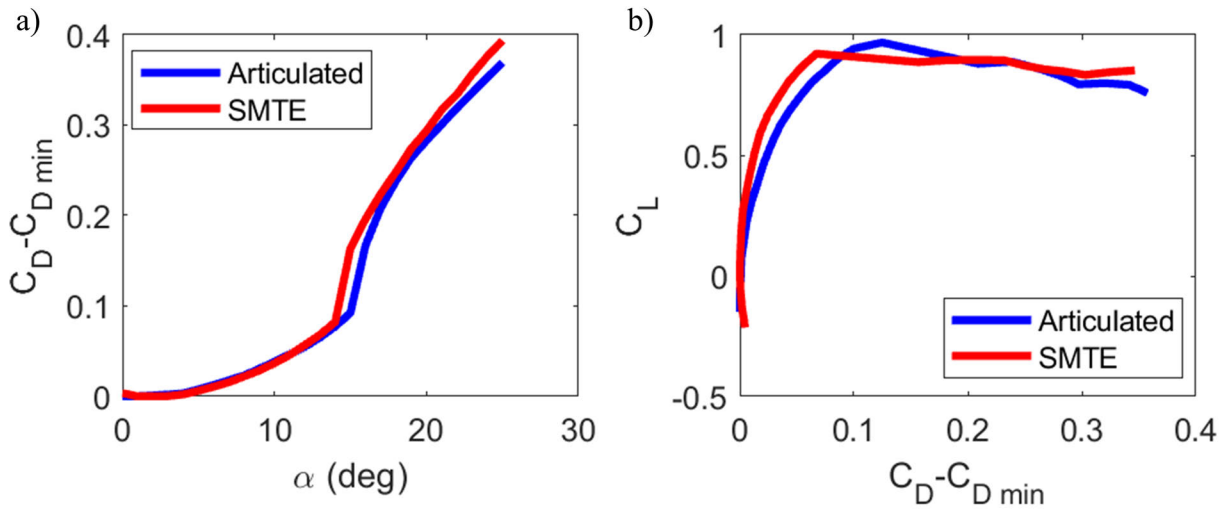

Figure 4.20: Comparison between the articulated and SMTE wings unadapted a) drag coefficient and b) lift-drag curves

The ability of the optimized model to predict the experimental data was then analyzed. In both the articulated and SMTE wings, the model predicts the pre-stall region ($0°$ to $16°$) relatively well with a mean squared error of 4.7% and 0.6% respectively. However, post-stall the experiments

deviate from the models. Although the curvature of the articulated wing bears resemblance to the modeled lift curve post-stall, the difference in stall angles results in a large error between the model and experiment. Conversely, the SMTE matches the model's stall angle accurately but due to the design of the wing, the lift plateaus and fails to correlate to the model, a trend which is not apparent in the 2D lift curves. This is thought to be caused by the compliance of the silicone skin on the SMTEs trailing edge which, if over-relaxed due to fatigue or age, could act as a sail at larger angles of attack.

Lastly, it is important to note the differences between the articulated and SMTE wings with respect to their drag reduction. Figure 4.21 presents the drag of each wing at the adapted and unadapted configurations in addition to the change in drag between the unadapted and the adapted configurations. Both cases demonstrate that, as expected, adaptation delays the onset of stall as is evident in the sharp decrease in the change in drag. Furthermore, these results show that the morphing SMTE reduces post-stall drag over twice the amount as the articulated wing in the post-stall region. This correlates to a 20% drag reduction from the unadapted condition. This result is dramatic and of substantial importance considering that the articulated wing's aileron deflections are on average 26% larger than the SMTE deflections.

While the model appears to have partially succeeded in predicting optimal flap configurations to recover from stall, flow visualization, shown in Figures 4.22 and 4.23, was used on both wings to verify whether or not flow separation was indeed eliminated or at least reduced. A smoke wand was inserted into the flow upstream of the wing and slow motion video was taken to capture images of the smoke stream at a high frame rate. This was conducted at each of the three scenarios: the on-design condition, the off-design unadapted condition, and the off-design adapted condition. Furthermore, the flow visualization was captured at the root, midspan, and tip of the wing at the

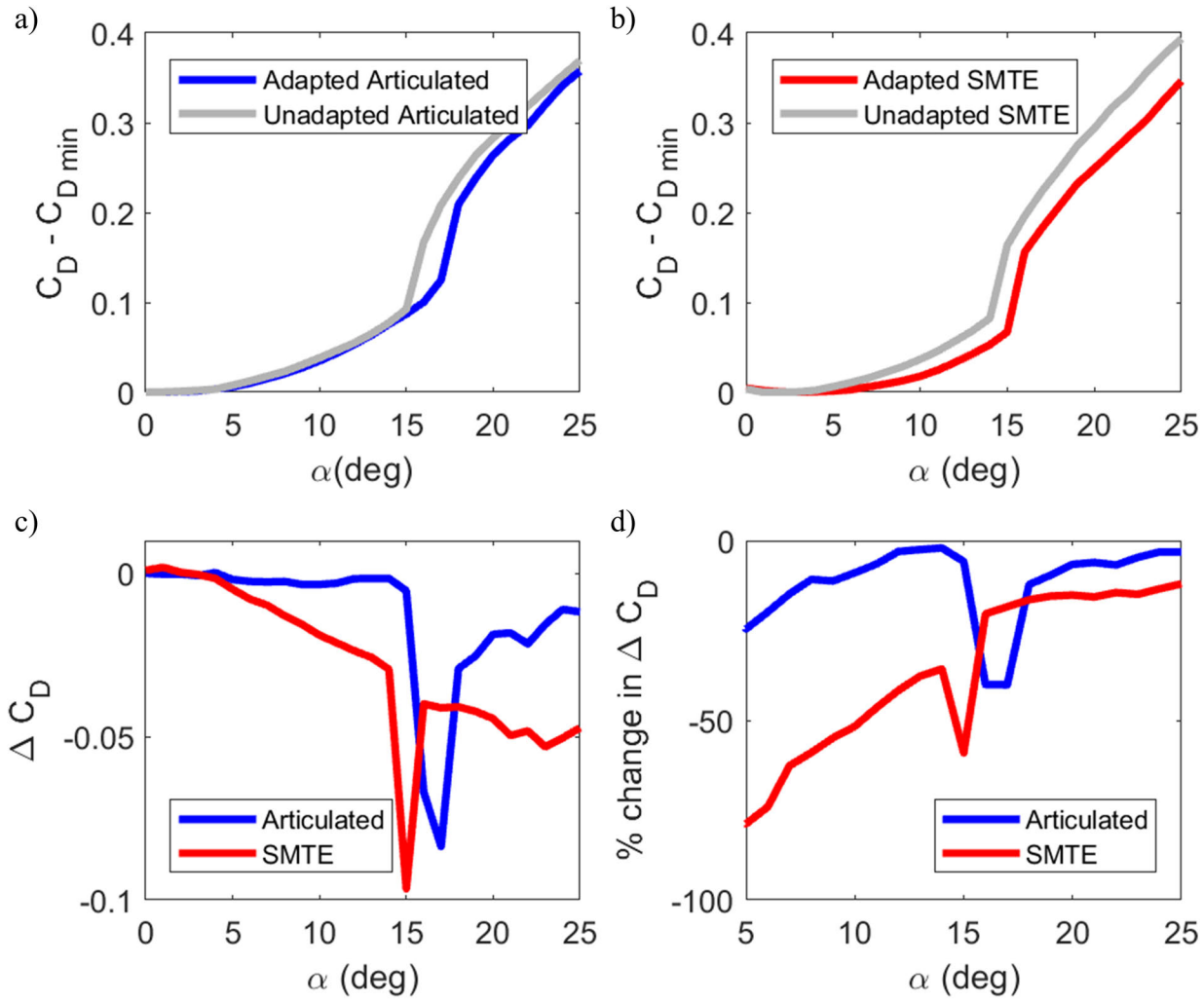

Figure 4.21: Experimental adapted and unadapted drag curves for a) articulated and b) SMTE wings c) difference in drag between the adapted and unadapted cases and d) percent change in drag

locations shown in Figures 4.22 and 4.23.

For both the articulated and SMTE wings, the flow at the on-design flight condition clearly remains attached across the entire span as expected. Then, when moved to the off design flight condition the root and midspan of both wings show strong vortex formations indicating that the wings are indeed stalled. Most interestingly is the adapted condition at the same angle of attack as the off design case. Both wings show almost complete elimination of the separation; however,

the SMTE appears to exhibit superior performance. This data serves to prove that the nonlinear optimization indeed predicts aileron deflections to adequately recover from stall.

The results presented here should be viewed as the first steps in analyzing the nonlinear aerodynamic performance of morphing finite wings. Further examination will investigate a variety of other design conditions to analyze the limitations of spanwise varying wings to adapt to stall. While the results presented here showed that the particular configuration tested was only partially successful at recovering from stall, this indicates that coupled morphing, such as aileron deflection in addition to reflex camber, may be able to achieve stall recovery over a broader range of design criteria.

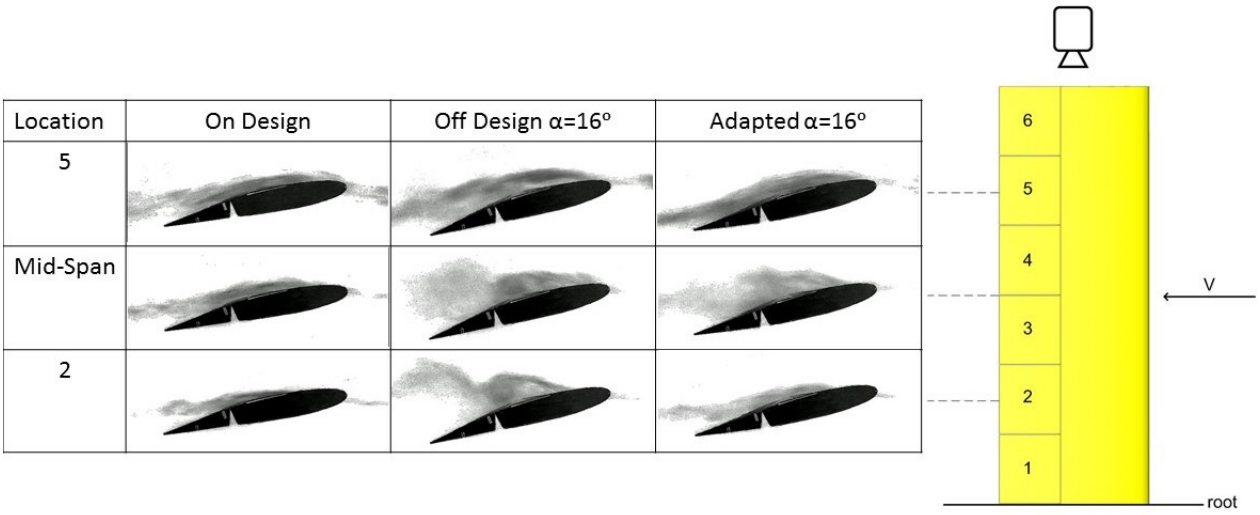

Figure 4.22: Flow visualization of the articulated wing at the on design and off design flight conditions

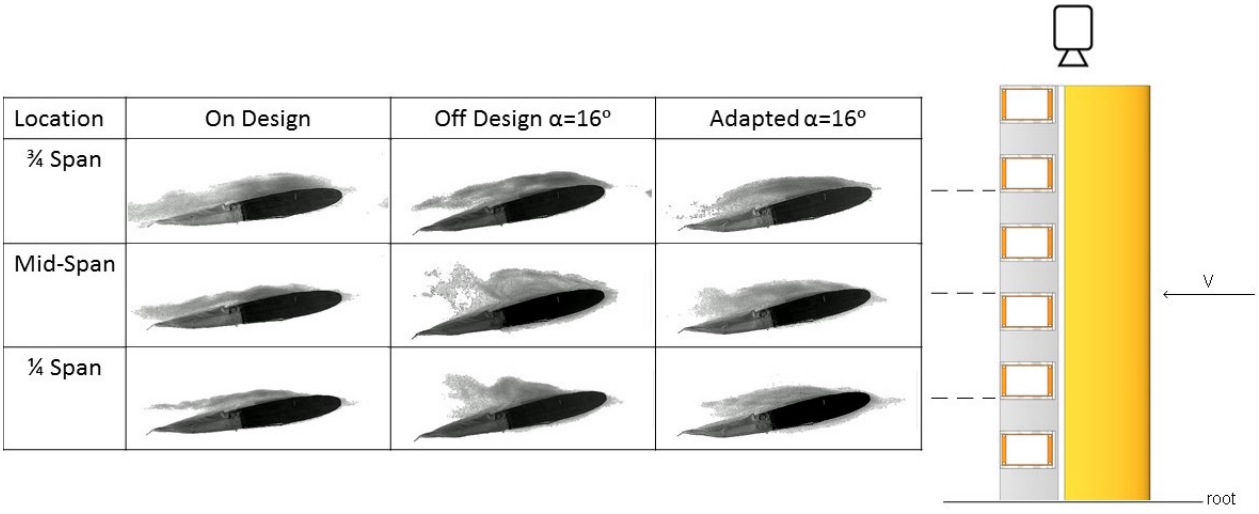

Figure 4.23: Flow visualization of the SMTE wing at the on design and off design flight conditions

4.5 Quantifying System Limitations

The previous section has shown through the proposed model and accompanying experiments that this method of recovery is successful in both a spanwise morphing wing and a discrete flap wing of equal spanwise capabilities, and has highlighted the superior performance of the morphing wing [92]. The current work builds upon this knowledge to quantify the limitations of such extreme adaptation with respect to the initial on-design lift constraint ($C_{L,on-design}$) and the off-design angle of attack ($\alpha_{off-design}$). This was accomplished by optimizing the actuator deflections, and thus the spanwise geometry of the wing, using the viscous nonlinear lifting line model to return to the on-design lift condition using the geometry of the SMTE. Overall, the following work serves to develop a model capable of analyzing the nonlinear aerodynamics of a spanwise morphing wing, analyze the extent of adaptable scenarios including stall recovery, contribute to the understanding of the strengths of spanwise morphing aircraft when handling nonlinear aerodynamics, and inform future morphing designs by suggesting critical improvements.

4.5.1 Extent of Recovery

By optimizing the spanwise trailing edge deflections of a morphing wing for a single set of flight conditions in Section 4.3, the wing successfully recovered from stall and returned to the on-design lift while maintaining the off-design angle of attack. This same procedure was conducted over a range of conditions to determine the limitations of a morphing wing such as the SMTE to adapt to both pre and post-stall conditions. For the unactuated geometry of the SMTE, the stall angle occurred at 15° and will be useful when comparing the range of off-design cases to the initial configuration.

The results of the optimization shown in Figure 4.24 were broken down into 4 categories: recovered, unrecovered, possible solution, and no possible solution. Physically, a wing either can or cannot recover from stall. A solution that recovered successfully adapted from the off-design condition such that the new flight condition occurred in a pre-stall region of the morphed wing's lift curve. This was assessed by comparing the off-design angle of attack to the angle of attack at maximum lift for the adapted lift curve. A solution that was unrecovered met the requirements defined in the optimization yet the new flight condition occurred in the post-stall region of the morphed wing's lift curve. Since this analysis includes a discussion on improving current morphing designs, a possible solution case was introduced upon observing that some results reached the maximum bounded value (8.85°) for the tip deflection. This indicated that perhaps recovery for these cases would be possible with a different morphing mechanism if the bound on the tip deflection was larger. The final category, no possible solution, was added to accommodate cases where the optimization failed to find an appropriate solution. While this case also represents a wing which has not recovered, it is distinguished from the unrecovered case in that the optimizer was

not able to match the initial lift condition within the constraints and tolerances of the optimization. These cases appear to be numerical artifacts and some but not all can be resolved by decreasing the relaxation factor; however, increased under-relaxation further approximates the solution and substantially changes the post-stall behavior.

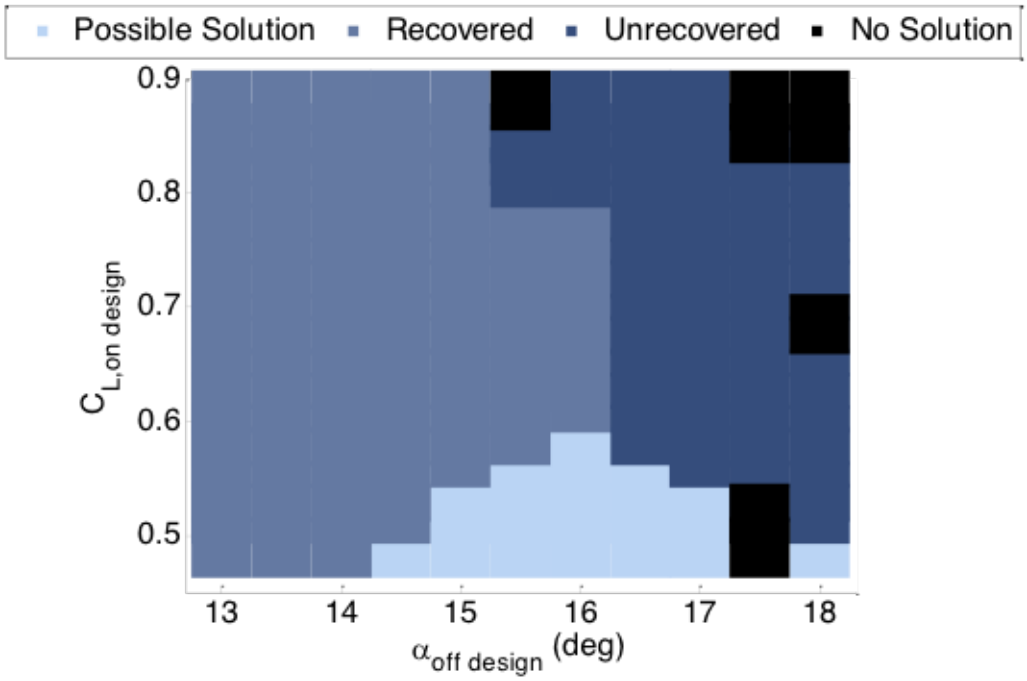

Figure 4.24: Design space for a spanwise morphing wing with respect to adaptation

The data show that the adaptability of a morphing wing to recover, especially from stall, is indeed limited. In fact, there appears to be three distinct regions which detail the conditions in which the wing is able to adapt. As expected, the wing was capable of adapting to off-design conditions that occur pre-stall; however, when the initial lift condition was low, the actuators could not provide sufficient deflection to match the on-design lift condition. This makes up the region of possible solutions. Furthermore, the wing was only able to adapt to off-design angles of attack that were at a maximum of $16°$, one degree past the stall angle for the unactuated wing. This matches

the 2D trends noted previously in Figure 4.6 where the 2D lift curves indicated that deflecting the actuator up only slightly delayed stall by shifting the lift curve. Thus, for situations where stall recovery over a broad range of flight conditions is desirable, changes in the design of morphing mechanisms should be considered.

Given these results, the first proposed method of improving the adaptability of morphing structures is to increase the range of tip deflections. This addresses the region of possible solutions where the initial lift condition is low, correlating to a large change in lift between the on-design and off-design conditions. This limited range of actuation is a persistent issue in smart morphing materials which do not rely on conventional actuators. One solution which retains the same morphing mechanisms assumed for this analysis, would be to add an active anterior point of rotation which can be actuated by another smart material like SMA wires. Hence, the trailing edge deflection would be compounded, including both the actuation of the SMA and MFC. The second improvement in morphing wings would require some mechanism of further delaying stall in the 2D lift curves and preventing flow separation, while maintaining adequate lift. Coincidentally, the same hinge suggested previously could provide the solution. In actuating the SMA and MFC in opposite directions, the airfoil experiences reflex camber. Pankonien *et al.* has shown that a morphing airfoil composed of a MFC trailing edge with anterior SMA hinge in reflex can achieve the same lift as an airfoil with monotonic actuation while maintaining attached flow [93]. Thus a single improvement to existing morphing designs, a continuous morphing hinge in addition to the camber morphing control surface, is suggested for future morphing aircraft designs with an emphasis on broad-range stall recovery.

4.6 Chapter Summary

Morphing aircraft provide a unique ability to adapt to changes in flight conditions. In this chapter, a method was developed for analyzing the ability of morphing wings with arbitrary variations in spanwise camber to adapt to these changes. An extended nonlinear lifting line model with low post-stall fidelity was used to simulate the aerodynamics of a finite wing. The section-based approach of this model was tailored to accommodate morphing aircraft where the spanwise geometry varies. This was accomplished using simulated 2D polars which correlated the airfoil geometry and angle of attack to predict the aerodynamic behavior.

The morphing wing under consideration had six camber-morphing actuators in order to adapt to nonlinear aerodynamics, with the ability to recover from stall using nontraditional stall recovery methods. Using the nonlinear aerodynamic model and a constrained minimization algorithm, the model was optimized to predict the adequate aileron deflections required to meet the design constraints by minimizing the total drag, ideally recovering from stall. It was shown that the nonlinear aerodynamic model had great potential for predicting the optimal aileron deflections of a spanwise morphing wing to adapt and recover from stall.

Experimental tests were also conducted for a a single recovery scenario to validate the nonlinear model and compare the recovery capabilities of the morphing SMTE and an equivalent articulated wing. The model was able to accurately adapt to meet the target lift constraint to within 7%, yet the optimized point was still in the negative region of the lift curve and thus was not capable of completely recovering from stall due to the assumed design conditions and the limits of the 2D lift and drag data. When uniform in span, the nonlinear model predicted the lift distribution to within less than 3% error. Incongruities within the physical models, namely the aeroelasticity of

the morphing wing, hindered exceptional agreement with post-stall experiments, yet showed good agreement in the linear regime.

Furthermore, it was shown that while both the SMTE and articulated wings were capable of adapting to stall and reducing the drag penalty associated with operating at the off-design condition, the morphing wing experienced greater drag reduction compared to the articulated wing, with significantly smaller actuations. Lastly, flow visualization shows that this method of adaptation successfully eliminated vortex formations in both the morphing and articulated wings, thus recovering from stall.

Further investigation which assessed the SMTEs recovery across a wide range of flight conditions identified that the ability of this particular spanwise morphing wing to adapt to stall in particular was limited to mid-range lift conditions relative to the maximum lift, and angles of attack encompassing pre-stall and near stall conditions. These limitations were driven by a requirement for larger tip deflections in addition to a mechanism to further shift the 2D lift curve to the right. This can be overcome through the addition of a continuous morphing hinge which would extend the range of actuation and allow for reflex camber. Thus, it is highly recommended that future designs within morphing aircraft encompass this additional degree of freedom which allows for control over the compounded trailing edge deflection and reflex camber of the airfoil.

CHAPTER 5

Development of a Multifunctional Tail

Motivated by the lack of research in tailless morphing aircraft in addition to the current inability to measure the resultant aerodynamic forces and moments of bird control maneuvers, this work aims to develop and test a multi-functional morphing control surface based on the horizontal tail of birds for a low-radar-signature UAV. Customized MFC actuators were designed to achieve yaw control across a range of sideslip angles by inducing three dimensional curvature as a result of bending-twisting coupling, a well-known phenomenon in classical fiber composite theory. This was hypothesized to allow for yaw control, pitch control, and limited air break control. The structural response of the customized actuators was determined numerically in order to optimize the fiber direction to allow for maximized deflection in both the out-of-plane and transverse directions. When implemented, this design can produce three control configurations: symmetric deflection for pitch control, single deflection for yaw control, and antisymmetric deflection for air brake control.

In particular, this chapter details the mechanics and implementation of both a piezoelectric and thermal model to characterize the response of the custom MFCs. Following this setup, the models were assessed based on the blocking force and free strain values reported by the manufacturer for a standard MFC geometry. This validation was conducted in order to determine both mod-

els' accuracies in addition to their feasibility for use in a custom MFC with unique geometry and fiber direction. Once an appropriate model was justified, the custom actuator geometry which was briefly mentioned prior in Chapter 3 was implemented. A series of cases were tested, changing the fiber direction in order to maximize the out-of-plane and transverse deformations. Upon finding an optimal fiber orientation, the model's predicted shape was compared to the experimentally determined 3D profile.

5.1 Modeling Macro Fiber Composites

In order to determine the appropriate fiber direction to produce maximized transverse bending-twisting coupling, a numerical model was required which accurately predicted the response of the MFCs. Unlike standard PZT actuators, the MFCs are composed of layers of PZT fibers, electrodes, adhesive and polymer in order to achieve its uniquely flexible characteristics. See Figure 5.1 for a macro image of the composite surface and Table 5.1 for the MFC material properties.

Table 5.1: Material Properties of M-8557-P1

Property	Value
E_1 (GPa)	30.34
E_3 (GPa)	15.86
ν_{12}	0.31
G_{12} GPa)	5.52
l (mm)	85
w (mm)	57
t (mm)	0.3
d_{33} (m/V)	$460e^{-12}$
d_{31} (m/V)	$-210e^{-12}$
ζ (F/m)	$8e^{-9}$

Here E_1 and E_3 represent the modulus of elasticity in the rod and electrode direction respectively, ν_{12} represents the Poisson ratio, G_{12} represents the shear modulus, l represents the MFC

length, w represents the MFC width, t represents the MFC thickness, d_{33} represents the piezoelectric coefficient in the rod direction, d_{31} represents the piezoelectric coefficient in the electrode direction, and ζ is the permittivity coefficient. It is important to note that the piezoelectric coefficients reported here are specific to the Navy type II PZT used in the MFC, and do not represent the total dielectric piezoelectric coefficients of the MFC itself. Two models are tested here in ABAQUS based off a specialized method which accounts for the MFCs modular structure [106]: a piezoelectric model and a thermal analogy [107].

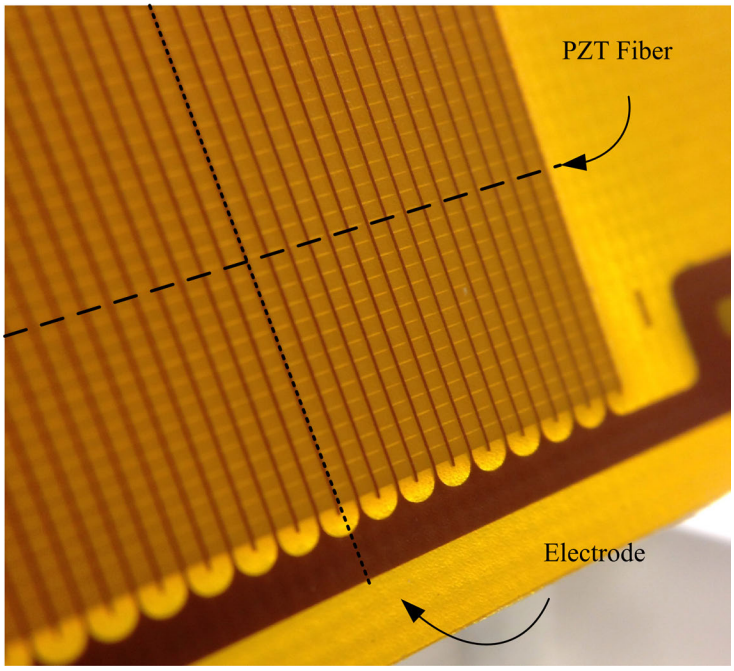

Figure 5.1: Macro image of MFC electrodes and fibers

5.1.1 Piezoelectric Model

Here, the piezoelectric material was assumed to be transversely isotropic and the response to an applied electric field was assumed to be linear as is common in basic IEEE standards [108]. For relatively low electric fields, this assumption produces fairly accurate results. The constitutive

relations were written as a set of two matrix equations representing actuator's response. The matrix equations can be written as:

$$\{\epsilon\} = [S^E]\{\sigma\} + [d]^T\{E\} \tag{5.1}$$

$$\{D\} = [d]\{\sigma\} + [\zeta^\sigma]\{E\} \tag{5.2}$$

where S^E is the material compliance in constant electric field conditions, ϵ is the strain, σ is the stress, d is the piezoelectric coefficient, D is the electric displacement, E is the electric field, and ζ^σ is the permittivity coefficient. These equations represent the converse piezoelectric effect, describing the piezoelectric actuation response due to an applied electric field, and the direct piezoelectric effect describing the piezoelectric sensing response.

To validate the model a standard M8557-P1 MFC was used which exhibits a d_{33}-effect. Due to its modular structure, the MFC consists of many small actuators which are defined by the PZT fiber between a pair of interdigitated electrodes. According to the manufacturer, each actuator unit was thus measured as the distance between the center of the interdigitated electrodes (500 μm) minus the width of the electrode (90 μm). The total number of actuator units in the MFC was determined by dividing the total active length of the MFC by the actuator unit width. As the electrode pitch across all manufactured MFCs is constant, all MFCs of the same length will have an equal number of units. For example, as the M8557-P1 MFC has an active length of 85mm, it would be composed of 202 PZT units.

The total piezoelectric coefficient of the MFC was calculated by multiplying the reported piezoelectric constant for the Navy type II PZT by the total number of units. This process was repeated

in order to calculate the MFC's d_{31} coefficient as well. In the model, the standard C3D20E piezoelectric element was used which contains 4 degrees of nodal freedom: one electric charge, and 3 translations. Lastly, the electric field was applied via a voltage boundary condition with one edge receiving 0 V and the opposite edge receiving 1500 V.

5.1.2 Thermal Analogy

The MFCs can also be modeled using a thermal analogy which draws parallels between an electrically actuated MFC and a thermally expanding transversely isotropic material. The analogy relates the electric field applied to the MFC to the thermal load, and the piezoelectric coefficients to the thermal expansion coefficients. Accordingly, the piezoelectric (left) and thermal (right) constitutive relations can be related as such

$$\{\epsilon\} = [S^E]\{\sigma\} + [d]^T\{E\} = [S]\{\sigma\} + \{\alpha\}\Delta T \tag{5.3}$$

where ΔT is the change in temperature, and α is the thermal expansion coefficient. Comparing the right and left sides of the equation, it is evident that the elastic contribution remains unchanged, characterized by Hooke's Law, while the piezoelectric contribution can be directly related to a thermal contribution. For the thermal model, the response is dependent upon the thermal expansion coefficients and change in temperature. The equation describing the relationship between the thermal expansion and piezoelectric coefficients can thus be written as

$$\begin{Bmatrix} \varepsilon_{33} \\ \varepsilon_{31} \end{Bmatrix}_{pzt} = \frac{\Psi_3}{s} \begin{Bmatrix} d_{33} \\ d_{31} \end{Bmatrix} = \Delta T \begin{Bmatrix} \alpha_{33} \\ \alpha_{31} \end{Bmatrix} \tag{5.4}$$

where Ψ_3 is the potential voltage difference between electrodes and s is the spacing between electrodes. This demonstrates that the piezoelectric coefficient is directly analogous with the piezoelectric thermal expansion coefficients while the electric field applied to the MFC is analogous to the applied thermal loading. To model the entire MFC as opposed to an individual PZT electrode pair, s was taken to be the total active length of the MFC and Ψ_3 was taken to be the applied voltage.

This model was implemented using ABAQUS finite element software. In this model, standard C3D8R general purpose linear brick elements with 8 nodes and reduced integration were used. Lastly, the thermal load was applied in the form of a constant predefined field as opposed to a boundary condition as will be discussed in the following section.

5.1.3 Model Analysis and Comparison

In order to determine the model's accuracy, the free-strain and blocking force were calculated numerically and compared to the manufacturer's reported values for an M8557-P1 MFC. It was assumed that the manufacturer's blocking force and free strain values were specified for the active area of the actuator. The free strain, as the name implies, is a measure of the axial strain experienced by the actuator when the maximum voltage is applied without constraints in the axial direction. Conversely, the blocking force is a measure of the axial force output by the actuator when axial deformation is restricted.

5.1.3.1 Boundary Conditions

Measuring the blocking force and free strain is a matter of defining the correct boundary conditions for each test. As these quantities are measured based on longitudinal actuation, the MFC

in both cases was constrained to in-plane motion by restricting out-of-plane U_1 and transverse U_2 deformations. To measure the free strain, one edge of the MFC was further restricted in the U_3 direction but the other was free. To measure the blocking force, both edges of the MFC were restricted in the U_3 direction. These structural boundary conditions are depicted in Figure 5.2.

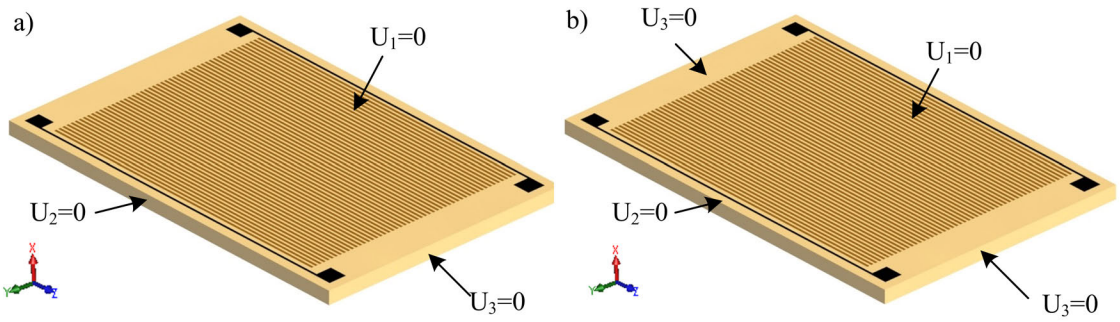

Figure 5.2: Enforced structural boundary conditions on the MFC for a) free strain and b) blocking force simulations where U_1,U_2, and U_3 corresponds to displacement in the *x, y, and z* direction respectively

The applied loadings to induce actuation for each model must also be considered. In the piezoelectric model, the applied electric field was prescribed as a voltage boundary condition. A 0 V electrical boundary condition was applied to one edge perpendicular to the fiber direction, while a 1500 V condition was applied to the opposite edge. Thus, the total voltage difference across the entire MFC was 1500 V. Conversely, the loading in the thermal model was applied as a predefined field throughout the entire active area. As described in Equation 5.4, the equivalent thermal loading was calculated by dividing the total electric potential by the total length in the rod direction. Accordingly, a $1500V/0.085m = 17647°C$ thermal loading was applied. These conditions are displayed in Figure 5.3.

The free strain in ppm was calculated by dividing the change in actuator length by the initial actuator length as described in Equation 5.5. The blocking force in *N*, was calculated by multi-

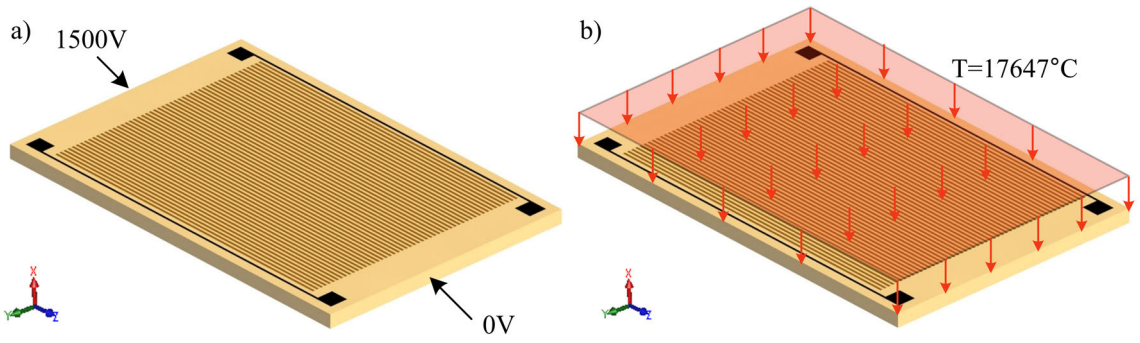

Figure 5.3: Enforced loading conditions on the MFC for a) the piezoelectric model and b) the equivalent thermal model

plying the average stress by the MFC's cross sectional area normal to the axis of elongation, in the z direction detailed in Equation 5.6. This can also be accomplished by looking at the reaction forces throughout the actuator. The results of both tests are shown in Table 5.2. Both models were able to predict the free strain and blocking force well, however the thermal model shows superior performance particularly with respect to the free strain with an error of 0.2% and a blocking force error of 7%. It is important to note that if the Navy type II d_{31} coefficient is not incorporated into the model, the accuracy decreases. The free strain and blocking force expressions are

$$\varepsilon_{free} = \frac{\Delta l}{l} 10^{-6} \tag{5.5}$$

$$F_{block} = \sigma t w \tag{5.6}$$

When choosing the appropriate model, it is necessary to consider not only the accuracy but also the robustness. In the piezoelectric model, the piezoelectric coefficient of the total MFC was based upon the number of units along the fiber length while the voltage was taken to be the maximum voltage. This works well for rectangular geometries, but introduces complexities and

uncertainties for other geometries where the PZT fiber length, and thus the number of units, is no longer constant and the voltage boundary conditions are more difficult to define. Conversely in the thermal model, the thermal loading was distributed evenly throughout the actuator and both the thermal loading and thermal expansion coefficient are dependent upon the actuator length. This effectively removes any dependence upon fiber length, so long as the length is taken to be the same in both the thermal load and coefficient calculations. Accordingly, the following methods implement the thermal model which was shown to provide better results and was also observed to be more robust when customizing the PZT fiber orientation and geometry.

Table 5.2: Comparison of FEM results between simulations and manufacturer's reported values

		F_{block}	ϵ_{free}
	Manufacturer	923	1800
Piezoelectric	ABAQUS	850.4	1714.1
	% Error	7.9%	4.8%
Thermal	ABAQUS	856.7	1804
	% Error	7.1%	0.2%

5.2 Customized Macro Fiber Composite Geometry

To determine the fiber orientation needed to achieve maximized deflection in both the out-of-plane and transverse directions, the thermal model [107] discussed in the prior section was implemented on a custom actuator geometry. The chosen geometry for the active area was based on the tail aspect ratio used in prior studies by Hummel *et al.* [34]. The finalized geometry and fiber angle is shown later in Figure 5.6. Note that in this optimization the model only considers the active area, as the validation mentioned prior was not suited for combined active and inactive area. The results of this section may provide some further insights into the effect of the inactive area on

the MFCs actuated profile. Lastly, this model was implemented with a 2.54e-5 m AMS 5519 fully hardened steel substrate to induce bending-twisting coupling. The epoxy layer, which is used to bond the MFC to the substrates, was not modeled here for simplicity as preliminary testing showed minimal impact on the outcome.

5.2.1 Fiber Angle Optimization

The PZT fiber orientation was optimized manually to maximize the tip deflection in the out-of-plane and transverse directions by modeling the custom MFC with fiber orientations between 0° and 90° in 5° increments. By maximizing the out-of-plane deflection, the control effectiveness in zero sideslip was guaranteed for pitch and yaw maneuvers. Furthermore, by maximizing the transverse deflection, the control surface remains effective in large sideslip angles unlike many traditional tailless aircraft control surfaces. It is worth noting that both cannot be maximized entirely without tradeoffs, meaning that the maximum value for the out-of-plane tip deflection does not correspond to the maximum transverse tip deflection.

Figure 5.4 plots the maximum displacement components (*x, y, z*) for each fiber angle. For all cases, this occurred at the trailing edge outer tip of the actuator. As 3D scatter plots can be difficult to decipher with 2D graphics, the projections of the 3D data onto each 2D plane are also displayed in grayscale and reduced marker size. Note that the material coordinate system changes as the fiber angle is tuned, and thus the axis convention labeled in the following figures represents the structural coordinate system. These results show that the relationship between fiber angle and displacement components is quite complicated.

The maximum transverse displacement (in the x direction) initially becomes more negative

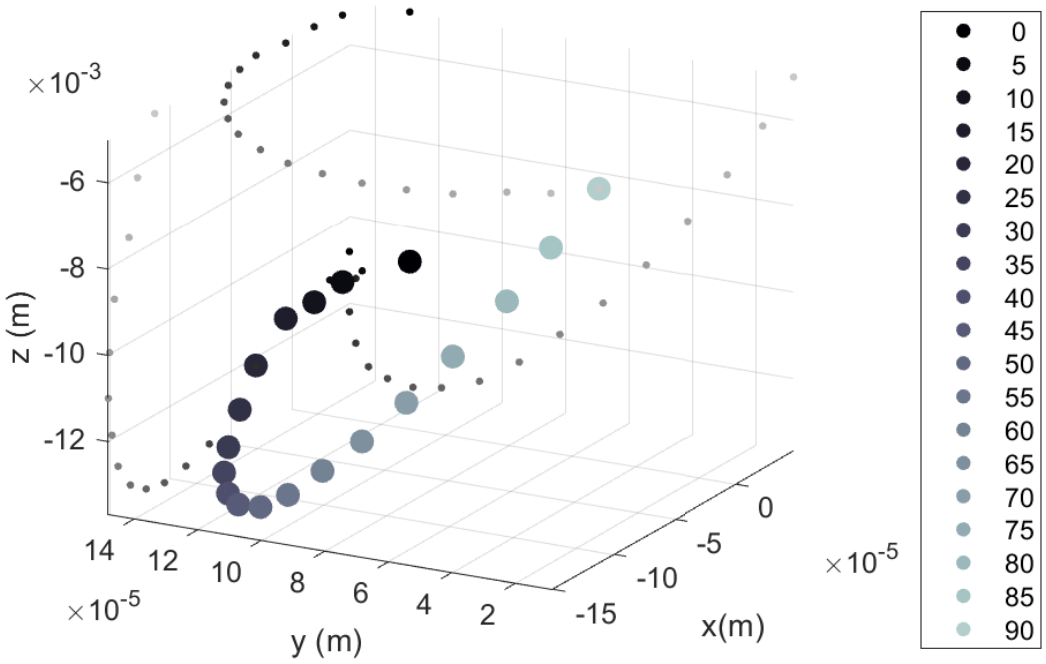

Figure 5.4: Maximum displacement components (*x, y, z*) of the custom MFC with data projected onto each 2D plane for fiber angles from $0°$ to $90°$

with fiber angle, pointing towards the body's longitudinal axis of symmetry. As this component lies perpendicular to the $0°$ fiber orientation, the direction of piezoelectric expansion further aligns with the *x* axis as the fiber is rotated. However at larger fiber angles, the amount of deflection begins to decrease. The fiber angle that achieves the maximum transverse deflection was $65°$. Alone, transverse deformation signifies a change in the width or side-to-side displacement of the actuator, however combined with out-of-plane deformation this maneuver is expected to generate a yaw response.

The data also show that the maximum longitudinal displacement (in the *y* direction) was largest at fiber angles below $20°$. For these low fiber angles, the fiber orientation is near-parallel to the *y* axis, thus a large displacement was expected. Alone, this response would increase the length of the actuator as the leading edge was constrained. Past $20°$, the fiber direction and thus the direction of

elongation begins to occur perpendicularly, resulting in a loss in displacement.

Lastly, the out-of-plane displacement in the z direction must be assessed. For a rectangular MFC with 0° fiber orientation, this displacement would correlate to the total tip displacement of the actuator. The displacement initially becomes more negative as the fiber angle increases with the maximum absolute out-of-plane displacement (in the z direction) occurring at 40°. This increase in downward deflection typically correlates to an increase in the control forces and moments magnitudes. However at larger fiber angles, the magnitude of the displacement in the z direction reduces dramatically, as the fiber angle becomes perpendicular to the actuator's length.

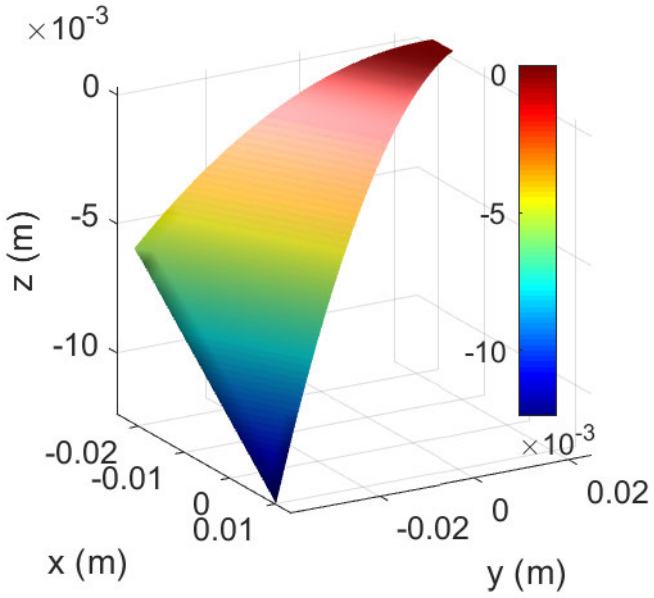

Figure 5.5: Deformation of custom shaped MFC with 55° rotated fiber orientation

Given these results, the optimal fiber orientation was chosen to be 55° which lies between the angles at which the custom MFC experiences maximum transverse and maximum out-of-plane displacement. The final deformed geometry is shown in Figure 5.5 and achieves a maximum tip

displacement of 12.7 mm. These results clearly indicate the 3D nature of the custom actuator, as the gradient of deformation does not solely lie along the *y* axis as would be typical in other camber-morphing applications. If an aircraft is not expected to exceed a certain sideslip angle, the fiber orientation can be more precisely optimized to maximize the desired output. The final dimensions and fiber angle for the actuator can be seen in Figure 5.6.

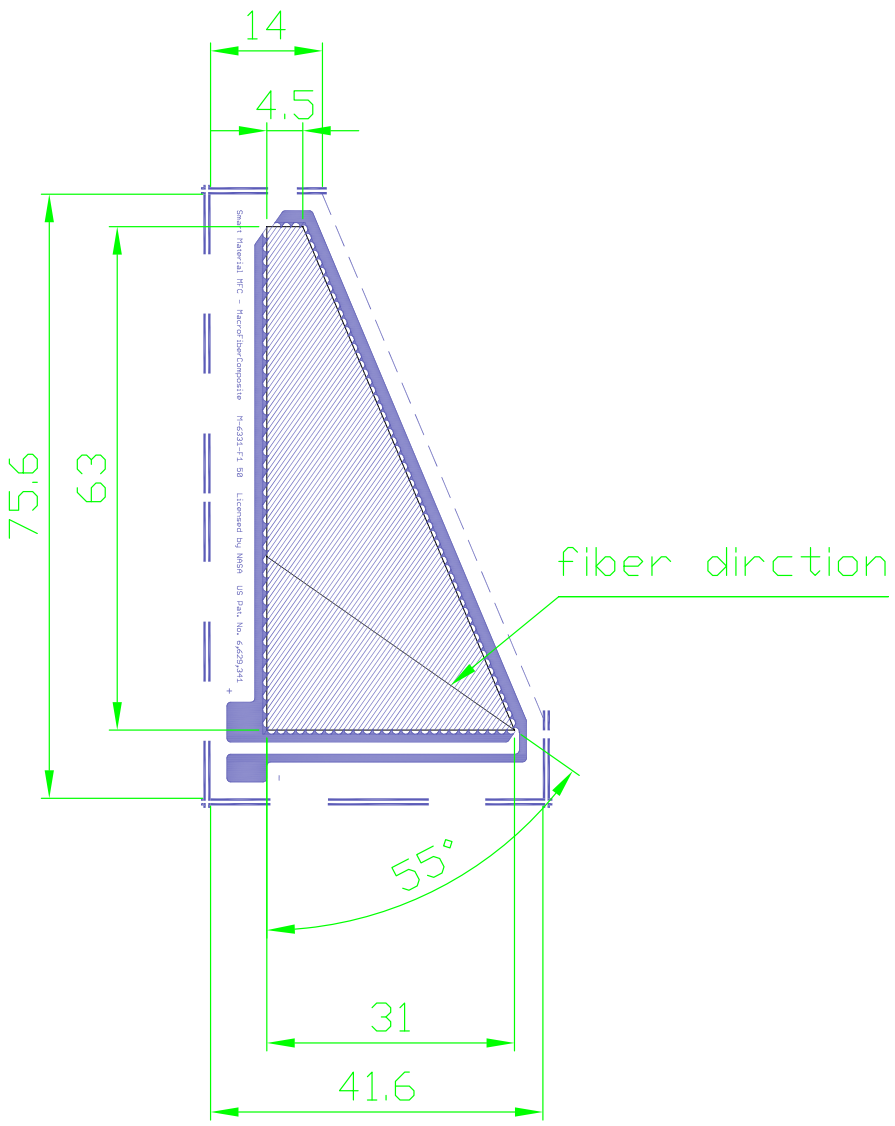

Figure 5.6: Final dimensions in mm of custom MFC depicting the active and inactive area, and the fiber orientation

It is important to note that this optimization and analysis is specific to the shape and size of the actuator presented here. As was implied earlier, the aspect ratio plays an important role in the resulting deformation. As the length and thus aspect ratio of the actuator increases, the out-of-plane deformations become more dominant and thus, the optimized fiber angle for achieving both transverse and out-of-plane displacement would be much different. In this scenario, a larger fiber

angle would likely be required to achieve adequate transverse displacement.

5.2.2 Model Validation

While the accuracy of the model was tested initially by comparing the simulated free strain and blocking force to the manufacturer's specifications while in the process of determining the most appropriate FEM model, further validation can be conducted to identify how well the thermal model captures the custom actuator's response. This was needed for ensuring accuracy and consistency in the proceeding experiments and analysis.

Prior to validating the model, some discrepancies between the manufactured and modeled actuator should be noted. Primarily, the model considers solely the active area of the actuator. Due to the composite nature of the MFCs, the manufacturer cannot make an actuator to size with solely active material. A thin margin of inactive material around the outer perimeter is required for packaging the PZT fibers, electrodes, etc. due to the size and available location for the MFCs' electrode terminals. As will be discussed, the experimental deformed active area is easy to extract, however the structural properties of the inactive margins may partially restrict the overall actuated geometry. Additionally, the actuator was assembled by bonding the steel substrate to the MFC. The epoxy layer was measured to be 0.05 mm, a fraction of the total thickness of the assembly. For simplicity, this was not incorporated into the model as preliminary testing indicated minimal effect on the overall deformed geometry.

5.2.2.1 Manufacturing

Upon receipt of the customized MFCs, the composite actuator was manufactured. For the most precise results, precautions were taken to ensure a complete bond between the MFC and the

substrate. The MFC and $2.54e^{-5}$ m thick AMS 5519 fully hardened steel substrate were cleaned to remove any particulate or oils which may create an incomplete bond between the two surfaces. The steel substrate was then secured to a thick aluminum plate lined with a fiberglass quick-release layer to ensure that no curvature was accidentally introduced during the adhesion process. A thin layer of 3M DP460 high sheer strength epoxy was applied before the MFC was secured on top as the final layer. The high sheer strength epoxy ensures that little to no shear deformations occur between each layer which would effectively reduce the actuated curvature.

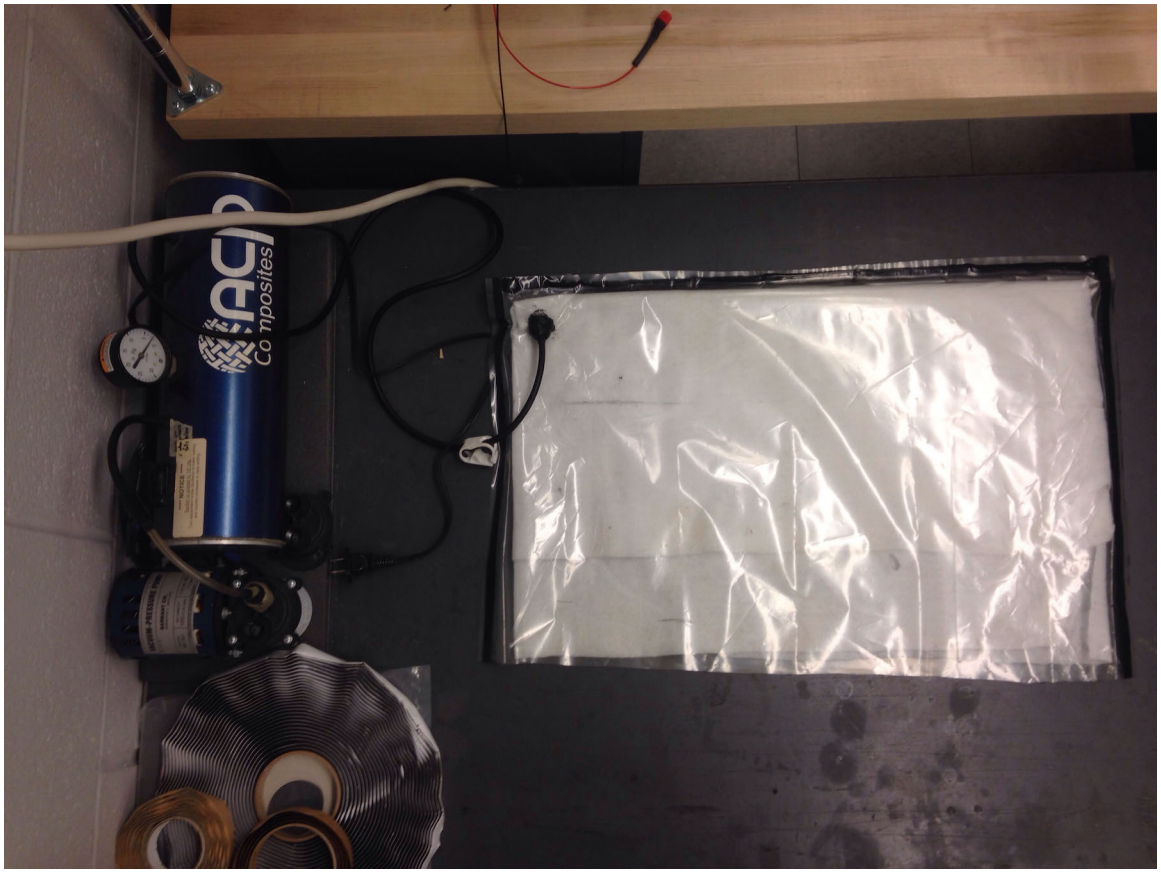

Figure 5.7: Experimental setup for vacuum bagging procedure

This particular epoxy has a work life of 60 minutes, a set time of 4 hours at room temperature and complete cure occurring after 24 hours. For best possible adhesion with no air pockets or

delimitation between layers, the composite layup was cured for 6 hours in a vacuum bag. The vacuum bonding process ensures an even pressure is applied across the actuator. After curing, the excess steel was trimmed from the MFC and high voltage wires were soldered to the electrodes. See Figure 5.7 for a depiction of the setup.

5.2.2.2 Measuring Custom Actuator Geometry

To validate the model and characterize the custom actuator's response, the entire 3D profile upon actuation was measured. This was accomplished using a NextEngine Desktop 3D Scanner in macro mode. The scanner uses MultiStripe Laser Triangulation (MLT) technology via an array of four twin Class 1M, 10 mW solid state lasers in parallel to reconstruct the surface geometry with $1/10000^{th}$ m dimensional accuracy for macro scans. The system was simultaneously capable of capturing synchronous surface color with 500 DPI for macro scans, allowing for high precision correlation between visual and structural features.

Figure 5.8 shows the experimental setup used to measure the custom actuator's deformed geometry. The actuator was mounted to the rotating base plate by suspending it from the stand with fishing line. This method minimized the impact of the mounting mechanism on the resulting deformed geometry. Other methods of mounting were investigated such as direct mounting to the stand, but were determined to slightly influence the resulting curvature of the actuator. The lead wires were also secured to the support strut so that rotation of the baseplate would not impact the orientation or deformation of the actuator. For macro scans, the model was positioned within 0.25 m of the optical sensors allowing for the highest possible resolution. To reconstruct the entire actuated surface, multiple scans at a resolution of 6.72 points mm^{-2} were collected by varying the rotation of the baseplate.

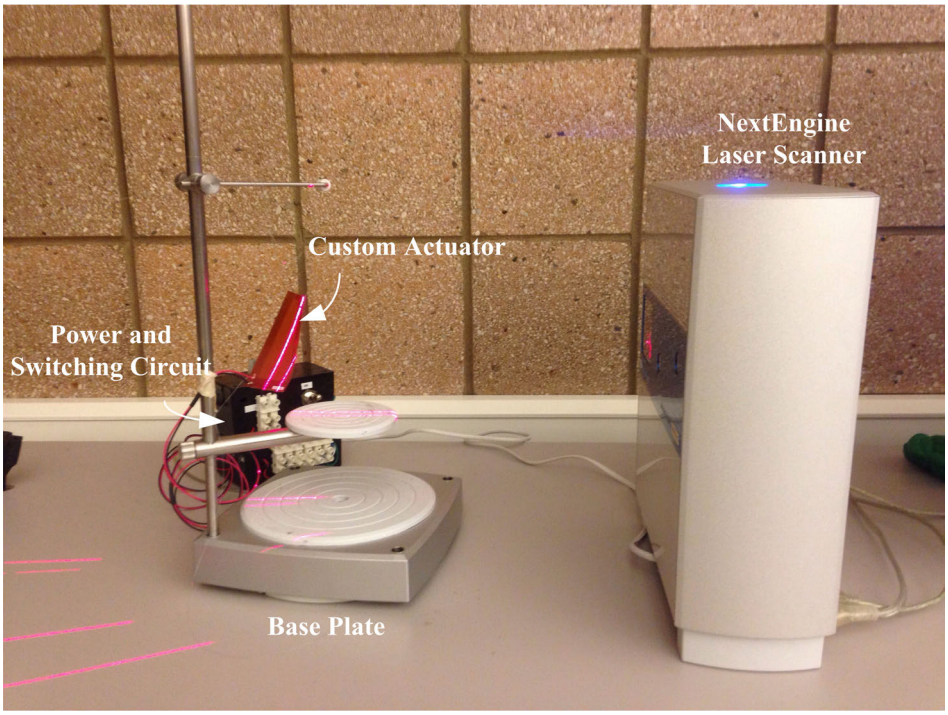

Figure 5.8: Experimental setup to measure 3D actuated profile using a NextEngine Desktop 3D Scanner

While conducting the tests, an AVID Dual Channel MFC Bimorph High-Voltage Driver was used to output a voltage of 1500 V. The amplifier required both supply power and an input signal to drive the output voltage. This is typically prescribed using a multi-output power supply. To simplify the system, both in terms of equipment and space, a standard outlet adapter designed to output 12 V at 1.5 A was converted allowing for elimination of a bulky power supply. Furthermore, as this test did not require incremental actuation a voltage divider was designed to output 2.5 V or 5 V at the flip of a switch, where the amplifier outputs 0 V when supplied 2.5 V, and 1500 V when supplied 5 V. This hardware can be seen in the experimental setup shown in Figure 5.8. Lastly, prior to data acquisition the MFC was allowed to reach steady state actuation.

The boundary of the MFC's inactive section was initially outlined with small reflective markers so that the active area could be isolated during post-processing. However upon assessing prelimi-

nary scans, it was noted that although the markers were fairly small, the high pixel density of the surface color data in comparison created some errors during post-alignment since the direct center of each marker was difficult to isolate. With the markers removed, the surface color data was clearly capable of distinguishing the junction between the active and inactive area.

Upon collection of the scans, the data was processed using Scan Studio software. Here, the scans were each aligned, merged, and trimmed to the active area to create a single file of the overall deformed geometry. This geometry was exported as (*x, y, z*) coordinates and imported into MATLAB for comparison with the ABAQUS results. As the scanned data was collected relative to an arbitrary coordinate system, it had to be aligned using 3D coordinate translations and rotations.

The results of the comparison are shown in Figure 5.9. The modeled results are displayed in color and a reduced subset of the scanned data coordinates are displayed as data points. The data show good agreement between the modeled and experimental geometries. Notably, the experimental out-of-plane tip displacement of the active area was 11.94 mm while the modeled tip displacement was 12.86 mm, within 6.2% error. Furthermore, the experimental transverse tip location was 29.5 mm while the modeled tip location was 30.9 mm within 1% error.

However, it is clear that the curvature of the experimental actuator was smaller than that of the model. As mentioned prior, this was hypothesized to be due to differences in the model and the physical actuator including the lack of incorporation of the inactive area and the epoxy lamina. Similar trends regarding an over-prediction of curvature have been noted in other MFC studies. Lee *et. al* [109] developed a bistable laminate solely with custom MFCs, where the induced prestress was generated by applying the maximum voltage to a $[0^{MFC}90^{MFC}]_T$ laminate. However, many of the hypothesized attributions of error were not incorporated into this study, including imperfect laminate layups, performance degradation due to prolonged actuation during the bonding

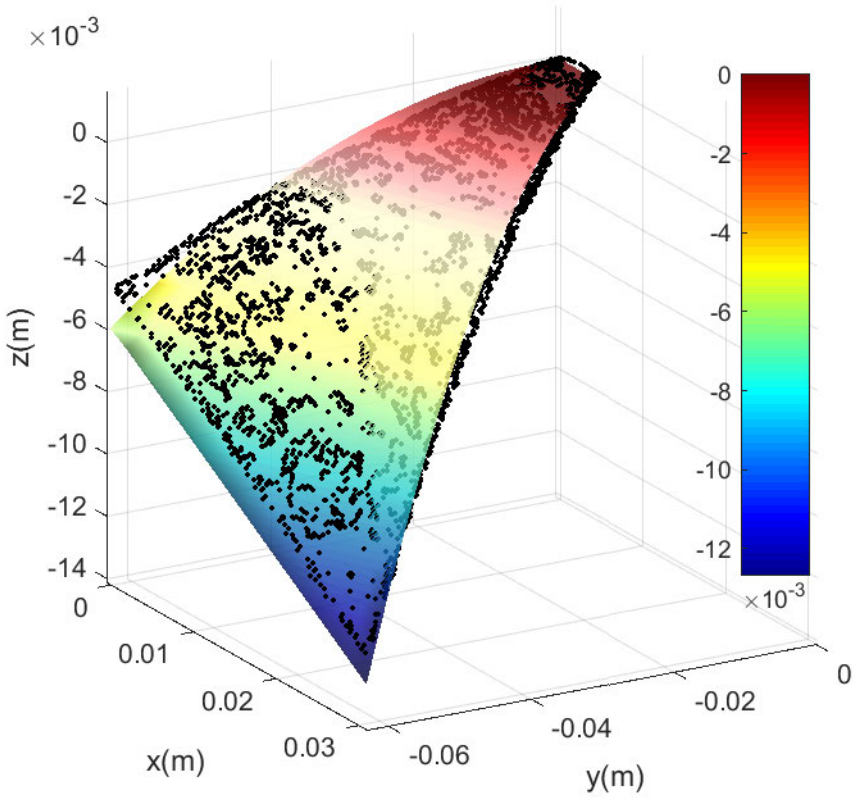

Figure 5.9: Comparison between experimental and modeled actuated geometry, modeled results displayed as unmeshed surface, experimental results displayed as data points

procedure, and variation between the piezoelectric constants of multiple MFCs. Furthermore, that work incorporated both the inactive area and epoxy lamina which were not included for simplicity in the present work, yet were hypothesized to be the main sources of error. This may still be attributed to the over-prediction of the actuator's curvature, but ultimately as the primary function of the model was to predict the out-of-plane and transverse tip displacement in order to manufacturer an adequate custom MFC to achieve yaw and pitch control, this minor discrepancy was deemed to be irrelevant in the current context.

5.3 Chapter Summary

This chapter presents the modeling and development of a customized multifunctional MFC actuator. Two different FEM models were developed to simulate the composite actuator. These models with a standard MFC shape were compared to the manufacturer's reported specifications. The thermal analogy showed better performance than the piezoelectric model and was more robust when dealing with customized geometries and large fiber angles.

With the thermal model, the fiber angle which maximized the out-of-plane and transverse deflections was determined to be 55°. This fiber angle resulted in a total tip displacement of 12 mm. While the preliminary model validation was only conducted with a standard MFC, the modeled results with the customized actuator was further validated with a 3D scanned profile of the physical actuator. These results showed that the model was fairly accurate in predicting the actuated profile of the custom MFC; however, it slightly over-approximated the curvature.

CHAPTER 6

Aerodynamic Characterization of the Bioinspired Tail

This chapter, motivated by the discrepancy between manmade and natural flight designs, investigates the aerodynamic effects of a smart morphing horizontal tail exhibiting bending-twisting coupling for control of a bio-inspired aircraft. The resulting complex curvature was hypothesized to be inherently effective for multifunctional control. Initial testing of the actuator's control of aerodynamic forces and moments was conducted using Reynolds Averaged Navier Stokes (RANS) simulations to verify that the modeled actuator was capable of controlling yaw. Upon verification, the performance of the bioinspired control surface was measured experimentally on a 3D printed half scale model with a 0.34 m span in a wind tunnel. A six axis load cell was used to measure the aerodynamic forces and moments about the geometric center of the aircraft body. In total, three control configurations were tested experimentally: symmetric deflection for pitch control, single-sided deflection for yaw control, and antisymmetric deflection for air brake control. The prior RANS fluid simulation was also used to compare with the experimental results for the unactuated baseline configuration. Directional moment and stability derivative are presented to gain insight into the effect of the morphing horizontal tail on yaw control.

Although the actuator's effectiveness in pitch and yaw was assessed with respect to sideslip, this is not a standard metric for measuring pitch effectiveness. Further experiments were conducted to investigate the actuator's ability to control pitch and yaw during changes in angle of attack. The control effectiveness was assessed via similar wind tunnel experiments to those mentioned prior. Alpha sweeps were conducted across a range of wind speeds. While the complex curvature of the actuator is desirable for control of both yaw and pitch, it also caused coupling between these two degrees of freedom. The magnitude of this coupling was also investigated.

As will be discussed in the proceeding analysis, the actuator was shown to provide better yaw control than traditional split aileron methods, remain effective in larger sideslip angles, and provide directional yaw stability when unactuated. It was shown to provide adequate pitch control in sideslip in addition to limited air brake capabilities. The pitch response with respect to angle of attack was also shown to be sufficient. Overall, this actuator design is proposed to provide complete aircraft control in concert with spanwise morphing wings

6.1 Initial Computation of Aerodynamic Forces

Preliminary simulations were conducted to verify that the actuation mechanism detailed in Chapter 5 would produce a yawing moment. The complete deformation of the actuator was determined with a FEM analysis combining the custom MFC actuator and an elastomeric honeycomb, consistent with the aircraft concept detailed in Chapter 3. Accordingly, the transversely isotropic composite thermal model was implemented while the honeycomb was modeled with the Tango Plus material properties specified by the manufacturer, Stratasys.

While the thermal model used to simulate the custom actuator was shown to achieve simi-

lar out-of-plane and translational tip deflection, a reduction in camber in experimental tests was observed. As the camber of control surfaces is well known to affect the control forces and moments, the results of the proceeding analysis will be useful from a qualitative but not quantitative perspective.

Lastly, upon development of the FEM model, the deformed geometry was exported to ANSYS Fluent to assess the aerodynamic forces in low Reynolds number flow generated due to actuation. Simulations were run at a wind speed of 10 m/s over a wide range of sideslip angles ($0° < \beta < 70°$). These results provided insight into the effects of the actuated tail on the aerodynamic coefficients and thus control of the UAV

6.1.1 ANSYS Computational Fluid Dynamic Model

The numerical simulations were conducted using a half-scale model of the full geometry due to the asymmetric nature of actuation. Using tetrahedral elements, the mesh was refined locally at the wing trailing edge and tail tip in addition to locations exhibiting substantial changes in curvatures such as the active control surface. The fluid was finely meshed with 1e6 elements. The simulations were performed using a three dimensional time-steady CFD analysis for low-speed incompressible flow. This required the use of a coupled pressure-based solver which simultaneously solves for the pressure and momentum equations. Due to the low Reynolds number nature of the problem, a suitable turbulence model was critical. Accordingly, a standard $k - \omega$ turbulence model was chosen.

Two primary quantities of interest were investigated from the fluid analysis: the yaw moment coefficient (C_η), and the static yaw stability coefficient ($C_{\eta\beta}$). The yaw moment coefficient was

a main concern for the current work. It is a non-dimensional parameter describing the moment about the vertical axis. In aircraft, this describes the restoring moment experienced by the aircraft in sideslip conditions and is written as

$$C_\eta = \frac{N}{\frac{\rho}{2}U^2 Sb} \tag{6.1}$$

where here U is the velocity, ρ is the density, N is the yaw moment, b is the half span and S is the reference area. It is important to note the reference quantities used to calculate the nondimensional coefficients used in this analysis. The reference area was chosen to be total wing area which is often used in flying wing or tailless aircraft studies.

Lastly, the yaw stability is a metric describing the aircraft's tendency to return to symmetric flight ($\beta = 0$) when the yaw angle is disturbed. When the stability derivative is positive, then an increase in sideslip generates a greater yaw moment indicating a stabilized system. For this analysis, this metric is used to ensure that stability is not lost with actuation. The stability derivative is calculated as

$$C_{\eta\beta} = \frac{\partial C_\eta}{\partial \beta} \tag{6.2}$$

representing the change in yaw moment divided by the change in sideslip angle.

6.1.2 Simulated Aerodynamic Results

The preceding results provide an analysis of the yaw moment characteristics of the aircraft wing, wing-tail, and wing-actuated tail configurations. By using non-dimensional parameters to characterize the performance of the aircraft, comparisons to other flight designs can be drawn since

these metrics are normalized by the speed, atmospheric conditions such as altitude, and size of the aircraft, thus they characterize how changes in the profile or geometry affect the fluid flow around the structure.

Results presented in Figure 6.1 show the control derivatives for the wing-tail combinations listed prior. A few trends can be noted from the data. The effect from the wings show a parabolic trend with a decreasing yaw moment coefficient ($\frac{\partial C_\eta}{\partial \beta} < 0$) at a sideslip of $45°$, indicating an unstable system. However, simply by adding a horizontal tail, the response of the yaw moment with respect to sideslip angle drastically changes. It is clear that the unactuated tail provides a substantial contribution to the yawing moment particularly at very large sideslip angles with a minimum contribution of 30% of the total yaw moment. However by actuating the tail, the minimum contribution is extended to 50% and in fact, below $20°$, the actuated tail doubles the contribution of the unactuated tail. This shows that the actuated tail is capable of contributing a significant yaw moment across a range of sideslip angles.

Furthermore, the contribution of the actuated tail to the yaw moment can be quantified. The difference between the actuated wing-tail combination and the unactuated wing-tail combination is shown in Figure 6.1. As expected, the actuated tail provides a positive contribution to the yaw moment and generally increases with sideslip since the moment arm and control surface area tend to increase with sideslip. However for $20° < \beta < 50°$, the yaw moment decreases, though still providing a larger contribution than the unactuated tail. This is thought to be due to the flow partially separating over the tail section, similar to how a lift-curve will decrease at stall and in many instances will increase again as the angle of attack continues to increase.

Insight can also be gathered regarding whether the tail's actuation or aspect ratio provides the primary contribution. This is demonstrated in Figure 6.2 which calculates the percent increase in

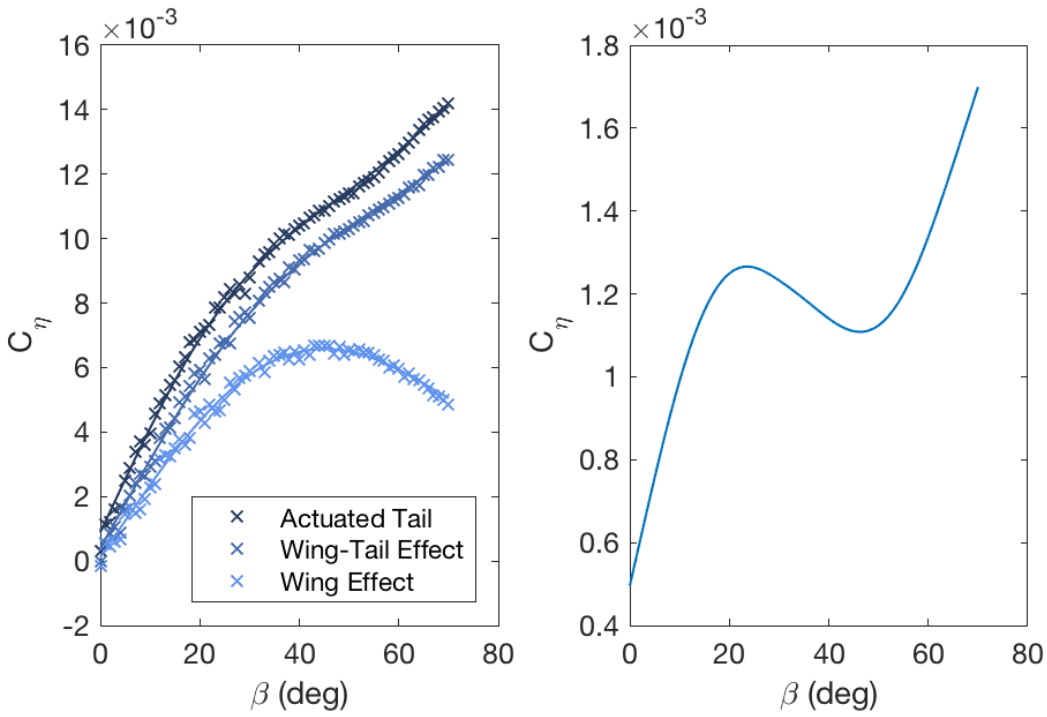

Figure 6.1: Yaw control moment for all configurations (left) and contribution of the morphed tail (right) with $S = .0183$ m^2, $b = .17$ m and $\delta = 10$ mm

yaw coefficient between the wing only model, and the unactuated and actuated models. Two factors in the morphing tail influence this change in yaw moment: the area perpendicular to the flow which induces the drag force component of the restoring moment, and the increase in moment arm as the aircraft experiences sideslip. These results indicate that the effects of cambered actuation are largest in sideslip ranging between $0°$ and $20°$, meaning that the area of the control surface plays a more important role in the moment coefficient at small to mid range sideslip angles. Conversely, at large angles the increase in yaw moment due to actuation is much smaller; thus, the moment arm is more influential in this sideslip regime. These results confirm previous observations that high aspect ratio tails outperform low aspect ratio tails since the larger moment arm provides superior yaw control and stability.

Finally, the stability derivatives can be investigated to gain insight into the effects of actuation

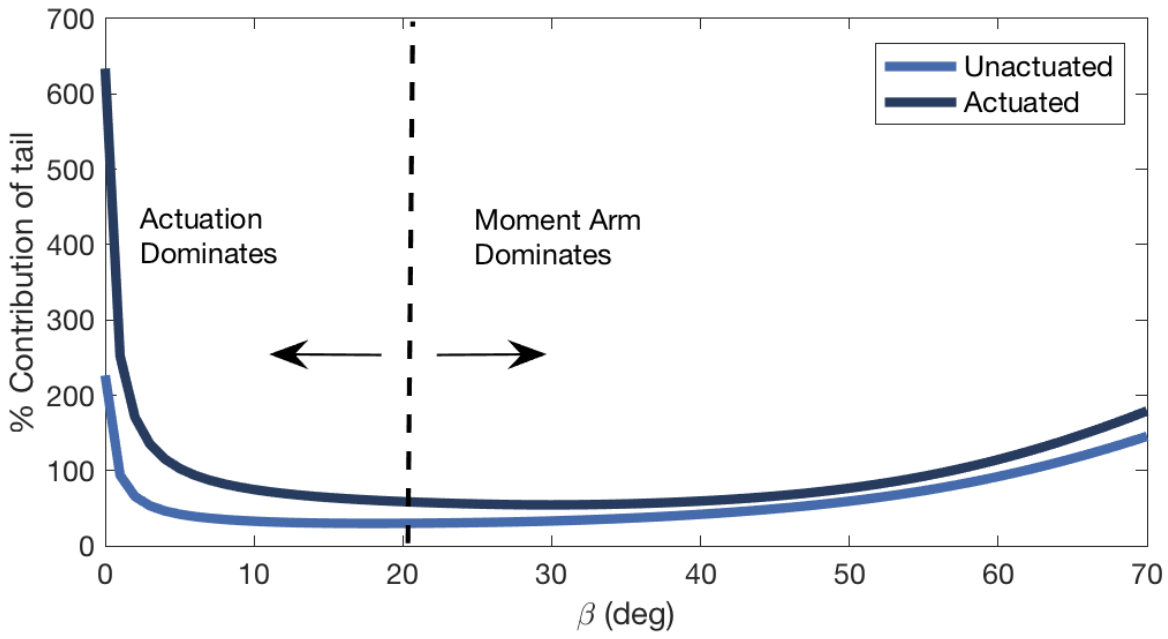

Figure 6.2: Percent increase in yaw with respect to the tailless model for the unactuated and actuated configurations

on the stability of the aircraft. For this metric, the sideslip angle is fixed at 10° while the pitch angle is varied in order to change the yaw coefficient. Figure 6.3 shows the stability derivatives for both the unactuated and actuated tail cases. The data confirms Sachs' observations that the unactuated horizontal tail adds directional stability to the aircraft. It is also shown that by actuating the tail section, yaw stability is not lost. In fact, for positive angles of attack (α, i.e. pitch) the stability practically remains unchanged. However, in dive maneuvers when the angle of attack is negative, the directional stability experiences a slight increases. While tail actuation is not specifically prescribed to stabilize the aircraft, these results show that stability is preserved if not increased with actuation.

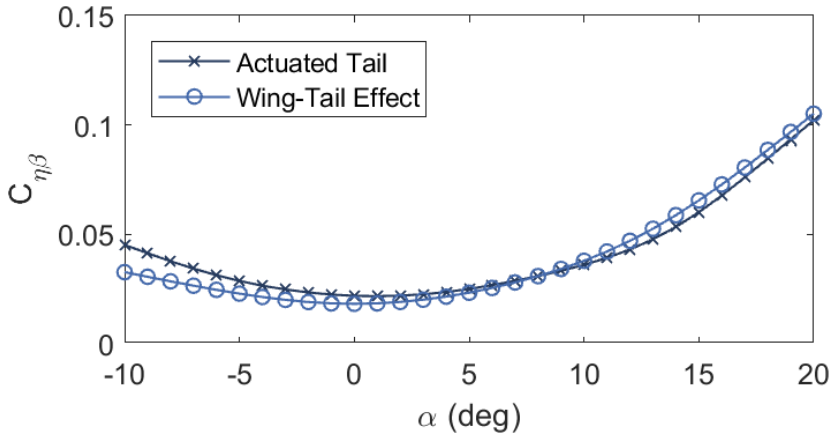

Figure 6.3: Stability derivatives for the actuated and unactuated configurations

6.1.3 Preliminary Conclusions

A smart morphing horizontal tail concept was shown to effectively increase the yaw moment coefficient in both a passive and active configuration. The passive tail section was confirmed to substantially increase the yaw control moment of the aircraft and improve directional stability at large angles of attack. More notably, the complex curvature of the tail section was shown to provide a substantial increase in yaw moment, particularly at sideslip angles less than 20° where the yaw moment response was doubled. Furthermore, the aircraft was proven to maintain directional stability when actuated and even increase stability in diving maneuvers. Further experiments should provide very concrete results regarding the control effectiveness of the morphing tail.

6.2 Experimental Model

This section details the integration of the actuator into the aircraft body. Experiments were also conducted to quantify the true tip displacement of the actuator when fully integrated into the aircraft.

6.2.1 Actuator Integration

The MFCs were manufactured with the fiber angle determined prior. While this geometry is symmetric, the voltage range and accordingly the actuation range of the MFCs is asymmetric, recalling that the minimum voltage is -500 V and the maximum voltage is 1500 V. To demonstrate yaw and pitch control of this actuator design, symmetric tail actuation is preferable and was achieved by bonding the substrate to the top surface of one MFC, and to the bottom surface of the MFC on the adjacent side. This allowed testing maximum actuations of [1500 V, 0 V] for yaw control, and [1500 V, 1500 V] for pitch control where these configurations represent the right and left actuators respectively. However, this limits the actuation for air brake tests to [-500 V, 500 V].

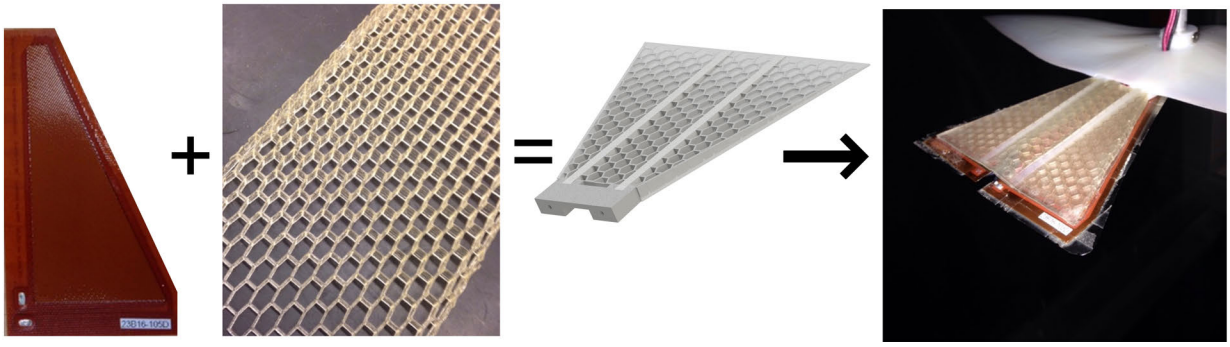

Figure 6.4: Actuator composition showing the integration of the custom shaped MFC and 3D printed honeycomb into the final tail structure

Each MFC is 0.3 mm thick, however in this application some thickness is desired to maintain static yaw stability. For that reason, a substrate was required which provided resistance to out-of-plane loads without substantially restricting the deformation of the MFCs. One method which has been heavily studied are cellular honeycomb structures [110]. A simple method of manufacturing such complex structures is with the aid of 3D printing which is capable of replicating complex geometries with high resolution. The honeycomb used in this work was 3D printed using the

multi-material Objet Connex printer which has the ability to combine a rigid digital material with an elastomeric digital material in different ratios to obtain an array of different rigidities. This allows for a multi-part assemblies to be manufactured in a single continuous and integrated print. In this work, it allows a flexible honeycomb substrate to be manufactured with a rigid connection to mount directly to the rest of the aircraft. A summary of integration is shown in Figure 6.4.

Upon integration of the tail, the wiring used to actuate the MFCs was embedded through the body of the aircraft to minimize the potential of developing loose connections in addition to minimizing the impact of the wiring on the aerodynamic results.

6.2.2 Mechanism Testing

Preliminary testing was conducted on the completed actuator mechanism. The purpose of this testing was to determine the relationship between applied voltage and MFC tip deflection. Measurements were taken using a Keyence LKG-402 laser displacement sensor. The laser displacement sensor was directed at the tip of the MFC and displacement data was collected in increments of 100 volts across the entire operating range of the MFCs. The voltage range of the MFCs is antisymmetric and spans from -500 V to 1500 V. This setup can be seen in Figure 6.5.

The results presented in Figure 6.6, show that for this tail geometry the tail can achieve over 1/4 inch of deflection. It is important to note that these results represent the deflection of the actuator upon full integration into the bioinspired UAV, including adhesion to the honeycomb layer. This explains the difference in actuator deflection between these experiments and the results detailed in Chapter 5. Still, given the size of the model the deflection presented in Figure 6.6 is a reasonable magnitude. Furthermore, the relationship between the voltage and out-of-plane tip displacement

of the MFC is approximately linear. This linear fit will be used in the latter sections to characterize the yaw moment with respect to the actuator deflection to align with standard convention.

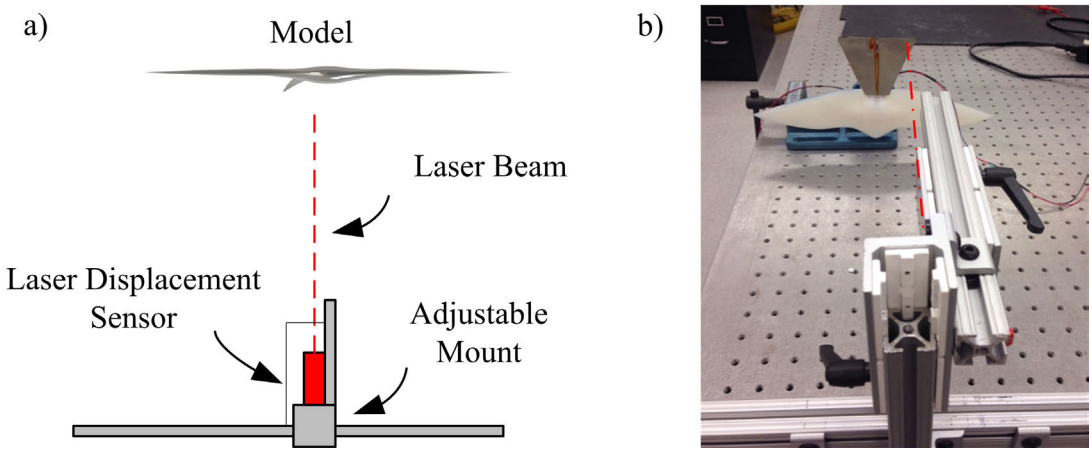

Figure 6.5: (a) Schematic from an aerial view of the experimental setup (b) laser displacement sensor setup for measuring relationship between applied MFC voltage and tip displacement

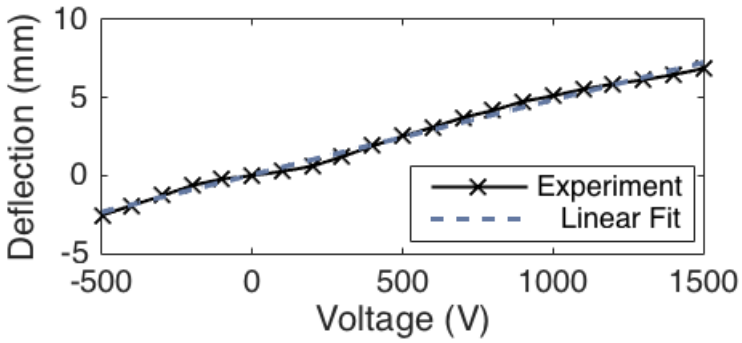

Figure 6.6: Mechanical characterization of the custom MFC's tip displacement with respect to applied voltage.

6.3 Sideslip Response

Upon integration and characterization of the actuator, experimental aerodynamic testing can be conducted. Specifically, this section details the experimental setup and results of the actuator's

control capabilities in sideslip. As the actuator can be deployed in multiple control configurations, each was tested.

6.3.1 Setup Description

Wind tunnel tests were conducted in the 0.6 m x 0.6 m open loop wind tunnel at the University of Michigan. The bioinspired aircraft was 3D printed in Vero White, the most rigid material of the Objet Connex resin products, and was mounted vertically to a ATI Nano17 Titanium 6-axis force balance. Given the scale of the model and wind tunnel, the blockage ratio was only 0.5%. The mount was then attached to a turntable which was used to vary the sideslip angle.

While tailless aircraft are typically mounted in wind tunnels using a sting mount, this was determined to be inappropriate for this model as the sting mount would interfere with the horizontal control surface. For this reason, a standard mounting rod through the center of the aircraft body was chosen. Ideally, the mounting rod would be long enough to place the model at the center of the wind tunnel section to guarantee uniform flow; however, a long mounting rod would overload the sensor due to torque causing permanent damage since the load cell is rated for such small loads in order to have adequate yaw moment resolution. Thus a compromise was reached by placing the model two inches from the wall where the flow is approximately uniform, well outside of the boundary layer. It is recommended that models lie away from the wind tunnel wall by at least 2-3 times their height. Given the height of the model is 0.64 inches at its thickest, this follows the recommendation; however, it is possible that some accelerated flow may exist beneath the model.

During the test, temperature, dynamic pressure, and load cell data were recorded and time averaged. Atmospheric temperature within the wind tunnel was recorded by a thermocouple mounted

upstream of the model. An Omega PX2650 differential pressure transducer was used to record the dynamic pressure via pitot tubes upstream of the wing. Lastly, the ATI Nano17 Titanium 6-axis load cell was used to record all 3 forces and 3 moments although in this study only lift, drag, yaw, and pitch are reported. This sensor has a force resolution of 1/171 N and a torque resolution of 5/184 Nmm in yaw, and 3/182 Nmm in pitch and roll. The entire experiment was coordinated in MATLAB using a DAQ and dSPACE MicroLabBox for data measurement and actuator control. The DAQ collected data from the thermocouple measuring the temperature inside of the wind tunnel while the dSPACE collected data from all 6 channels of the load cell as well as the differential pressure transducer. No fluid velocity measurements were taken; however, it can be inferred from Bernoulli's principle using the pressure and temperature readings.

The data collection algorithm continuously monitored the velocity so that it remained within 5% of the desired velocity. Furthermore, the dSPACE controlled the output signals throughout the experiment. Two signals were sent to the actuators, one for right and left MFCs. These signals first went to an AVID Dual Channel MFC Bimorph High-Voltage Driver which amplifies a 0 V to 5 V signal to -500 V to 1500 V for the MFC actuators. These high voltage drivers are designed to operate with a 8-12 V supply from a standard 2-3 Lithium Polymer battery and consume 1-3 A depending upon the amount of actuation [111]. This is a slight increase in power consumption from standard servo actuators, some of which operate above 1 A. The dSPACE also output the signal to the stepper motor which controlled a rotary table to set the sideslip angle. This allowed the entire experiment to be automated and eliminate human error. A flow diagram of the experiment is depicted in Figure 6.7.

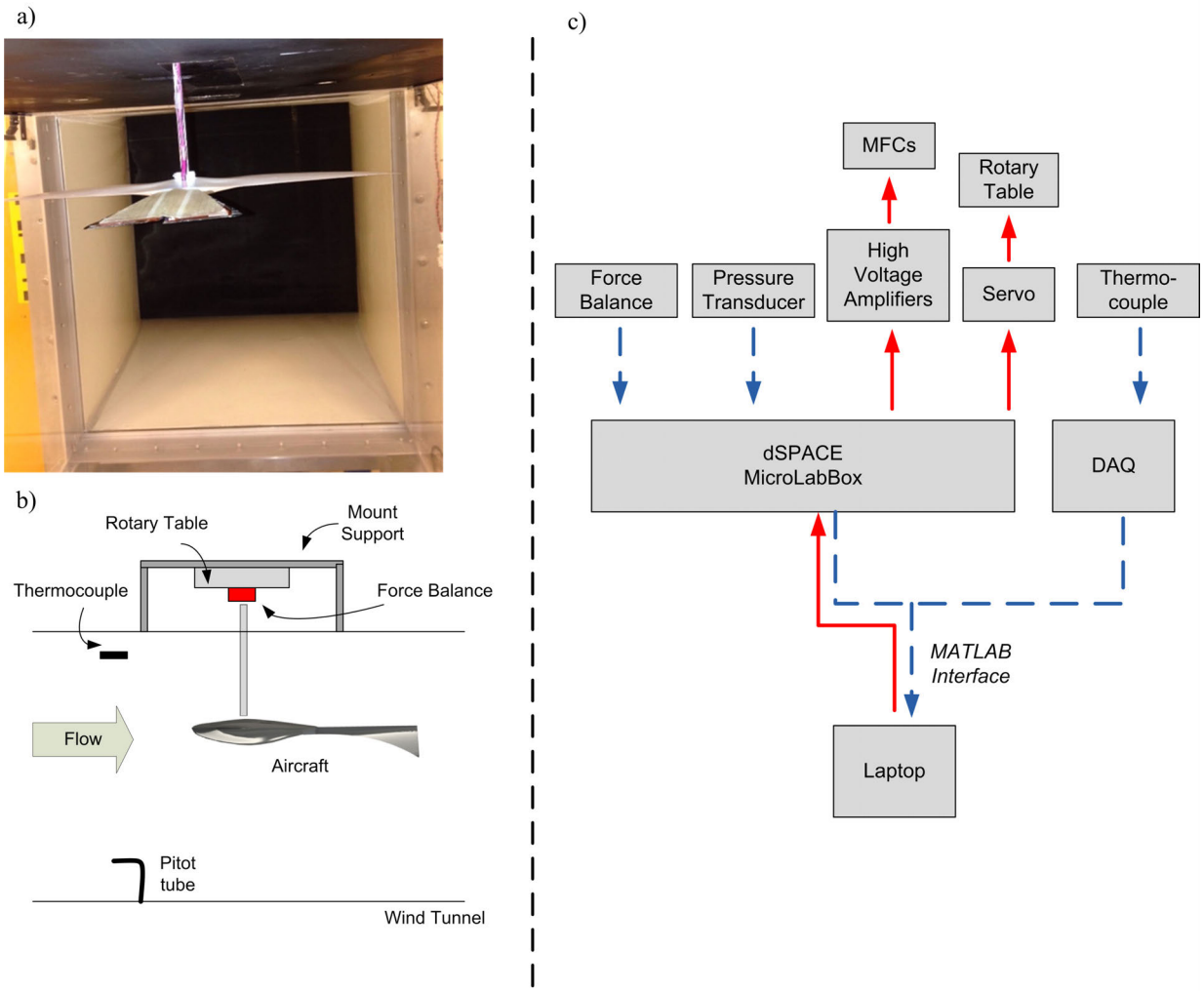

Figure 6.7: (a) Schematic of experimental setup (b) mounted aircraft in wind tunnel (c) experimental data flow

6.3.2 Test Method

Before conducting any tests, the pressure transducer was tared without any air loads and the load cell was tared with the model attached. This established a new zero point given the weight of the model and the atmospheric conditions which may vary from day to day. Additionally, to account for any errors due to manufacturing tolerance of the mounting setup, a preliminary experiment was conducted with zero tail actuation. Since the aircraft is symmetric, there will be

no yaw moment at 0° sideslip angle. Thus, this preliminary test identified the angle offset which was applied to the prescribed sideslip angle in the dSPACE controller. Aerodynamic tests were conducted at 10 m/s for a variety of tail configurations: to test the yaw control one MFC was actuated in increments of 250 V, to test the pitch control both MFCs were actuated symmetrically in increments of 250 V. To test the air brake capabilities, the MFCs were actuated asymmetrically at [500 V, -500 V].

The nondimensional aerodynamic forces and moments were recorded. The characteristic length of the bioinspired wing, used in the calculation of the other aerodynamic coefficients, was calculated as the mean aerodynamic chord shown below

$$MAC = \frac{2}{S}\int_0^{b/2} c^2 dy \tag{6.3}$$

where MAC represents the mean aerodynamic chord, and c represents the wing chord at location y. All other parameters required are consistent with those previously discussed in Section 6.1.1.

6.3.3 Results

This section presents the results of the aerodynamic testing and a discussion of their implications. The goal was to show that this bio-inspired actuator was capable of providing yaw and pitch control with respect to change in angle of attack and assess its abilities to potentially act as an air brake.

6.3.3.1 Yaw Moment Coefficient

Figure 6.8 depicts the nondimensional coefficients for the yaw configuration where C_η, C_L, C_D, and C_m correspond to the yaw moment, lift, drag, and pitch moment coefficients respectively. For the unactuated case [0 V, 0 V], the yaw moment coefficient exhibits a positive linear trend with respect to yaw angle, demonstrating that the restoring moment increases with sideslip. This indicates that even when unactuated, the horizontal tail alone provides a restoring yaw moment as has been previously observed [33] [34]. This is significant as an increase in yaw moment will tend to restore the aircraft to symmetric flight.

These results were compared to the numerical RANS simulations performed on the unactuated geometry using a three dimensional time-steady CFD analysis for low-speed incompressible flow. This required the use of a coupled pressure-based solver which simultaneously solves for the pressure and momentum equations. Due to the low Reynolds number nature of the problem, a suitable turbulence model was critical. Accordingly, a standard $k - \omega$ turbulence model was chosen. The yaw moment coefficient for the unactuated simulations and experiments practically coalesce, demonstrating that the experimental data show very good agreement with the simulations while validating the results and ensuring confidence in the latter tests. It is important to note that while the magnitude of the yaw moment coefficient may appear small, the values reported here are consistent with the data reported by Sachs [33] and Stenfelt *et al.* [79] [81].

By actuating one side of the tail for a yawing maneuver, the yawing moment increased, thus it can be deployed in sideslip if the static characteristics of the unactuated tail alone are not enough to restore the aircraft to symmetric flight. Even in zero sideslip, the actuator was capable of generating a positive yawing moment which indicates that the tail is effective at controlling yaw in forward

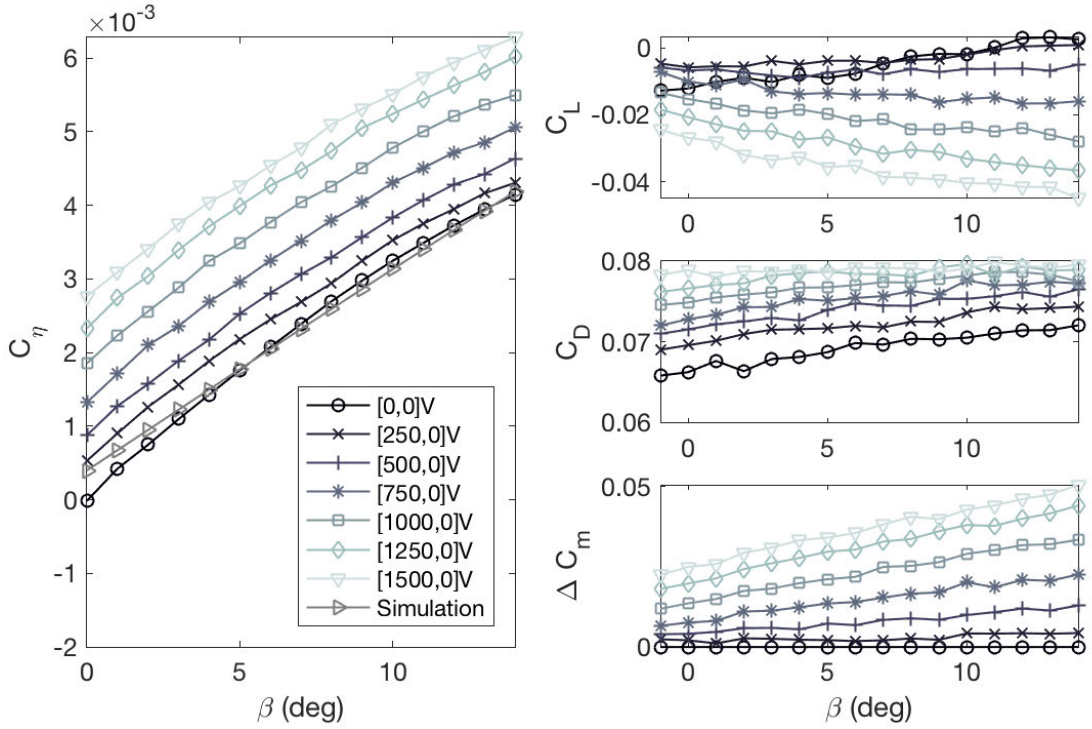

Figure 6.8: Nondimensional coefficients versus sideslip angle for yawing maneuvers (single sided actuation)

flight. Furthermore, the slope of the yaw moment coefficient was constant across all degrees of actuation which indicates that the tail remained just as effective even as actuation increased. Since the slope was approximately linear, the actuator also did not loose effectiveness even as sideslip increased.

The lift, drag, and pitching moment coefficients were also measured to analyze any coupling effects. The magnitude of the lift coefficient was very small compared to what one would expect from a primary lifting surface such as the wings. Although actuating the tail did show a slight decrease in lift coefficient, it was not sufficient to contribute significantly. As expected, the drag increased with actuation since the surface area of the MFC which was perpendicular to the flow will increase with sideslip angle due to its 3D curvature. The drag also showed a minor increase

with sideslip which can again be attributed to an increase in surface area perpendicular to the flow due to the 3D curvature of the control surface. Lastly, the pitching moment exhibited some increase with actuation and sideslip. This is inevitable due to the coupled deformation of the actuator.

6.3.3.2 Yaw Control Effectiveness

To better understand the effectiveness of the actuator, the yaw coefficient versus actuator tip deflection which was derived from the testing described in Section 6.2.2 is shown in Figure 6.9 for various sideslip angles. The control effectiveness in symmetric flight showed a quasi-linear increase with actuator deflection. The yaw coefficient at maximum deflection is very comparable in magnitude to the results presented by Stenfelt *et al.* [79] [81], although the actuator response in those studies was shown to be exponential across multiple sideslip angles which indicates that the actuator is substantially less effective at small to mid range deflections compared to the actuator presented in this study.

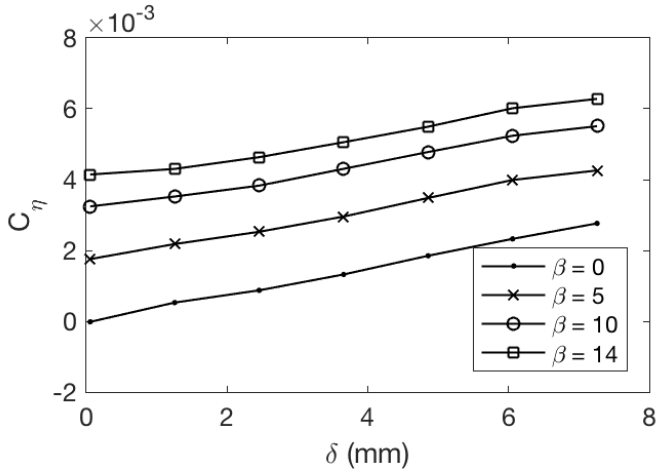

Figure 6.9: Yaw moment coefficient vs. actuator deflection for sideslips ranging from $0°$ to $14°$, demonstrating the effectiveness of the actuator

Further contrary to those studies, the control effectiveness increases with sideslip angle sub-

stantially. This can be attributed to both the tail aspect ratio and the 3D curvature of the actuator. Specifically, as the aircraft experienced sideslip, the moment arm of the actuator increased since it lies aft of the center of gravity. Thus, one can imagine how having a higher aspect ratio tail would further increase the control effectiveness. Furthermore, the control effectiveness of the tail did not degrade with increasing sideslip which is evident by the near constant slope across all sideslip cases. Though not experienced here, a decrease in slope would indicate a decrease in effectiveness with sideslip while data that collocated with the symmetric flight results would indicate a lack of contribution of the actuator's aspect ratio.

6.3.3.3 Yaw Stability

Yaw stability analysis is frequently conducted by prescribing a specified sideslip and sweeping through a series of pitch angles to vary the lift. The experimental setup detailed in Section 6.3.1 was only capable of commanding one degree of freedom as opposed to both yaw and pitch; however, the yaw stability derivative (Equation 6.2) at 0° pitch angle can be inferred from the data presented in Figure 6.9. As noted prior, the slope of the yaw moment coefficient remained practically constant across all sideslips and tip deflection, indicating that the yaw stability derivative for the unactuated and actuated configurations were similar within the range of sideslip angles tested. By taking the derivative, the magnitude of the yaw stability was calculated to be near 0.017 rad^{-1}, larger than other reported stability derivatives for tailless UAVs but consistent with studies on the tail effect of birds [33]. As this value is positive, it demonstrates stability in both the unactuated and actuated configurations at 0° pitch angle. For comparison, it is recommended that typical aircraft exhibit a stability derivative of 0.057 $1/rad$ for sufficient flight dynamics [112].

Additionally, using the RANS model for the unactuated geometry presented prior, the stability

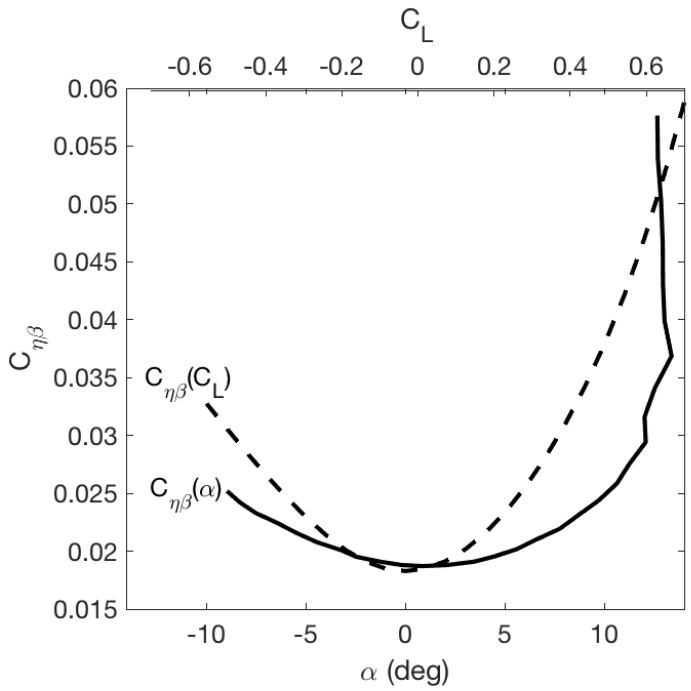

Figure 6.10: Yaw stability versus angle of attack ($C_{\eta\beta}(\alpha)$) and lift coefficient ($C_{\eta\beta}(C_L)$) for unactuated configuration at $\beta = 10°$. Angle of attack is plotted on the lower x axis, and lift coefficient is plotted on the upper x axis

derivate can be modeled numerically for further analysis. A $10°$ sideslip was prescribed while the angle of attack was varied. The data presented in Figure 6.10 show that the unactuated geometry never experienced a negative stability derivative indicating that the aircraft is always stable. Thus, the tail geometry alone acts as a static yaw stabilizer and acts to restore the attitude of the aircraft towards symmetric flight, confirming the findings of other works mentioned prior. Even in dive maneuvers, when the angle of attack is negative, the stability derivative remained positive. The stability derivative with respect to the lift coefficient was also incorporated here for comparison purposes across disciplines [33]. Since it was shown that actuating the tail increases the yaw moment coefficient, it is reasonable to conclude that stability is not lost in the actuated configurations.

6.3.3.4 Pitch Control

The pitching moment is more complex. Typically, the pitching moment of a straight wing is measured about the quarter chord as the wing changes angle of attack. In this work, not only were the wings tapered non-uniformly, but the mounting rod between the aircraft and load cell acts as a moment arm which increases the measured pitching moment readings. The tapered wing was addressed in the prior discussion of reference values used in calculating the nondimensional parameters. However, to address the biased readings due to the mounting rod, some data processing must be incorporated. Since the goal in this analysis was to quantify how much the tail affects the pitching moment, a simple solution was to subtract the measured pitching moment coefficient for the unactuated configuration from the other datasets. This will directly show the contribution to pitching moment due to the actuated control surface. This post-processing was also applied to the pitching moment data discussed above.

Figure 6.11 presents the nondimensional aerodynamic coefficients for the symmetrically actuated tail to control pitch. The data show that the pitching moment increased with tail actuation regardless of the sideslip angle. Furthermore, the slope of the pitch coefficient was relatively small, indicating that the effects of the tail on pitching moment remained relatively constant over the range of sideslips tested. It should be noted that the pitching moment coefficient for these configurations was approximately twice the pitching moment experienced with only one MFC actuated, as in the yaw control experiment conducted prior and shown in Figure 6.8. Again, the lift remained near zero with a slight decrease with actuation. The drag remained relatively constant as well, though it experienced a unique trend.

When the tail was symmetrically actuated, the drag decreased with sideslip. Since the normal

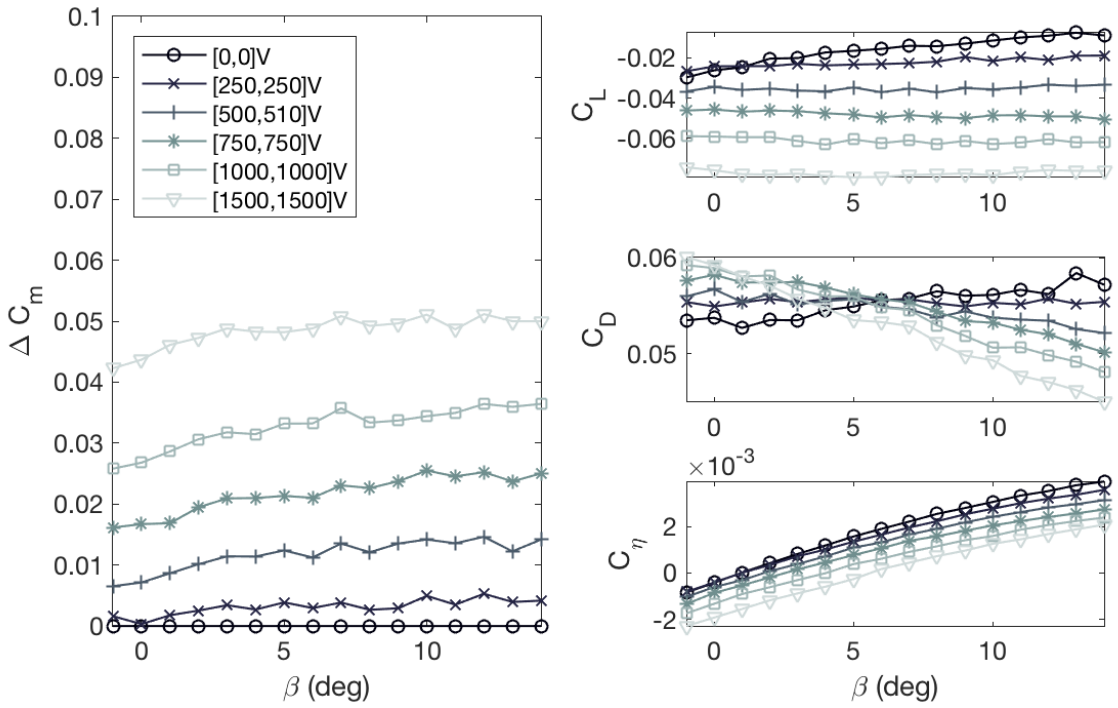

Figure 6.11: Nondimensional coefficients versus sideslip angle for pitching maneuvers (symmetric actuation)

vector of the left MFC turns away from the free stream flow with increasing sideslip, the area of that control surface decreases. Due to the shape of the control surface and the orientation of the PZT fibers in the MFC, the decrease in the effective area of the left control surface exceeds the increase in effective area of the right control surface causing an overall reduction in drag with sideslip for the range of angles tested. Lastly, since the MFCs were actuated symmetrically, the yaw moment at 0° should be equal to zero regardless of the amount of actuation. For these configurations, the yaw moment was slightly negative with increasing actuation. This indicates that perhaps the MFCs were not actuating entirely symmetrically and supports the incorporation of a displacement sensor to guarantee exact displacements for future experiments.

6.3.3.5 Air Brake Control

Finally, the results of the air break analysis are presented in Figure 6.12. Given the limited effect of actuation on drag in the previous experiments, only the unactuated and maximum deflection cases were tested to determine whether using this morphing mechanism as an air break is feasible. Although the split drag maneuver [500 V, -500 V] did experience an increase in drag of approximately 0.012, it did not appear significant compared to the typical increase in drag coefficient with air brakes or drag rudders which well exceeds 0.05. Even if the tail had full voltage range [1500, -1500], the increase in drag coefficient would only be approximately 0.045 assuming that it scales linearly. This indicates that the current configuration would not be adequate as an air brake.

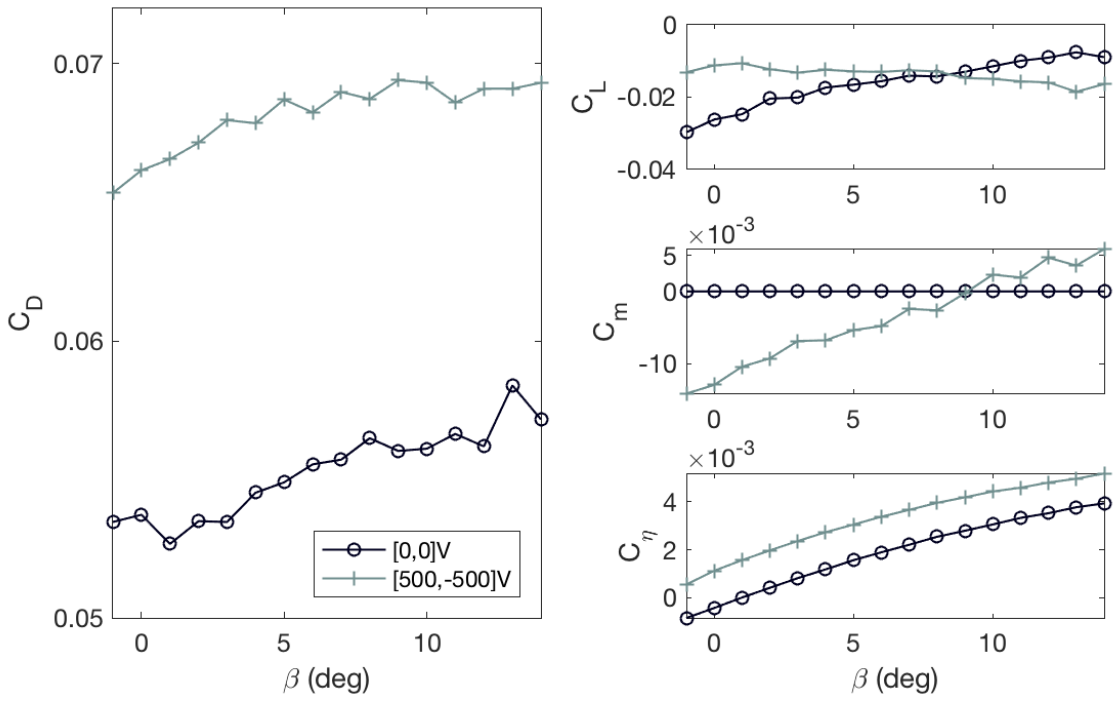

Figure 6.12: Nondimensional coefficients versus sideslip angle for air brake maneuvers (asymmetric actuation)

However, if the control surface area could be increased further when actuated, this might still

be possible. This could be achieved if more of the deformation was in the out of plane direction. One possible solution might be to use a bimorph configuration with a 55° MFC layer and a 0° MFC layer which would allow the control surface shape to be further customizable in flight. To deploy the air break, the 0° layer would be actuated which would generate a 2D cambered shape like the cascading bimorph concept, maximizing the control surface area perpendicular to the free stream flow, though it would have a more dramatic effect on pitching moment. This replicates how birds pitch their tails down during landing maneuvers to rapidly decrease speed. Furthermore, both the 55° and 0° layers could be actuated independently to tailor the in plane and out of plane deformations of the tail during yaw and pitch maneuvers.

6.3.4 Preliminary Conclusions

In these experiments, the deflection of the custom MFC actuator was characterized before conducting wind tunnel tests to determine its aerodynamic capabilities with respect to sideslip. Single sided actuation was conducted to test yaw performance, symmetric actuation was conducted to test pitch performance, and antisymmetric actuation was conducted to test air break performance. The control surface was shown to exhibit greater yaw control effectiveness than current traditional designs, retain effectiveness in sideslip, and maintain yaw stability in both the actuated and unactuated configurations. These results indicate that in the event the static stability characteristics of the tail alone are insufficient in restoring forward flight during sideslip, one side of the tail can deploy to significantly increase the restoring yaw moment. Furthermore, even in forward flight, the tail is capable of generating a yaw moment which can be used as small amplitude corrective input for dynamic stabilization.

Not only was the actuator capable of controlling yaw, but it exhibited good pitch control as well, demonstrating that the actuator is capable of controlling pitch as both dynamic stabilization during forward flight, and large-scale attitude control even in sideslip. While experiments to characterize the air brake qualities of this control surface were conducted, the effect was shown to be insignificant. However, it offers insight into methods of improving this design in future iterations. This could include using a bimorph configuration where the second MFC layer would have a 0° fiber orientation. These MFCs could be actuated independently, allowing for more tailored control over the curvature of the control surface. By actuating the 0° MFCs alone, the curvature would be strictly 2D and would increase the pitching moment coefficient and could also be used in braking maneuvers as birds do while landing. Alternately, for yaw control one of the 55° MFCs could be actuated alone or in unison with the 0° MFC to tune the 3D curvature to suit the sideslip conditions. These preliminary results motivated further investigation into the effectiveness of this control surface on pitch authority.

6.4 Angle of Attack Response

Given that the results presented in Section 6.3 showed great potential for pitch control as was shown by the magnitude of pitching moment with respect to changes in sideslip angle, further testing was needed to characterize the pitch control with respect to angle of attack. This section details wind tunnel testing which was conducted to quantify the control moments and stability derivatives of both the yaw and pitching maneuvers using aerodynamic force and moment data. The control effectiveness of the actuator was also quantified.

6.4.1 Setup Description

Traditionally, wind tunnel testing on rudderless aircraft is conducted with a sting mount, however this was determined unsuitable for the current model due to its interference with the horizontal actuator. Thus, for these tests a single strut mounting L-rod was used. A Parker RT-series turntable, accurate to 2 arc-minutes and repeatable to 12 arc-seconds, was mounted on top of the wind tunnel to command rotation in the horizontal plane. For a ceiling mounted model this rotation is analogous to sideslip angle. However, the aim of this work is geared towards assessing the actuator's effectiveness in pitching maneuvers. Thus, an L-rod transforms the vertical rotation of the turntable into pitching angle of attack. To minimize any effect of the mounting rod on the downstream flow over the actuator, the rod diameter was minimized to 6 mm. This sizing places the start and end of the actuator downstream by 6.4 and 16.7 times the rod chord length respectively. Lastly, the dimensions of the L-rod are 0.063 m long by 0.245 m tall which places the tip of the model 50 mm away from the wall of the wind tunnel, twice the thickness of the body.

As in the experimental setup detailed in Section 6.3, the pressure and temperature within the wind tunnel was recorded with an Omega PX2650 differential pressure transducer and thermocouple respectively. With the exception of the thermocouple which uses its own NI-DAQ, all measurement data was collected on a dSPACE Microlab Box. The dSPACE was also configured to output the voltage signal required to actuate the tail. This signal was sent to an AVID Dual Channel MFC Driver Board amplifier which was used to actuate the MFCs, which operate at high voltage (-500 V to 1500 V). Due to the size of the actuator, no internal sensors were integrated to monitor the tip displacement of the actuator. However, an initial calibration was conducted which correlated the supplied voltage to the unloaded tip displacement of the MFCs. The details of this

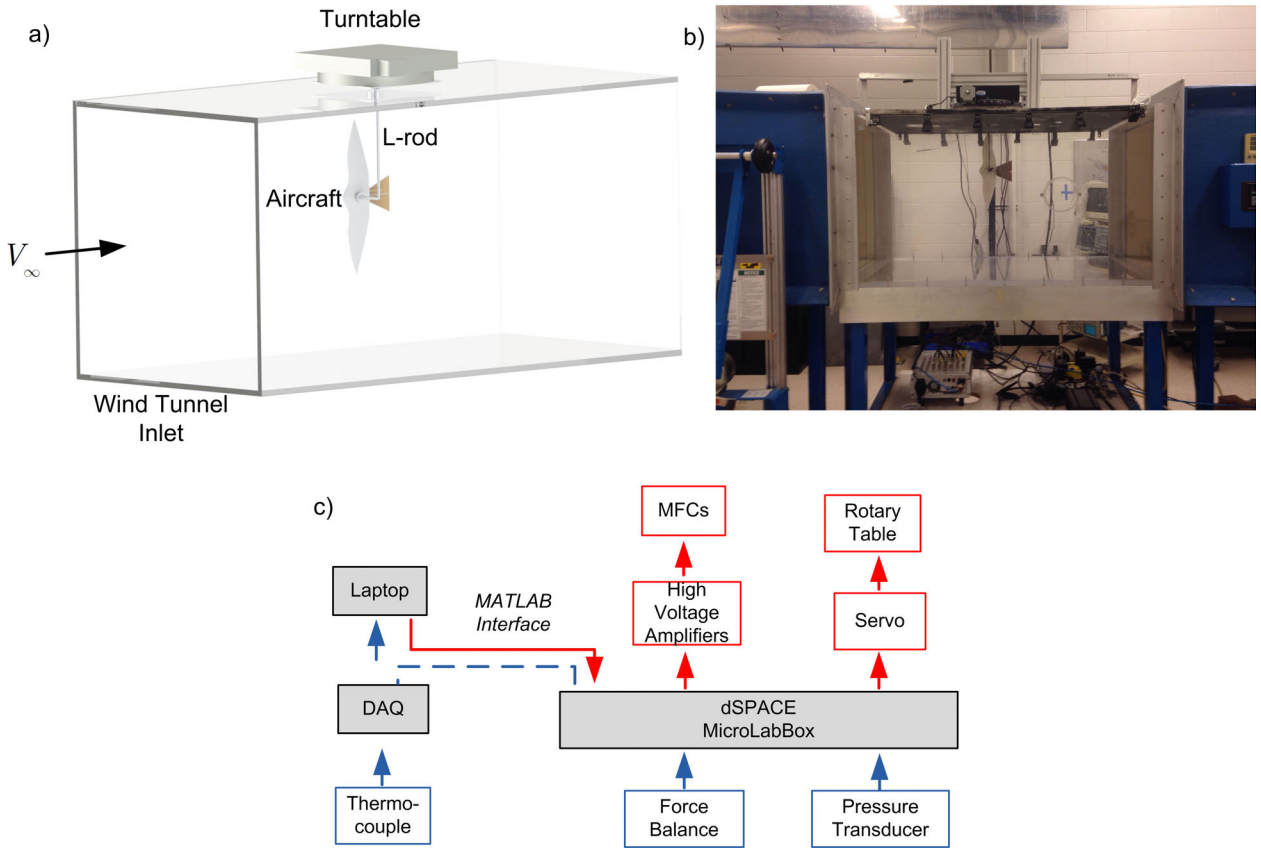

Figure 6.13: a) Graphical representation of the experimental setup b) actual experimental setup from a head-on perspective with inlet on the left c) experimental data flow

calibration can be found in Section 6.2.2.

The aerodynamic forces and moments again were collected with an ATI Nano17 Titanium load cell. While the previous tests for yaw control mounted the load cell directly to the turn table so that it was located outside of the wind tunnel and minimized any unwanted aerodynamic effects on the model, this was not feasible for the current mounting system. The dimensions of the L-rod would cause substantial torques under aerodynamic loading which would have overloaded the load cell. Accordingly, the load cell was relocated to be housed within the model with the resolving center placed at the geometric center of the model body. Here the geometric center is defined as the point

of intersection between the wing tip-to-tip plane, and the plane of spanwise symmetry. A complete summary of the experimental setup can be seen in Figure 6.13.

6.4.2 Test Method

Prior to testing, unloaded force and moment data was collected to account for the weight distribution of the model on the load cell. These loads were accounted for when determining the aerodynamic coefficients. Experiments were conducted at a flow speed of 10 m/s. With the real-time measurements of pressure and temperature, the wind speed was monitored such that it maintained the desired flow speed to within 5% error. Nondimensional force and moment data was collected by time averaging the loads for a range of angles of attack, from -15° to 15° in increments of 2°. These angle sweeps were repeated at a variety of degrees of actuation from 0 V to 1500 V in increments of 250 V, representing the full range of actuation.

A second set of tests was also conducted to quantify the control potential across various Reynolds numbers. The flow speeds chosen were 5 m/s, 7 m/s, 10 m/s, 13 m/s, and 15 m/s representing Reynolds numbers of 2.2e4, 3e4, 4.3e4, 5.6e4, and 6.5e4 respectively. These Reynolds numbers are typical for this scale of bird and UAV. As the control forces are dependent upon the angle of attack, these tests were conducted at angles of -5°, 0°, and 5°. These angles were chosen for two reasons. Primarily, so the increased loads acting upon the load cell were within the tolerable limits of the sensor. Additionally, these angles were deemed to be within typical operation of the aircraft.

6.4.3 Results

This section presents the results of the aerodynamic testing and a discussion of their implications. The goal was to show that this bio-inspired actuator was capable of providing yaw and pitch control with respect to change in angle of attack.

6.4.3.1 Aerodynamic Forces

The results presented in the following section detail the raw nondimensional forces and moments for the configurations tested. They show the lift, drag, pitching moment and yaw moment respectively (C_L, C_D, C_m, C_η) in Figure 6.14, in addition to the resulting change in coefficients due to actuation in Figure 6.15 . It is important to note the magnitude of the change in coefficients relative to their original values when interpreting the data. For each, multiple states of actuation are shown. Figure 6.14 in particular shows the aerodynamic response to symmetric actuation of the tail. The resulting forces detail a few clear trends.

First investigating the pitching moment, the data show a distinct increase in nose-up pitching moment as the degree to which the tail was actuated is increased up to a maximum of 1500 V. This is similar to the response of an elevator on a standard aircraft, which induces a downwards force on a positively deflected actuator and thus results in a nose up pitching moment since the control surface is located aft of the center of gravity. It is important to note that the pitching moment coefficient is heavily influenced by the location of the trunnion or resolving center of the load cell. For these experiments, this location was restricted as the load cell had to lie within the aircraft body. This can be partly attributed to the positive slope of the pitching moment for pre-stall angles of attack.

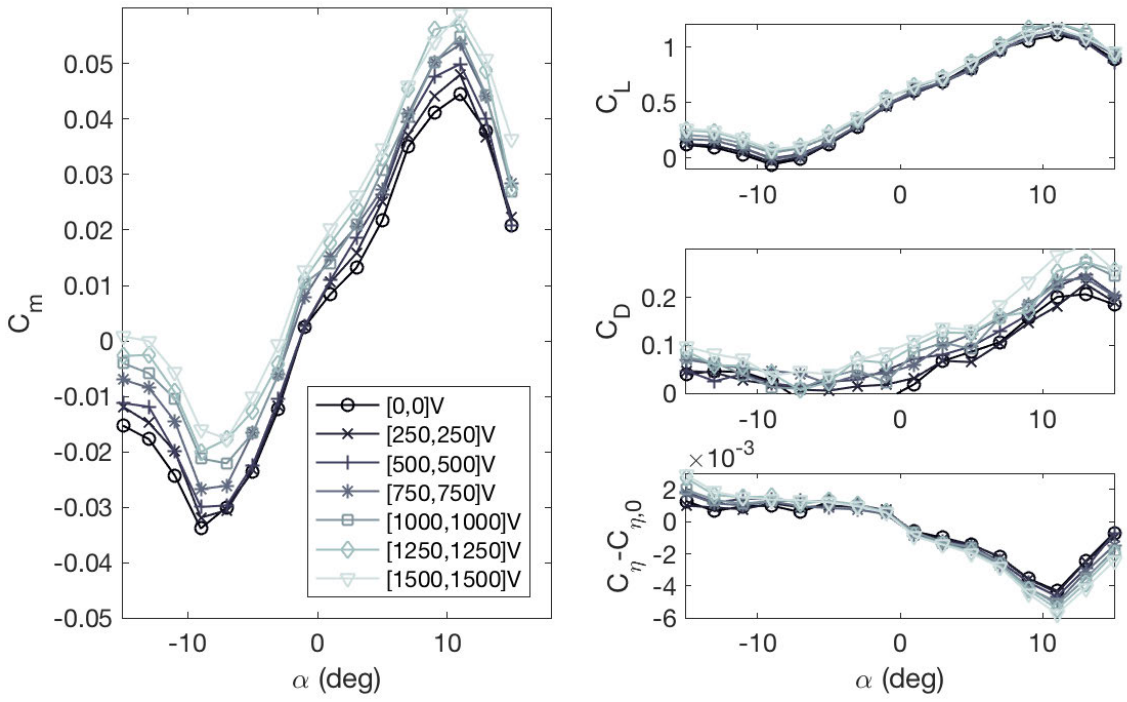

Figure 6.14: Raw nondimensional aerodynamic forces due to actuation for a pitching actuator configuration

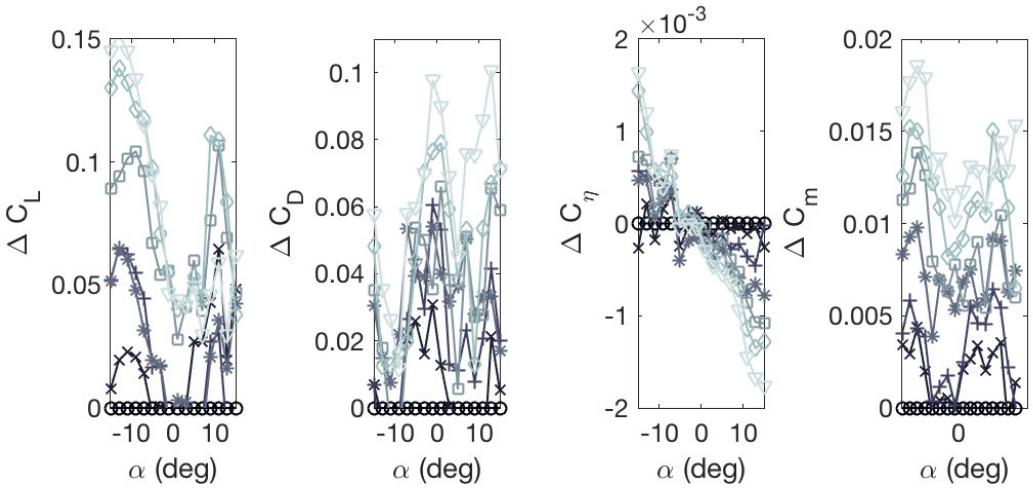

Figure 6.15: Change in aerodynamic forces due to actuation for a pitching actuator configuration

Further analysis of the aerodynamic coefficients reveals that symmetric actuation had little effect on the linear portion of the lift curve or the location of the stall angle. This is desirable, as it means that controlling the aircraft pitch can be achieved independently without effecting the function of the lifting surface. Looking at the drag coefficient, it is evident that actuation effectively increased the profile drag due to the induced camber of the actuator. Lastly, the effect on yaw moment was minor for small angles of attack, but as the angle of attack increased some influence of either asymmetric flow, or actuation was observed. This yaw moment data has been presented as a difference between the actual data and the measured 'neutral' yaw moment for each set of experiments which occurs at no tip deflection and 0° angle of attack. With this, any offsets that may occur between runs are accounted for.

A similar analysis was conducted for the yawing moment maneuver, with the results presented in Figure 6.16 and Figure 6.17. Again, the data show little effect on the overall stall angle, lift coefficient or pitching moment curves, and the drag curves tend to show an increase with actuation. The yaw moment coefficient showed an interesting trend. At high angles of attack, actuating the right MFC effectively reduced the yaw moment from the unactuated design, resembling a yawing rotation to the left, while at largely negative angles of attack this maneuver tended to increase the yaw moment, resembling a yawing rotation to the right. Considering the bending-twisting coupling of the custom MFCs, the increase in yaw with actuation in dive maneuvers can be attributed to the asymmetric increase in profile drag similar to how cambering an airfoil's trailing edge upwards increases drag across negative angles of attack. Conversely, the reduction in yaw moment observed with actuation at large angles suggests that in nose-up maneuvers the upwards camber of the tail acts to asymmetrically unload the aircraft in drag. It is noted that the yaw moment data has some degree of variability, notably due to the minute torques acting on the load cell in response to

actuation. Unlike previous sideslip experiments, the control moment arm (i.e. the length of the tail) is not dependent upon the angle of rotation and thus the change in control moment is expected to be small.

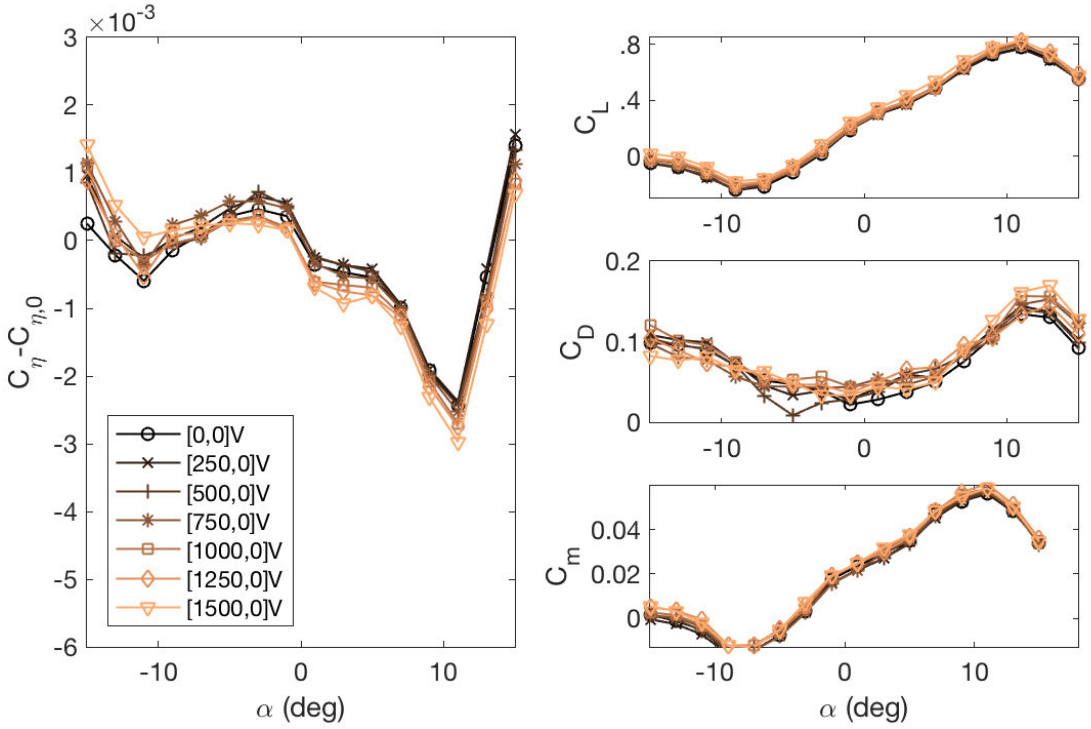

Figure 6.16: Raw nondimensional aerodynamic forces due to actuation for a yaw actuator configuration, where the scale of the latter has been kept consistent with Figure 6.14

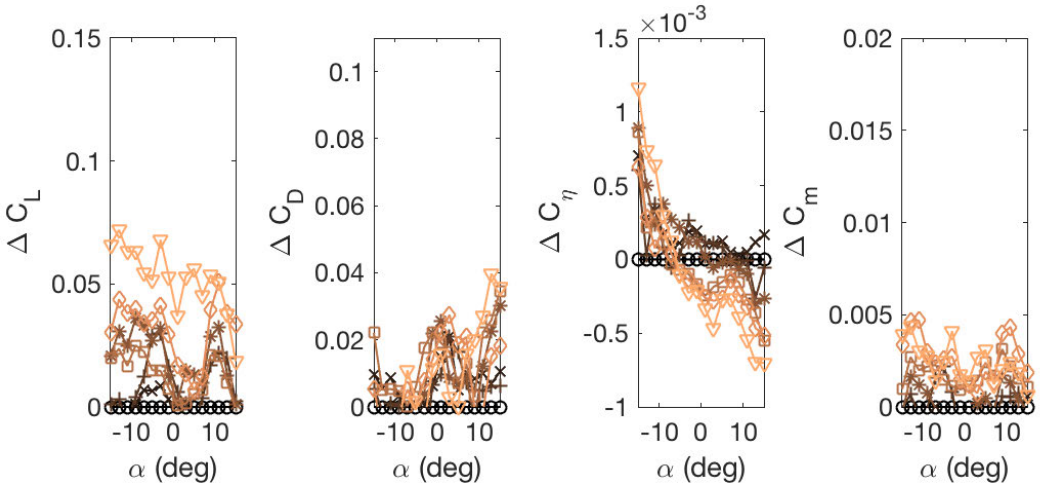

Figure 6.17: Change in aerodynamic forces due to actuation for a yaw actuator configuration, where the scale of the latter has been kept consistent with Figure 6.15

6.4.3.2 Force Validation

The shape of the yaw moment curves shown in Figure 6.16 is also of interest. Primarily, even when unactuated there exists a distinct and somewhat unexpected trend line. One would expect that for a symmetric aircraft, the yaw moment coefficient would be close to if not equal to zero for all angles of attack. But the trend observed in Figure 6.16 demonstrates a quasi-parabolic yet asymmetric yaw response for pre-stall angles. However post-stall, the yaw moment experienced a sharp increase in yaw. This was initially believed to be a consequence of the mounting rig and load-cell configuration. However, further verification of the aerodynamic response with respect to yaw actuation was conducted with RANS simulations. Simulations were conducted with a standard $k - \omega$ turbulence model. Only simulated alpha sweeps of the unactuated and maximum yaw actuated configurations were tested. The location of the resolving center was set to be the same as in experiments, however the mounting mechanism was not incorporated into the geometry, and

thus the ensuing analysis strictly represents the aerodynamics of the aircraft alone and ignores the influence of the mounting rod on the surrounding flow. Going forward, only the trends of that analysis will be highlighted.

Figure 6.18 shows the simulated pitch and yaw moment coefficients respectively. Notably, the simulated yaw moment also showed a similar semi-parabolic trend with peaks near the stall angle. Actuation was also observed to increase yaw moment in dive maneuvers when the deformation of the control surface is facing into the flow. Though the cause of these peaks has not been definitely identified, it is hypothesized that this can be attributed to strong flow separation over the actuator causing an asymmetric increase in pressure drag.

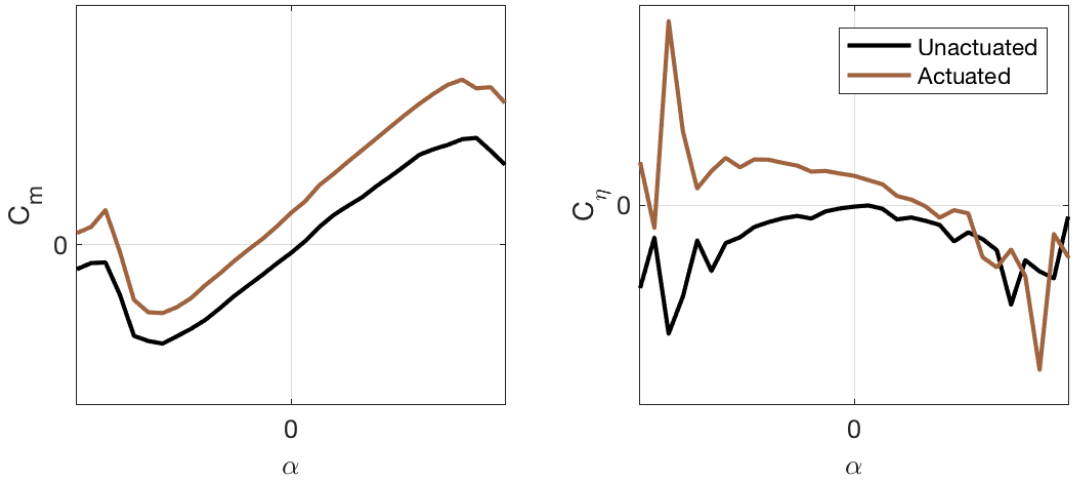

Figure 6.18: Simulated pitch and yaw moments for a yaw actuated configuration at 10 m/s, using a low-Reynolds number $k-\omega$ turbulence model. Simulated model geometry does not account for aeroelastic deformations of the actuator

The simulated pitching moment did indeed show a positive slope in the linear section of the moment curve, in addition to an increase in pitching moment with actuation both of which were observed in the experimental data. The confirmation of a positive slope at pre-stall angles of attack is notable, as a positive slope tends to indicate that the aircraft is unstable. Furthermore, a

symmetric airfoil in theory should experience a near zero pitching moment in unseparated flow. However, recall that while the wings were manufactured with a symmetric airfoil, the aircraft body was not. As is seen in Figure 6.19, the main discrepancy between high and low pressure over the aircraft occurs very close to the leading edge as a result of high pressure on the lower surface and suction on the upper surface. Comparatively, the pressure on the upper and lower surfaces of the tail are relatively similar. This discrepancy would result in an increase in pitching moment with angle of attack, in addition to the boundary layer growth which occurs as the aircraft approaches stall [113]. Lastly, the sharp nose down pitching moment is the result of separation post stall.

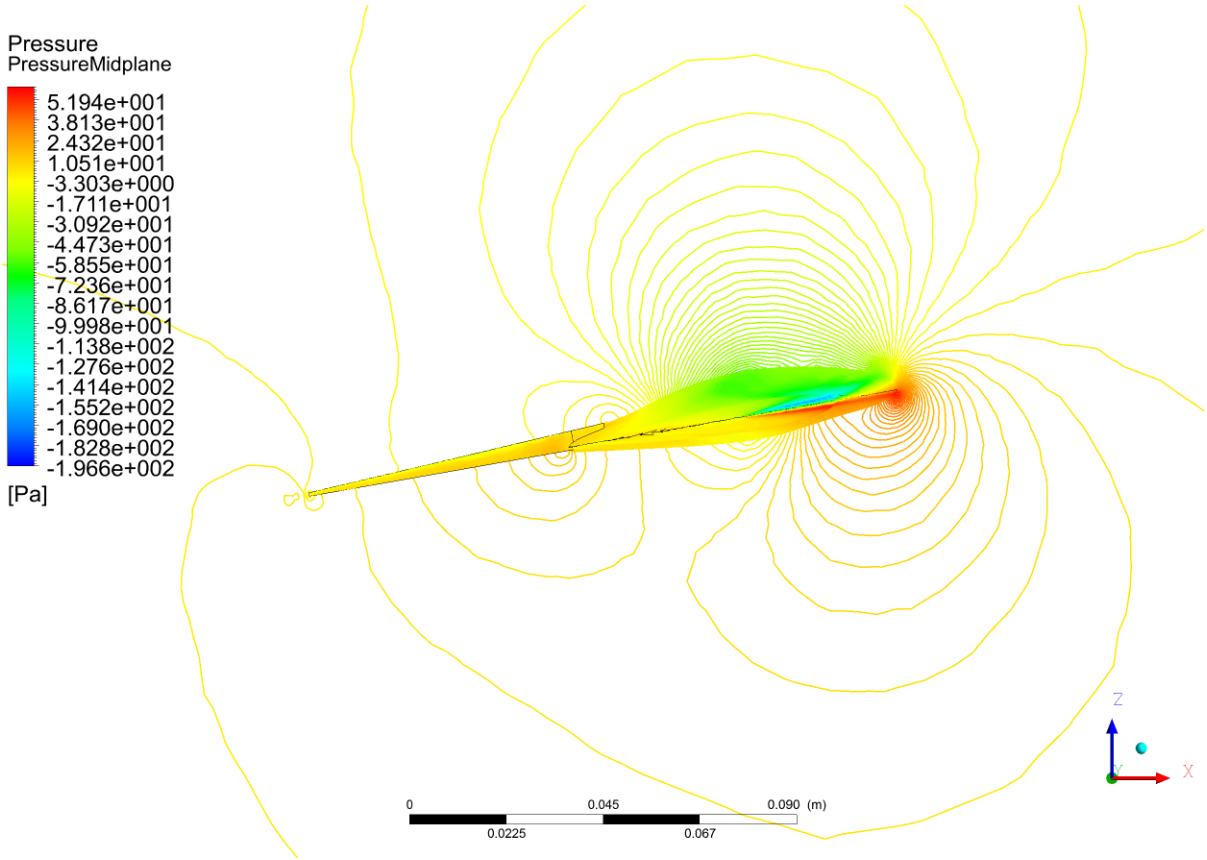

Figure 6.19: Pressure contour at the plane of symmetry for the unactuated model at $\alpha = 10°$

6.4.4 Control Derivatives

Given the nondimensional coefficients determined experimentally prior, the effectiveness of the actuator can also be assessed via calculating the control derivatives. The control derivatives were calculated by dividing the change in nondimensional coefficient from the unactuated configuration, to the degree of actuation. Mathematically this is represented by the following equation which has been written with respect to the pitching moment, but any nondimensional coefficient can be substituted.

$$C_{m\delta} = \frac{\partial C_m}{\partial \delta} = \frac{\partial C_m - \partial C_{m_{\delta=0}}}{\delta} \tag{6.4}$$

This quantity is traditionally calculated for standard elevators by dividing the change in pitch moment by the change in hinge angle of the actuator.

6.4.4.1 Aerodynamic Response

As the deformation of the MFC actuator in the current work is both cambered and three-dimensional, quantifying the tip deflection relative to single angle is fairly arbitrary, and a comparison between standard control derivative quantities and the ones presented in the current work would be relatively meaningless. Accordingly, the following analysis will focus on the change in control moments versus the predicted out of plane tip displacement which, recall, was determined in the absence of aerodynamic loadings. This data is presented below in Figure 6.20.

The control derivatives provide an even more detailed look into how increasing the deflection of the actuator affect the aerodynamic loads. In pitching maneuvers, the pitching moment varies almost linearly relative to the actuator tip deflection. Interestingly, the control performance is at its

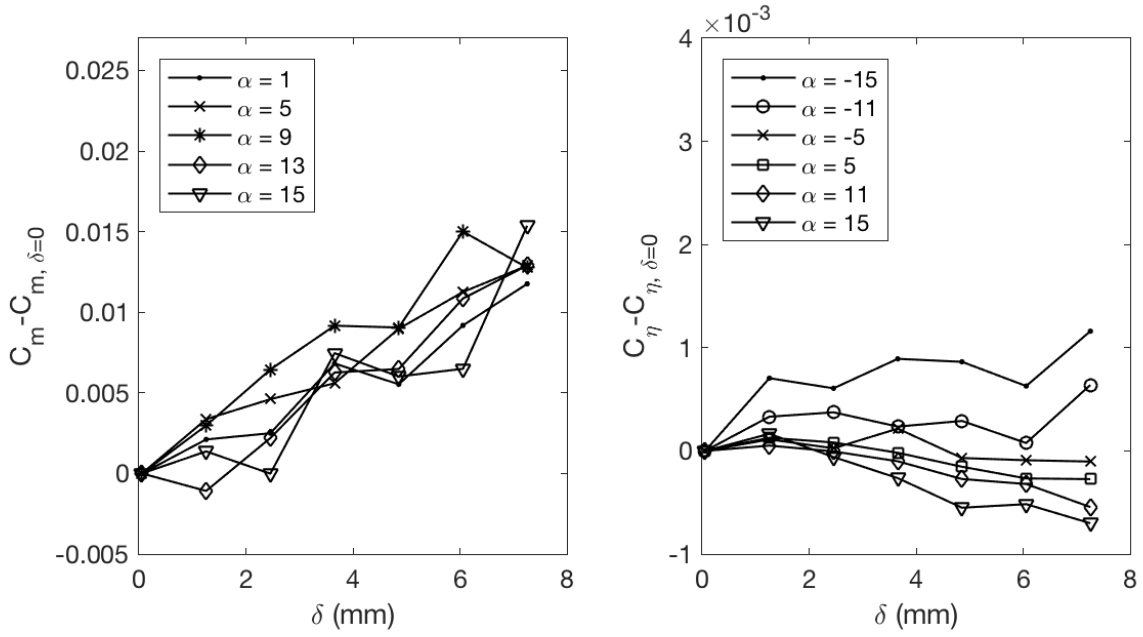

Figure 6.20: Experimentally measured control derivatives for a range of angles of attack for the pitching maneuver (left), and yawing maneuver (right)

maximum just prior to the stall angle, at an angle of attack of $9°$. This is evident as is indicated by the larger change in pitching moment than other angles tested. Only positive angles are presented here, as the data presented in Figure 6.16 showed a very symmetric pitch response. For yaw maneuvers, data for both positive and negative angles of attack are presented, as the response was shown to be highly dependent upon the angle of attack. These results further detail the dependency of yaw actuation on the angle of attack. For a fixed angle, the data show that the response of the actuator is relatively linear; however, the slope of the control responses decreased with increasing angle of attack. This implies that the effectiveness of the actuator is heavily dependent upon the aircraft's inclination.

6.4.5 Reynolds Number Effect

Further tests were conducted which assessed the control effectiveness of the pitching maneuver with respect to Reynolds number. Shown in Figure 6.21, these experiments revealed a few interesting trends. Foremost, the actuator shows greatest pitch effectiveness at negative angles of attack when the curvature of the MFC is facing into the flow, validating the prior results. However, the data also show that the actuator is more effective at low Reynolds numbers. This potentially indicates a loss of effectiveness due to increased aeroelastic deformations with increasing aerodynamic loading from increasing flow speeds. Further investigation indicates that the drag is increased at low Reynolds numbers, due to the dominant viscous forces at low speeds. Lastly, the direction of the lift response is dependent upon the Reynolds number. At low angles, there is little effect on lift. But at angles of $+/-5^{\circ}$, low Reynolds numbers yield decreases in lift with actuation while higher Reynolds numbers increase the lift. This is likely the result of the mounting mechanism which is thought to have affected the pressure distribution on the underside of the aircraft. As the lift is highly dependent upon the difference in pressure between the upper and lower surface, an unequal disturbance like this may reasonably alter the lift, becoming prevalent with changes in Reynolds numbers.

6.4.6 Quantifying Aeroelastic Deformations

While preliminary testing was conducted in Section 6.2.2 to correlate the applied voltage to the integrated actuator's displacement, this did not account for any aerodynamic loadings. The aerodynamic loadings acting upon the tail in sideslip are very small in comparison to the aerodynamic loads in pitch, as a smaller portion of the tail is perpendicular to the flow in the former. For these

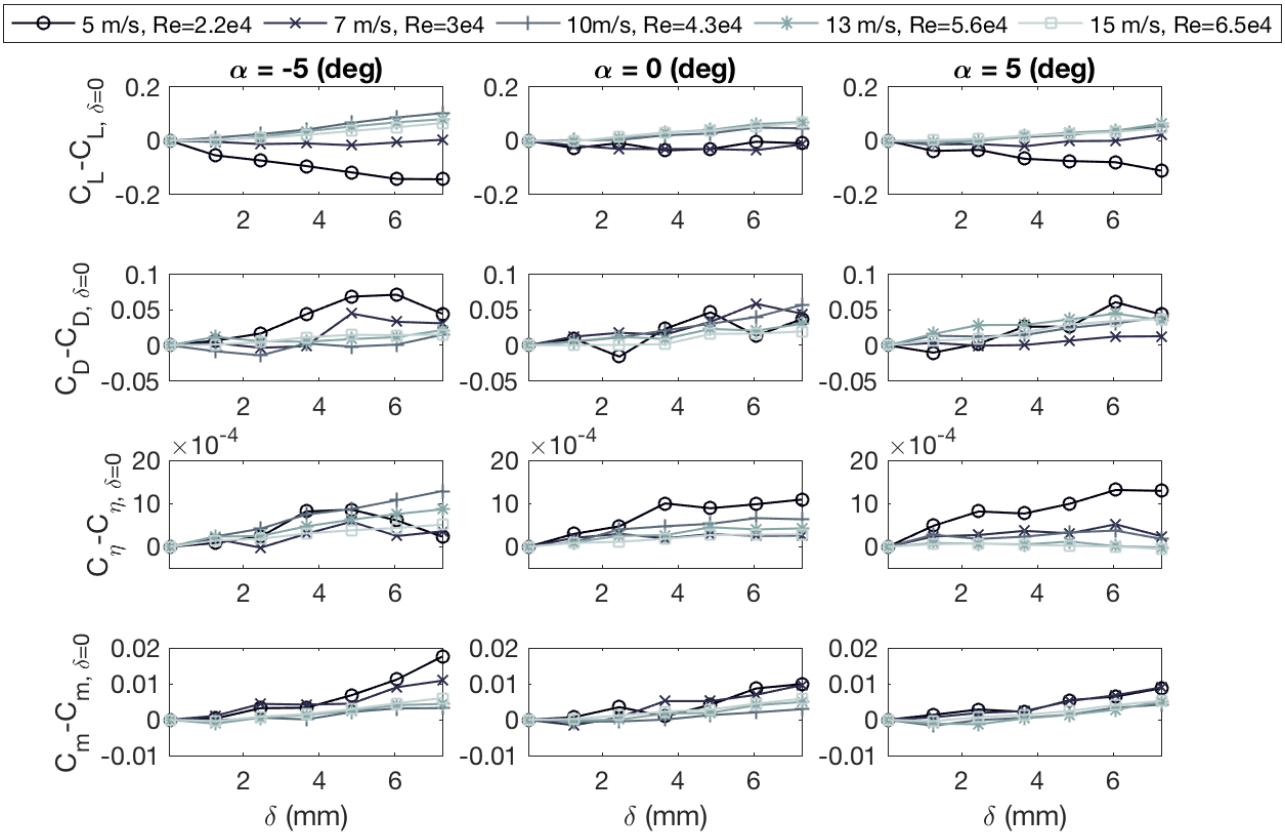

Figure 6.21: Experimentally measured control derivatives for a variety of Reynolds numbers, detailing the control effectiveness with respect to flow speed. Columns indicate the angle of attach at which data was collected

reasons, it was important to quantify the degree of aerodynamic deformation in the presence of aerodynamic forces specifically for pitching maneuvers.

As incorporating internal sensors which measure continuous curvature was previously deemed to be unfeasible for this particular actuator, external sensors were required. A Keyence LJ-V7300 Ultra High Speed In-line Profilometer was used to measure the 2D profiles of the actuator under aerodynamic loading. This sensor is composed of a blue semiconductor laser and utilizes laser triangulation to recreate 2D profiles with up to 5 μm repeatability out-of-plane. The profilometer was mounted statically outside of the test section with the beam directed at the tail through the

tunnel's plexiglass wall. It is important to note that since the laser was oriented perpendicular to the wind tunnel and not the tail itself, the z location does not directly correlate to the simulated out-of-plane tip displacement when the model is at a non-zero angle of attack. An image of this test setup can be seen in Figure 6.22.

As the aerodynamic loading increases with both wind speed and angle of attack, it is reasonable to conclude that any aeroelastic deformations will be most pronounced at the maximum angle of attack and wind speed tested. Accordingly, the aeroelastic deformations were recorded at $\alpha = -15^{\circ}$ for each of the Reynolds numbers assessed in the prior section. For the first test, the profilometer's laser sheet was directed across the width of the actuator to characterize the spanwise out-of-plane deformation. A second test was conducted in order to characterize the chordwise out-of-plane deformation. However, due to the actuator's triangular geometry obtaining a full cross section is not possible. Tradeoffs must be drawn between capturing the deformation near the tip of the actuator, where the majority of the actuated deflection occurs, and capturing the deformation near the root of the actuator, where the actuator may be prone to bending. The location of the chordwise laser placement is shown in Figure 6.22. Lastly, the tail was actuated upwards to its maximum extent for all tests.

The results presented in Figure 6.23 show the 2D spanwise and chordwise profiles of the actuator in various wind speeds. Note that the magnitude of the raw data output from the profilometer for the height and x-location are relative to the profilometer's origin. Post-processing has been conducted here to shift the center of the unactuated control surface to the origin for ease of analysis. This was applied to all spanwise data. Looking at the spanwise data, one trend is initially evident. As the wind speed is increased, the actuator's displacement in the z direction shifts downwards substantially, particularly at the maximum wind loading. While this may initially appear trouble-

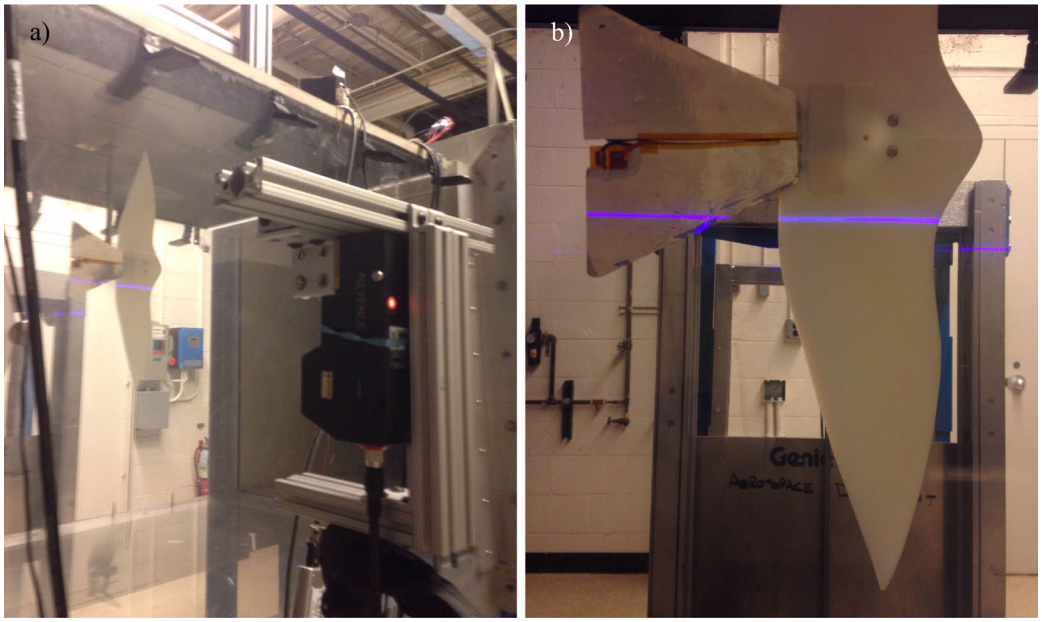

Figure 6.22: a) Experimental setup detailing laser profilometer data collection b) Closeup demonstrating chordwise laser positioning

some, further investigation shows that the spanwise geometry does not actually change shape as the 2D profile remains consistent across all speeds. This indicates that actuator is experiencing little to no spanwise aeroelastic deformations, but may be experiencing chordwise deformations.

Figure 6.23b shows the chordwise deformation. As is shown in Figure 6.22, the laser sheet is directed at both the tail and wings. This results in a break in the data, with the wing accounting for the left portion of data and the tail accounting for the right portion of data. A similar post-processing procedure has been performed in order to center the wing's leading edge at the origin.

Note that while the unactuated profile for the wing section appears to be absent from this dataset, it is indeed present and overlaps entirely with the actuated 0 m/s case, attesting to the repeatability of the profilometer. The data demonstrates a few notable trends. First, although the wing itself is rigid, it is experiencing a downward displacement as the wind speed increases as well. This implies that not only was the displacement noted in the spanwise results not fully

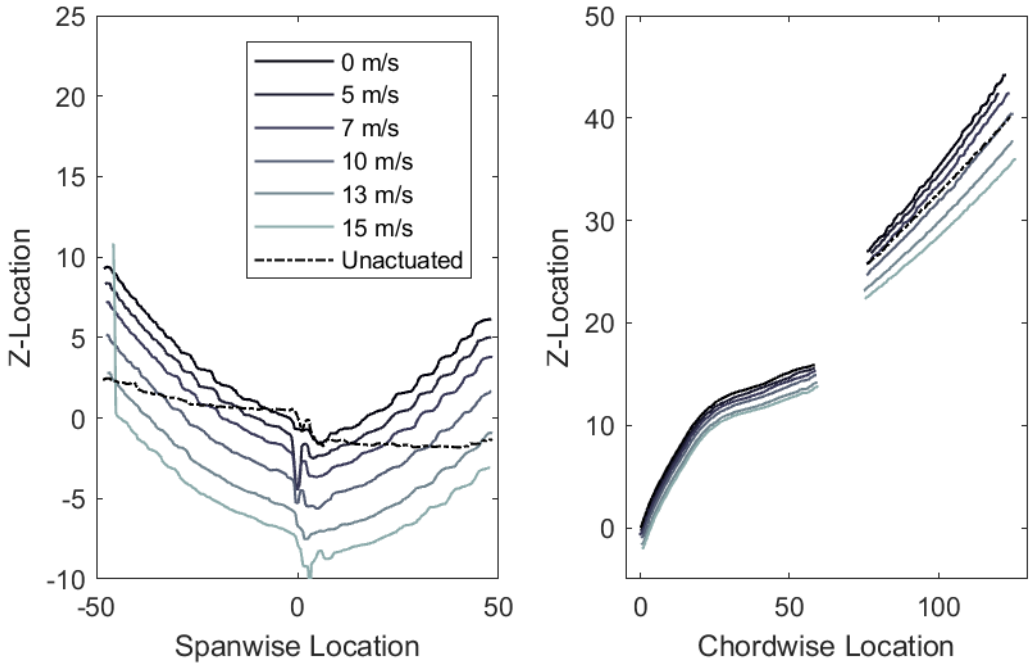

Figure 6.23: Custom actuator's 2D deformation at -15° angle of attack with respect to various wind speeds for a) a spanwise cross section and b) a chordwise cross section

attributed to the actuator's displacement, but also that the increase in loading causes minor bending deformations in the mounting rod. Analyzing the tail's chordwise aeroelastic deformations, the data show that the profile experiences a downwards displacement as the wind speed increases. But again, the overall curvature of the actuator does not appear to be significantly affected. This indicates that the majority of the aeroelastic deformation is in fact occurring at the root of the actuator where the cross sectional area and thus bending rigidity is smallest.

This can be further validated by assessing the aeroelastic response at a $\alpha = 15^{\circ}$ angle of attack, shown in Figure 6.24. This data shows that under increased wind loading, the actuator's spanwise profile translates upwards either due to aeroelastic effects of the tail, or due to the structural compliance of the mounting strut. Investigating the chordwise profile shows similar trends to those noted before. The rigid wing in fact translates upwards under wind loading, confirming

some compliance in the support structure. Interestingly, unlike the results presented in Figure 6.23, the aeroelastic effects on the tail at positive angles of attack appear to be less substantial than they were at negative angles of attack. Specifically, the actuated tail's profile appears to experience mostly upwards translation as opposed to rotation about the root. For positive angles of attack, actuating the tail upwards would unload the actuator in a similar fashion to how an aileron deflecting upwards causes the lift curve to shift downwards. With a reduced loading on the actuator, less aeroelastic deformations would be expected.

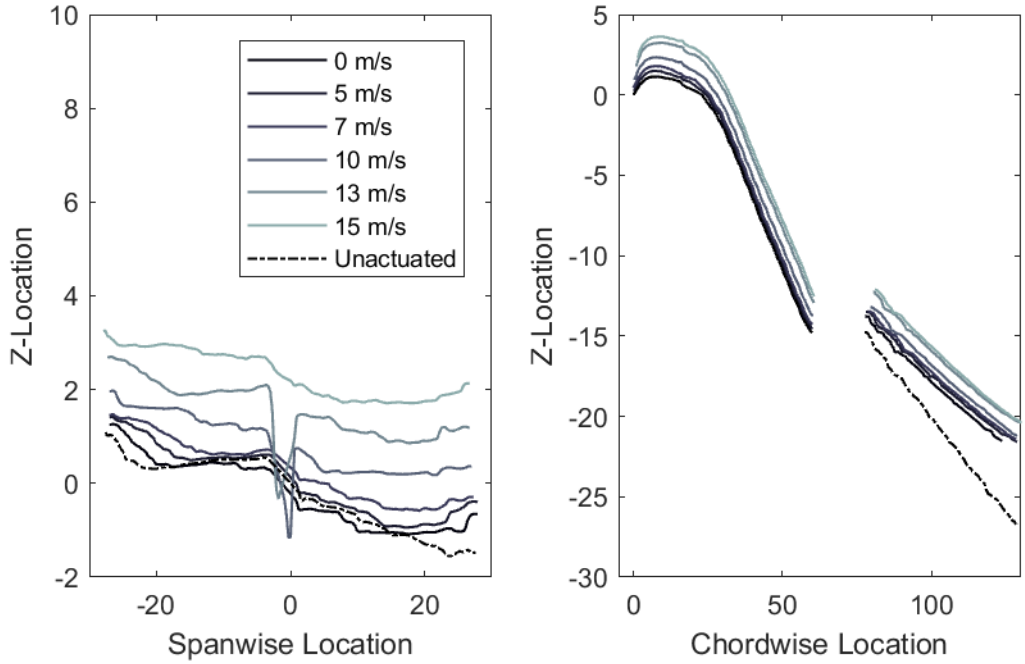

Figure 6.24: Custom actuator's 2D deformation at 15° angle of attack with respect to various wind speeds for a) a spanwise cross section and b) a chordwise cross section

6.4.7 Preliminary Conclusions

The results from the prior chapters, which had designed, modeled and developed the actuation mechanism discussed in the current work, had shown good yaw control performance in tests of

sideslip response. Due to the complex 3D curvature of the tailored MFC actuator, the mechanism was theorized to provide pitch control as well when the actuators were deployed in a symmetric configuration. Here, the effectiveness of the bioinspired actuator with respect to pitch angle was assessed experimentally and briefly validated through RANS simulations. Experiments were conducted with both symmetric and asymmetric actuation to investigate both the pitch and yaw controllability.

The experimentally measured nondimensional aerodynamic forces and moments showed that the actuator, when deployed in a symmetric configuration, was capable of generating substantial pitching moments. While its effectiveness extended over the full range of angles of attack tested, it showed best performance at high angles of attack with up to a 32% increase in control moment. This was shown to be fairly uncoupled from changes in lift particularly in the linear portion of the lift curve. When tested in an asymmetric configuration, the yaw control capabilities of the actuator were observed to reverse in control direction depending on whether the aircraft was in a dive or pitch maneuver. Thus, deployment of either the right or left actuator is dependent upon both the desired yaw direction and the angle of attack. Lastly, the actuator effectiveness in pitch maneuvers was observed to be dependent upon the Reynolds number. Most notably, it was observed to decrease in effectiveness with increasing Reynolds number, thought to be due in part to increased aerodynamic loadings and thus increased aeroelastic deformations.

These results motivate further advances within multifunctional morphing actuators. One such advancement should involve embedded distributed sensor networks to characterize 3D deformed geometries. As aerodynamic loadings may affect the actuated control surface's geometry, monitoring and adjusting the deformation to achieve the desired response is crucial. For the particular mechanism detailed in the current work, one further advancement would be to implement a custom

bimorph configuration with two tailored MFC layers. For example, given a top MFC layer with 0° fiber direction, and a bottom MFC layer with 55° fiber orientation, the two could be actuated either independently or combined to tailor the 3D curved geometry of the actuator specifically for either pitch or yaw maneuvers. This would effectively reduce or eliminate the coupling between yaw and pitch observed, if desired.

6.5 Chapter Summary

In this chapter, the results and analysis from an initial simulation and subsequent experimental investigation of a bioinspired actuator were presented. Initial modeling indicated that the bioinspired aircraft showed both static yaw stability in addition to notable yaw control with the customized actuator. This was further validated with wind tunnel experiments which investigated control effectiveness in sideslip for a variety of combined maneuvers. The results showed that the novel actuator's yaw control effectiveness was on-par with other standard and non-morphing actuators. Similar tests were conducted for a pitching and air brake configuration which showed no potential for air brake control with the current actuator, but great potential for pitch control. Subsequent testing confirmed that yaw and pitch control was maintained with respect to changes in angle of attack. Increases in wind speed did demonstrate a reduction in control effectiveness due to aeroelastic deformations, but at 10 m/s it was still quite effective.

While aeroelastic analysis showed that the actuator experienced deformation, particularly at maximum aerodynamic loadings, it is notable that the measured control derivatives were still plenty adequate. The aeroelastic effects were determined to be mostly due to the reduced cross sectional area and the compliant 3D printed substrate at the root. If greater control is desired, further steps

could be taken in future design iterations to minimize root bending by using the multimaterial properties of the Objet Connex 3D printer to manufacture the honeycomb substrate with a stiffness gradient that concentrates rigidity at the root. In doing so, the control effectiveness of the actuator is expected to improve further. Future work should also concentrate on incorporating additional degrees of freedom to the tail. One such example would be the inclusion of planform morphing which would further improve pitch and yaw controllability.

CHAPTER 7

Conclusion

As a whole, this dissertation discuses the development and analysis of a rudderless aircraft concept. Emphasis was placed upon targeting known challenges in rudderless designs and extending existing morphing aircraft concepts to a wider range of operating conditions.

7.1 Comprehensive Chapter Summary

7.1.1 Chapter 2

A nondimensional derivation was developed which assesses the response of a flier as a function of wind speed and direction. It was formulated such that only a single readily determinable parameter, the nondimensional velocity, is required to characterize the response. In conducting a comprehensive literature review, it was determined that the nondimensional velocity tends to correlate to flight altitude and thus flier scale.

The results of this derivation highlighted the overwhelming aerodynamic adversities that small scale low-altitude fliers face. For static gusts with constant magnitude and direction, low-altitude fliers experienced much larger resultant sideslips than high-altitude fliers. In some scenarios, the gust magnitude can be so large that the resultant sideslip of the low-altitude flier approaches the

initial gust direction. Much more drastic maneuvers and/or more effective control methods, like those feasible with morphing actuators, would be required to restore the flier to it's desired flight course. Further analysis into the sensitivity of sideslip with respect to changes in wind magnitude also showed an interesting phenomenon characterized by substantial peaks in sensitivity for low-altitude fliers, up to five times larger than that of high-altitude fliers. Winds were also shown to have a much larger affect on low-altitude fliers resultant speeds which directly affects the flier's lift force. Restoring lift could be achieved by further inducing camber in the wings, alternately restoring wind speed could be achieved by altering the overall thrust.

A similar derivation considering dynamic gusts, specifically crosswinds, showed that the time constant associated with the dynamic response was dependent upon the weight, velocity and wing area such that low altitude fliers are characterized by small time constants. The dynamic analysis further demonstrated that low-altitude fliers experience much larger changes in acceleration upon experiencing a crosswind. Low-altitude fliers were also shown to experience larger maximum accelerations during the dynamic gust.

7.1.2 Chapter 3

The design for the rudderless aircraft and actuator were detailed in full. The concept for the actuator itself was a novel approach to rudderless yaw control, aiming to explore alternate methods that exceed the boundaries of traditional control methods. This culminated in a unique cross-disciplinary approach with the intention of informing both biological and aerospace knowledge sets. This design was aided through the use of smart material actuators and additive manufacturing which enables tailored structural design and construction. Finally internal sensing mechanisms

for the aircraft were assessed. The performance of the existing wing sensors was improved by increasing the sensitivity over four-fold and reducing the error by 70%.

7.1.3 Chapter 4

An extended nonlinear LLT theory was applied to morphing aircraft. The section based approach of the model allows for tailored wing geometry via the 6 actuators of the SMTE along the wing span. As the model is purely aerodynamic, this was accounted for via the sectional aerodynamic properties. This required a continuous 3D surface of aerodynamic characteristics which related the actuator's displacement and local angle of attack to the nondimensional coefficients. The model showed excellent agreement with experimental results on a rigid wing with symmetric NACA0012 profile.

The validated model was then used to optimize the wing geometry for a post-stall adaptation scenario. The goal was to return to a pre-stall lift condition by tailoring the actuators' deflections and minimizing the drag accordingly. The model was successfully capable of recovering from stall for both a morphing and articulated wing, and the results were validated through wind tunnel experiments. Both wings showed separation reduction if not complete flow reattachment upon prescribing the optimized actuator deflections for each case. However, the morphing wing experienced 20% drag reduction during adaptation, twice the amount compared to the articulated wing.

A complete analysis of potential adaptation scenarios was then conducted for the morphing wing. This analysis showed that the wing was capable of successfully adapting to the vast majority of pre-stall conditions. For low initial lift conditions near stall, the optimizer predicted the

maximum tip deflection, indicating that the constraints of the actuator limited adaptation. However, post-stall, particularly high lift, scenarios were not capable of complete adaptation due to the limitations of the 2D actuated profile.

7.1.4 Chapter 5

A piezoelectric and thermal model were implemented to simulate the deformation of the custom MFC actuator. These models captured the composite nature of the smart material. Both models were shown to accurately predict the blocking force and free strain within 8% and 5% respectively. The thermal model was observed to be more robust for custom geometries and PZT fiber angles. A parameter study of the custom MFC with a range of fiber angles was conducted. A fiber angle of 55° was shown to maximize the transverse and out-of-plane displacements for this particular geometry. The model overall was shown to have good agreement with experimental 3D scans of the deformed actuator, however the curvature was slightly overestimated. Incorporating the inactive area of the MFC could further improve accuracy if desired.

7.1.5 Chapter 6

Preliminary CFD simulations were conducted with the custom actuator to verify that the 3D curvature was capable of controlling yaw. The simulations showed that the unactuated configuration was passively stable in yaw even at large sideslip angles due to the high aspect ratio tail aft of the center of gravity. It was also capable of controlling yaw maneuvers. The simulation provided additional insight, indicating that the passive tail was responsible for the majority of the restoring yaw moment for sideslip angles below 20° while the moment arm of the tail provided the majority

of the restoring moment for larger angles. Upon confirmation of potential control, experiments were conducted.

The custom MFC actuator's capabilities were assessed upon integration into the aircraft with the 3D printed compliant honeycomb. Fully integrated, the custom actuator was capable of achieving approximately 7 mm of displacement. Experimental wind tunnel tests showed that the custom actuator's yaw control effectiveness was equivalent in magnitude to other traditional yaw control methods. Interestingly, it exhibited a much more linear response than other methods. It also showed some pitch control capabilities in sideslip.

Further tests demonstrated excellent pitch control and some yaw control capabilities with respect to angle of attack. The trends of these results were validated with simulations. Further experiments of Reynolds number effects indicated that control was still feasible at higher flow speeds but that the aircraft experienced decrease in effectiveness. This was verified through aeroelastic measurements of the actuator under aerodynamic loadings. The actuator showed some deformation at the root of the tail but the overall spanwise curvature in addition to the majority of the chordwise curvature appeared to be unaffected.

7.2 Primary Dissertation Contributions

The results of this dissertation present 4 primary contributions to the field of morphing aircraft.

- The first analytical derivation was formulated which justifies the need for morphing aircraft based on the impact of wind gusts on flight path and velocity. The results emphasize the need for at least two separate categories of morphing aircraft: aero-adaptive morphing, and mission-adaptive morphing. This is distinguished by the fact that low-altitude fliers are

prone to much more severe changes in flight path and speed. This further strengthens the foundation of most recent morphing aircraft research which has been limited to aircraft at the UAV scale due in part to the challenging load requirements of large scale aircraft wings.

- Tailored wing-based stall recovery was achieved. This represented not only the first study of nonlinear aerodynamic adaptation, but also the first to assess the extent to which morphing wings are capable of adapting. Additionally, this work showed that the spanwise shape of the wing can be optimized to fly more efficiently.

- While MFC actuators have previously been used in many morphing studies, this work represents the first to customize them both in terms of geometry and fiber angle in order to obtain a complex morphed geometry. This opens up many more morphing possibilities than were previously available. Furthermore, this work sets the foundation for modeling these customized active composites.

- This work developed the first rudderless morphing concept which was not an extension of wing morphing. This was accomplished using a multifunctional actuator which was capable of controlling both yaw and pitch separately. Furthermore, the results of this work contributed to exhisting biological knowledge by quantifying the possible control effectiveness of the tail in similar pitch and yaw maneuvers.

7.3 Recommendations for Future Work

Stall recovery was successfully demonstrated; however the design space analysis indicated that recovery could be further extended to more severe aerodynamic by incorporating a second

degree of freedom such as an anterior hinge. One of the challenges in implementing this within the nonlinear LLT model is the sectional aerodynamic properties. For a single degree of freedom the aerodynamic properties were dependent upon only two parameters, the angle of attack and the degree of freedom. From this data, a 3D surface could be generated, but given two degrees of freedom this data would instead be characterized by a 3D volume. Further research would need to be conducted to understand the relationship between the aerodynamic coefficients and a multi-degree of freedom airfoil.

As this work has shown that continuous spanwise morphing wings offer advantages to discrete articulated wings, and that custom MFCs can be fairly accurately modeled to produce customized shapes, a logical progression would be to combine those two advances. For example, as opposed to using 6 standard MFC actuators with 0° fibers to tailor the spanwise wing shape, customized MFC actuators could be manufactured to further streamline the actuated profile. One such design modification could include incorporating a fanned fiber pattern on either side of the 0° fiber section such that the overall deformation would be more sinusoidal. This would also reduce the required area for the compliant section which would theoretically reduce the aeroelastic deformations as well making the wing more structurally sound.

While tail pitch and twist were primarily addressed in the current work, planform morphing is known to be another control mechanism that birds actively use in nature. Incorporating planform morphing into the tail design presented in this work would prove very useful. This would allow for the actuator to be deployable, increasing the active area when needed, but minimizing the profile when not needed. This could not only increase efficiency by reducing drag, but also provide increased control effectiveness. One such method of incorporating planform morphing would be with the use of SMA springs which experience much larger strains than standard SMA wires,

allowing them to achieve greater deformations in smaller package spaces.

Lastly, a key improvement upon the current design would be the incorporation of internal sensors. Though still in development, one such method would be to use flexible distributed sensor networks to gain an overall picture of the structural deformation of the aircraft. This could potentially replace the internal variable resistors within the wings of the aircraft and extend to the tail actuator as well. Ideally, the curvature, out-of-plane displacement, and transverse displacement of the tail would be distinguishable. Furthermore, with the use of internal sensors a controller, such as a PID controller, could be implemented to achieve an accurate prescribed tip displacement. This would ensure repeatability with respect to control, regardless of the aerodynamic loadings.

7.4 Associated Publications

The results of this dissertation have been published in a multitude of both conference papers and peer reviewed journal articles.

The nondimensional derivation developed to characterize the static response of a flier as a function of wind speed and direction and the corresponding results were published in Applied Physics Letters [1].

The extended nonlinear LLT model and accompanying wind tunnel experiments were presented at the 26th International Conference on Adaptive Structures and Technologies Conference [92]. A peer reviewed version of this article which further analyzed the adaptation capabilities of the SMTE to a much wider range of aerodynamic conditions was later published in The American Institute of Aeronautics and Astronautics Journal [42].

The MFC model comparison and custom actuator CFD simulations were presented at the 5th

International Conference of Smart and Multifunctional Materials, Structures and Systems [114]. The experimental validation and aerodynamic testing with respect to sideslip was presented at the 27th International conference on Adaptive Structures and Technologies [115]. A peer reviewed journal article combining these two studies was published in Bioinspiration and Biomimetics [116]. The experimental aerodynamic testing with respect to angle of attack was presented at [117].

APPENDIX A

Coupling Local and Global Morphing

While the bulk of this work focused on aero-adaptive morphing mechanisms, a wide range of benefits may be obtained by combining both aero-adaptive and mission-adaptive morphing technologies. They are typically separated by the magnitude of the motion involved, divided into local morphing [93, 118], and global morphing [37, 119]. This concept has not been readily assessed in primary literature, though some prior studies have investigated the effects of combining span morphing and camber morphing on mission performance [120]. This appendix investigates the coupled effects of sweep and camber morphing on a bioinspired wing through both RANS simulations and wind tunnel experiments.

A.1 Coupled Geometries

For this study, the minimally swept geometry of a bioinspired wing at 5° sweep angle was obtained from prior experiments in swifts [3]. However, it is important to note that increasing wing sweep in birds is also associated with a reduction in wing area and changes in the mean aerodynamic chord. It is well known that both the planform area and chord location substantially effects the aerodynamic performance of a wing. This study was primarily concerned with isolating

the effects of sweep from both so that the resulting aerodynamic analysis can be fully attributed to sweep alone. Accordingly, for each of the other swept wing configurations, the wing's planform area and root chord remained consistent with the original, minimally swept configuration. Hence, wing sweep is the only global scale variable that varies between cases. For this study, the wing root chord was 0.053 m while the planform area was $7.07e10^{-3}m^2$ for all test cases.

As the global morphing variable, three sweep angles were of interest in this study: $5°$, $30°$, and $55°$. The secondary local morphing parameter was chosen to be the airfoil shape. This work was focused on 3 shapes in particular, symmetric NACA0012, cambered, and reflexed. Such shapes have been achieved through camber morphing MFC actuators, and through the addition of a SMA hinge to induce reflex.

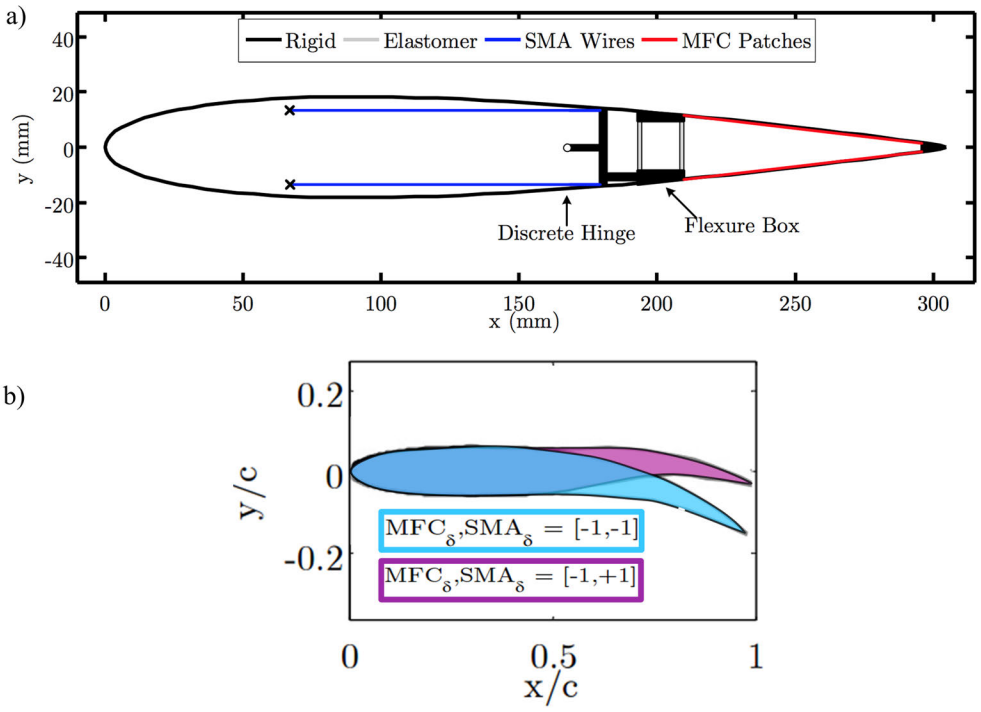

Figure A.1: a) Synergistic smart morphing aileron diagram and b) SSMA monotonic and reflexed airfoils, data from from [90]

In particular, this study focuses in the SSMA concept which combines MFCs and SMAs to

address some of the pitfalls of both mechanism individually such as low work density, slow actuation time, and restricted tip displacements. Together, the MFC component exhibits high bandwidth actuation up to kHz, while the SMA component exhibits high work density, allowing for a morphing airfoil mechanism capable of extended and reflexed camber which can also achieve larger displacements than either concept alone, carry larger loads, and respond quickly. Unlike the MFCs which actuate via electric current, the SMA wires rely on Joule heating and must be pre-strained to repeat the actuation cycle. To ensure a repeatable process, the hinge utilizes two antagonistic SMA wires, thus actuating one wire pre-strains the other and vice versa. A diagram of this specific morphing airfoil concept is shown in Figure A.1a.

The airfoil profiles used were were from experimental results of SSMA concept which allows for a greater range of airfoil geometries. These airfoil profiles are shown in Figure A.1b, and correspond to an undeformed profile, the maximum cambered profile which compounds the tip deflection of the MFC and SMA, and the maximum reflexed profile in which the MFC and SMA are actuated in opposite directions to create a serpentine camber line. Prior studies on the reflexed airfoil shape in particular have shown that at large angles of attack close to stall, it is capable of achieving similar lift with forces with much less drag forces when compared to the standard cambered airfoil [90].

Accordingly, a total of 9 configurations were generated which combines the 3 sweep angles and the 3 airfoil profiles. The complete array of wing shapes tested can be seen in Figure A.2. Note that half span models were used as this work was not focused on asymmetric actuation or geometries.

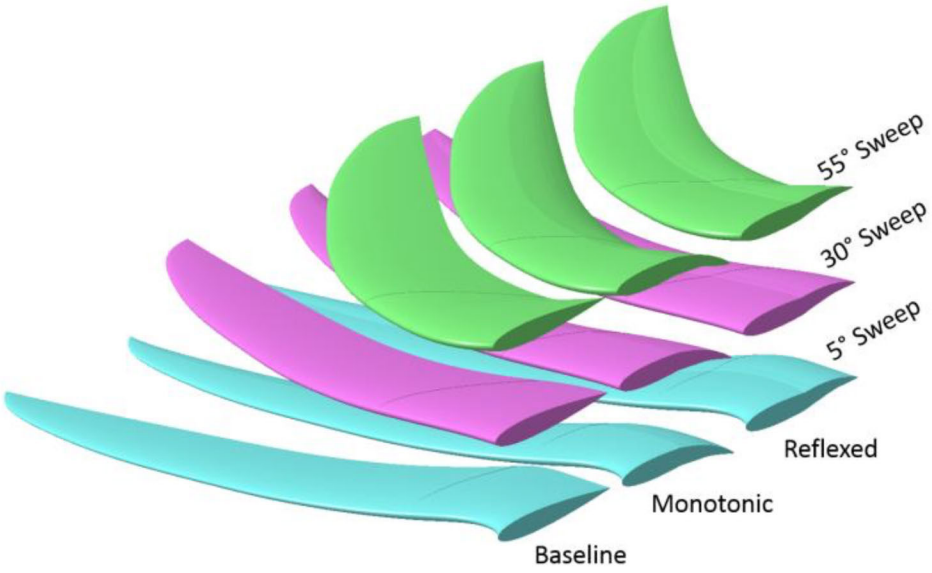

Figure A.2: Nine configurations combining various sweeps and cambers, 3D printed for preliminary wind tunnel testing

A.2 RANS Simulations

ANSYS Fluent was used to simulate the aerodynamic forces and moments on the multi-scale morphing wings numerically. Due to the complex nature of the geometries, this was conducted using three-dimensional time-steady simulations via a coupled pressure-based solver. As both small UAVs and natural fliers operate at low altitudes and thus low Reynolds numbers, a suitable viscous model was required. A standard $k - \omega$ turbulence model was used which is typical in low Re applications, particularly when dealing with large curvatures and flow separation. Lastly, an unstructured mesh with tetrahedral elements was used which was locally refined around high curvatures or edges such as the wing tip and trailing edge. Examples of the mesh can be seen in Figure A.3.

Simulations were conducted on the 9 configurations at a free stream velocity of 10 m/s for a range of angles of attack between $-25°$ to $25°$ in increments of $1°$. The two primary metrics of

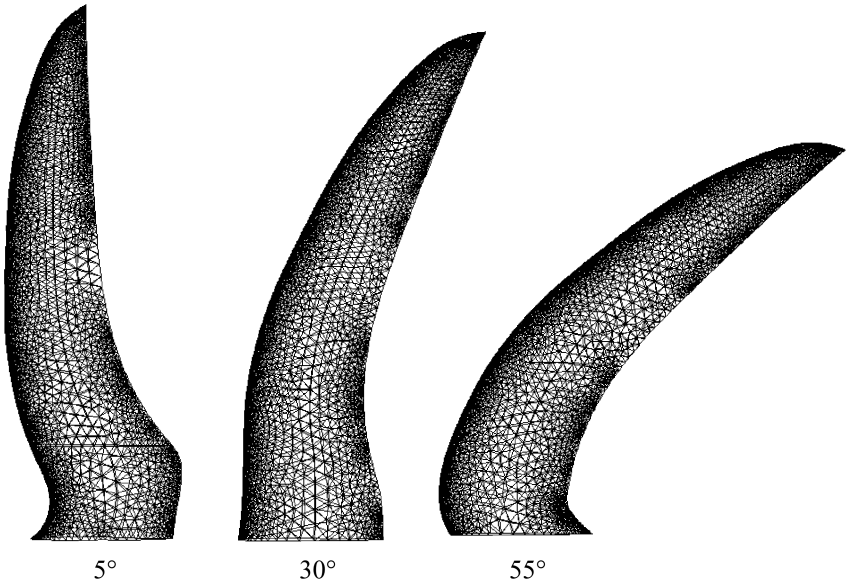

Figure A.3: Example mesh for swept configurations

interest were the lift and drag coefficients which can also identify each wing's efficiency. Identifying where each wing configuration is most efficient will provide a global understanding of how a multi-scale morphing wing could be beneficial across a range of flight scenarios.

Figures A.4 through A.6 depict the results of the simulations. As validation, a brief analysis was conducted between the experimental results presented in [3] and the simulated results presented here for the 5° sweep angle and NACA 0012 airfoil profile. It's important to note that the experimental profile of the wing was not quantified, thus this comparison serves as an estimate and not a reproduction. Comparing the two, there was a %9 difference is lift and a %13 difference in drag at an angle of attack of 6°, solidly within the pre-stall regime. In addition to the discrepancies in the airfoil profile, the simulations presented here do not consider aeroelastic effects which were observed during experiments [3]

The lift coefficient vs. angle of attack is shown in Figure A.4. These results demonstrate a few noteworthy trends. First, the changes in camber appear to show the most drastic effects. This

effectively widens the operating conditions of the aerodynamic performance envelope and at most doubling the maximum lift from the baseline configuration. Furthermore, while the reflexed airfoil does not experience a drastic increase in lift at small angles of attack, the post-stall behavior shows a very strong increase in lift, even matching the lift of the cambered airfoil. This behavior was observed to occur regardless of sweep angle. Assessing the effects of the sweep angle, the data shows that there is little difference in lift between the 5° and 30° sweep cases in the linear region of the lift curve. However for all airfoil geometries, the 30° geometry delays the onset of stall and is able to maintain a high lift condition for longer. This effect is strongest in the monotonic cambered airfoil. Conversely, the wing with 55° sweep angle tend to experience a reduction in lift; but post-stall, the lift matches and in some instances exceeds that of the other cases.

The drag coefficient, shown in Figure A.5 can also provide insight into the effects of combining both sweep and camber. The largest effect in drag is due to the effects of monotonic actuation which shifts the drag curve to the left. Effectively, this increases the drag at positive angles of attack and decreases it at negative angles of attack. Upon initial observation it appears that highly swept wings appear severely disadvantaged as seen by the low glide ratio and the restricted drag polar range across all airfoil configurations. But a deeper analysis shows that at sweep angles of 55°, the wing experiences a decrease in drag as indicated by a downwards shift in the drag curve at positive angles of attack. Specifically, the highly swept wing experiences an 18% reduction in drag at 0° angle of attack. Both the monotonic and reflexed airfoils demonstrate similar trends. This shows that even in the absence of reductions in planform area, bioinspired swept wings still decrease the drag substantially.

Lastly the drag polar and glide ratio as a function of angle of attack, are shown in Figure A.6. Note that a high-lift low-drag configuration is ideal from an efficiency standpoint. These results

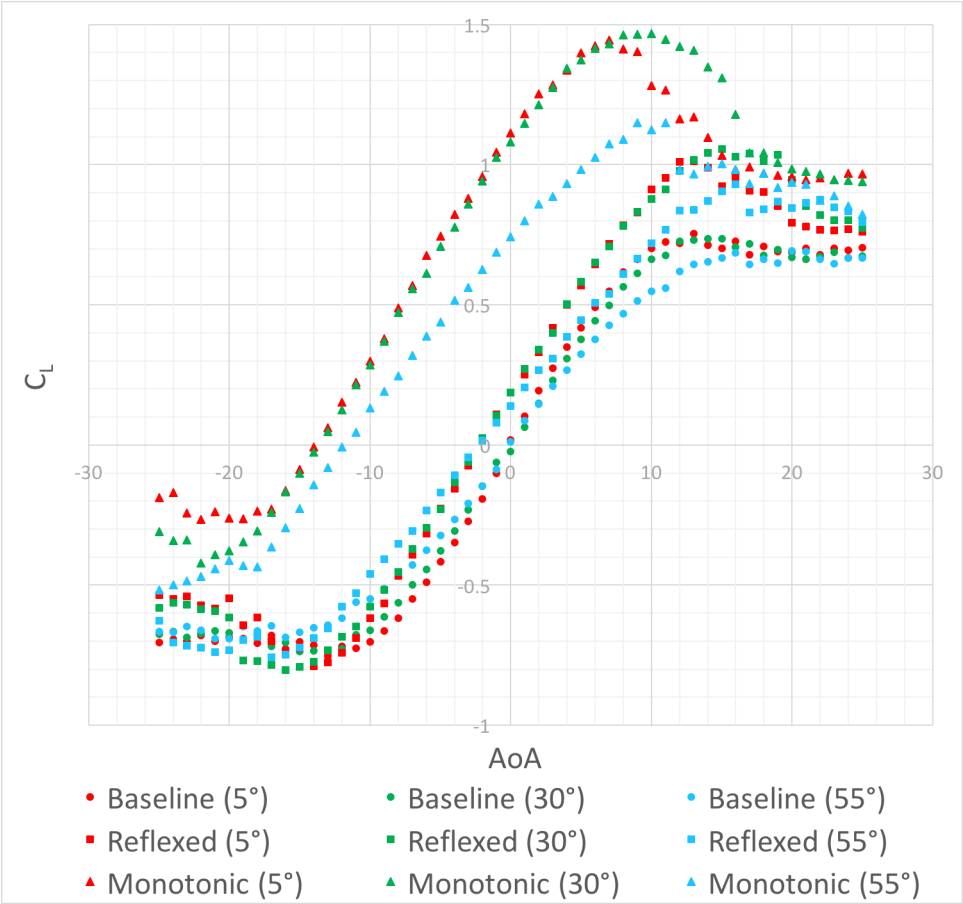

Figure A.4: Variations in simulated lift coefficient as a function of angle of attack for the nine combinations of sweep and camber

really highlight the diversity in aerodynamic performance that is achievable across angles of attack. This data indicates that for the majority of operating conditions, the cambered airfoil exhibits the greatest lift at the lowest drag penalty. However, these results also highlight a stark performance gain with reflex camber. At near and post-stall angles of attack, the reflexed airfoil shows a sharp increase in glide ratio from both the baseline and monotonic profiles. This is attributed to its ability to maintain similar lift coefficients at a much lower drag coefficient due to the cambered tailing edge but profile reduction due to reflex actuation. This is particularly interesting since aerodynamic forces increase with increasing the AoA, which is expected to passively induce reflex in the trailing

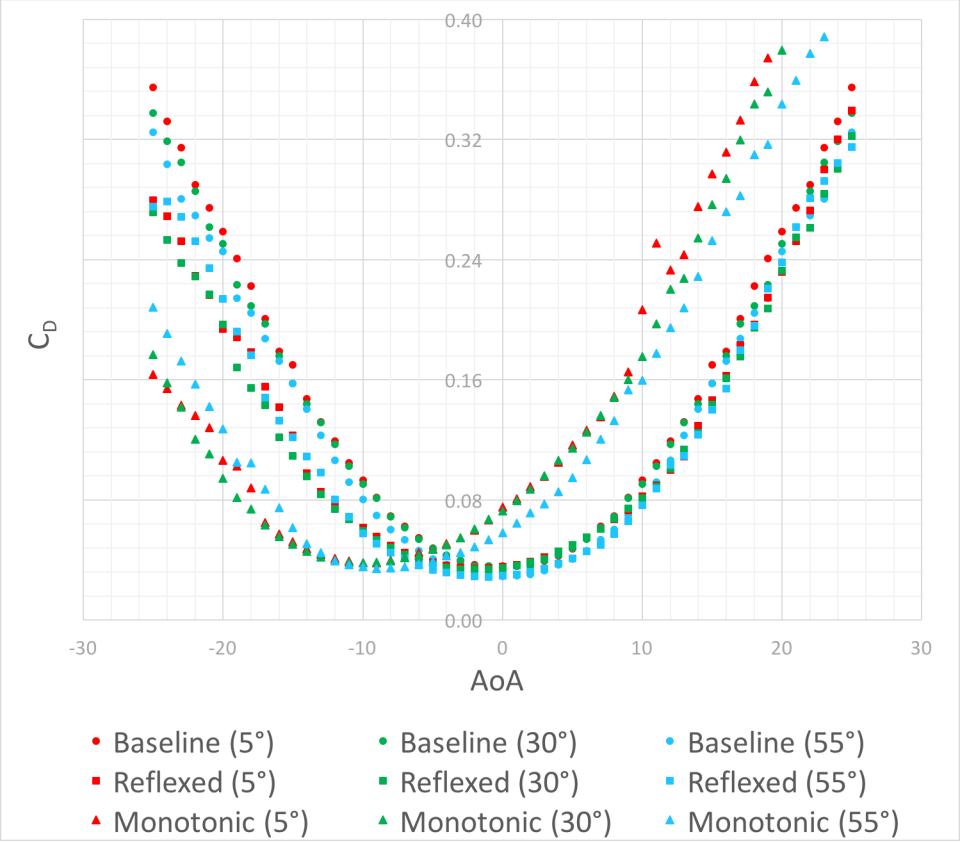

Figure A.5: Variations in simulated drag coefficient as a function of angle of attack for the nine combinations of sweep and camber

edge feathers of birds, indicating that bird wings may inherently take on a low-drag configuration. Lastly, in the fully separated region, high sweep angles appear to slightly outperform low and moderately swept wings.

A.3 Wind Tunnel Experiments

As this work focuses not on the morphing mechanism, but on the aerodynamic effects of coupled camber and sweep, an active morphing model for the wind tunnel was not required. Thus, the 9 geometries were 3D printed at the University of Michigan with the Projet 3500 HD MAX printer

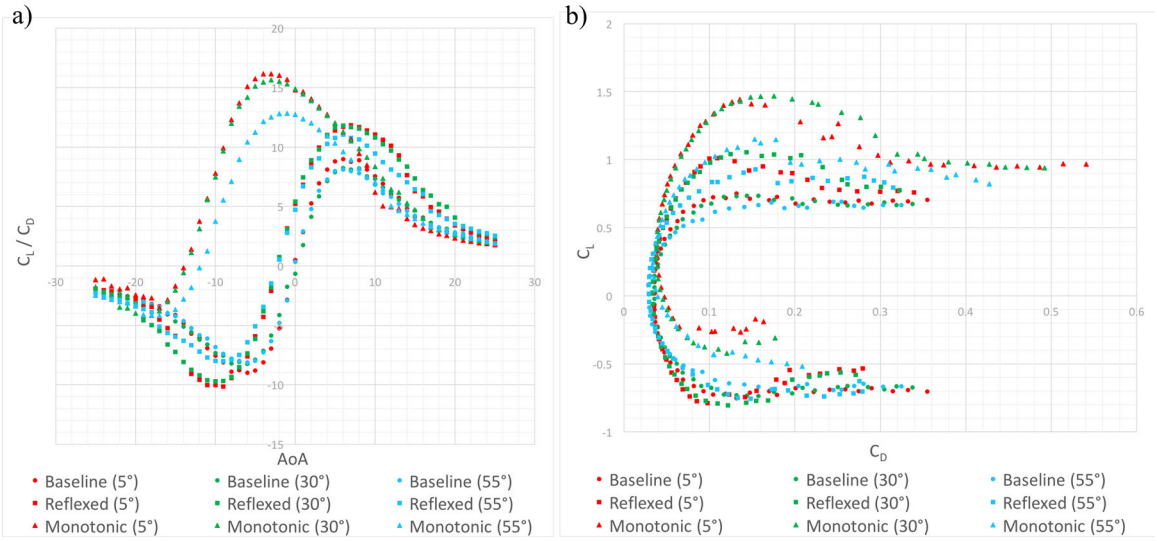

Figure A.6: a) Variations in simulated glide ratio and b) drag polar as a function of angle of attack for the nine combinations of sweep and camber

using VisiJet M3-X high strength acrylic resin. With its high resolution printing capabilities (up to 16 microns), the complex curvatures of the wing geometries were capable of being captured smoothly. It is important to note that this printer uses a wax-based support material which requires removal through a warm oil bath. Some minor warping, specifically in wing dihedral and twist, was observed after removal.

Wind tunnel experiments were conducted in a 2 ft. x 2 ft. open loop wind tunnel at the University of Michigan, shown in Figure A.7. The 3D printed models were mounted vertically at the root's quarter chord, 50 mm away from the tunnel wall outside of the boundary layer to ensure uniform flow around the wing. The mount was attached to a force balance and turntable which was used to vary the wing's angle of attack. Static aerodynamic tests were conducted at 10 m/s over a range of angles of attack. The aerodynamic forces and moments were collected using a NI-9205 DAQ at a sampling rate of 1 kHz and time averaged over 400 samples.

The results of the wind tunnel tests are shown in Figure A.8 and A.9. Thought the data is not

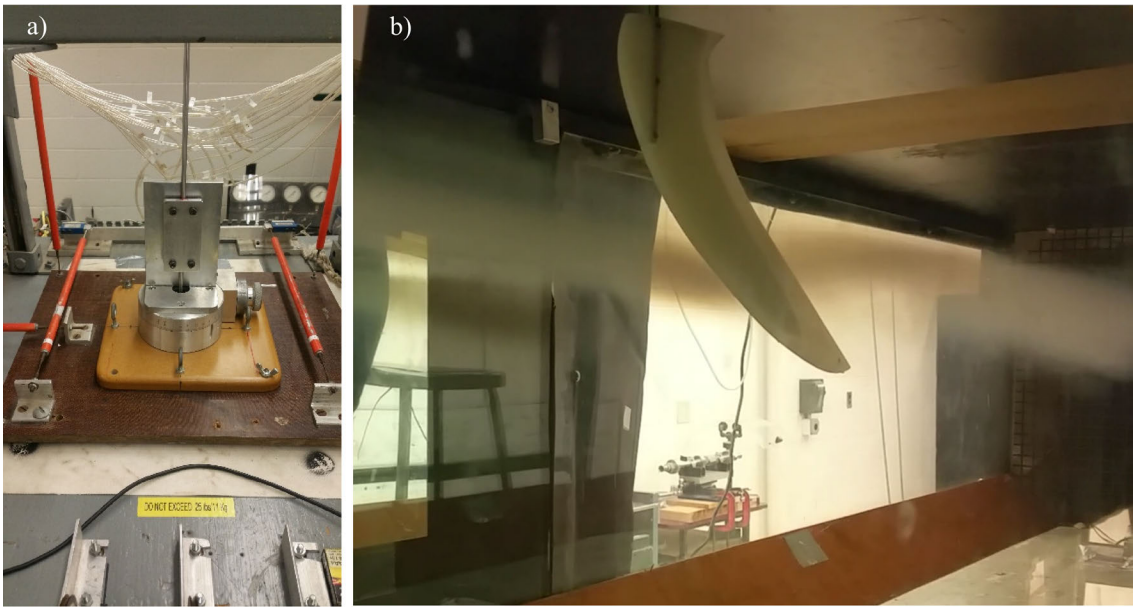

Figure A.7: a) Force balance setup with the load cells and the turn table and b) in-tunnel testing of the monotonic 55° swept wing with flow visualization demonstrating flow separation

as clean as the results of the simulations presented prior, the general results match fairly well and demonstrate the same trends. However, there are a few noteworthy discrepancies which will be discussed. The simulations slightly over-estimated the lift for all sweep angles of the monotonic airfoil. But interestingly, the difference in maximum lift and delay in stall between the 5° and 30° sweep cases was much larger in the experiments. This could imply that the performance benefits of a 30° swept wing exceeds the predicted performance. Furthermore the 55° swept wing shows much better post-stall performance, almost exceeding that of the 30° swept wing. Lastly, the post-stall behavior in all of the simulations predicted a much deeper stall than was observed during experiments.

Investigating the experimental drag coefficients, the data shows that the simulations under-estimated the drag particularly in the highly swept monotonic and reflexed airfoils. This could be attributed, in part, due to the warping of the wings which occurred during the removal of the support

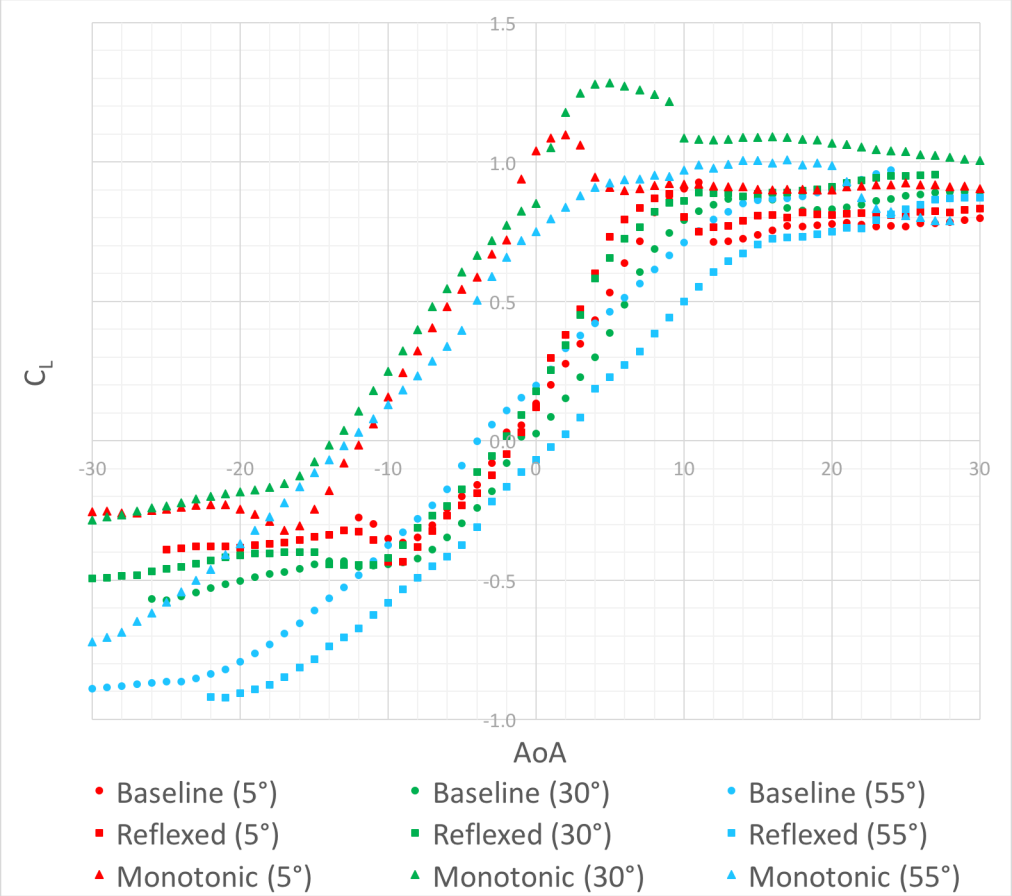

Figure A.8: Variations in experimental lift coefficient as a function of angle of attack for the nine combinations of sweep and camber

material. While the overall magnitude of the drag coefficient is on-par with the simulations, the consistency between runs is limited. As the magnitude of the drag force is typically much smaller than the lift, this indicates that the load cells in the force balance might not have been as repeatable for this scale of measurement. This would also explain the near-zero drag readings at small angles of attack in some instances.

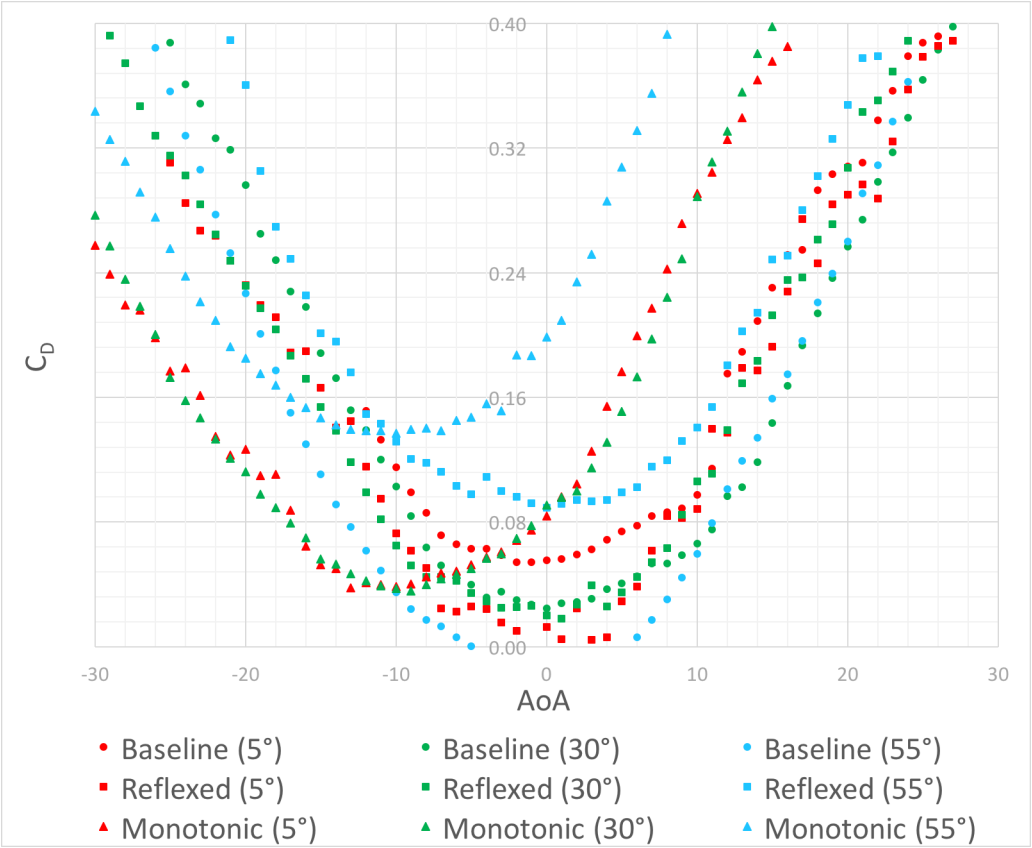

Figure A.9: Variations in experimental drag coefficient as a function of angle of attack for the nine combinations of sweep and camber

A.4 Reynolds Number Effects

As swept wing configurations are typically desirable at higher Reynolds numbers, the simulations were extended to greater wind speeds. Specifically, these models were re-run for 10 m/s, 15 m/s, and 20 m/s.

Figure A.10 shows the raw data from the simulations in terms of the lift and drag coefficients, grouped by wind speed. From this a few trends are evident. The monotonic airfoil has a high lift performance across all angles of attack regardless of wind speed and sweep, in addition to a higher drag coefficient. However, the highly swept wing exhibits a substantial loss in lift when compared to the other two sweep angles. This is in part due to a reduction in the lift-curve slope which is

a trend seen in low aspect ratio wings. Careful observation reveals that this trend is also present in the other two airfoil configurations. Hence, the wing sweep effectively reduces the wing aspect ratio. This can be further validated using the general equation for aspect ratio which is given as

$$AR = b^2/s \tag{A.1}$$

For a wing of fixed length, the wing span decreases with increasing sweep. Thus from Equation A.1 it is clear that the aspect ratio effectively decreases with increasing sweep. Furthermore, though not as prominent as the effects of airfoil shape, the drag coefficient decreases with increasing wing sweep for positive angles of attack and the lift increases with wind speed across all configurations. These trends were anticipated, as was mentioned in the introduction. However, further analysis is required to fully detail when each of these configurations may be useful. This is particularly evident given the minor differences in drag across wind speeds and the crossover in the lift between the cases at large angles of attack.

Figure A.11 illustrates the glide ratio as a function of the angle of attack for all nine configurations grouped together based on velocity. As expected, the glide ratio increases with wind speed across all configurations. Specifically, the glide ratio increases with speed by 11%, 19%, and 33% for baseline, monotonic, reflexed airfoils respectively. This trend is particularly prominent in the reflexed wings. The reflexed wings also outperform both the monotonic and baseline wings at high angles of attack near and post-stall. This can be attributed to the airfoil's ability to generate lift with relatively low drag consequences. This region of interest widens substantially as the wind speed increases, as is shown by the outlined areas of the curve. Lastly, while most configurations demonstrate that swept wings tend to reduce the glide ratio, the reflexed wings experience a crossover

phenomenon which indicates that the coupling effect of sweep and reflex camber are not directly dependent upon the wind speed. This region is marked on each plot by an asterisk. It shows that at 10 m/s, the 30° and 55° sweep reflexed wings perform fairly equally. But as the wind speed increases to both 15 m/s and 20 m/s, the 30° sweep wing shows a substantial increase in glide ratio compared to the 55° wing. While it was shown that the highly swept wing does exhibit a smaller drag coefficient, its substantial reduction in lift coefficient proves to be its downfall with respect to the glide ratio. However, the dependence of these aerodynamic parameters on the angle of attack is not always useful.

Another way of viewing this data is through the drag polar which eliminates any dependence upon the angle of attack. These plots are fairly consistent across wind speeds and any trends present have already been noted in the prior analysis. Thus, only the 20 m/s case is shown in Figure A.11d. This very clearly shows that the ability of the wing to morph its airfoil shape between baseline, monotonic and reflex substantially widens the performance envelope. However given all of this information, a question which remains unanswered is when each of these configurations is useful.

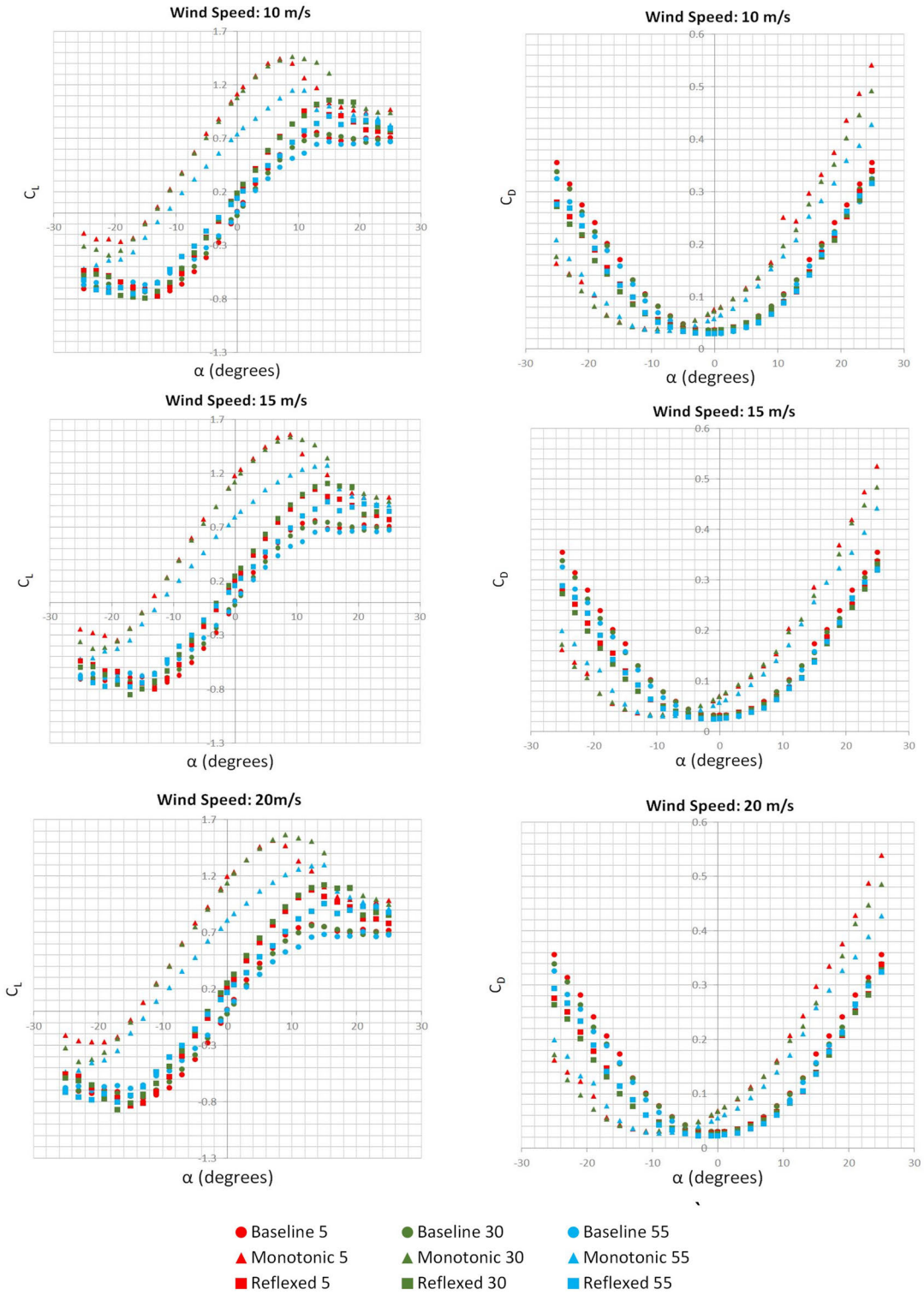

Figure A.10: Comparison of lift and drag coefficients across configurations, grouped by wind speed

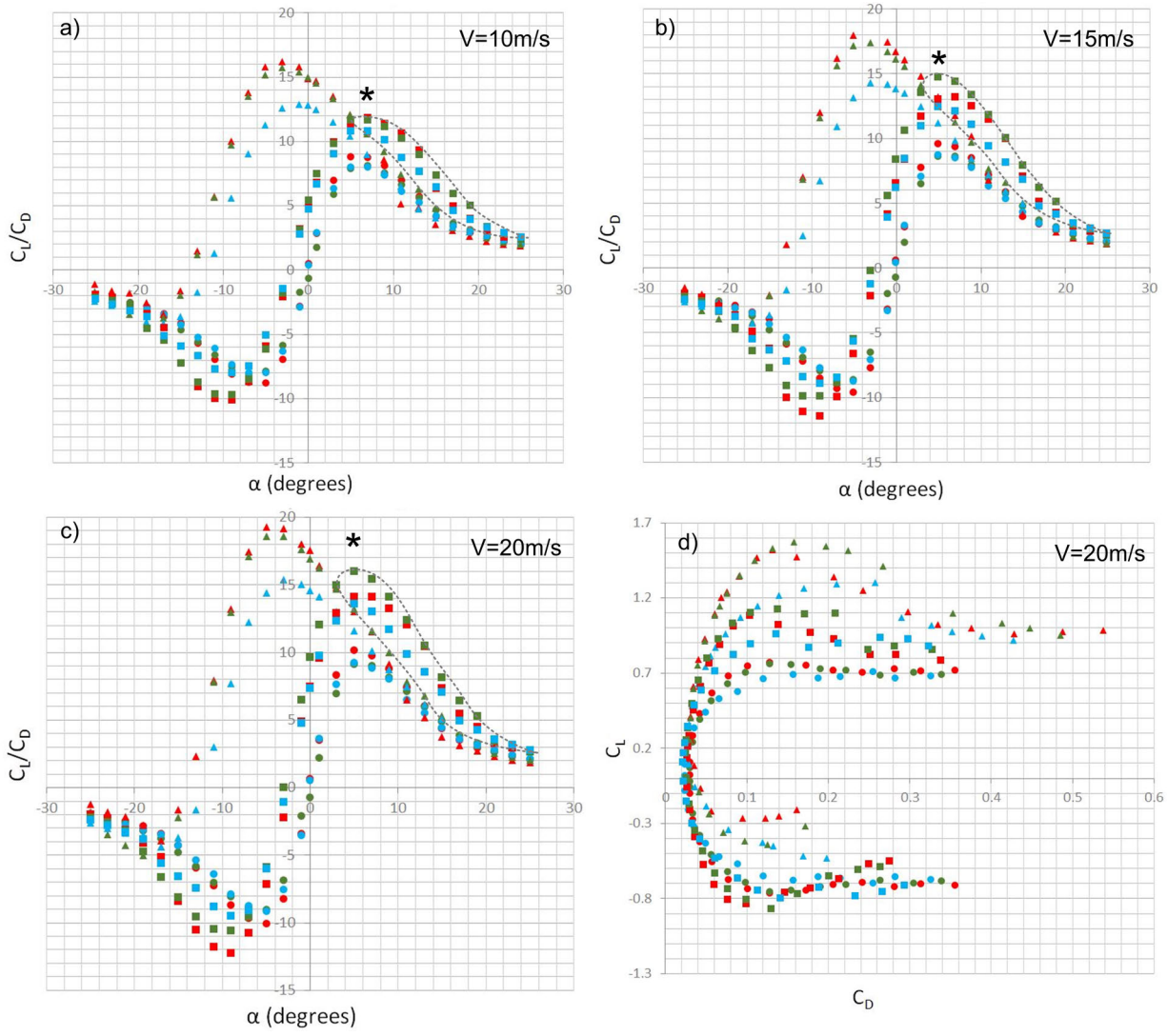

Figure A.11: Gliding performance using the same labeling convention as in Fig. 5 for a) 10 m/s b) 15 m/s c) 20 m/s; and d) Drag polar at 20 m/s

BIBLIOGRAPHY

[1] Gamble, L. L. and Inman, D. J., "Why morphology matters in birds and UAV's: How scale affects attitude wind sensitivit," *Applied Physics Letters*, Vol. 111, No. 20, 2017, pp. 203701.

[2] Mller, U. K. and Lentink, D., "Turning on a Dime," *Science*, 2004.

[3] Lentink, D., Muller, U. K., Stamhuis, E. J., Kat, R. D., Gestel, W. V., Veldhuis, L. M., P.Henningsson, Hedenstrom, A., Videler, J. J., and Leeuwen, J. L. V., "How swifts control their glide performance with morphing wings," *Nature*, Vol. 7139, No. 446, 2007, pp. 1082–1085.

[4] Gillies, J. A., Thomas, A. L. R., and Taylor, G. K., "Soaring and manoeuvring flight of a steppe eagle Aquila nipalensis," *Journal of Avian Biology*, Vol. 42, No. 5, 2011, pp. 377386.

[5] Tucker, V. A., "Gliding birds: the effect of variable wing span," *Journal of Experimental Biology*, Vol. 133, No. 1, 1987, pp. 33–58.

[6] Pennycuick, C. J., "A Wind-Tunnel Study of Gliding Flight in the Pigeon Columba Livia," *Journal of Experimental Biology*, Vol. 49, 1968, pp. 509–526.

[7] Kumar, R. and Shkarayev, S., "Kinematic and Aerodynamic Response of Locusts in Sideslip," *International Journal of Micro Air Vehicles*, Vol. 7, No. 2, 2015, pp. 159–180.

[8] Willmott, A. P. and Ellington, C. P., "The mechanics of flight in the hawkmoth Manduca sexta. I. Kinematics of hovering and forward flight," *Journal of experimental Biology*, Vol. 200, No. 21, 1997, pp. 2705–2722.

[9] Gibbs-Smith, C. H., "The Wright Brothers and Their Invention of the Practical Aeroplane," *Nature*, Vol. 198, 1963, pp. 824826.

[10] Culick, F. E. C., "The Wright Brothers: First Aeronautical Engineers and Test Pilots," *AIAA Journal*, Vol. 41, No. 6, 2003, pp. 985–1006.

[11] Jakab, P. L., "Visions of a Flying Machine: The Wright Brothers and the Process of Invention," *The American Historical Review*, Vol. 96, No. 4, 1991, pp. 1311.

[12] Padfield, G. D. and Lawrence, B., "The birth of the practical aeroplane: An appraisal of the Wright brothers' achievements in 1905," *The Aeronautical Journal*, Vol. 109, No. 1098, 2005, pp. 421–437.

[13] Weisshaar, T. A., "Morphing Aircraft Systems: Historical Perspectives and Future Challenges," *Journal of Aircraft*, Vol. 50, No. 2, 2013, pp. 337–353.

[14] Grant, R. G., "Flight100 years of aviation," *Aircraft Engineering and Aerospace Technology*, 2003.

[15] Gettelman, A., Kinnison, D. E., Dunkerton, T. J., and Brasseur, G. P., "Impact of monsoon circulations on the upper troposphere and lower stratosphere," *Journal of Geophysical Research: Atmospheres*, Vol. 109, No. 22, 2004.

[16] Shepard, E. L. C., Williamson, C., and Windsor, S. P., "Fine-scale flight strategies of gulls in urban airflows indicate risk and reward in city living," *Philosophical Transactions of the Royal Society B: Biological Sciences*, Vol. 371, 2016.

[17] Roth, M., "Review of atmospheric turbulence over cities," *Quarterly Journal of the Royal Meteorological Society*, Vol. 126, No. 564, 2007.

[18] R.Garratt, J., "Review: the atmospheric boundary layer," *Earth-Science Reviews*, Vol. 37, No. 1, 1994, pp. 89–134.

[19] Macdonald, R. W., "Modelling the mean velocity profile in the urban canopy layer," *Boundary-Layer Meteorology*, Vol. 97, No. 1, 2000, pp. 25–45.

[20] Tran, L. D., Cross, C. D., Motter, M. A., Neilan, J. H., Qualls, G., Rothhaar, P. M., Trujillo, A., and Allen, B. D., "Reinforcement Learning with Autonomous Small Unmanned Aerial Vehicles in Cluttered Environments," *15th AIAA Aviation Technology, Integration, and Operations Conference*, No. 2899, AIAA, 2015.

[21] Barry, A. J., Florence, P. R., and Tedrak, R., "Highspeed autonomous obstacle avoidance with pushbroom stereo," *ournal of Field Robotics*, Vol. 35, No. 1, 2018, pp. 52–68.

[22] Tennekes, H., *The simple science of flight: from insects to jumbo jets*, The MIT Press, 2009.

[23] Carruthers, A. C., Thomas, A. L., and Taylor, G. K., "Automatic aeroelastic devices in the wings of a steppe eagle Aquila nipalensis," *Journal of Experimental Biology*, 2007.

[24] Sachs, G. and Moelyadi, M. A., "CFD Based Determination of Aerodynamic Effects on-Birds with Extremely Large Dihedral," *Journal of Bionic Engineering*, Vol. 7, No. 1, 2010, pp. 95–101.

[25] Aldheeb, M. A., Asrar, W., Sulaeman, E., and Omar, A. A., "A review on aerodynamics of non-flapping bird wings," *Journal of Aerospace Technology and Management*, Vol. 8, No. 1, 2016, pp. 7–17.

[26] Dakin, R., Segre, P. S., Straw, A. D., and Altshuler, D. L., "Morphology, muscle capacity, skill, and maneuvering ability in hummingbirds," *Science*, Vol. 359, No. 6376, 2018, pp. 653–657.

[27] Withers, P. C., "An aerodynamic analysis of bird wings as fixed aerofoils," *Journal of Experimental Biology*, Vol. 90, No. 1, 1981, pp. 143–162.

[28] Sachs, G., "What can be learned from birds for achieving directional stability without a fin," *9th International Conference on Mathematical Problems in Engineering, Aerospace and Science*, Vol. 1493, AIP, 2012, pp. 838–846.

[29] Sachs, G., "Why birds and miniscale airplanes need no vertical tail," *Journal of Aircraft*, Vol. 44, No. 4, 2007, pp. 1159–1167.

[30] Sachs, G., "Yaw stability in gliding birds," *Journal of Ornithology*, Vol. 146, No. 3, 2005, pp. 191–199.

[31] Sachs, G., "Aerodynamic yawing moment characteristics of bird wings," *Journal of theoretical biology*, Vol. 234, No. 4, 2005, pp. 471–478.

[32] Tucker, V. A. and Parrott, G. C., "Aerodynamics of gliding flight in a falcon and other birds," *Journal of Experimental Biology*, Vol. 52, No. 2, 1970, pp. 345–367.

[33] Sachs, G., "Tail effects on yaw stability in birds," *Journal of Theoretical Biology*, Vol. 249, No. 3, 2007, pp. 464–472.

[34] Hummel, D., "Aerodynamic investigations on tail effects in birds," *Zeitschrift fr Flugwissenschaften und Weltraumforschung*, Vol. 16, No. 3, 1992, pp. 159–168.

[35] Pennycuick, C., "Chapter 1 - MECHANICS OF FLIGHT," *Avian Biology*, edited by D. S. FARNER and J. R. KING, Academic Press, Amsterdam, 1975, pp. 1 – 75.

[36] Thomas, A. L., "Why do Birds have Tails¡ The Tail as a Drag Reducing Flap and Trim Control," *Journal of Theoretical Biology*, Vol. 183, No. 3, 1996, pp. 247–253.

[37] Barbarino, S., Bilgen, O., Ajaj, R. M., Friswell, M. I., and Inman, D. J., "A Review of Morphing Aircraft," *Journal of Intelligent Material Systems and Structures*, Vol. 22, No. 9, 2011, pp. 823–877.

[38] Smith, J. W., Lock, W. P., , and Payne, G. A., "Variable-camber systems integration and operational performance of the AFTI/F-111 mission adaptive wing," Tech. Rep. 4370, NASA, 1992.

[39] McGowan, A.-M. R., Washburn, A. E., Horta, L. G., Bryant, R. G., Cox, D. E., Siochi, E. J., Padula, S. L., and Holloway, N. M., "Recent results from NASA's morphing project," *Industrial and Commercial Applications of Smart Structures Technologies*, SPIE, 2002.

[40] Wlezien, R., Horner, G., McGowan, A., Padula, S., Scott, M., Silcox, R., and Simpson, J., "The aircraft morphing program," *39th AIAA/ASME/ASCE/AHS/ASC Structures, Structural Dynamics, and Materials Conference and Exhibit*, No. 3326, SPIE, 1998.

[41] McGowan, A.-M. R., Horta, L. G., Harrison, J. S., and Raney, D. L., "Research Activities Within NASA's Morphing Program," Tech. Rep. ADP010487, National Aeronautics and Space Administration Hampton VA Langley Research Center, 2000.

[42] Gamble, L. L., Pankonien, A. M., and Inman., D. J., "Stall Recovery of a Morphing Wing via Extended Nonlinear Lifting-Line Theory," *AIAA*, Vol. 55, No. 9, 2017, pp. 2956–2963.

[43] Sanders, B., Eastep, F. E., and Forster, E., "Aerodynamic and Aeroelastic Characteristics of Wings with Conformal Control Surfaces for Morphing Aircraft," *Journal of Aircraft*, Vol. 40, No. 1, 2003, pp. 94–99.

[44] Bilgen, O., Kochersberger, K. B., and Inman, D. J., "Macro-fiber composite actuators for a swept wing unmanned aircraft," *The Aeronautical Journal*, Vol. 113, 2009, pp. 385–395.

[45] Otsuka, K. and Ren, X., "Physical metallurgy of TiNi-based shape memory alloys," *Progress in materials science*, Vol. 50, No. 5, 2005, pp. 511–678.

[46] Salowitz, N., Guo, Z., Li, Y.-H., Kim, K., Lanzara, G., and Chang, F.-K., "Bio-inspired stretchable network-based intelligent composites." *ournal of Composite Materials*, Vol. 47, No. 1, 2013, pp. 97–105.

[47] Phillips, D. M., Ray, C. W., Hagen, B. J., Su, W., Baur, J. W., and Reich, G. W., "Detection of flow separation and stagnation points using artificial hair sensors," *Smart Materials and Structures*, Vol. 24, No. 11, 2015, pp. 115026.

[48] Sr., J. U., Nguyen, N. T., and Dykman, J., "Development of Variable Camber Continuous Trailing Edge Flap System," *Fundamental Aeronautics Technical Conference*, 2012.

[49] Kaul, U. K. and Nguyen, N. T., "Drag optimization study of variable camber continuous trailing edge flap (VCCTEF) using OVERFLOW," *32nd AIAA Applied Aerodynamics Conference*, AIAA, 2014, p. 2444.

[50] Kaul, U. K. and Nguyen, N. T., "A 3-D Computational Study of a Variable Camber Continuous Trailing Edge Flap (VCCTEF) Spanwise Segment," *AIAA Applied Aerodynamics Conference*, A, 2015.

[51] Kota, S., Hetrick, J. A., Osborn, R., Paul, D., Pendleton, E., Flick, P., and Tilmann, C., "Design andapplication of compliant mechanisms for morphing aircraft structures," *Industrial and Commercial Applications of Smart Structures Technologies*, Vol. 5054, SPIE, 2003, pp. 24–34.

[52] Kota, S., Osborn, R., Ervin, G., Maric, D., Flick, P., and Paul, D., "Mission adaptive compliant wingdesign, fabrication and flight test," *RTO Applied Vehicle Technology Panel (AVT)*, 2009.

[53] Bowman, J., Sanders, B., and Weisshaar., T., "Evaluating the impact of morphing technologies on aircraft performance," *43rd AIAA/ASME/ASCE/AHS/ASC Structures, Structural Dynamics, and Materials Conference*, 2002.

[54] Seigler, T. M., Neal, D. A., Bae, J.-S., and Inman, D. J., "Modeling and flight control of large-scale morphing aircraft," *Journal of Aircraft*, Vol. 44, No. 4, 2007, pp. 1077–1087.

[55] Faria, C. T., Marqui, C. D., Inman, D. J., and Lopes, V., "Nonlinear dynamic model and simulation of morphing wing profile actuated by shape memory alloys," *Topics in Nonlinear Dynamics*, Society of Experimental Mechanics, 2012.

[56] Sofla, A. Y., Elzey, D. M., and Wadley., H. N., "An antagonistic flexural unit cell for design of shape morphing structures," *International Mechanical Engineering Congress and Exposition*, ASME, 2004.

[57] Woods, B. K. and Friswell, M. I., "Advanced kinematic tailoring for morphing aircraft actuation." *AIAA Journal*, Vol. 52, No. 4, 2014, pp. 788–798.

[58] Woods, B. K., Dayyani, I., and Friswell, M. I., "Fluid/structure-interaction analysis of the fish-bone-active-camber morphing concept," *Journal of Aircraft*, Vol. 52, No. 1, 2014, pp. 307–319.

[59] Ajaj, R. M., Flores, E. I. S., Friswell, M. I., and la O., F. D. D., "Span morphing using the compliant spar," *Journal of Aerospace Engineering*, Vol. 28, No. 4, 2014.

[60] Molinari, G., Quack, M., Dmitriev, V., Morari, M., Jenny, P., and Ermanni, P., "Aerostructural optimization of morphing airfoils for adaptive wings," *Journal of Intelligent Material Systems and Structures*, Vol. 22, No. 10, 2011, pp. 1075–1089.

[61] Bilgen, O., Kochersberger, K. B., Inman, D. J., and Ohanian, O. J., "Novel, Bidirectional, Variable-Camber Airfoil via Macro-Fiber Composite Actuators," *Journal of Aircraft*, Vol. 47, No. 1, 2010, pp. 303–314.

[62] Bilgen, O., Friswell, M., and Landman, D., "Low reynolds number behavior of a solid-state piezocomposite variable-camber wing," *54th Structures, Structural Dynamics, and Materials Conference*, 2013.

[63] Pankonien, A. M. and Inman, D. J., "Experimental Testing of Span-wise Morphing Trailing Edge Concept," *Smart Structures and Materials and Nondestructive Evaluation and Health Monitoring*, SPIE, 2013.

[64] Pankonien, A. M. and Inman, D. J., "Aerodynamic Performance of a Span-wise Morphing Trailing Edge Concept," *25th International Conference on Adaptive Structures and Technologies*, 2014.

[65] Pankonien, A. M. and Inman, D. J., "Spanwise Morphing Trailing Edge on a Finite Wing," *Active and Passive Smart Structures and Integrated Systems*, Vol. 9431, SPIE, 2015.

[66] Wickenheiser, A. M. and Garcia, E., "Optimization of perching maneuvers through vehicle morphing," *Journal of Guidance, Control, and Dynamics*, Vol. 31, No. 4, 2008, pp. 815–823.

[67] Regan, C., "In-flight stability analysis of the X-48B aircraft," *AIAA atmospheric flight mechanics conference and exhibit*, AIAA, 2008.

[68] Cusher, A. A. and Gopalarathnam, A., "Drag reduction methodology for adaptive tailless aircraft," *Journal of Aircraft*, Vol. 49, No. 1, 2012, pp. 161–172.

[69] Vicroy, D., "Blended-wing-vody low-speed flight dynamics: Summary of ground tests and sample results," *In 47th AIAA Aerospace Sciences Meeting including the New Horizons Forum and Aerospace Exposition*, 2009.

[70] Tomac, M. and Stenfelt, G., "Predictions of stability and control for a flying wing," *Aerospace Science and Technology*, Vol. 39, No. 179-186, 2014.

[71] Bye, D. and McClure, P., "Design of a morphing vehicle," *48th AIAA/ASME/ASCE/AHS/ASC Structures, Structural Dynamics, and Materials Conference*, 2007.

[72] Love, M., Zink, P., Stroud, R., Bye, D., Rizk, S., and White, D., "Demonstration of morphing technology through ground and wind tunnel tests," *48th Structures, Structural Dynamics, and Materials Conference*, A, 2007.

[73] Wildschek, A., Judas, M., Aversa, N., Grnewald, M., Maier, R., Deligiannidis, N., and Steigenberger, J., "Multi-Functional Morphing Trailing Edge for Control of All-Composite, All-Electric Flying Wing Aircraft," *The 26th Congress of ICAS and 8th AIAA ATIO*, 2008.

[74] Paranjape, A. A., Chung, S.-J., Hilton, H. H., and Chakravarthy, A., "Dynamics and performance of tailless micro aerial vehicle with flexible articulated wings," *AIAA journal*, Vol. 50, No. 5, 2012, pp. 1177–1188.

[75] Molinari, G., Arrieta, A. F., and Ermanni, P., "Planform, aero-structural, and flight control optimization for tailless morphing aircraft," *Active and Passive Smart Structures and Integrated Systems*, No. 9431, SPIE, 2015.

[76] Guiler, R. and Huebsch, W., "Control of a swept wing tailless aircraft through wing morphing," *26th International Congress of the Aeronautical Sciences*, 2008.

[77] Guiler, R. and Huebsch, W., "Wind tunnel analysis of a morphing swept wing tailless aircraft," *23rd AIAA Applied Aerodynamics Conference*, AIAA, 2005.

[78] Cai, G., Lum, K.-Y., Chen, B. M., and Lee, T. H., "A brief overview on miniature fixed-wing unmanned aerial vehicles," *Control and Automation (ICCA)*, IEEE, 2010, pp. 285–290.

[79] Stenfelt, G. and Ringertz, U., "Yaw control of a tailless aircraft configuration," *Journal of Aircraft*, Vol. 47, No. 5, 2010, pp. 1807–1811.

[80] Jeong, B., Lee, D., Shim, H., Ahn, J., Choi, H.-L., Park, S.-O., , and Oh, S.-Y., "Yaw-Control Spoiler Design Using Design of Experiments Based Wind Tunnel Testing," *Journal of Aircraft*, Vol. 52, No. 2, 2014, pp. 713–718.

[81] Stenfelt, G. and Ringertz, U., "Lateral stability and control of a tailless aircraft configuration," *Journal of Aircraft*, Vol. 46, No. 9, 2009, pp. 2161–2164.

[82] Warrick, D. R., Hedrick, T. L., Biewener, A. A., Crandell, K. E., and Tobalske, B. W., "Foraging at the edge of the world: low-altitude, high-speed manoeuvering in barn swallows," *Philosophical Transactions of the Royal Society B*, Vol. 371, 2016.

[83] Spear, L. B. and Ainley, D. G., "Flight speed of seabirds in relation to wind speed and direction," *Ibis*, Vol. 139, No. 2, 1997, pp. 234251.

[84] Kalnay, E., Kanamitsu, M., Kistler, R., Collins, W., Deaven, D., Gandin, L., Iredell, M., Saha, S., White, G., Woollen, J., Zhu, Y., Chelliah, M., Ebisuzaki, W., Higgins, W., Janowiak, J., Mo, K. C., Ropelewski, C., Wang, J., Leetmaa, A., Reynolds, R., Jenne, R., , and Joseph, D., "The NCEP/NCAR 40-Year Reanalysis Project," *Bulletin of the American Meteorological Society*, Vol. 77, No. 3, 1996, pp. 437–472.

[85] Burley, M. W., Ritchie, E. M., and Gray, C. R., "Winds of the upper troposphere and lower stratosphere over the united states," *Monthly Weather Review*, 1956, pp. 11–18.

[86] Alerstam, T., Rosn, M., Bckman, J., Ericson, P. G. P., and Hellgren, O., "Flight speeds among bird species: allometric and phylogenetic effects," *PLoS Biology*, Vol. 5, No. 8, 2007, pp. 1656–1662.

[87] Schmidt, L. V., *Introduction to aircraft flight dynamics*, AIAA, 1998.

[88] Lentink, D., Haselsteiner, A. F., and Ingersoll, R., "In vivo recording of aerodynamic force with an aerodynamic force platform: from drones to birds," *Journal of The Royal Society Interface*, Vol. 12, No. 1, 2015.

[89] Pankonien, A. M., *Smart Material Wing Morphing for Unmanned Aerial Vehicles*, Ph.D. thesis, University of Michigan, 2015.

[90] Pankonien, A. M., Duraisamy, K., Faria, C. T., and Inman, D. J., "Synergistic smart morphing aileron: Aero-structural performance analysis," *22nd Adaptive Structures Conference*, AIAA/ASME/AHS, 2014.

[91] Anderson, J. D., *Fundamentals of Aerodynamics*, McGraw-Hill, 1984.

[92] Gamble, L. L., Pankonien, A. M., and Inman, D. J., "Stall Recovery of the Span-wise Morphing Trailing Edge Concept via an Optimized Nonlinear Model," *26th International conference on Adaptive Structures and Technologies*, 2015.

[93] Pankonien, A. M., Faria, C. T., and Inman, D. J., "Synergistic smart morphing aileron: Experimental quasi-static performance characterization," *Journal of Intelligent Material Systems and Structures*, Vol. 26, No. 10, 2015, pp. 1179–1190.

[94] Sivells, J. C. and Neely, R. H., "Method for Calculating Wing Characteristics by Lifting-Line Theory using Nonlinear Section Lift Data," Tech. Rep. 865, NASA, 1947.

[95] Piszkin, S. T. and Levinsky, E. S., "Nonlinear Lifting Line Theory for Predicting Stalling Instabilities on Wings of Moderate Aspect Ratio," Tech. Rep. ADA027645, General Dynamics, 1976.

[96] Chattot, J.-J., "Analysis and Design of Wings and Wing/Winglet Combinations at Low Speeds," *42nd AIAA Aerospace Science Meeting and Exhibit*, Vol. 220, AIAA, 2004.

[97] Wickenheiser, A. and Garcia, E., "Aerodynamic modeling of morphing wings using an extended lifting-line analysis," *ournal of Aircraft*, Vol. 44, No. 1, 2007, pp. 10–16.

[98] Wickenheiser, A. and Garcia, E., "Extended nonlinear lifting-line method for aerodynamic modeling of reconfigurable aircraft," *Journal of Aircraft*, Vol. 48, No. 5, 2011, pp. 1812–1817.

[99] Tani, I., "A simple method of calculating the induced velocity of a monoplane wing," Tech. Rep. 111, Aeronautical Research Institute, Tokyo Imperial University, 1934.

[100] Gopalarathnam, A. and Segawa, H., "Use of Lift Superposition for Improved Computational Efficiency of Wing Post-Stall Prediction," *Applied Aerodynamics Conference*, AIAA, 2008.

[101] Chattot, J.-J., "Low speed design and analysis of wing/winglet combinations including viscous effects," *Journal of Aircraft*, Vol. 43, No. 2, 2006, pp. 386–389.

[102] Chattot, J.-J., "Optimization of Wind Turbines Using Helicoidal Vortex Model," *Journal of Solar Energy Engineering*, Vol. 125, No. 4, 2003, pp. 418–424.

[103] Gallay, S., Ghasemi, S., and Laurendeau, E., "Sweep effects on non-linear Lifting Line Theory near Stall," *Scitech: Aerospace Sciences Meeting*, No. 1105, AIAA, 2014.

[104] Aranake, A. C., Lakshminarayan, V. K., and Duraisamy, K., "Computational analysis of shrouded wind turbine configurations using a 3-dimensional RANS solver," *Renewable Energy*, Vol. 75, 2015, pp. 818–832.

[105] Bremseth, J. and Duraisamy, K., "Computational analysis of vertical axis wind turbine arrays," *Theoretical and Computational Fluid Dynamics*, Vol. 30, No. 5, 2016, pp. 387–401.

[106] Latalski, J., "Modelling of macro fiber composite piezoelectric active elements in ABAQUS system," *Eksploatacja i Niezawodnosc-Maintenance and Reliability 4*, Vol. 4, 2011, pp. 72–78.

[107] Cote, F., Masson, P., Mrad, N., and Cotoni, V., "Dynamic and static modelling of piezoelectric composite structures using a thermal analogy with MSC/NASTRAN," *Composite Structures*, Vol. 65, No. 3, 2004, pp. 471–484.

[108] "Standard on Piezoelectricity," 1988.

[109] Lee, A. J., Moosavian, A., and Inman, D. J., "Control and characterization of a bistable laminate generated with piezoelectricity," *Smart Materials and Structures*, Vol. 26, No. 8, 2017.

[110] Olympio, K. R. and Gandhi, F., "Flexible skins for morphingaircraft using cellular honeycomb cores," *Journal of Intelligent Material Systems and Structures*, Vol. 21, No. 17, 2010, pp. 1719–1735.

[111] Pankonien, A. M. and Inman, D. J., "Aeroelastic performance evaluation of a flexure box morphing airfoil concept," *Active and Passive Smart Structures and Integrated Systems*, Vol. 905716, SPIE, 2014.

[112] Donlan, C. J., "An interim report on the stability and control of tailless airplanes," Tech. Rep. 796, Langley Stability Research Center, 1944.

[113] Bragg, M. B., "Experimental aerodynamic characteristics of an NACA 0012 airfoil with simulated glaze ice," *Journal of Aircraft*, Vol. 25, No. 9, 1988, pp. 849–854.

[114] Gamble, L. L. and Inman, D. J., "Yaw Control of a Smart Morphing Tailless Aircraft Concept," *5th International Conference on Smart and Multifunctional Materials, Structures and Systems*, 2016.

[115] Gamble, L. L. and Inman, D. J., "Aerodynamic Performance of a Bioinspired Morphing Tailless Aircraft Concept," *27th International conference on Adaptive Structures and Technologies*, 2017.

[116] Gamble, L. L. and Inman, D. J., "A tale of two tails: Developing an avian inspired morphing actuator for yaw control and stability," *Bioinspiration and Biomimetics*, Vol. 13, No. 2, 2018.

[117] Gamble, L. L. and Inman, D. J., "Bioinspired pitch control using a piezoelectric horizontal tail for rudderless UAVs," *Smart Structures and Materials and Nondestructive Evaluation and Health Monitoring*, SPIE, 2018.

[118] Previtali, F., Arrieta, A. F., and Ermanni, P., "Performance of a three-dimensional morphing wing and comparison with a conventional wing," *AIAA*, Vol. 52, No. 10, 2014, pp. 2101–2113.

[119] Marks, C. R., Joo, J. J., and Reich, G. W., "A reconfigurable wing for biomimetic aircraft," *54th Structures, Structural Dynamics, and Materials Conference*, A, 2013.

[120] Beaverstock, C. S., Woods, B. K., Fincham, J. H., and Friswell., M. I., "Performance Comparison between Optimised Camber and Span for a Morphing Wing," *Aerospace*, Vol. 2, No. 3, 2015, pp. 524–554.